

# University of St Andrews



Full metadata for this thesis is available in  
St Andrews Research Repository  
at:

<http://research-repository.st-andrews.ac.uk/>

This thesis is protected by original copyright

# Effects of Atmospheric Turbulence on Millimetre Wave Propagation in the Surface Boundary Layer

By

Mark Evans

Thesis submitted to the  
UNIVERSITY OF ST ANDREWS  
in candidature for the Degree of  
Doctor of Philosophy



School of Physics and Astronomy  
University of St Andrews  
2004

Th  
E600

Declarations:

(i) I, Mark Evans, hereby certify that this thesis, which is approximately 35,000 words in length, has been written by me, that it is the record of work carried out by me and that it has not been submitted in any previous application for a higher degree.

Mark Evans  
April 2004

(ii) I was admitted as a research student in October 1999 and as a candidate for the degree of Ph.D. in October 2000; the higher study for which this is a record was carried out in the University of St Andrews between 1999 and 2003.

Mark Evans  
April 2004

(iii) I hereby certify that the candidate has fulfilled the conditions of the Resolution and Regulations appropriate for the degree of Ph.D. in the University of St Andrews and that the candidate is qualified to submit this thesis in application for that degree.

James C G Lesurf  
April 2004

In submitting this thesis to the University of St Andrews I understand that I am giving permission for it to be made available for use in accordance with the regulations of the University Library for the time being in force, subject to any copyright vested in the work not being affected thereby. I also understand that the title and abstract will be published, and that a copy of the work may be made and supplied to any bona fide library or research worker.

Mark Evans  
April 2004

## *Acknowledgements*

In carrying out the research presented in this thesis I received help and advice from a number of people. Firstly, I would like to express my gratitude to Dr Ammad Akram for providing me with the opportunity to study for a PhD. Also, for their guidance throughout the work described in this thesis, I would like to thank Professor Paul Cannon, Dr Anil Shukla, Dr Jim Lesurf and Dr Graham Smith.

Finally, I would like to thank my parents for their constant encouragement and my wife for her understanding and support during the many ups and downs of writing this thesis.

Mark Evans

## *Abstract*

The turbulent atmosphere imposes natural limitations on the propagation of radiowaves at millimetre wavelengths. Fluctuations in temperature, pressure and relative humidity produce small-scale refractive index inhomogeneities that are transported through the atmosphere by thermal convection and advection, appearing to millimetre wave signals as lenses that focus and defocus the propagating wavefront. The rapid lensing produces amplitude, phase and angle-of-arrival fluctuations that impair communication and sensing systems. These impairments can be particularly significant in the Earth's surface boundary layer where turbulent fluxes are at their most significant.

The research presented in this thesis has considered the effects of atmospheric turbulence on millimetre wave propagation in the surface boundary layer. This was accomplished using a specially designed five-element array to measure the temporal and spatial properties of tropospheric amplitude scintillation. Analysis of collected data from a month long measurement campaign shows amplitude scintillation events with peak-to-peak fluctuations of 10dB and event durations of up to 20 minutes. The intensity of scintillation is shown to follow a diurnal cycle that reaches a peak in the afternoon when air temperature is a maximum and falls to a minimum during nocturnal hours when air temperature is a minimum. The strongest individual scintillation events were measured during nocturnal and early morning hours when deep clear-air multipath fading ( $>17\text{dB}$ ) was also observed. It is therefore concluded that the most significant impairments to millimetre wave propagation in the surface boundary layer occur during nocturnal hours.

An analysis of the spatial characteristics of amplitude scintillation showed the decorrelation distance of turbulence follows a diurnal cycle that is inversely related to the cycle of turbulence intensity. Hence, when turbulence intensity peaks in the afternoon its spatial decorrelation is a minimum. Measurement of the spatial decorrelation of scintillation was found to be larger than predicted by Tatarski's correlation function. It was shown that turbulent structures producing scintillation in the surface boundary layer are 2 times larger than the predicted first Fresnel zone size.

Temporal measurements of amplitude scintillation were also used to predict wavefront distortion using structure functions. Scintillation data was converted to values of the refractive index structure function parameter in the range 3 to  $17 \times 10^{-14} \text{ m}^{-2/3}$ . It is shown that spatial phase fluctuations of  $20^\circ$  are predicted for antenna separation distances of 10m, with  $0.23^\circ$  angle-of-arrival fluctuations resulting in tracking errors of up to 200m for path lengths of 50km.

In conclusion, the research described in this thesis shows that atmospheric turbulence in the surface boundary layer can significantly impair systems operating at millimetre wave frequencies. This applies to single and array based antenna systems.

# Contents

## Chapter One

### Introduction

1.1	Background.....	1
1.2	Thesis structure.....	3

## Chapter Two

### Review of Millimetre Wave Propagation

2.1	Introduction.....	4
2.2	Atmospheric factors governing millimetre wave propagation.....	4
2.2.1	Gasèous absorption.....	5
2.2.2	Hydrometeor attenuation and cross-polarisation.....	8
2.2.2.1	<i>Rain</i> .....	8
2.2.2.2	<i>Snow, hail, graupel, sleet and the melting layer</i> .....	12
2.2.2.3	<i>Fog and cloud</i> .....	13
2.2.3	Sand and dust.....	16
2.2.4	Refractive index structure of the atmosphere.....	17
2.2.4.1	<i>Radio refractive index</i> .....	17
2.2.4.2	<i>The effect of the large scale refractive index structure of the atmosphere on radiowave propagation</i> .....	18
2.2.4.3	<i>The effect of the medium scale refractive index structure of the atmosphere on radiowave propagation</i> .....	21
2.2.5	Summary.....	27
2.3	Atmospheric turbulence.....	29
2.3.1	The structure of the tropospheric boundary layer.....	29
2.3.2	Turbulent flows and energy transfer.....	32
2.3.2.1	<i>Kolmogorov spectrum</i> .....	32
2.3.2.2	<i>Reynolds number</i> .....	35
2.3.2.3	<i>Taylor's 'Frozen-in' Hypothesis</i> .....	36
2.4	Turbulence induced impairments to wave propagation.....	37
2.4.1	Scintillation.....	37
2.4.1.1	<i>Definition of the first Fresnel zone</i> .....	38
2.4.1.2	<i>Fluctuation spectral density</i> .....	39
2.4.1.3	<i>Spatial decorrelation distance of eddy induced fluctuations</i> .....	42
2.4.1.4	<i>Previous investigations into scintillation</i> .....	46
2.4.2	Wavefront distortion.....	49
2.4.2.1	<i>Previous investigations into wavefront distortion</i> .....	51
2.5	Summary.....	52

## Chapter Three

### Design of a Sensor Array for Measuring the Temporal and Spatial Effects of Atmospheric Turbulence

3.1	Introduction.....	54
3.2	Requirements of the sensor array.....	54
3.2.1	Experimental link.....	56
3.3	Detailed design.....	57
3.3.1	Lens horn antennas.....	60
3.3.2	MMIC receivers.....	61

3.3.3	Second stage down conversion.....	64
3.3.4	LO signal generation.....	64
3.3.5	Filtering and amplification.....	65
3.3.5.1	<i>Filter sub-circuit</i> .....	67
3.3.5.2	<i>Amplifier sub-circuit</i> .....	69
3.3.6	Data acquisition.....	70
3.3.7	Mechanical structure.....	72
3.4	Link budget analysis.....	74
3.5	System performance.....	76
3.6	Summary.....	80

## **Chapter Four**

### **Clear-air Multipath from Tropospheric Layers**

4.1	Introduction.....	82
4.2	Multipath from ground-based layers.....	82
4.2.1	Evolution of nocturnal radiative layers.....	83
4.2.2	Nocturnal multipath occurrence.....	85
4.2.3	Late morning multipath.....	89
4.3	Multipath from oscillating layers.....	95
4.4	Impact of clear-air multipath on system performance.....	99
4.5	Summary.....	100

## **Chapter Five**

### **Tropospheric Amplitude Scintillation**

5.1	Introduction.....	102
5.2	Log-amplitude scintillation.....	102
5.3	Log-amplitude scintillation variance.....	104
5.4	Probability density.....	109
5.5	Power spectral density.....	113
5.5.1	Analysis method for extracting scintillation spectra.....	114
5.5.2	Experimental data.....	115
5.6	Diurnal variation.....	117
5.7	Simultaneous scintillation and clear-air multipath.....	123
5.8	Summary.....	125

## **Chapter Six**

### **Spatial Characteristics of Amplitude Scintillation**

6.1	Introduction.....	128
6.2	Theory.....	128
6.2.1	Tatarski's correlation function.....	129
6.3	Experiment results.....	131
6.3.1	Sensor array configuration.....	131
6.3.2	Results.....	132
6.4	Implication of measured decorrelation scale-length.....	148
6.5	Summary.....	151

## **Chapter Seven**

### **Wavefront Distortion**

7.1	Introduction.....	153
-----	-------------------	-----

7.2	Structure functions.....	153
7.2.1	The refractive index structure function parameter.....	156
7.3	Calculation of $C_n^2$ from measured values of $\sigma_\chi^2$ .....	158
7.3.1	Evaluation of $C_n^2$ calculated values.....	161
7.4	Refractive index fluctuations.....	163
7.5	Phase fluctuations.....	164
7.6	Angle-of-arrival fluctuations.....	166
7.7	Summary.....	170

## Chapter Eight

### Conclusions

8.1	Purpose of research.....	171
8.2	Summary of results.....	171
8.3	Future work.....	174

<b>References</b> .....	176
-------------------------	-----

# Chapter One

## Introduction

### 1.1 Background

The demand placed on the electromagnetic spectrum for wider bandwidths to be made available for higher data rate communication systems is ever increasing. To satisfy the requirements for greater spectrum utilisation frequencies in the millimetre wave band (30-300GHz) are being considered for a diverse range of applications in commercial and military systems.

The millimetre wave band provides large bandwidths for multimedia video and Internet access (Craig, 1999; Dettmer, 2000; Fowler, 2001). The atmosphere, however, imposes limitations on such systems through turbulence, gaseous absorption and hydrometeor attenuation. The purpose of the research presented in this thesis is to investigate the effects of atmospheric turbulence on millimetre wave propagation.

The term atmospheric turbulence refers to small-scale refractive index inhomogeneities (eddies) that are produced by fluctuations in temperature, pressure and humidity. These small-scale eddies are transported through the atmosphere by convection and advection, appearing to millimetre wave signals as lenses that focus and defocus the propagating wavefront. The rapid lensing of the propagating signals (scintillation) produce amplitude, phase and angle-of-arrival variations that impairs communication and sensing systems.

Turbulence occurs in the atmosphere by one of three mechanisms: wind shear, cloud entrainment and thermal convection. Wind shears produce turbulence through frictional drag of cold and warm wind interactions that predominantly occur at high altitudes and can be sufficiently intense that aircraft stability is affected. Turbulence is produced in clouds when differences in saturated and unsaturated air masses entrain (mix). This can lead to long periods (hours) of scintillation on Earth-space communication links. Turbulence generated by thermal convection occurs through evaporation of water vapour from the Earth's surface following solar heating. This leads to scintillation on communication links and radar systems in the surface boundary layer.

The research in this thesis is concerned with turbulence in the surface boundary layer. This is the lowest 10% of the tropospheric boundary layer (~100m above the Earth) where turbulence is most significant. Previous research into tropospheric scintillation in the surface boundary layer has been sparse in comparison to Earth-space communication systems. This was identified in the final report of the European Commission's Cooperation in the field of Science and Technology (COST) action 235 (COST, 1996). This action, titled 'Radiowave propagation and its effects on next generation fixed-service terrestrial telecommunications systems', states that it is difficult to characterise the effect of scintillation on links in the surface boundary layer because there is very limited experimental data. This conclusion was further endorsed by the later COST action 280 (Propagation impairment mitigation techniques for millimetre wave radio systems). The research presented in this thesis will therefore provide valuable information in an area that is recognised as being under researched.

## 1.2 Thesis structure

The structure of this thesis consists of a literature review, five subject areas and conclusions. It is divided into the following chapters:

*Chapter Two* reviews the factors that govern millimetre wave propagation including gaseous absorption, hydrometeor attenuation and turbulence.

*Chapter Three* presents the design of a five-element sensor array that has been specifically developed for investigating atmospheric turbulence in the surface boundary layer.

*Chapter Four* describes clear-air multipath from tropospheric refractive index layering correlated with ground-based meteorology.

*Chapter Five* presents a detailed study of the temporal characteristics of tropospheric amplitude scintillation.

*Chapter Six* examines the spatial characteristics of amplitude scintillation including the decorrelation of atmospheric turbulence.

*Chapter Seven* investigates wavefront distortion using temporal measurements of amplitude scintillation and Tatarski's (1961) phase structure function.

*Chapter Eight* concludes the thesis with a review of the research carried out and plans for future work.

# Chapter Two

## Review of Millimetre Wave Propagation

### 2.1 Introduction

This chapter reviews the meteorological factors that influence millimetre wave propagation. Specific reference is made to frequencies around 36GHz as the experimental work described in later chapters was performed at this frequency.

The characteristics of atmospheric turbulence are presented including a review of the current state of research into turbulence-induced scintillation and wavefront distortion. To set turbulence-induced impairments in context, this review begins by considering gaseous absorption and hydrometeor attenuation.

### 2.2 Atmospheric factors governing millimetre wave propagation

Millimetre waves have for some time been used for remotely sensing the structure of the atmosphere. This is because of their interaction with atmospheric gases (e.g. oxygen), which absorbs and re-emits the energy as radiation at specific spectral lines (Hall et al, 1996). An unfortunate consequence of this interaction process is that millimetre wave communications are limited in path length and availability. In the following sections the main factors that limit millimetre wave propagation are presented along with models used to predict their impact on system performance.

### 2.2.1 Gaseous absorption

The main gaseous constituents of the atmosphere that affect millimetre wave propagation are oxygen and water vapour. They impair wave propagation by absorbing electromagnetic energy thereby attenuating signal strength. The specific attenuation can be calculated at any value of pressure, temperature and humidity by summing the individual oxygen and water vapour resonance lines (International Telecommunication Union–Radio (ITU-R) P.676). Alternatively, ITU–R P.676 recommends a simplified model based on curve fitting to the line-by-line method for frequencies in the range 1 to 350GHz, and from sea level to an altitude of 5km. The accuracy of the curve fitting technique when compared to the line-by-line method is reported in ITU–R P.676 to vary between 0.1dB/km to 0.7dB/km with a peak error occurring near 60GHz. The curve fitting technique consists of four models that are functions of path elevation angle ( $\varphi$ ). They are:

- (a) For horizontal paths close to the ground:

$$A = (\gamma_o + \gamma_w)r_o \quad \text{dB} \quad (2-1)$$

where  $r_o$  (km) is the path length,  $\gamma_o$  (dB/km) is the specific attenuation due to oxygen and  $\gamma_w$  (dB/km) is the specific attenuation due to water vapour. Both  $\gamma_o$  and  $\gamma_w$  are frequency dependant terms.

- (b) For  $0^\circ < \varphi < 10^\circ$ :

$$A = \frac{\sqrt{R_e}}{\cos \varphi} \left[ \gamma_o \sqrt{h_o} F \left( \tan \varphi \sqrt{\frac{R_e}{h_o}} \right) + \gamma_w \sqrt{h_w} F \left( \tan \varphi \sqrt{\frac{R_e}{h_w}} \right) \right] \quad \text{dB} \quad (2-2)$$

where  $\varphi$  is in degrees,  $R_e$  is the effective Earth radius (8500km),  $F$  is a function defined by:

$$F(x) = \frac{1}{0.661x + 0.339\sqrt{x^2 + 5.51}} \quad (2-3)$$

and  $h_o$  (km) and  $h_w$  (km) are equivalent scale heights for oxygen and water vapour respectively. The concept of equivalent height is based on the assumption of an exponential atmosphere specified by a scale height to describe the decay in density with altitude. The equivalent height is used to obtain the attenuation for slant and zenith paths from specific attenuation.

(c) For  $10^\circ < \varphi < 90^\circ$ :

$$A = \frac{\gamma_o h_o + \gamma_w h_w}{\sin \varphi} \quad \text{dB} \quad (2-4)$$

(d) For  $90^\circ$ :

$$A = \gamma_o h_o + \gamma_w h_w \quad \text{dB} \quad (2-5)$$

An example of the specific attenuation at sea level for standard atmospheric values of pressure, temperature and water vapour density is shown in Figure 2-1.

Figure 2-1 illustrates the frequency dependence of gaseous attenuation through the microwave and millimetre wave bands. The high attenuation spectral regions for oxygen are 60 and 119GHz, and for water vapour are 22, 183 and 325GHz. There is currently little application for communication systems at these frequencies, with the exception of 60GHz where the high degree of attenuation is advantageously used for secure (short range) communications.

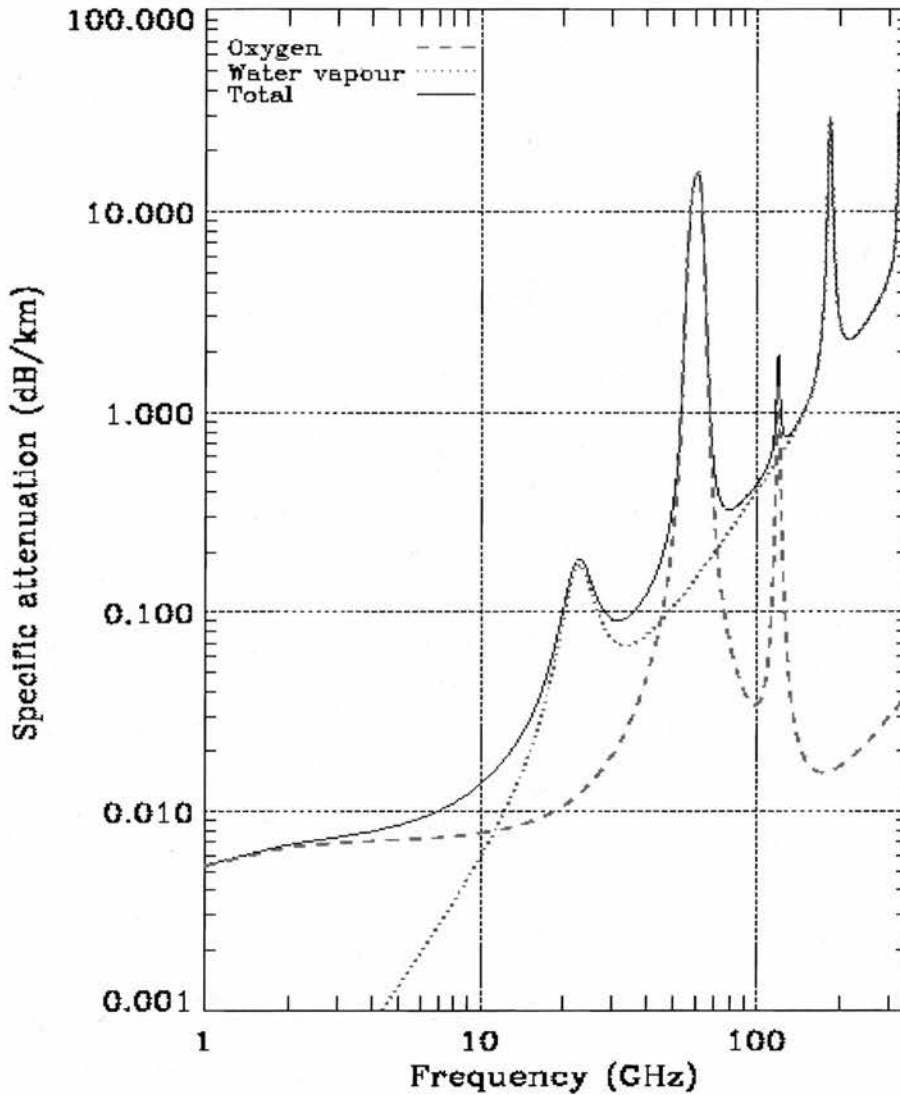


Figure 2-1 Specific gaseous attenuation at ground level (ITU-R P.676). The pressure is 1013hPa, the temperature is 15°C and the water vapour density is 7.5g/m<sup>3</sup>.

The low attenuation spectral regions, called propagation windows, occur at frequencies of 35, 95, 130 and 220GHz. These spectral regions are becoming more important for communication systems as the demand for wideband multimedia applications increases, and the availability of spectrum in the microwave band (3-30GHz) diminishes. The 35GHz region, which is the focus of this thesis, is currently of most interest to system designers as it offers low gaseous attenuation (~0.1dB/km) across a large spectral region (~35-42GHz).

The above description of gaseous attenuation shows that atmospheric windows define regions where millimetre wave communication systems can operate with relatively low attenuation. This description, however, is incomplete as weather mechanisms can impair regions of the millimetre wave band to a far greater extent than gaseous attenuation, e.g. many 10s of dB/km. The most significant of these, especially for frequencies in the 35GHz region, are hydrometeors.

## 2.2.2 Hydrometeor attenuation and cross-polarisation

The most significant atmospheric impairment to millimetre wave propagation is attenuation by hydrometeors, e.g. rain, hail, sleet, snow, fog and cloud. Attenuation results from small displacement currents set up in the hydrometeors by the interaction process with the electromagnetic wave. The small displacement currents, the magnitude of which depends on drop size, give rise to re-radiation (scattering) and absorption due to heating (Hall, 1979). At microwave frequencies the wavelength (1-10cm) is long in comparison to drop size (typically 5mm) and absorption is generally greater than scattering. At millimetre wave frequencies (1-10mm) the opposite is true.

The following considers each type of hydrometeor individually and outlines the models used to predict their affect on millimetre wave communication systems.

### 2.2.2.1 Rain

The method used by communication system planners to predict attenuation exceeded in the average year due to rainfall is given by the function (ITU-R P.838):

$$\gamma_R = kR^\alpha \quad \text{dB/km} \quad (2-6)$$

where  $R$  (mm/h) is the rainfall rate for a given geographical location that can be measured or predicted (ITU-R P.837), and both  $k$  and  $\alpha$  are coefficients that are dependant on frequency (in the range 1 to 400GHz), path elevation angle and antenna polarisation. Some of the important properties of rainfall to consider for millimetre wave propagation are:

- a. Small raindrops (e.g. 1mm) are approximately spherical and attenuate horizontally and vertically polarised waves equally.
- b. Large raindrops (e.g. > 1mm) are for the purpose of modelling considered oblate spheroids with their axis of symmetry in the vertical plane (Prupacher and Pitter, 1971). A more precise definition of their shape suggests an oblate spheroid with a flattened base that becomes concave as the raindrop size increases above 4mm (Hall et al, 1996).
- c. Raindrops larger than 9mm are hydrodynamically unstable and break up on descent.
- d. The oblate shape of large raindrops means that absorption and reflectivity is greater for horizontally polarised waves than vertically polarised waves (Chu, 1974; Oguchi and Hosoya, 1974). For circular polarisation attenuation is the sum of half the horizontal plus half the vertical attenuation.
- e. At high elevation angles the projection of raindrops on the plane normal to the propagation path is circular. In this case the attenuation of horizontal and vertical polarisation is similar.

- f. The orientation of raindrops can be shifted (called a canting (tilt) angle) by wind shears and turbulence (Saunders, 1971). A tilt in the orientation of raindrops due to wind shear (Brussaard, 1976) or a spread of orientations due to turbulence can affect the attenuation relationship between vertically and horizontally polarised signals.

The high degree of spatial inhomogeneity in rain intensity needs to be considered when predicting attenuation, i.e. constant rain intensity does not extend uniformly over the total length of the propagation path. To account for this inhomogeneity an effective path length is used to represent the propagation distance through an equivalent constant rain volume. For terrestrial paths the rain attenuation exceeded 0.01% of the average year is given by ITU-R P.530 as:

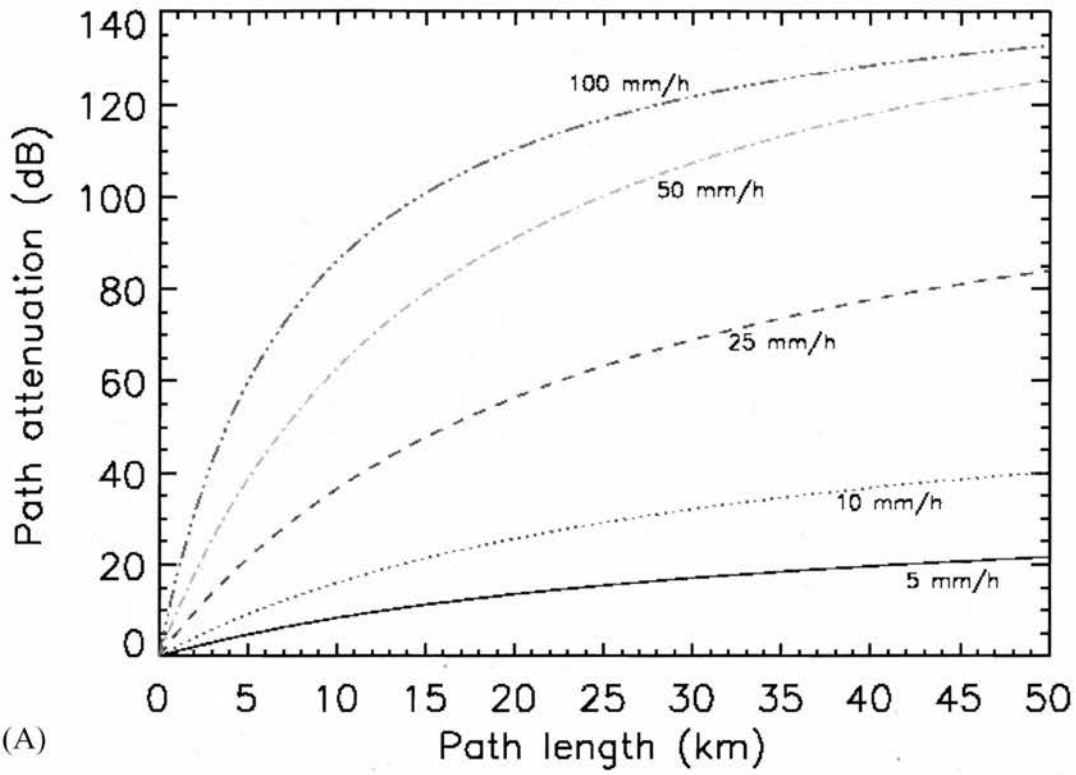
$$A_{0.01} = \gamma_R d_{eff} \quad \text{dB} \quad (2-7)$$

where  $d_{eff}$  (km) is the effective path length including a path length reduction factor to compensate for the spatial inhomogeneity in rain intensity. For Earth-space paths the attenuation exceeded 0.01% of the average year is given by ITU-R P.618:

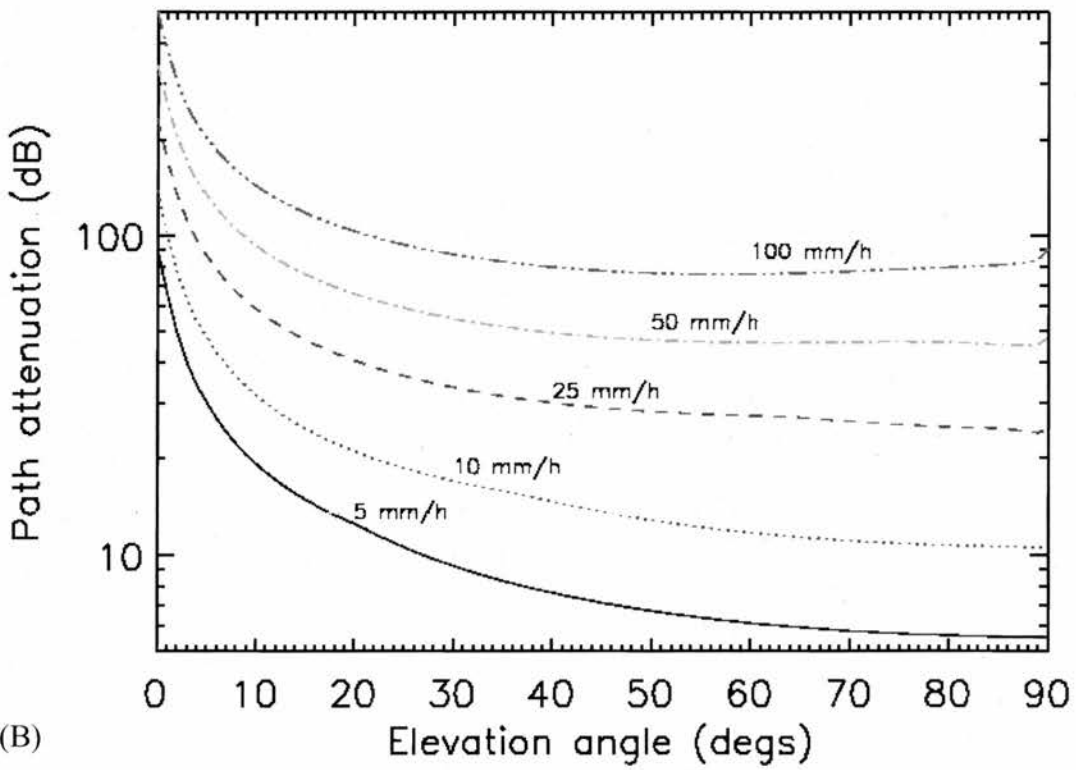
$$A_{0.01} = \gamma_R L_E \quad \text{dB} \quad (2-8)$$

where  $L_E$  (km) is the effective path length that incorporates a path length reduction factor to take account of the 0°C isotherm, i.e. the transition from liquid to frozen water.

Examples of the attenuation predicted by the models given in equations (2-7) and (2-8) are shown in Figure 2-2. They describe the attenuation exceeded for 0.01% of the average year at 36GHz for rain rates of 5–100mm/h and vertically polarised antennas.



(A)



(B)

Figure 2-2 (A) Rain attenuation exceeded for 0.01% of the average year as a function of path length (ITU-R P.530), and (B) elevation angle (ITU-R P.618), for a selection of rainfall rates. The frequency considered is 36GHz and the polarisation is vertical.

Figure 2-2 shows that attenuation decreases with elevation angle and increases with rainfall rate and path length. For a 36GHz, 20km terrestrial link in the surface boundary layer a rainfall rate of 25mm/h exceeded for 0.01% of the year (the annual average in the UK given by ITU-R P.837) attenuates signal strength by 55dB. This amount of attenuation is more than that usually factored into system fade margins, which is typically in the region of 25dB for a 36GHz commercial link. For this reason, the availability of 36GHz radio links in the UK is primarily dependent on rainfall occurrence.

#### 2.2.2.2 Snow, hail, graupel, sleet and the melting layer

Snow consists of aggregated ice crystals that form large flakes when the temperature is just below freezing and crystal surfaces become sticky (Hall, 1996). Dry snow does not appear to significantly attenuate radiowave propagation because of its low liquid water density structure (generally around  $0.1\text{g/m}^3$ ) giving it a permittivity close to unity. The specific attenuation of frozen water is given by (Hall, 1979):

$$\gamma_w = aM^b \quad \text{dB/km} \quad (2-9)$$

where  $a$  and  $b$  are functions of particle size, frequency and temperature, and  $M$  is the liquid water density.

Hail and graupel are formed by the accretion of super-cooled cloud droplets in convective storms (Hall, 1996). Hail particles are typically spherical in shape and have a density similar to liquid water. Graupel is typically conical in shape and has a density between that of snow and hail. Hail and graupel have a significant effect on millimetre wave propagation when they begin to melt and scatter radiowaves like very large raindrops. A technique used to evaluate the scatter from a particle of radius  $a$

and refractive index  $n$  is the Rayleigh method (Hall, 1996). The Rayleigh method is applicable when the scattering particle is both electrically small ( $2\pi a/\lambda \ll 1$ ) and phase shifts across it are small ( $2\pi na/\lambda \ll 1$ ). The Rayleigh approximation is particularly useful for cloud droplets and atmospheric ice crystals.

Sleet is a mixture of frozen water particles and rain that have a potentially significant effect on millimetre wave propagation. At present, however, there is little measurement data available and no established model to predict attenuation due to sleet. The UK Radiocommunications Agency is however investigating the effect of sleet with a view to developing an attenuation prediction model.

The melting layer is a region approximately 500m deep that occurs around the 0°C isotherm. It is a region where melting snowflakes combine over a large horizontal spatial extent (e.g. 10s of kilometres) with a large apparent permittivity. The melting layer produces intense scattering of radiowaves at microwave and millimetre wave frequencies, which is observed as a bright band in radar reflectivity studies. Because of its much larger horizontal extent the melting layer scatters horizontally polarised waves more strongly than vertically polarised waves.

### 2.2.2.3 Fog and cloud

Fog and cloud consist of small water droplets that absorb electromagnetic energy in a similar way to light rainfall. The specific attenuation of fog consisting entirely of small water droplets (less than 0.1mm) is expressed by ITU-R P.840 (from Gunn and East, 1954) for frequencies below 200GHz as:

$$\gamma_f = K_f M \quad \text{dB/km} \quad (2-10)$$

where  $K_l$  (dB/km/gm<sup>-3</sup>) is the specific attenuation coefficient and  $M$  (g/m<sup>3</sup>) is the total water content per unit volume. Typical values of  $M$  in fog range from 0.05g/m<sup>3</sup> to 0.5g/m<sup>3</sup> for medium to thick fog. This equates to an optical visibility range of approximately 400m down to 90m (Ryde, 1946).

Figure 2-3 shows the specific attenuation of a medium and thick fog at a temperature of 10°C as a function of frequency. It shows that the attenuation of a medium fog remains less than 1dB/km up to 200GHz, whereas in a thick fog it can be as much as 5dB/km. As thick fogs can extend over distances of many kilometres the total path attenuation of a 36GHz terrestrial communication system (0.5dB/km) could amount to many decibels. Even so, there is currently no established model to predict fog attenuation statistics for radio systems planning.

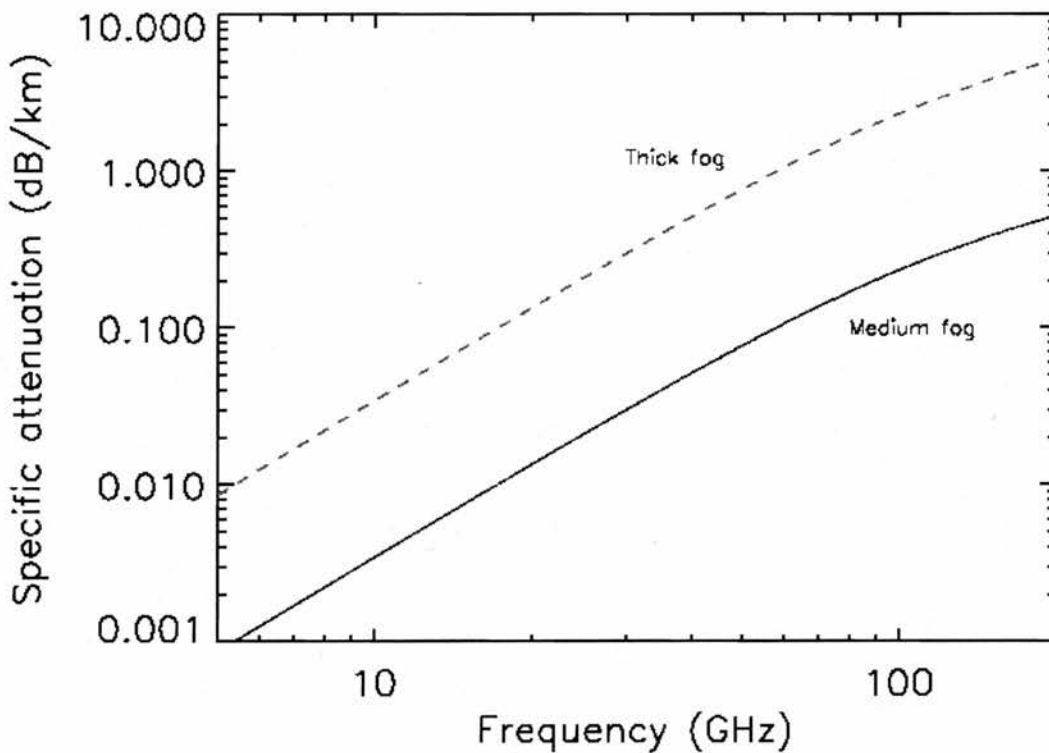


Figure 2-3 Specific attenuation due to medium and thick fogs with liquid water densities of 0.05 and 0.5g/m<sup>3</sup> respectively (ITU-R P.840).

In contrast to fog, cloud attenuation on Earth-space paths can be statistically predicted for frequencies up to 200GHz using ITU-R P.836. The attenuation ( $A$ ) due to cloud as a function of elevation angle ( $\theta$ ) is given by:

$$A = \frac{LK_l}{\sin \theta} \quad \text{dB} \quad (2-11)$$

where  $L$  ( $\text{kg/m}^2$ ) is the total columnar content of liquid water.

Figure 2-4 shows the predicted attenuation of a 36GHz signal due to cloud with total columnar liquid water contents of  $0.1\text{kg/m}^2$  and  $0.8\text{kg/m}^2$ , which correspond to normalised values (to  $0^\circ\text{C}$ ) exceeded for 20% and 1% of the average year in the UK respectively.

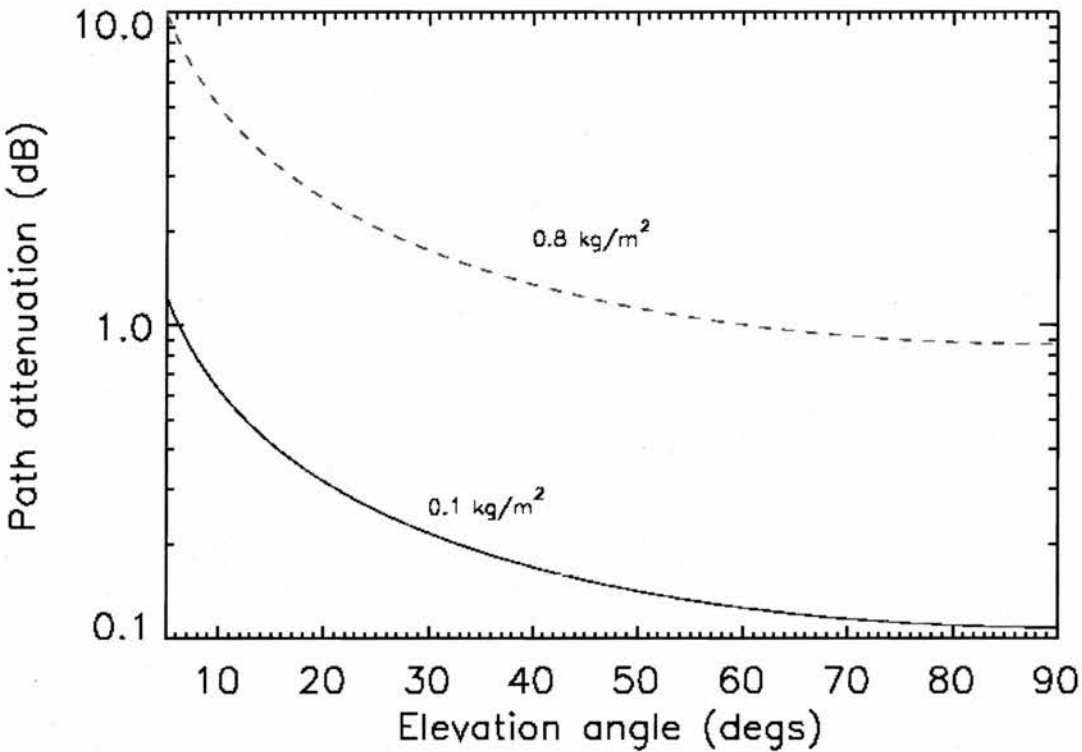


Figure 2-4 Attenuation at 36GHz due to cloud with total columnar liquid water contents of  $0.1$  and  $0.8 \text{ kg/m}^2$  (ITU-R P.840).

Figure 2-4 shows that cloud attenuation at low elevation angles can be in the order of 10dB for 1% of the average year in the UK. Compared to rainfall, this depth of fade could be considered negligible. However, 10dB fades for 1% of the average year could have a significant effect on the availability of Earth-space communication systems, especially very small aperture terminals (VSAT) that can have fade margins as low as 3dB.

### **2.2.3 Sand and dust**

Sand and dust storms impair millimetre wave signals by attenuation and depolarisation. Unlike water vapour droplets attenuation from sand and dust particles is primarily due to scattering (absorption is negligible). Measurements at 10GHz using simulated dust and sand particles found the specific attenuation to be less than 0.1dB/km for sand and 0.4dB/km for clay dust (Hall, 1979). At frequencies above 100GHz and visibility less than 10m the specific attenuation is reportedly 4dB/km (Brussaard and Watson, 1995).

Wave depolarisation due to sand and dust particles is dependent on wave polarisation and path elevation angle. For a combination of poor location, low elevation angle and high frequency, cross-polarisation discrimination exceeded for 0.01% of the year can be as low as 20dB (Brussaard and Watson, 1995).

Having reviewed the effects of particulates on millimetre wave propagation, the following section considers the effect of the refractive index structure of the atmosphere.

## 2.2.4 Refractive index structure of the atmosphere

The refractive index structure of the atmosphere is characterised by three scales (Hall et al, 1996):

- a. Large-scale (global) → horizontal stratification.
- b. Medium-scale (100m to 100km) → spatial and temporal variations.
- c. Small-scale (<100m) → turbulent mixing.

The large-scale refractive index structure of the atmosphere impairs propagation at millimetre wave frequencies by spreading the beam (defocusing) and changing the apparent direction (boresight) of the transmitter on Earth-space paths (see Section 2.2.4.2). Medium scale variations can lead to signal strength variations by ducting and multipath (see Section 2.2.4.3), while small-scale variations lead to scintillation and scattering. In this section large and medium scale refractive index anomalies are briefly considered. This follows a summary of the method used for calculating the radio refractive index structure from meteorological parameters. Small-scale effects are discussed in Section 2.4.

### 2.2.4.1 Radio refractive index

The radio refractive index ( $n$ ) structure in a stable atmosphere decreases exponentially with height. As it varies by only small amounts from unity it is convenient to express it as units of refractivity defined as (ITU-R P.453):

$$N \equiv (n-1) \times 10^6 \quad \text{N - units} \quad (2-12)$$

For frequencies up to 100GHz the empirical method used to calculate the refractivity (to within 0.5% of its true value) from meteorological parameters is given by (ITU-R P.453):

$$N = N_{wet} + N_{dry} \quad \text{N - units} \quad (2-13)$$

where,

$$N_{wet} = 3.732 \times 10^5 \frac{e}{T^2} \quad (2-14)$$

$$N_{dry} = 77.6 \frac{P}{T} \quad (2-15)$$

where  $P$  (hPa) is the pressure,  $T$  (K) is the temperature and  $e$  (hPa) is the water vapour pressure given by:

$$e = \frac{He_s}{100} \quad \text{hPa} \quad (2-16)$$

where  $H$  (%) is the relative humidity and  $e_s$  (hPa) is the saturation water vapour pressure at temperature  $t$  (°C) given by:

$$e_s = a \exp\left(\frac{bt}{t+c}\right) \quad \text{hPa} \quad (2-17)$$

where  $a=6.11$ ,  $b=17.5$  and  $c=241$  for water.

#### **2.2.4.2 The effect of the large scale refractive index structure of the atmosphere on radiowave propagation**

In a statically stable atmosphere the large-scale refractive index structure of the atmosphere decreases with altitude only. The decrease with altitude is due to the exponential decrease of pressure and linear decrease of temperature (typically

6.5°C/km). The large-scale refractive index structure of the atmosphere can be expressed by (ITU-R P.453):

$$N = N_s \exp^{-(h/H)} \quad (2-18)$$

where  $N_s$  is the surface refractivity,  $h$  (km) is the height above the surface and  $H$  (km) is the scale height. Typical mid latitude values in ITU-R P.453 are  $N_s=315$  and  $H=7.35$ km, giving a gradient in the first kilometre of  $-40$ N/km.

Since the refractive index of the atmosphere decreases with height, ray paths launched from a transmitter are bent down towards the Earth according to Snell's Law. This effect can result in an error in the boresight direction of a satellite from a ground station. The apparent boresight angle (the angle to the satellite station taking account of atmospheric refraction) is given by (ITU-R P.834):

$$\theta = \theta_0 + \tau(h, \theta_0) \text{ degs} \quad (2-19)$$

where  $\theta_0$  (degs) is the free space elevation angle to the space station,  $h$  (km) is the altitude of the ground station and  $\tau(h, \theta_0)$  is the refractive index correction factor given by:

$$\tau(h, \theta_0) = \left[ \begin{array}{l} 1.728 + 0.5411\theta_0 + 0.03723\theta_0^2 + h(0.1815 + 0.06272\theta_0) \\ + 0.0138\theta_0^2 + h^2(0.01727 + 0.008288\theta_0) \end{array} \right]^{-1} \quad (2-20)$$

Angular ray deviations in a standard atmosphere with a 2° elevation-angle have been measured (ITU-R P.453) at 0.32°, 0.36°, 0.38° and 0.47° for polar continental, temperate continental, temperate maritime and tropical maritime air respectively.

In addition to boresight errors, the regular decrease of refractive index with height spreads (defocuses) the radiowave energy as a result of the differential refraction

across the beam. Attenuation due to beam spreading ( $A_{bs}$ ) is independent of frequency through a large part of the spectrum (1-100GHz) and is negligible for elevation angles greater than  $3^\circ$  (ITU-R P.618). The beam spreading loss is however dependent on ground-station latitude ( $\xi$ ). This is summarised as follows:

- a. For elevation angles less than  $5^\circ$ , the beam spreading loss in the average worst month at latitudes less than  $53^\circ$  is given by:

$$A_{bs}(< 53) = 2.27 - 1.16 \log(1 + \theta) \text{ dB} \quad A_{bs} > 0 \quad (2-21)$$

where  $\theta$  (mrad) is the apparent boresight elevation angle taking account of the effects of refraction.

- b. At elevation angles less than  $6^\circ$  and latitudes greater than  $60^\circ$  the beam spreading loss in the average worst month is given by:

$$A_{bs}(> 60) = 13 - 6.4 \log(1 + \theta) \text{ dB} \quad A_{bs} > 0 \quad (2-22)$$

- c. At latitudes between  $53^\circ$  and  $60^\circ$  the median beam spreading loss is given by:

$$A_{bs}(53 - 60) = A_{bs}(> 60) - \frac{60}{7} \Delta A_{bs} + \frac{1}{7} \Delta A_{bs} \xi \text{ dB} \quad (2-23)$$

where  $\Delta A_{bs} = A_{bs}(> 60) - A_{bs}(< 53) \text{ dB}$ .

The above models are expressed graphically in Figure 2-5.

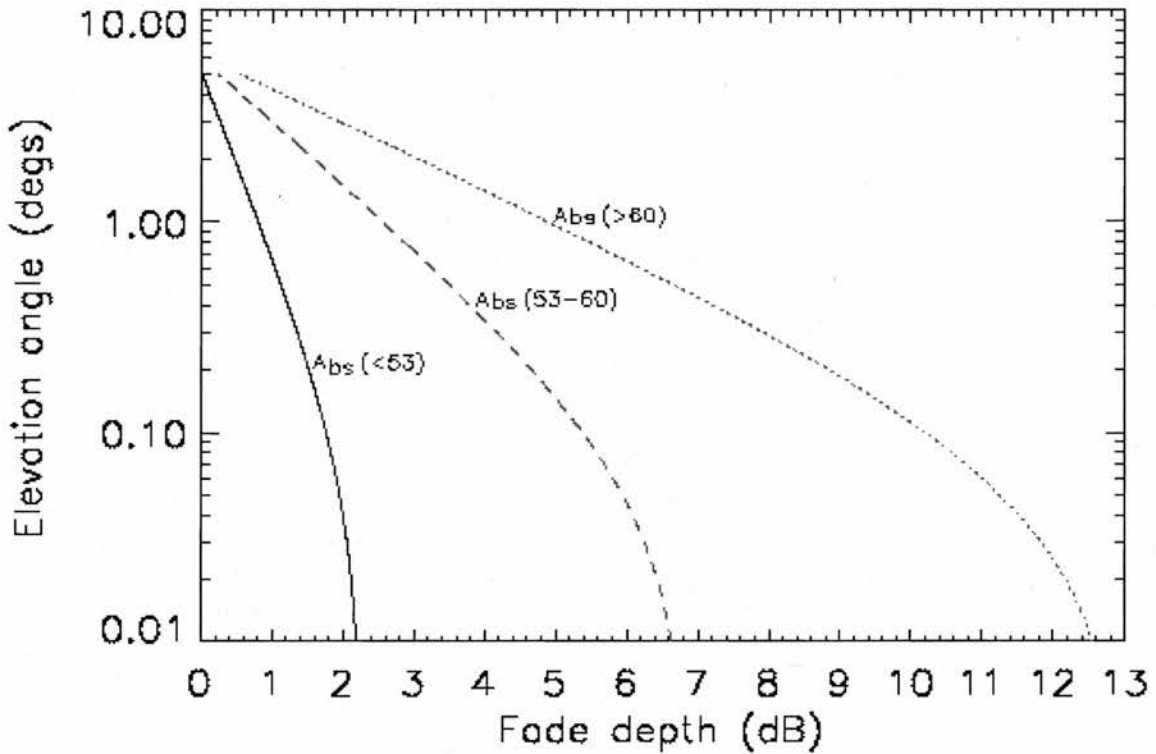


Figure 2-5 Attenuation due to beam spreading as a function of latitude and elevation angle (ITU-R P.618).

### 2.2.4.3 The effect of the medium scale refractive index structure of the atmosphere on radiowave propagation

Medium scale refractive layering of the atmosphere occurs when temperature or relative humidity gradients (lapse rates) are inverted.

Anomalous refractive layers in the atmosphere are classified in terms of their refractive gradient and modified refractive gradient ( $M$ ). The modified refractive gradient is a convenient term for identifying radio ducts. It is given by:

$$\frac{dM}{dh} = \frac{dN}{dh} + \frac{1}{a} \quad (2-24)$$

where  $a$  is the Earth's radius (6370km). For a standard atmosphere  $dM/dh$  in the first kilometre above the surface is 117N/km.

A classification of anomalous refractive layering is given in Table 2-1 and illustrated in Figure 2-6.

Refractive Condition	Gradient (N/km)	Modified Gradient (M/km)
Sub-refractive	$0 < dN/dh < -40$	$157 < dM/dh < 117$
Standard	$dN/dh = -40$	$dM/dh = 117$
Super-refractive	$-157 \leq dN/dh \leq -40$	$0 \leq dM/dh \leq 117$
Ducting	$dN/dh \leq -157$	$dM/dh \leq 0$

Table 2-1 Classification of refractivity gradients and modified refractivity gradients.

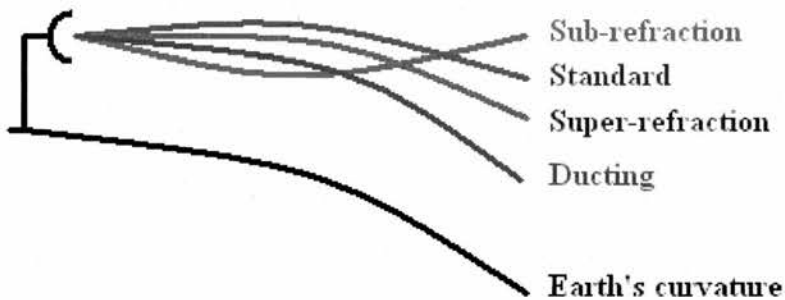
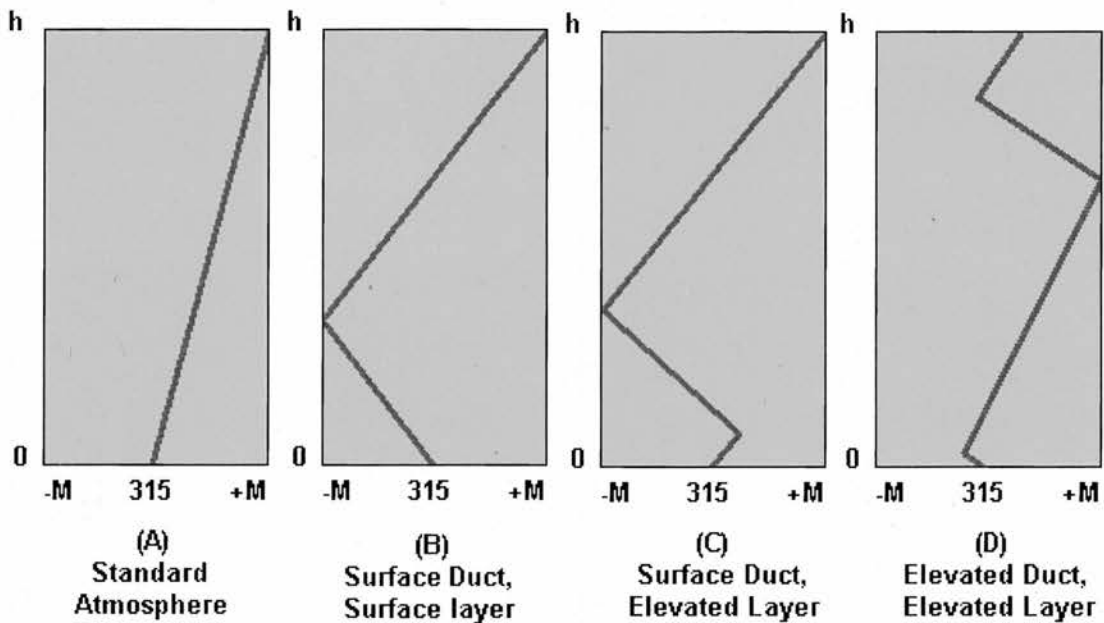


Figure 2-6 Ray bending due to refractive index gradients.

In sub-refractive conditions the downward curvature of propagating rays decrease, reducing the radio horizon and terrain clearance on terrestrial paths. In contrast, super-refraction increases ray bending which extends the radio horizon and terrain clearance. In ducting conditions the modified refractivity gradient is less than zero, which results in ray curvature greater than the curvature of the Earth. This occurs when anomalous refractive layers form at the surface of the Earth (surface ducts) or at altitude (elevated ducts). Duct types are illustrated in (Figure 2-7).



*Figure 2-7 Duct types ( $h$  is height above the surface). The gradients are shown as functions of the modified refractivity gradient from a mean ground based refractivity of 315 N units.*

Figure 2-7 shows two types of duct:

- a. Surface duct – An inversion layer that traps radiowave energy between the boundary of the Earth or sea and an anomalous refractive layer. The layer may be directly above the surface (a surface layer), or at some elevation above the surface (an elevated layer).
- b. Elevated duct – Radiowave energy is trapped between two boundary layers, e.g. a surface layer and an elevated layer.

The formation of anomalous refractive layers occur from one of the following four meteorological conditions:

- i. Evaporation - formed primarily by a rapid decrease in water vapour above the surface of the sea.

- ii. Nocturnal radiation – formed by the formation and break-up of radiative fogs over land.
- iii. Subsidence inversion - inversion of the temperature gradient from the centre of anticyclones<sup>1</sup>. As the anticyclone spreads out (500-1000km) hot air cools and descends back to the surface forming an elevated layer.
- iv. Advection – anticyclones generated in geographic regions of warm dry air can be carried by advection to regions of cooler, moister air, where a temperature inversion can occur. They are generally found in coastal regions.

The ability of ducts to trap radiowaves depends on the refractive index gradient through the duct, the duct thickness, signal frequency and path elevation angle. These parameters have been combined into empirical models for calculating the minimum trapping frequency ( $f_{min}$ ) (Hall, 1979) and maximum elevation angle ( $\theta_{max}$ ) required for ducting (ITU-R P.834). They are given below and illustrated in Figure 2-8.

$$f_{min} = \frac{3790}{\left( \sqrt{\left| \frac{dM}{dh} \right|} \right) \Delta h^{3/2}} \quad \text{GHz} \quad (2-25)$$

$$\theta_{max} = \sqrt{2 \times 10^{-6} \left| \frac{dM}{dh} \right| \Delta h} \quad \text{degs} \quad (2-26)$$

where  $\Delta h$  (m) is the duct thickness.

---

<sup>1</sup> Anticyclones are bodies of moving air with higher pressure than the surrounding air. The pressure in anticyclones decreases away from its centre.

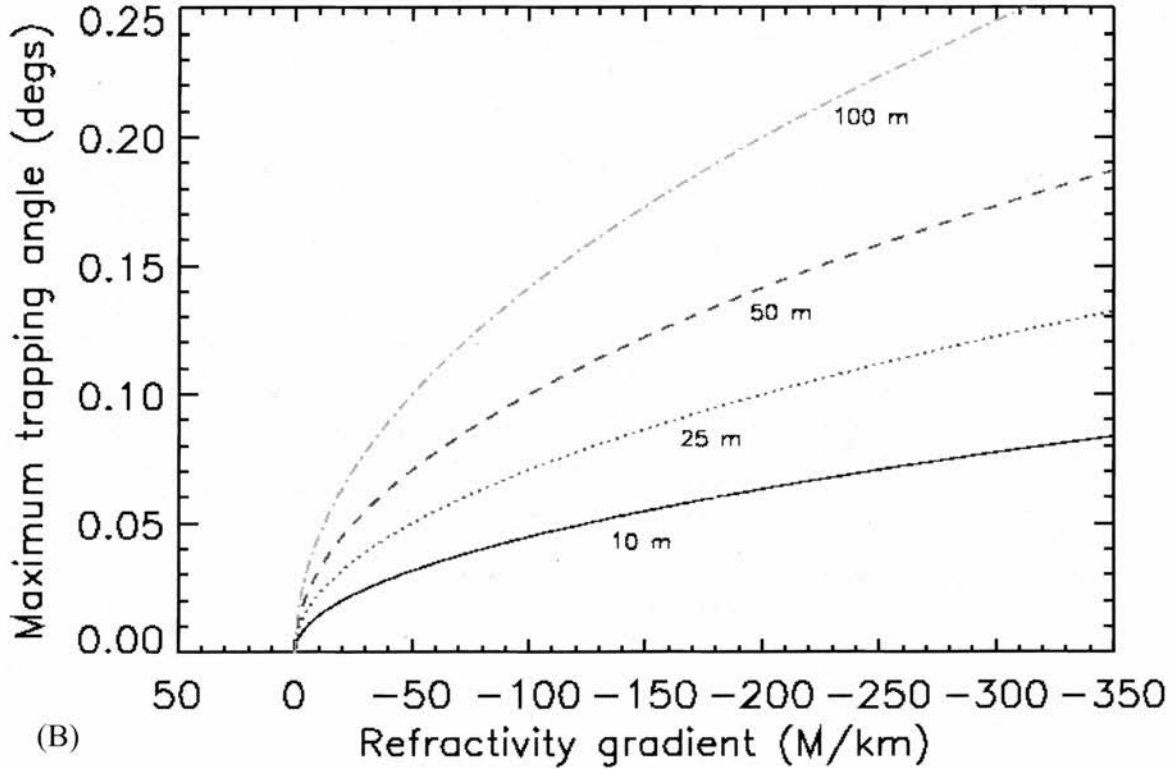
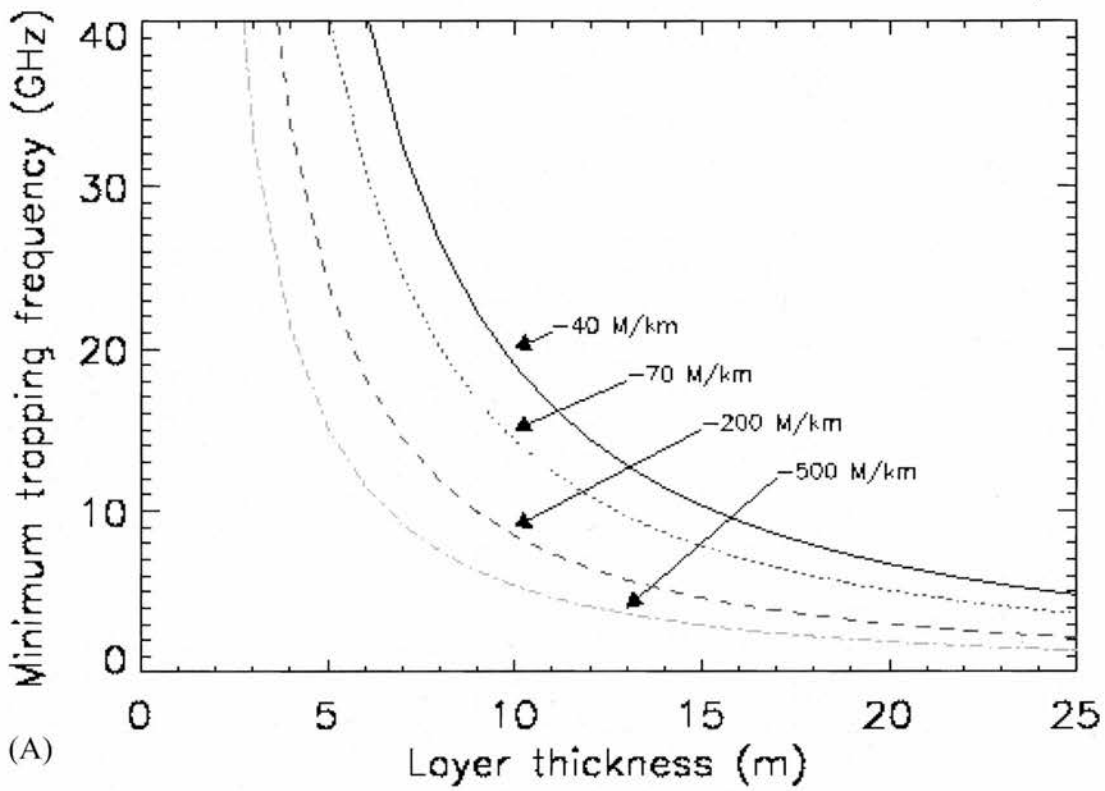


Figure 2-8 (A) Minimum trapping frequency (Hall, 1979) and (B) Maximum trapping angle (ITU-R P.834).

Figure 2-8 illustrates that ducting is significantly more likely to occur at microwave frequencies and above where layer thickness and refractivity gradients are relatively modest. At lower frequencies, e.g. VHF, ducts need to be several tens of metres thick to trap radiowaves. As ducts of this thickness develop primarily from anticyclone conditions, ducting of VHF signals would generally be associated with advection duct formation. Additionally, radiowave trapping would only be expected at low elevation angles. Even at elevation angles of  $0.2^\circ$  ducts need to be several tens of metres thick with high refractivity lapse rates to trap radiowaves.

Tropospheric layering that traps radiowaves in a duct may alternatively reflect incident rays if the refractive layer forms a discontinuity. A layer is considered a discontinuity if its thickness satisfies the following criteria (Hall et al, 1996):

$$\Delta h < \frac{14\lambda}{\theta} \quad (2-27)$$

where  $\lambda$  (m) is the signal wavelength and  $\theta$  (degs) is the angle of incidence.

When a signal reflected from a tropospheric layer is combined in a receiving aperture with a signal from the direct path the received signal strength varies in accordance with the phase difference (delay) between the two signals. This mechanism, called clear-air multipath, may result in significant impairment (fading and enhancement) to low elevation millimetre wave links.

Predicting the impairment from clear-air multipath for terrestrial and low elevation Earth-space paths is provided by ITU-R recommendations P.530 and P.618 respectively. These empirical models (the Earth-space path model includes beam spreading and scintillation) are quite involved, as they take into consideration a wide range of parameters. These include link information (e.g. frequency and elevation

angle), refractivity gradient statistics (called the multipath occurrence factor ( $P_0$ )) and the geoclimatic factor (or alternatively measured fade statistics) that depends on terrain type and global factors, e.g. latitude. Examples of predicted multipath fading and enhancement using ITU-R P.530 and P.618 are shown in Figure 2-9.

Figure 2-9 shows average annual multipath fading and enhancement distributions for terrestrial and Earth-space paths operating at 36GHz. The 25km terrestrial path is located in the southern UK (53°N), and the Earth-space path ground station is at the same location. In both cases the fade depth increases by 10dB/decade for fades greater than 20dB, and increases by 3dB/decade for enhancements greater than 3dB. The figures show that clear-air multipath mitigation is possible by reducing  $P_0$ , e.g. choosing an alternative site, lowering the frequency (see Figure 2-8A) or increasing the elevation angle (see Figure 2-8B).

### 2.2.5 Summary

The above description of factors governing millimetre wave propagation has shown that there are a number of impairments that affect the performance of millimetre wave communication systems. They range from signal fading at 36GHz due to rainfall to attenuation from oxygen absorption at 60GHz. These forms of impairment are well understood, as they have been investigated for many years by satellite communication researchers. In contrast, atmospheric turbulence induced effects have been addressed to a lesser extent, particularly for long path scenarios (>10km) through the surface boundary layer. To explain the propagation impairments caused by atmospheric turbulence the next section describes turbulence and its formation in the atmosphere. This is followed by a review of turbulence induced propagation impairments.

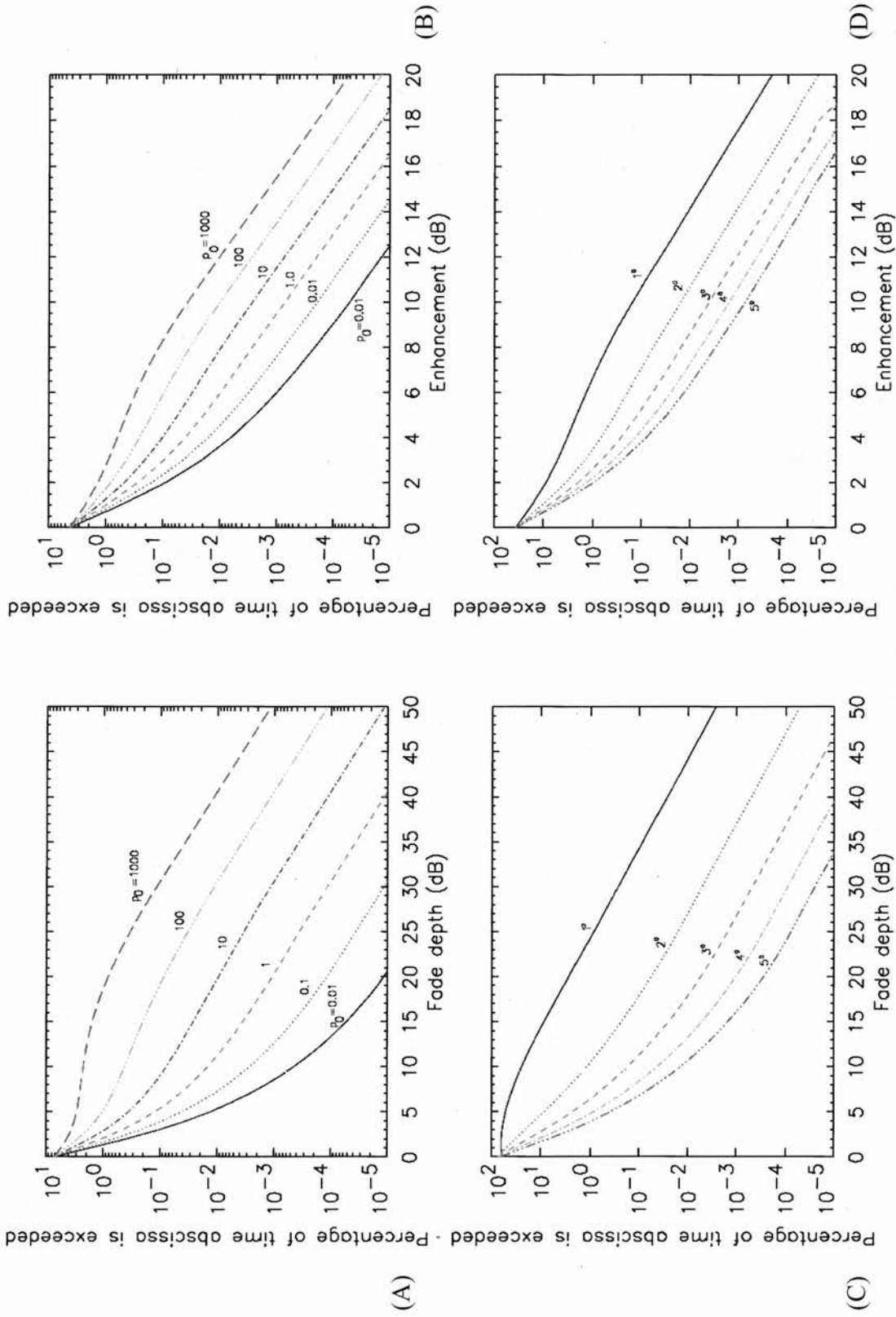


Figure 2-9 Cumulative frequency distributions of clear-air multipath fading and enhancements. (A) Fading and (B) enhancements for a 36GHz terrestrial path of 25km in the southern UK as a function of the multipath occurrence factor  $P_0$  (ITU-R P.530). (C) Fading and (D) enhancements for a 36GHz Earth-space path in the southern UK (ITU-R P.618).

## 2.3 Atmospheric turbulence

The term atmospheric turbulence refers to instabilities in the mean state of the atmosphere due to small-scale anomalies in temperature, pressure and humidity. The small-scale anomalies (eddies) modify the refractive index structure of the atmosphere thereby producing a dynamically varying medium. The following describes turbulence mechanisms that affect radiowave propagation, starting with an overview of the most turbulent part of the Earth's atmosphere, the tropospheric boundary layer.

### 2.3.1 The structure of the tropospheric boundary layer

The troposphere is the lowest part of the Earth's atmosphere. Temperature in the troposphere decreases with height because air is compressible. This results in a decrease in density with height allowing rising air to expand and then cool. The height of the troposphere depends on latitude, ranging from 16km at the equator to 8km at the poles. The height difference is due to increased solar heating at equatorial regions.

The troposphere is divided into two regions, the boundary layer and the free atmosphere. While the free atmosphere contains relatively little mass, the boundary layer (the lowest 100m at the poles to 3000m at the equator) contains 75% of the total gaseous mass (predominately Nitrogen (~78%) and Oxygen (~21%)) and almost all the water vapour of the atmosphere (Barry and Chorley, 1998).

The boundary layer is defined as the part of the troposphere that is directly influenced by the presence of the Earth's surface, and responds to surface forcings on time-scales of an hour or less (Stull, 1988). The forcings include frictional drag, evaporation, heat transfer, pollutant emission, and terrain induced flow modification. Transport of

moisture, heat and pollutants in the boundary layer is controlled by a mean wind in the horizontal direction and by convection in the vertical direction. The graphical representation of the boundary layer shown in Figure 2-10 indicates that the tropospheric boundary layer can be subdivided, with each sub-division characterised by a height and time-scale.

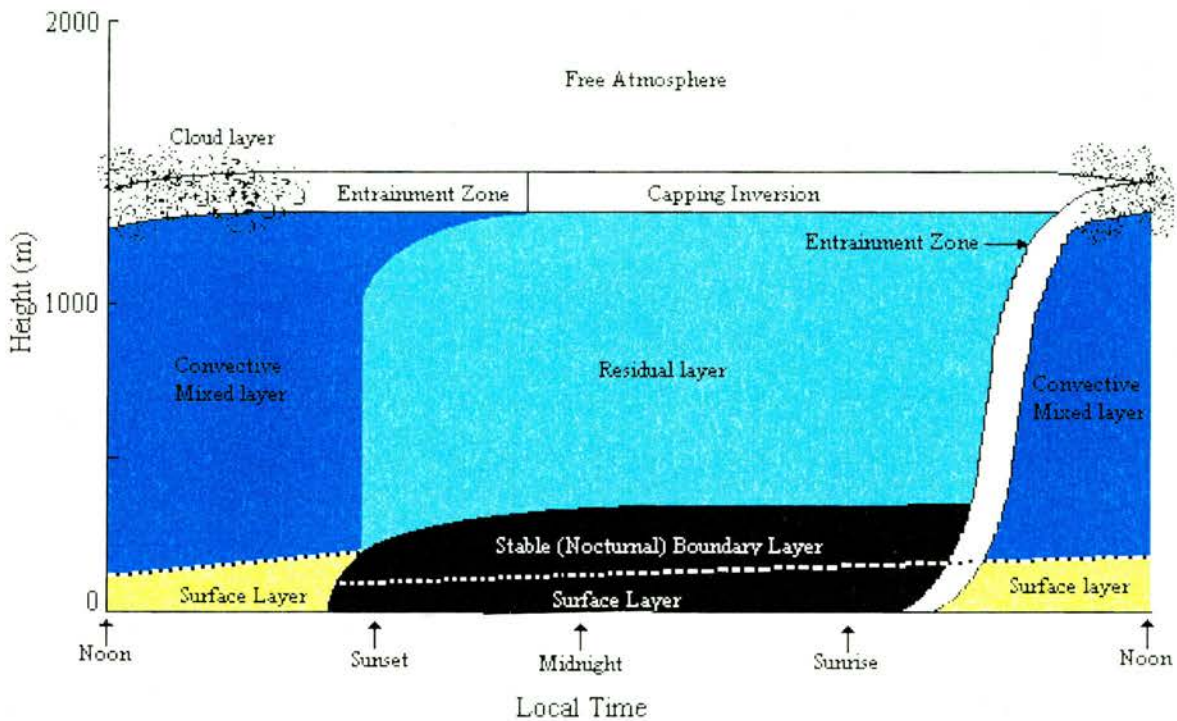


Figure 2-10 The structure of the tropospheric boundary layer (Stull, 1988).

*The surface boundary layer* is the bottom 10% of the boundary layer where turbulence is at its most significant.

*The convective mixed layer* forms approximately thirty minutes after sunrise on initially cloud-free days and reaches a maximum depth by late afternoon. Between noon and sunset convection dominates the boundary layer with thermals of warm air rising from the ground and thermals of cool air sinking from the cloud layer. This

process (called entrainment) homogenises temperature, pressure and humidity that characterise the boundary layer.

In addition to the convection process, turbulence production can also be generated from wind shear across the top of the mixed layer. The growth of the mixed layer is controlled (or capped) by cool-air thermals entraining down into the mixed layer, which are counteracted by warm air rising thermals, i.e. the tropopause.

*The residual layer* forms between sunset and sunrise. It is called the residual layer as it initially takes on the mean characteristics of the mixed layer. However as thermals cease, the residual layer becomes neutrally stratified and turbulence intensity becomes nearly equal in all directions. At the top of the residual layer warm-air thermals form a stable capped layer that frequently forms a temperature inversion.

*The stable (nocturnal) boundary layer* is characterised by statically stable air with weaker, more sporadic turbulence. Although the wind at ground level is usually calm between sunset and sunrise (2-10m/s), the wind above ground level (>200m) can reach speeds of 10-30m/s in a phenomenon called low-level jet or nocturnal jet. While the calm ground level wind tends to suppress turbulence, the nocturnal jet enhances wind shears that in-turn generates turbulence. This may result in relatively short turbulent periods that can cause mixing throughout the stable boundary layer.

The above description is satisfactory for weather phenomena, but for radiowave propagation a small-scale description of turbulent flows and energy transfer is required to develop an understanding of the impact on millimetre wave propagation. The following section briefly summarises the complex subjects of turbulent flows and energy transfer.

## 2.3.2 Turbulent flows and energy transfer

In the previous section the mechanisms that generate atmospheric turbulence were identified. The next requirement is to identify methods used to characterise turbulence and the process of energy transfer. Such methods, which are described in the following sections, characterise eddy energy and its transport (Kolmogorov spectrum), eddy properties (Taylor's 'frozen-in' hypothesis), and a turbulent flow indicator (Reynolds numbers). Each of these characteristics is described in the following sections.

### 2.3.2.1 Kolmogorov spectrum

A turbulent flow is visualised as comprising of parcels of eddy velocity fluctuations. The size of eddies range from  $\sim 1\text{mm}$  in the inner scale (also called the dissipation range) of turbulence ( $l_0$ ), to hundreds of metres in the outer scale (also called the input range) of turbulence ( $L_0$ ). The region between the input and dissipation ranges is called the inertial sub-range. In this region, eddies gain all their energy from the inertia of larger eddies and not by direct forcings such as wind shear or thermal convection. The collective name for the input range, inertial sub-range and the dissipation range is the Kolmogorov spectrum (Frisch, 2001). This spectrum is illustrated in Figure 2-11 and expressed mathematically in equation (2-28) as a refractive index spectral density (Tatarski, 1961).

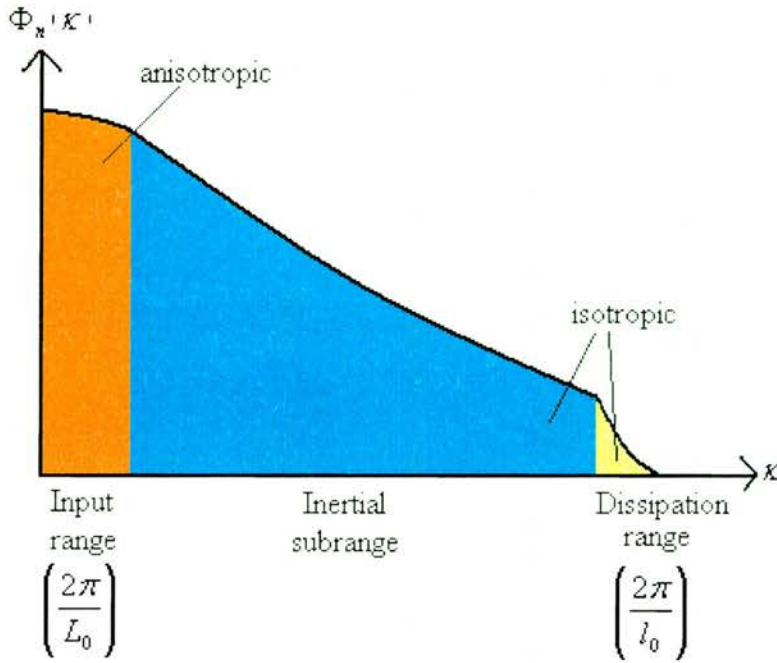


Figure 2-11 The Kolmogorov spectrum of turbulence (Tatarski, 1961).  $\kappa$  is the spatial wavenumber ( $= 2\pi / \text{eddy size}$ )

$$\Phi_n(\kappa) = 0.033 C_n^2 \kappa^{-11/3} \exp\left(\frac{-\kappa}{\kappa_m}\right)^2 \text{ m}^3 \quad \text{for } \kappa > 2\pi / L_0 \quad (2-28)$$

where  $C_n^2$  ( $\text{m}^{-2/3}$ ) is the refractive index structure function constant and  $\kappa_m = 5.91 / l_0$ . Average values of the structure constant in the atmosphere range between  $10^{-14} \text{m}^{-2/3}$  for strong turbulence to  $10^{-18} \text{m}^{-2/3}$  for weak turbulence.

The Kolmogorov spectrum is valid only for eddies smaller than the outer scale of turbulence. This is because eddies in the outer scale are specific to the mechanism that generated them, e.g. convection, and therefore cannot be mathematically generalised. For this reason, the Kolmogorov spectrum is said to be a model of fully developed turbulence.

The anisotropy in the input range and isotropy in the inertial sub-range and dissipation range is due to a process called return to isotropy (Tennekes and Lumley, 1972),

which relates to the time-scale of the straining motion of eddies. This can be explained by considering the pure shear flow in Figure 2-12.

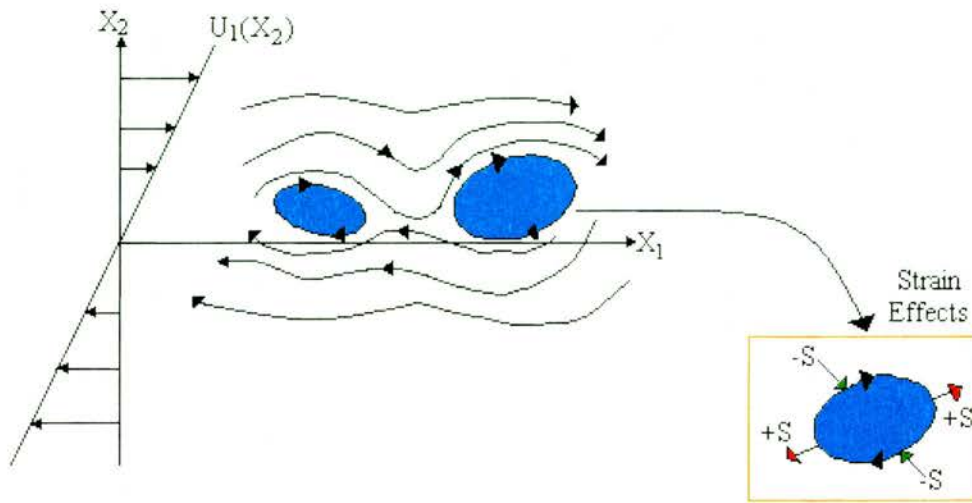


Figure 2-12 Strain effects from a pure shear flow (Tennekes and Lumley, 1972).

Figure 2-12 shows two eddies in a pure shear flow. It is a pure shear flow as the mean wind component is a function of  $X_2$  only, i.e. wind speed varies with height only. The shear force rotates the eddies placing them in a vortex, whilst at the same time distorting their shape from isotropic to anisotropic with major axes in the positive direction of the mean flow (positive strain  $S$ ), and minor axes in the negative direction of the strain. Eddies may therefore be visualised as rotating blobs that are simultaneously stretched at a strain rate  $s(\kappa)$ . The time it takes for eddies to return to isotropy is therefore equal to  $1/s(\kappa)$ , where  $s(\kappa) \propto \kappa^{2/3}$  (Tennekes and Lumley, 1972). This states that eddies in the input range (small wavenumbers) have slow strain rates (low frequency) compared to the inertial sub-range and dissipation range. Consequently, eddies in the input range take longer to return to isotropy than eddies in the inertial sub-range and dissipation range. For example, an eddy of 100m will take 6.3s to return to isotropy compared to 0.29s for a 1m eddy. As the strain rate of eddies in the input range is comparable to the strain rate of the mean flow (which maintains a

steady orientation), input range eddies remain anisotropic. Conversely, the strain rate of small eddies in the inertial sub-range and the dissipation range is large compared to the mean flow and therefore no permanent anisotropy can be induced, i.e. they have a mean isotropy.

The process by which eddies transfer their energy from the input range to the output range is called vortex stretching (Tennekes and Lumley, 1972). Vortex stretching is the process that occurs when smaller eddies are exposed to the strain rate field of larger eddies. Because of the straining, the vorticity (rotational frequency) of the smaller eddies increase with a consequent increase in their energy (kinetic) at the expense of the energy of the larger eddies. In this way there is a flux of energy from larger eddies to smaller eddies. The energy transfer is by cascade from the largest size eddies to the smallest size eddies. It is proposed (Tennekes and Lumley, 1972) that the cascade occurs because energy is more efficiently transferred when eddy strain rates are closely correlated.

### 2.3.2.2 Reynolds number

The Reynolds number is the most frequently used method for quantifying viscous (laminar) and inertia (turbulent) forces. The Reynolds number ( $R_e$ ) is given by (Lumley and Panofsky, 1964):

$$R_e = \frac{\rho UL}{\mu} \quad (2-29)$$

where  $\rho$  ( $\text{kg/m}^3$ ) is the fluid density,  $U$  (m/s) is the flow speed,  $L$  (m) is the characteristic length of the flow and  $\mu$  ( $\text{kg/s/m}$ ) is the viscosity. Typical values in the

boundary layer are  $\rho = 1.21\text{kg/m}^3$ ,  $U = 5\text{m/s}$ ,  $L = 100\text{m}$  and  $\mu = 1.81 \times 10^{-5} \text{ kg/s/m}$ , giving a Reynolds number of  $3.3 \times 10^7$ .

The actual numerical value of the Reynolds number is not important, as it can in practice be difficult to accurately measure the speed and characteristic length of the flow. For this reason, only large or small values relative to unity or changes of magnitude are considered significant indicators of turbulent activity.

### 2.3.2.3 Taylor's 'Frozen-in' Hypothesis

To acquire information on the properties and relative motion of eddies it was proposed (Taylor, 1938) that turbulence could under certain conditions be treated as 'frozen-in'. The structure of eddies can therefore be considered unchanged over a defined spatial range. Under such conditions, time-sample measurements of a moving eddy at a single sensor equate to measurements from spatially separated sensors. For this condition to be satisfied eddies have to evolve over time-scales that are greater than the time it takes for the eddy to move past the time-sampling measuring sensor. For example, the properties (e.g. temperature) of a 6m eddy moving at 5m/s would remain unchanged for more than 1.2s under frozen-in conditions. Taylor's hypothesis is said to be applicable when (Willis and Deardorff, 1976):

$$\sigma_M < 0.5M \quad (2-30)$$

where  $\sigma_M$  is the standard deviation of the total wind speed magnitude  $M$  given by:

$$M = \sqrt{U_1^2 + U_2^2 + U_3^2} \quad \text{m/s} \quad (2-31)$$

The discussion in this section has concentrated on the fundamental features of atmospheric turbulent flows. It has been shown that random anomalies in the refractive index structure of the atmosphere are generated and transported through the atmosphere by wind in the horizontal and convection in the vertical. In the next section the effect of turbulence on radiowave propagation is considered.

## **2.4 Turbulence induced impairments to wave propagation**

### **2.4.1 Scintillation**

Scintillation is the term used to describe rapid variations in amplitude, phase and angle-of-arrival of a signal due to the movement of eddies traversing the propagation path (Figure 2-13). In Figure 2-13 the received signal  $A(t)$  is seen to fluctuate as a result of the lensing of signals having reached the receiver via a number of paths having different refractive indexes, and therefore different path lengths. Scintillation is therefore a term used to describe the summation of signals with random delays that produce time (and space) varying received signals at a rate depending on the movement of eddies, i.e. by mean wind speed  $U_r$ . Such random variations in received signal strength could in many cases lead to link outages and increased bit error rates during scintillation fading, and interlink interference from an increase in propagation range during scintillation enhancements. For example, in the final report of the European Commission's COST 235 (1996) project, peak-to-peak scintillation amplitudes of 12dB on a 34.5GHz 10km link were reported.

The second observation to make about Figure 2-13 is the first Fresnel zone. The first Fresnel zone is fundamentally important when analysing the effects of turbulence on wave propagation as it relates eddy size to fluctuation intensity (Tatarski, 1961). To

explain this relationship it is necessary to review the Tatarski derived fluctuation spectral density functions (Section 2.4.1.2). Firstly, however, the first Fresnel zone is defined.

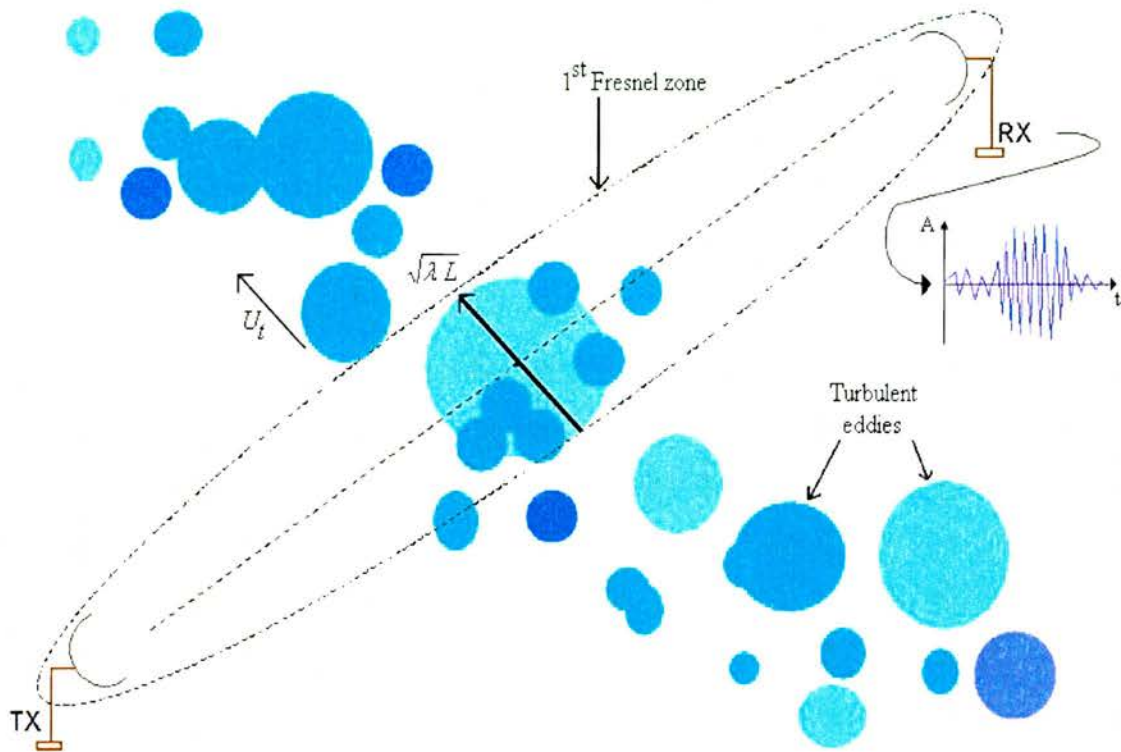


Figure 2-13 An illustration of eddies advected across a propagation path at mean wind speed  $U_t$ .

### 2.4.1.1 Definition of the first Fresnel zone

The first Fresnel zone is defined as the locus of all points surrounding the direct signal path that produce exactly half a wavelength path difference (Blaunstein, 1999). It is described by an ellipsoid of revolution having foci at the transmitter and receiver. The first Fresnel zone is characterised by its width ( $f_1$ ), which is given by:

$$f_1 = 2\sqrt{\frac{\lambda d_1 d_2}{d_1 + d_2}} \quad \text{m} \quad (2-32)$$

where  $d_1$  and  $d_2$  (m) are the distances from a point on the ellipsoid to the receiver and transmitter foci respectively. When the path lengths  $d_1$  and  $d_2$  are equal the maximum size of the first Fresnel zone is given by:

$$f_1 = \sqrt{\lambda L} \quad \text{m} \quad (2-33)$$

where  $d_1=d_2=L/2$ , i.e.  $L$  (m) is the path length between transmitter and receiver.

Equation (2-33) is throughout this thesis referenced when discussing scintillation and wavefront distortion. Its significance is reviewed in the following sections.

#### 2.4.1.2 Fluctuation spectral density

The relationship between eddy size and signal variability is described by Tatarski's (1961) fluctuation spectral density functions. The functions for amplitude ( $F_z(\kappa)$ ) and phase ( $F_s(\kappa)$ ) fluctuations are given by:

$$F_z(\kappa) = \pi k^2 L \left( 1 - \frac{k}{\kappa^2 L} \sin \frac{\kappa^2 L}{k} \right) \Phi_n(\kappa) \quad (2-34)$$

$$F_s(\kappa) = \pi k^2 L \left( 1 + \frac{k}{\kappa^2 L} \sin \frac{\kappa^2 L}{k} \right) \Phi_n(\kappa) \quad (2-35)$$

where  $L$  (m) is the turbulent path length.

Equations (2-34) and (2-35) show the spectral densities of amplitude and phase fluctuations are functions of the refractive index spectral density function (based on the Kolmogorov spectrum of turbulence (equation (2-28)), a constant term  $\pi k^2 L$ , and a spectral filter function given by the terms between the brackets:

$$f_{Amplitude}(\kappa) = \left(1 - \frac{k}{\kappa^2 L} \sin \frac{\kappa^2 L}{k}\right) \quad (2-36)$$

$$f_{Phase}(\kappa) = \left(1 + \frac{k}{\kappa^2 L} \sin \frac{\kappa^2 L}{k}\right) \quad (2-37)$$

The spectral filters are thought of as eddy filters, i.e. some eddy sizes have a greater affect on fluctuation spectral density than others. Examination of the response of the spectral filters with example parameters, e.g.  $L = 17.3\text{km}$  and  $k = 754$  (a frequency of 36GHz) is shown in Figure 2-14.

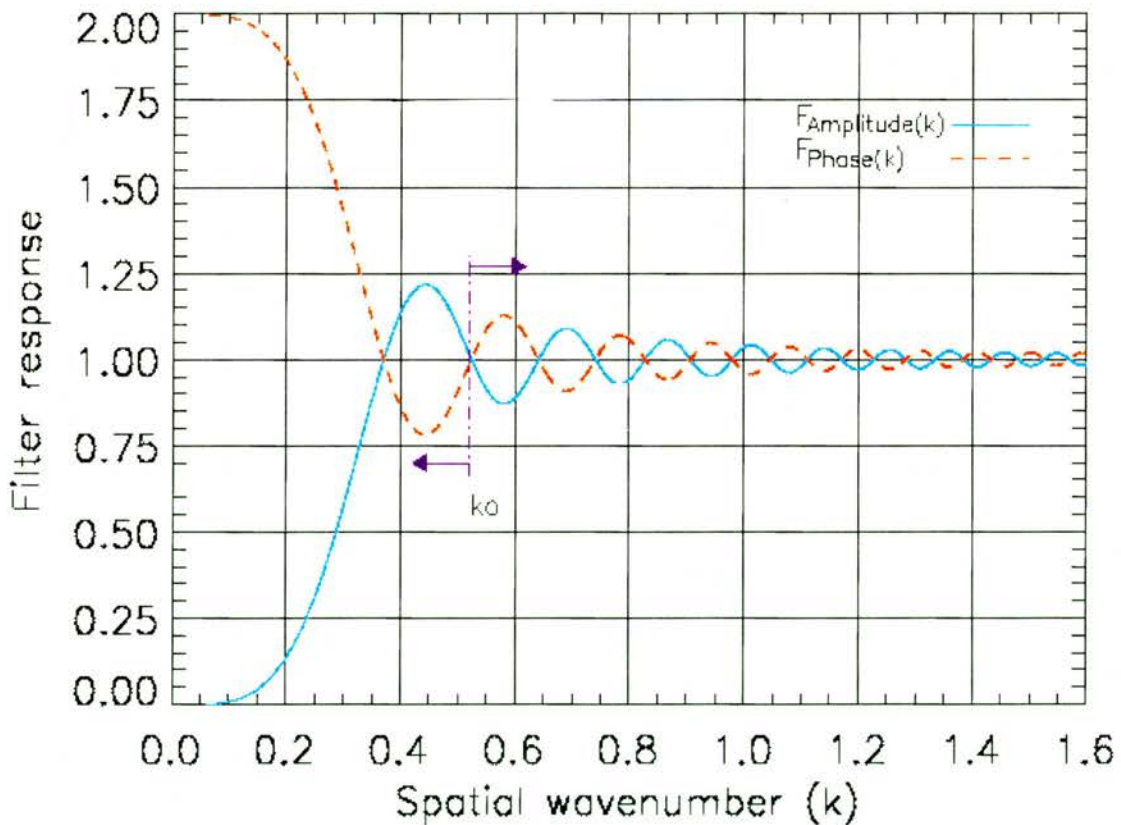


Figure 2-14 Spectral filter functions for amplitude fluctuations ( $f_{Amplitude}(\kappa)$ ) and phase fluctuations ( $f_{Phase}(\kappa)$ ) derived by Tatarski (1961).

Figure 2-14 plots the amplitude and phase fluctuation spectral filter responses verse spatial wavenumber ( $2\pi/\text{eddy size}$ ). The  $\kappa_0$  position is the approximate boundary

point of the filter responses. At this position wavenumbers larger than  $\kappa_0$  (decreasing eddy size) filter phase fluctuations the most and amplitude fluctuations the least, where as eddies smaller than  $\kappa_0$  (increasing eddy size) filter phase fluctuations the least and amplitude fluctuations the most. As the value of  $\kappa$  at  $\kappa_0$  is 0.52 for the example parameters (17.3km and 36GHz),  $\kappa_0$  corresponds to an eddy size of 12m. Therefore, eddies larger than 12m are filtered less than smaller eddies in terms of amplitude fluctuations, while eddies larger than 12m are filtered more than smaller eddies in terms of phase fluctuations. It could also be concluded from Figure 2-14 that eddies of the order of  $\kappa_0$  have the potential to induce the strongest amplitude fluctuations (and weakest phase fluctuations) as a result of the oscillatory behaviour of the filter responses in the region of  $\kappa_0$ .

The relationship between eddy spectral filters and the first Fresnel zone size is evident by calculating equation (2-33) for the same link parameters of 17.3km and 36GHz. The result of this calculation, also 12m, illustrates that the maximum size of the first Fresnel zone ( $\sqrt{\lambda L}$ ) defines the boundary condition between eddies that have a greater or lesser affect on fluctuation intensity. This boundary condition will be observed throughout this thesis when analysing turbulence induced scintillation and wavefront distortion.

The above description of fluctuation intensity concentrated solely on eddy spectral filter functions. It is however apparent from equations (2-34) and (2-35) that scintillation intensity is also a function of the refractive index spectral density ( $\Phi_n(\kappa)$ ). Hence the combination of spectral filters, refractive index spectral density and position of  $\sqrt{\lambda L}$  with respect to the inner and outer scales of turbulence defines

the intensity of scintillation. Moreover, the combination of these parameters also defines the spatial extent of eddy-induced fluctuations. The following section describes how the combination of these parameters affects fluctuation intensity and the spatial extent of fluctuations.

### 2.4.1.3 Spatial decorrelation distance of eddy induced fluctuations

From equations (2-34) and (2-35) it is apparent that fluctuation intensity depends upon the product of the functions illustrated in Figure 2-11 (refractive index spectral density) and Figure 2-14 (spectral filters). The product of these functions is dependent on the size (position) of  $\sqrt{\lambda L}$  in relation to the inner ( $l_0$ ) and outer scale of turbulence ( $L_0$ ). Three conditions (positions of  $\sqrt{\lambda L}$ ) can be specified:

- i.  $\sqrt{\lambda L} \ll l_0$ .
- ii.  $l_0 \ll \sqrt{\lambda L} \ll L_0$ .
- iii.  $L_0 \ll \sqrt{\lambda L}$ .

Each of the above conditions are considered next.

#### 2.4.1.3.1 Fluctuation intensity and decorrelation distance when $\sqrt{\lambda L} \ll l_0$

When the size of the first Fresnel zone is smaller than the size of the inner scale of turbulence the spectral densities  $F_z(\kappa)$  and  $F_s(\kappa)$  take the form illustrated in Figure 2-15.

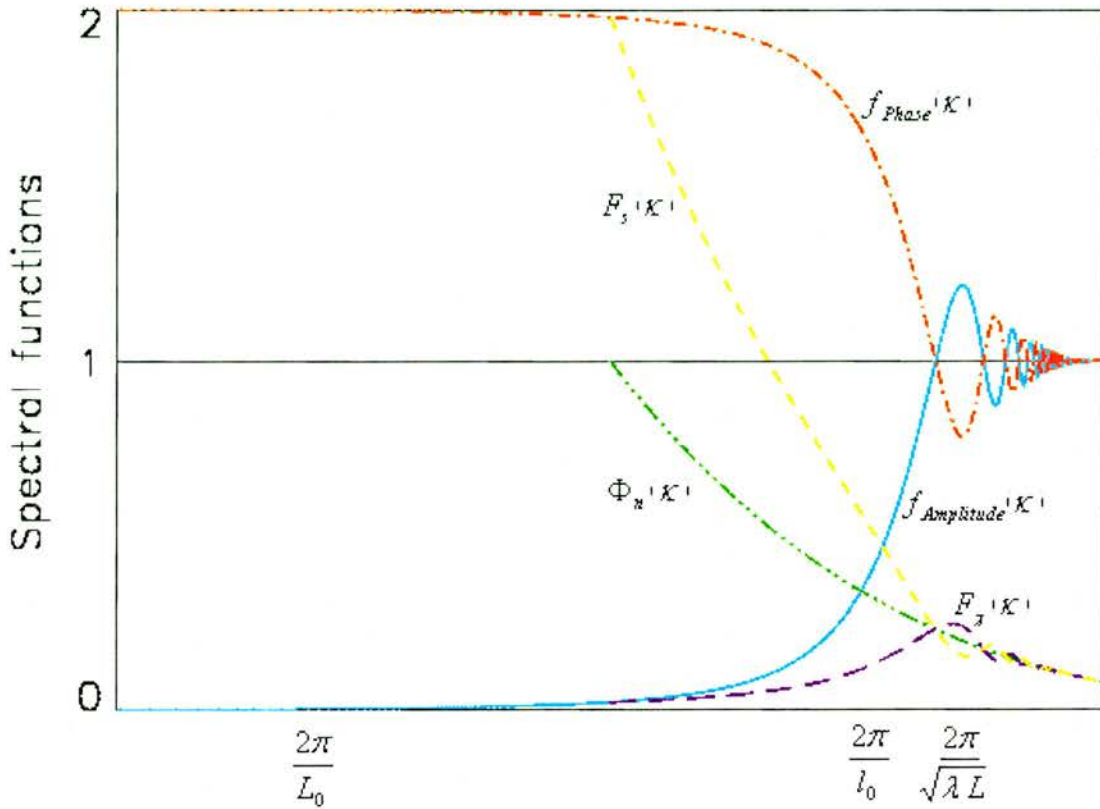


Figure 2-15 An illustration (not actual values) of spectral densities  $F_x(\kappa)$  and  $F_s(\kappa)$  when  $\sqrt{\lambda L} \ll l_0$ .

Figure 2-15 illustrates that under the condition  $\sqrt{\lambda L} \ll l_0$  the spectral density of phase fluctuations increases with eddy size. By contrast, the spectral density of amplitude fluctuations peak for eddy sizes equal to the inner scale of turbulence. It is therefore possible to mitigate amplitude fluctuations (but not phase fluctuations) by spatially separating sensors a distance greater than  $l_0$ .

The condition  $\sqrt{\lambda L} \ll l_0$  is in practice only plausible for optical links where wavelengths are micrometers and smaller. For millimetre wavelengths, e.g. 8mm, the path length would need to be  $<0.125\text{mm}$  to satisfy the condition  $\sqrt{\lambda L} \ll l_0$  given typical  $l_0$  sizes of 1mm. In all practical millimetre wave radio applications the size of  $\sqrt{\lambda L}$  is always larger than  $l_0$ , such as in the condition described next.

2.4.1.3.2 Fluctuation intensity and decorrelation distance when

$$l_0 \ll \sqrt{\lambda L} \ll L_0$$

When the size of the first Fresnel zone lays between the inner and outer scales of turbulence, spectral densities  $F_z(\kappa)$  and  $F_s(\kappa)$  take the form shown in Figure 2-16.

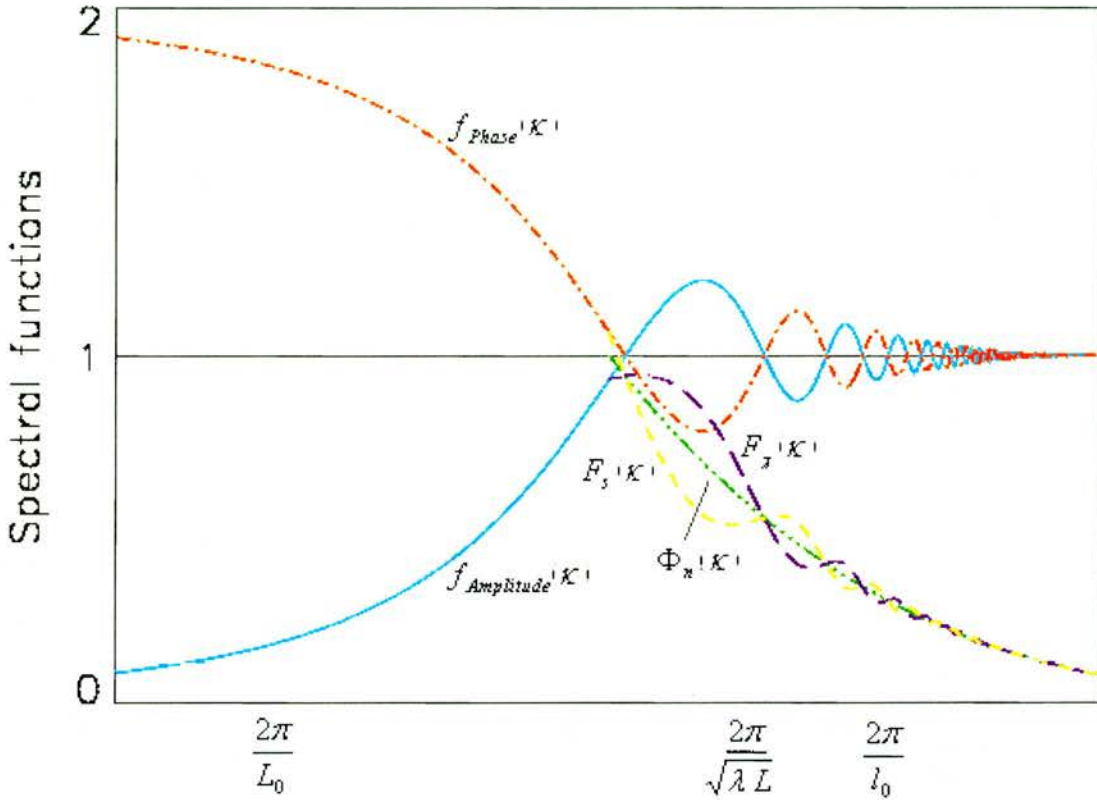


Figure 2-16 An illustration (not actual values) of spectral densities  $F_z(\kappa)$  and  $F_s(\kappa)$  when  $l_0 \ll \sqrt{\lambda L} \ll L_0$ .

Figure 2-16 shows that when the size of  $\sqrt{\lambda L}$  is between the inner and outer scale of turbulence the combination of spectral filter and refractive index spectral density increases the amplitude spectral density and decreases the phase spectral density. Importantly, the amplitude spectral density function reaches a maximum in the region where eddy sizes are approximately equal to  $\sqrt{\lambda L}$  in size. This is a classical result of Tatarski's correlation model. It states that the effects of eddies (amplitude

scintillation) can be mitigated by spatially separating antennas a distance greater than  $\sqrt{\lambda L}$ .

Though the above result was originally applied to optical frequencies it has also been applied to spatial diversity distances at millimetre wave frequencies. Its applicability to millimetre wave propagation in the surface boundary layer has however not been widely investigated and confirmed with experimental data. A comparison of experimental data with Tatarski's decorrelation distance would therefore be of significant interest.

#### 2.4.1.3.3 Fluctuation intensity and decorrelation distance when $L_0 \ll \sqrt{\lambda L}$

The final condition that is applied to fluctuation intensity is when the size of the first Fresnel zone is larger than the outer scale of turbulence. This condition is illustrated in Figure 2-17. It shows that amplitude and phase fluctuation spectral densities are equal under this condition because their spectral filter responses are equal, i.e.

$\frac{k}{\kappa^2 L} \sin \frac{\kappa^2 L}{k} \approx 0$ . Fluctuation intensity from eddies larger than the size of the first

Fresnel zone cannot however be assessed under this condition as there are no models that take account of the outer scale of turbulence. The decorrelation scale length required is greater than the outer scale of turbulence.

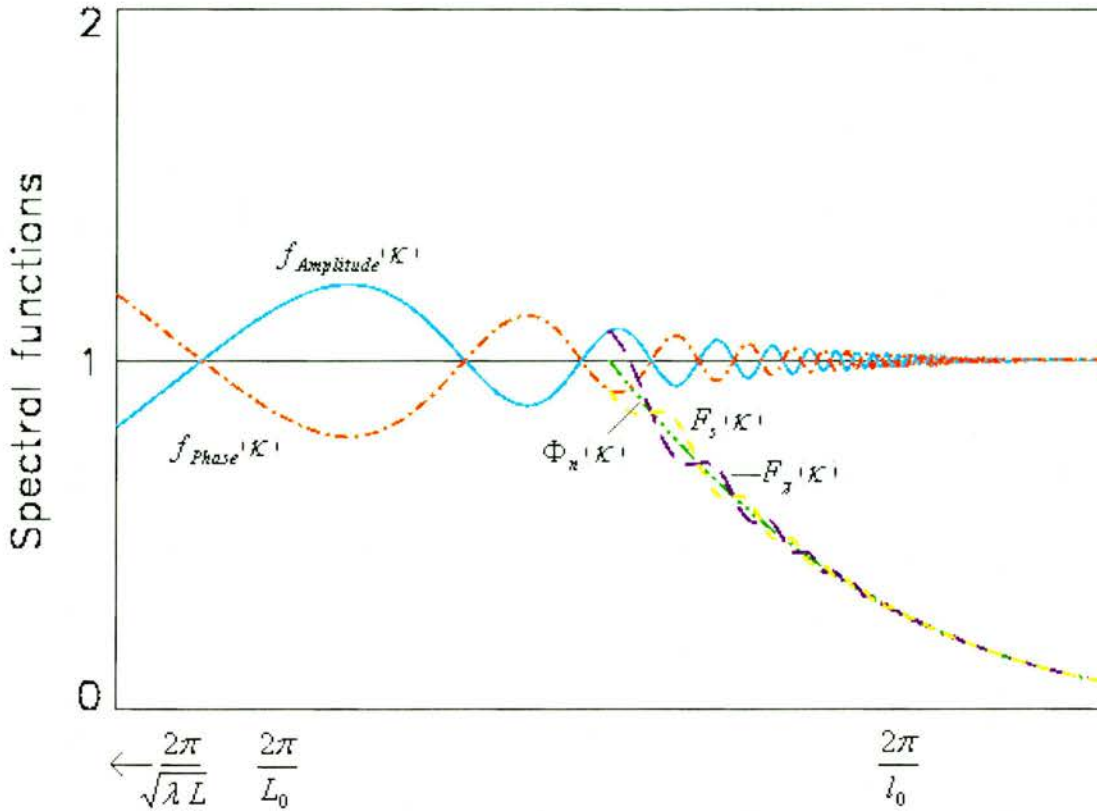


Figure 2-17 An illustration (not actual values) of spectral densities  $F_z(\kappa)$  and  $F_s(\kappa)$  when  $L_0 \ll \sqrt{\lambda L}$ .

#### 2.4.1.4 Previous investigations into scintillation

Previous investigations of tropospheric scintillation have concentrated on Earth-space paths. Measurements at 19 and 29GHz (Cox, 1981) have indicated that scintillation amplitudes are most significant on Earth-space paths when the propagation path traverses fair weather cumulus clouds. At 38GHz, scintillation amplitudes exceeding 20dB peak-to-peak and lasting for periods of several hours have been measured using a low elevation ( $<4^\circ$ ) slant path (Shukla and Harrod, 2001).

Data from Earth-space path experiments has also confirmed that the spectral density of scintillation (first formulated by Ishimaru (1978)) follows a  $f^{-8/3}$  spectrum for the inertial sub-range of Kolmogorov's turbulence spectrum (Lloret et al, 2001). This

theory was later extended (Haddon and Vilar, 1986) to account for aperture smoothing<sup>2</sup>. The probability density of scintillation has also been characterised using Earth-space path data. It has been shown that over short periods, i.e. less than 10 minutes, scintillation is normally distributed (Ortgies, 1985), while for periods greater than 10 minutes scintillation is log-normally distributed (Moulsley and Vilar, 1982).

Millimetre wave scintillation affecting terrestrial paths has been researched to a far lesser extent than Earth-space paths. Terrestrial experiments have predominantly been over relatively short path distances (<1km), where clear-air turbulence has been identified as having a detrimental effect on system reliability (McMillan and Bohlander, 1987). The most detailed terrestrial experiments at 36 and 94GHz were carried out over a 4.1km path (Ho et al, 1978; Cole et al, 1978). The data from this experiment confirmed the validity of Tatarski's (1961) scintillation variance models for terrestrial links.

The spatial decorrelation of scintillation in the surface boundary layer has on just one previous occasion been considered (Lee and Waterman, 1968). The experiment was carried out at 35GHz over a 28km path in San Francisco, USA. Measured data showed good agreement with Tatarski's (1961) decorrelation model for both horizontal and vertical antenna spacing.

The data collected from experiments such as those described above have in some cases been used to develop scintillation prediction techniques. Two different types of approach have been developed. The first type is mathematically rigorous, and uses

---

<sup>2</sup> Small aperture antennas (wide beam widths) reduce the effect of scintillation by spatially smoothing a number of uncorrelated ray paths. Narrow beam width antennas are therefore affected to a greater extent by scintillation.

turbulence models to describe the interaction between eddies and electromagnetic waves. Examples of such model approaches are (Riva, 2002):

- a. Annual scintillation prediction (Vasseur et al, 1996 and 1998). This technique uses long-term (>1year) radiosonde data and a statistical model based on meteorological data (Warnock et al, 1985) to determine the turbulent characteristics of the slant path from which scintillation is predicted.
- b. Monthly scintillation prediction (Peeters et al, 1997). Two types of monthly log-amplitude scintillation variance prediction models have been developed called the direct physical-statistical prediction (DPSP) method and modelled physical-statistical prediction (MPSP) method. The DPSP method is derived from surface temperature and the MPSP method is derived from surface refractivity. Both slant path methods are based on the correlation between surface meteorology and the monthly average of log-amplitude scintillation variance.
- c. Hourly scintillation prediction (Marzano et al 1998). This further group of slant path models predicts log-amplitude scintillation variance derived from surface based measurements of temperature, refractivity and integrated water vapour.

The second type of scintillation model takes a statistical approach assuming the short-term probability density of scintillation is Gaussian. This type of model, which is the most widely used for planning communication systems, calculates the log-amplitude variance or standard deviation of scintillation from statistical relationships based on measured slant path data and ground-based meteorology. Examples of statistical

approaches to modelling scintillation, which are all very similar, are referred to in the literature as:

- d. ITU-R 618.
- e. Karasawa (1988).
- f. Otung (1996).
- g. Ortgies (1993).
- h. Van de Kamp (1999).

The above scintillation prediction methods, both physical and statistically based, have in common their applicability, i.e. they are all applicable to slant paths only. Even though communication systems using millimetre wave frequencies are becoming more widely used for terrestrial applications there are currently no scintillation prediction models available for surface boundary layer links. The reason for the absence of terrestrial scintillation models is the shortage of experimental data. Data from experiments in the surface boundary layer are therefore in demand by link planners.

#### **2.4.2 Wavefront distortion**

Phase and amplitude fluctuations that characterise scintillation are present spatially as well as temporally. The turbulence-induced spatial variations in phase and amplitude distort wavefronts that are normally considered planar. This process is illustrated in Figure 2-18. It shows that eddies lead to spatially random focusing and defocusing of the wavefront.

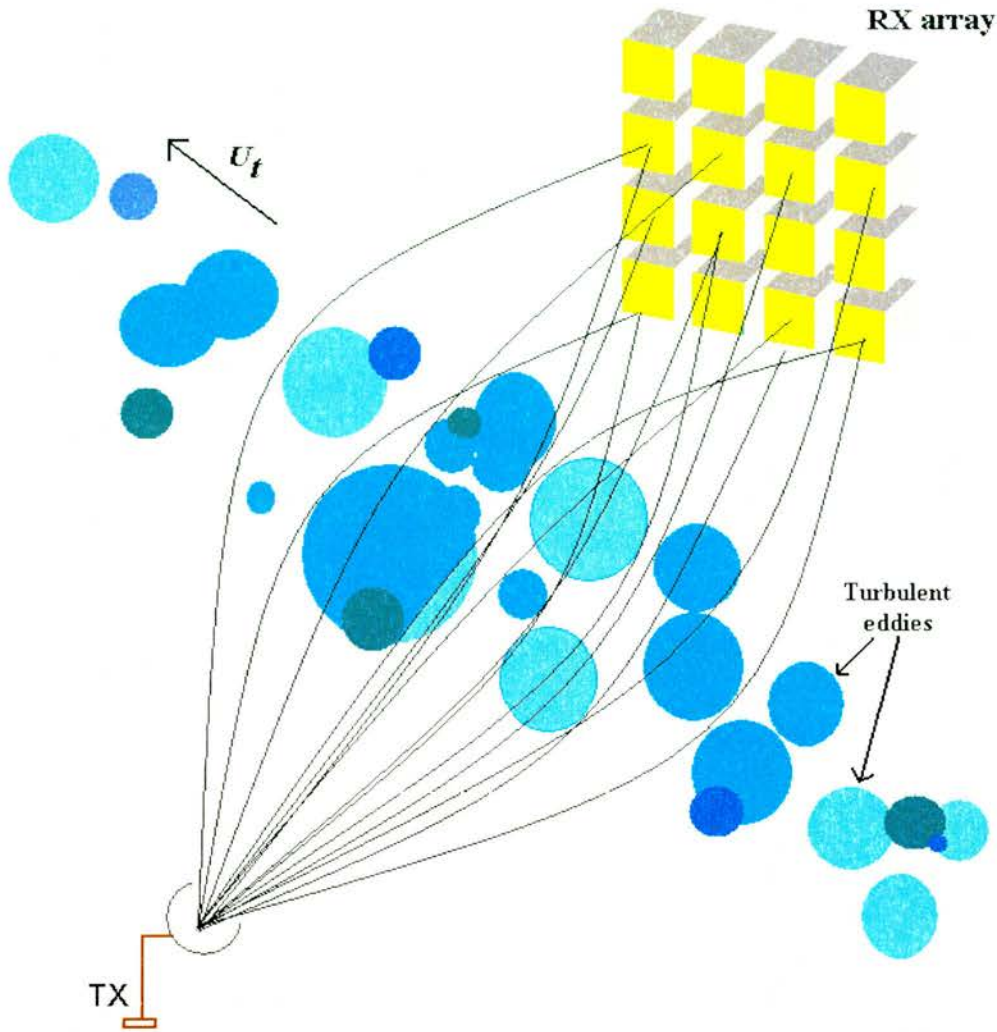


Figure 2-18 Wavefront distortion across a millimeter wave array due to eddies traversing the propagation path at mean wind speed  $U_t$ .

Wavefront distortion, also called phase-front distortion, is commonly defined as an antenna to medium propagation loss (Hall et al, 1996). The problem with this definition is that it refers to a single antenna rather than an antenna array. For applications using antenna arrays the difference in phase across an array of elements could lead to significant performance limitations. Such impairments would be especially evident in applications that require accurate tracking of mobile sources, as current tracking algorithms do not take account of the random fluctuations in the angle-of-arrival. Systems that have been documented as performance limited by wavefront distortion are optical telescopes (Tyson, 1991) and synthetic aperture radars

(Porcello, 1970). Phase errors impact these systems by limiting the attainable resolution. The limitation on array based communication system performance has so far to be defined.

#### 2.4.2.1 Previous investigations into wavefront distortion

Some of the earliest measurements of microwave phase errors were performed at 9.5GHz over a 25km, 7° elevated path in Hawaii (Norton et al, 1961). The experiment consisted of measuring the phase difference at a single antenna and between a series of separated antenna pairs transverse to the propagation path. The results from the experiment showed that the phase could vary by thousands of degrees over measurement durations of 15 minutes. Phase differences between antenna pairs separated by tens of wavelengths was  $\sim 0.5^\circ$ , separated by more than a  $100\lambda$  was  $>100^\circ$ , and separated by more than  $1,000\lambda$  it was  $>1,000^\circ$ . In terms of spectral density, phase fluctuations ranged from tens of degrees/Hz for small antenna separations to tens of thousands of degrees/Hz for antennas separated by thousands of wavelengths. These large values of spectral density were limited to sub-hertz frequencies, typically in the range 0.001 to 0.01Hz.

In support of the above experiment a further study was conducted using the same path geometry and frequency (Thompson and Janes, 1970). The experiment considered phase fluctuations at a single receiver (range power spectra), phase difference between two spatially separated receivers (range-difference power spectra), and the difference between two range differences using a common antenna (second order range-difference power spectra). The range and range-difference spectra for antenna separation distances of 1.25 to 790m showed that phase fluctuations occurred mostly

at sub-hertz frequencies ( $<0.1\text{Hz}$ ), with spectral densities in the order of  $10^{-3}$  to  $10\text{cm}^2/\text{Hz}$ . Second order range-difference spectral densities were generally larger than range-difference densities.

In contrast to the above microwave measurements of wavefront distortion there is no record of wavefront distortion measurements at millimetre wave frequencies. There have however been temporal phase fluctuation measurements by a number of experimenters. One such measurement campaign was carried out over a 64km path ( $2.5^\circ$  elevation angle) between Hawaii and Maui (Thompson et al, 1975). The measurement campaign consisted of four links ranging in frequency from 9.5 to 33.3GHz. The results obtained showed phase shifts greater than a wavelength occurring at all frequencies considered. The spectral density of phase variations was approximately the same for all frequencies ( $\propto f^{-8/3}$ ), with density values similar to those discussed above. Interestingly, the coherence between phase variations at different frequencies (e.g. 9.5 and 22.2GHz) was very high ( $>0.99$ ) up to fluctuation frequencies of 0.1Hz. As the majority of phase fluctuations occurred at frequencies below 0.1Hz, the high coherency would indicate that frequency diversity would not mitigate scintillation or wavefront distortion.

## 2.5 Summary

This review chapter has described the meteorological parameters that influence the performance of millimetre wave communication and sensor based systems. It has been shown that while hydrometeors are the dominant impairments to millimetre wave propagation, small-scale anomalies in the refractive index structure of the atmosphere can also significantly impair system performance.

It is apparent from reviewing the literature on millimetre wave propagation that there is currently a sparse amount of data available from long-range paths ( $>10\text{km}$ ) through the surface boundary layer. In particular, it is very difficult to obtain any measurement data of the spatial variability of scintillation. This finding is widely acknowledged by researchers in the field of millimetre wave propagation and has been documented by both COST 235 and COST 280. The work presented in this thesis will therefore provide much needed information on the temporal and spatial characteristics of tropospheric scintillation in the surface boundary layer.

# Chapter Three

## Design of a Sensor Array for Measuring the Temporal and Spatial Effects of Atmospheric Turbulence

### 3.1 Introduction

A sensor array has been developed to investigate the effects of atmospheric turbulence on millimetre wave propagation. The purpose of the sensor array is to measure the properties of scintillation due to eddy transport through the tropospheric surface boundary layer. In this way, the array is capable of separating out the temporal and spatial characteristics of scintillation.

The sensor array specification is defined in the first part of this chapter. The specification considers the functional, mechanical, and electrical performance criterion required of the sensor array to provide the necessary level of data integrity. Consideration is also given to the experimental link used for collecting data.

### 3.2 Requirements of the sensor array

The first step in developing a sensor array to measure spatial and temporal channel characteristics is to define the system requirements. The system definition phase identifies the functional requirements so that a detailed specification can be produced (Evans, 1999). The requirements of the sensor array are summarised as follows:

- a. Measurement parameters – The data collected from the sensor array will primarily be used to measure the spatial and temporal characteristics of

tropospheric amplitude scintillation. Phase information used to analyse wavefront distortion will be predicted from measurements of amplitude scintillation (the method is described in Chapter seven). The measured parameter will therefore be a time series of power fluctuations.

- b. Waveform – A 36GHz (atmospheric window) continuous wave signal will simplify the design (compared to a wideband design) and satisfy the time series data requirements.
- c. Array configuration – The more elements there are in an array will increase the spatial resolution of the measurements. Ideally an array would have elements in both the vertical and horizontal directions so that eddy transport can be investigated in two dimensions. For practical purposes it was decided that the array would initially comprise of five elements in the horizontal only, with a view to rearranging two of the elements into the vertical at a later date.
- d. Measurement stability – To characterise scintillation the short-term (minutes) and long-term (days, month) stability of the sensor array are important. The array is required to have a short-term variation of  $\leq 1\text{dB}$  and a long-term variation of  $\pm 1\text{dB}$  from the mean level of the benign channel, i.e. free of anomalies. These values were specified on the basis that individual tropospheric scintillation events, which typically last for periods of two to three minutes, require a stable reference level from which to measure fluctuations. Also, scintillation less than 1dB will not normally have an impact on the performance of a communication link. The long-term specification ensures that events measured throughout the data collection period have a common baseline.

- e. Environment (deployment) – The sensor array will be deployed outdoors where continuous operation under harsh weather conditions can be expected. It is therefore required that the array be fully weatherproofed and mechanically stable, i.e. a rigid metal frame to prevent movement in the array elements.
- f. Data capture and storage – The data capture and storage system should sample and archive data from the five sensors at a rate greater than the frequency of tropospheric scintillation, i.e. generally sub-Hertz. A sampling frequency of 10Hz is judged to be sufficient.

The above requirements describe the array in the broadest of terms. The next step in producing a detailed design is to consider the experimental link used for data collection. This will provide information for the link budget and component selection.

### **3.2.1 Experimental link**

The link chosen to collect data is located in central England, UK. The transmitter site (TX) of the link is in the Bredon Hills (height=211m, 52° 3.573'N, 2° 4.047'W) and the receiver site (RX) is in the Malvern Hills (height=75m, 52° 5.983'N, 2° 18.849'W). The link (Figure 3-1) was selected on the basis that it has clear line-of-sight across 17.3km of countryside and therefore has a clutter free first Fresnel zone. Fluctuations in signal strength are therefore assumed to be atmospheric related.

Meteorological stations (MS) measuring wind speed, wind direction, temperature, relative humidity, pressure, rainfall and light intensity were located at the link mid-point (height=30m, 52° 3.73'N, 2° 11.801'W, 3 minutely samples) and at the receiver array location (height=60m, ~120m north of the array, 10 minutely samples). The

difference in sampling rate is a result of reduced memory capacity of the sensor array located met station.

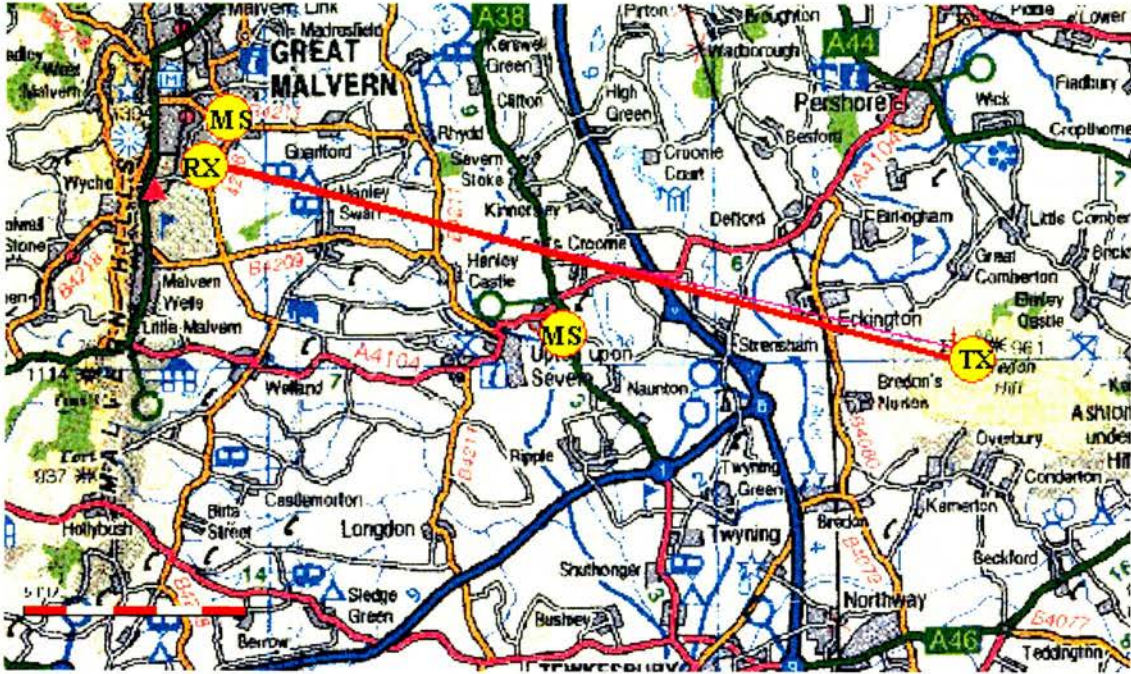


Figure 3-1 The location of the experimental link.

The next stage in the sensor array development process is to produce a detailed design. This is described in the following section.

### 3.3 Detailed design

In the previous section the following design features were identified:

- a. Frequency of operation: 36GHz continuous wave (CW).
- b. Number of elements: 5.
- c. Configuration: linear horizontal.
- d. Array length: 10m.
- e. Data storage: time series of power measurements.

- f. Long-term stability:  $\pm 1$ dB, short-term stability:  $\leq 1$ dB.
- g. Sampling rate: 10Hz.
- h. Mechanical variation across the array: minimised, weatherproofed to IP 65 (water resistant up to the point of submersion).

The above requirements were translated in to the system architecture shown in Figure 3-2. It consists of three sub-assemblies:

- i. Antenna units. These contain a lens horn antenna (LHA), monolithic microwave integrated circuit (MMIC) receiver and second stage mixer.
- ii. Signal-conditioning unit. Provides the local oscillator (LO) signals for the MMIC receivers and second stage mixers, together with power supplies, filtering and amplification.
- iii. Data acquisition system. Performs simultaneous sampling and storage of data for the 5 sensors. Data acquisition processing is performed on a PCI card housed in a dedicated PC.

The array can be considered as a five-channel superheterodyne millimetre wave receiver. The MMIC receivers translate the 36GHz CW signal to 4GHz before further down conversion to audio frequency (AF). The resulting signals are filtered and amplified prior to data acquisition. Data analysis is carried out off-line.

In the following sections the main components of the sensor array are described.

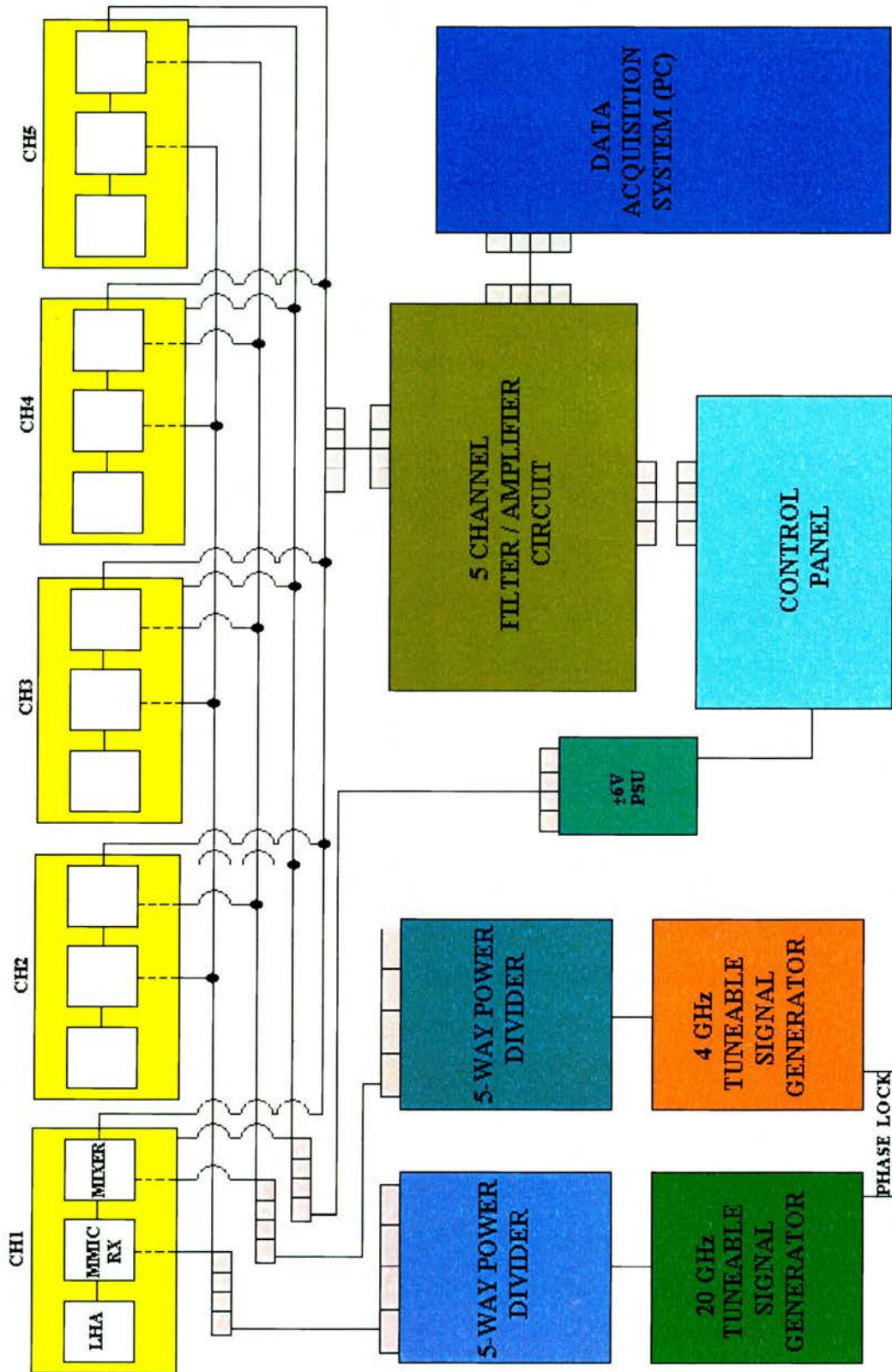
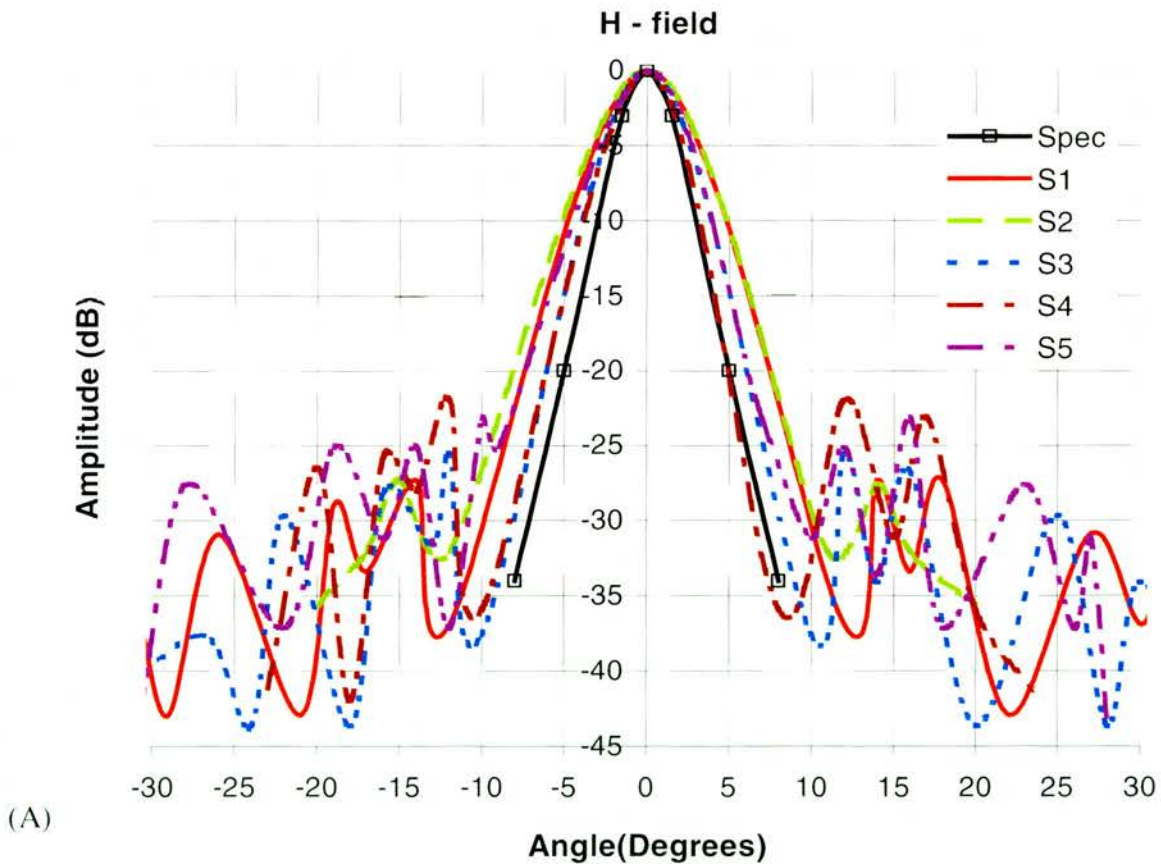


Figure 3-2 A block diagram of the sensor array instrument showing its main functional blocks.

### 3.3.1 Lens horn antennas

The reason for choosing LHAs (Flann Microwave) instead of parabola dishes is twofold. Firstly, LHAs are robust and can operate in varying climatic conditions. LHAs offer less wind resistance, low thermal mass to combat snow and ice and a weather proofing membrane that prevents formation of condensation. Secondly, LHAs are industry standard for 36GHz terrestrial systems and therefore the data collected from the array will be directly relevant to commercial terrestrial links.

The LHA gain patterns were measured in both azimuth (H-field) and elevation (E-field). The measured patterns are shown in Figure 3-3.



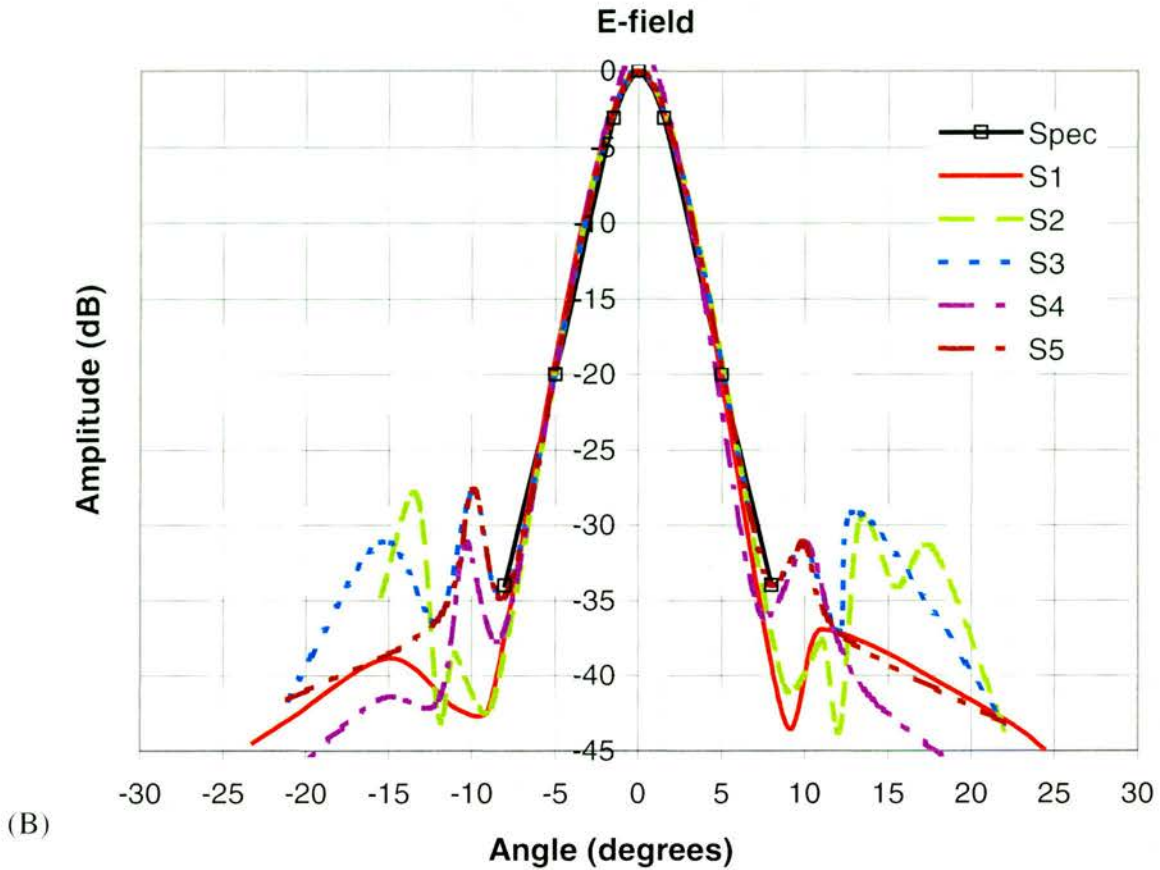


Figure 3-3 (A) The H-field patterns and (B) E-field patterns of all five sensor array LHAs.

The antenna pattern measurements were performed over the experimental link using the sensor array and not in an anechoic chamber. They show good agreement with the manufacturers specification for half power beam widths of  $3.1^\circ$  and  $3.7^\circ$  for the E-field and H-field respectively. The main lobe peak to side lobe level is approximately 28dB (average for the five horns considering E and H fields).

### 3.3.2 MMIC receivers

The MMIC receivers (designed by QinetiQ Electronics Dept) are fully packaged radio frequency (RF) devices. The devices were selected for the array because of their compact size, wide intermediate frequency (IF) range and stability in comparison to

voltage-controlled cavity oscillators. The internal structure and physical implementation of a MMIC receiver is shown in Figure 3-4.

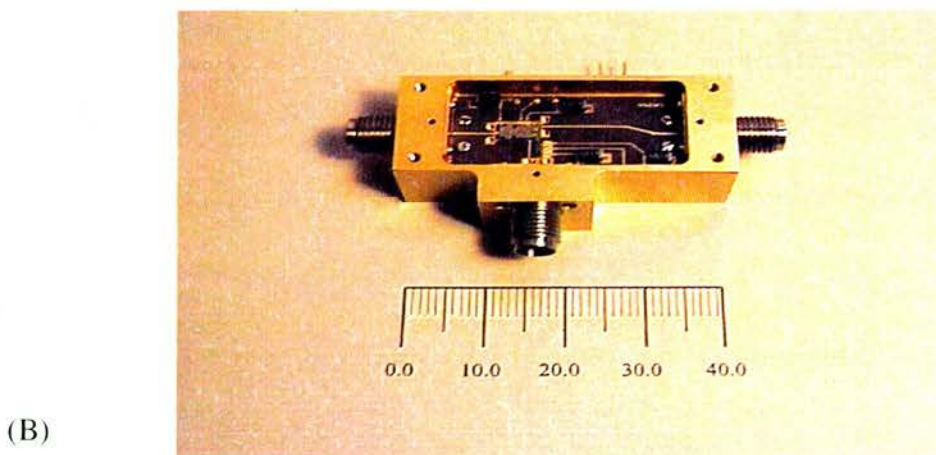
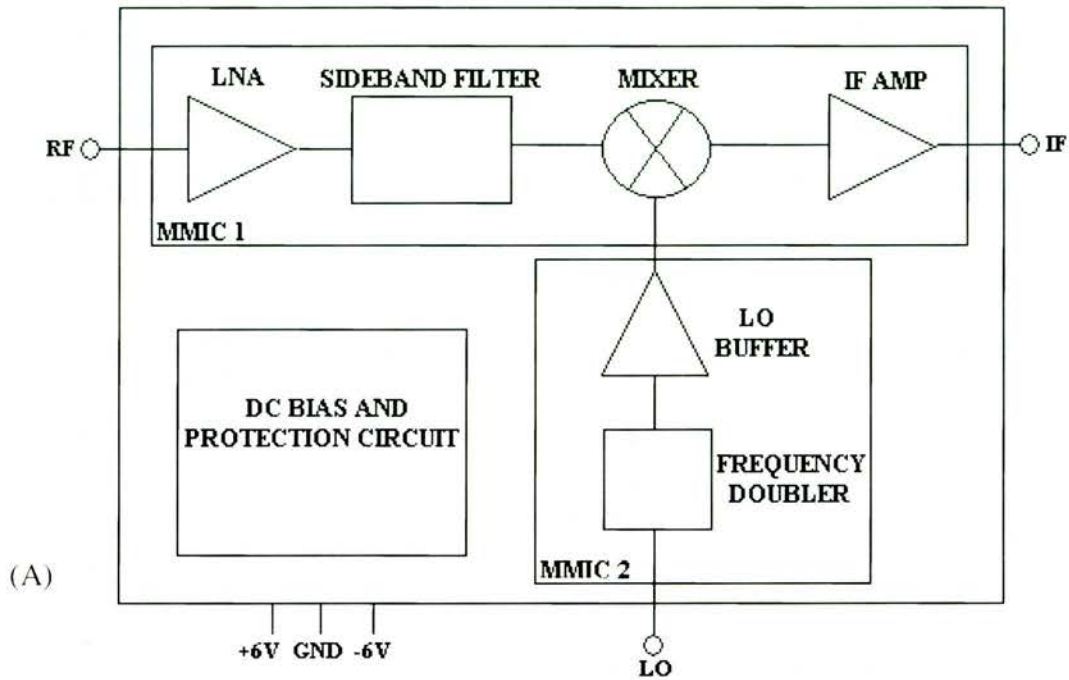


Figure 3-4 (A) The internal structure of a 36GHz MMIC receiver. (B) A photograph of a MMIC receiver. The physical size of the device is 42mm x 27mm x 15mm.

Figure 3-4 shows a MMIC receiver consisting of two MMICs and a DC board. The function of MMIC 1 is to amplify, filter (image reject), and down convert the RF input signal prior to IF amplification. The function of MMIC 2 is to buffer the frequency doubled LO signal that is later mixed with the incoming RF signal. For this

particular receiver the LO frequency range is 16–19GHz, the IF range is 2–8GHz and the RF range is 34–40GHz. The mean NF at 36GHz is 4.8dB.

The IF output power to LO input power was also measured at 36GHz (Figure 3-5). The results show that at low LO input powers the conversion gain of each MMIC receiver is quite different (~20dB for a -3dBm LO). The reason for this is that inadequate power is being supplied to properly bias the mixer, and therefore in the case of S2 a significant conversion loss is experienced. For LO input powers above 3dBm the conversion gain remains approximately constant (a maximum) at 20–25dB depending on the receiver.

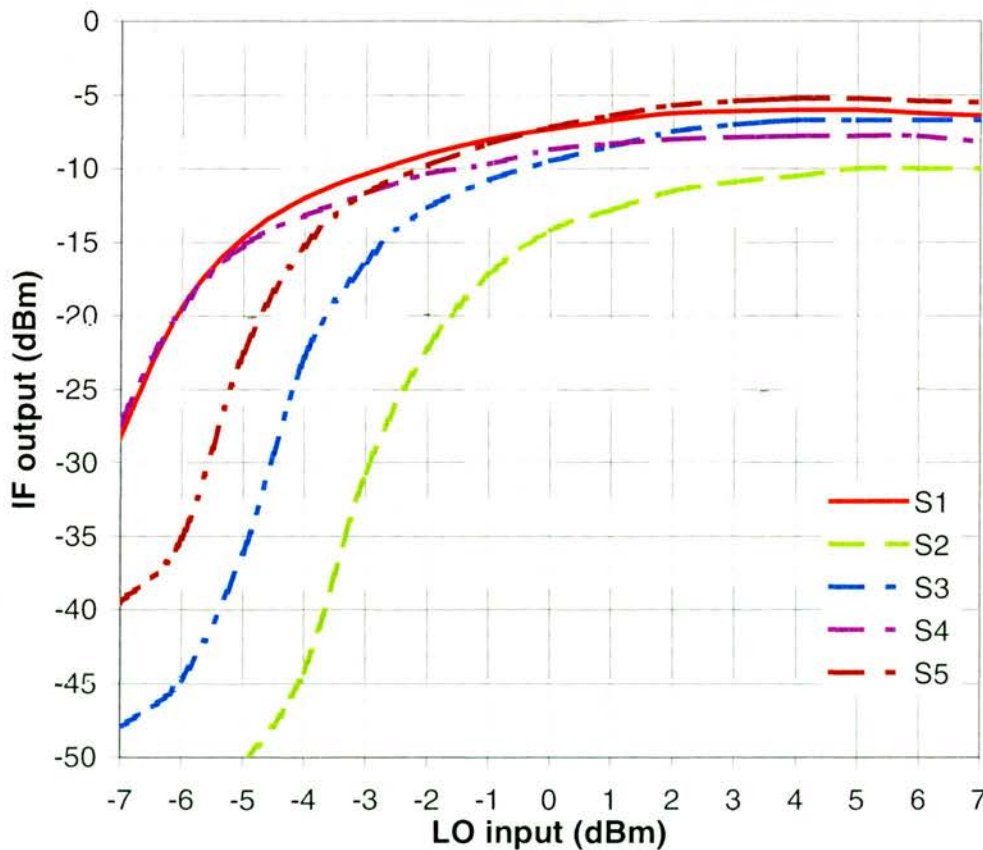


Figure 3-5 A plot of IF output power as a function of LO input power for the five MMIC receivers of the sensor array. The RF input is -30dBm.

The conversion gain difference between each MMIC receiver does not have a significant impact on the array performance as long as the difference is constant. If the

gain is not constant it could appear that an atmospheric effect such as scintillation was occurring. To ensure this did not occur the signal generator used to provide LO power was tested and found to vary by a less than 0.1dB.

Although the conversion gain difference described above did not result in measurement inaccuracy a more significant problem was later found with MMIC receivers S2 and S4. It was found that the operation of these two devices became unpredictable, working only for periods of a few hours at a time before effectively switching off. The reason for their failure was due to faulty wafer fabrication that was later resolved at the foundry where they were produced. For this reason the results presented in this thesis refers to data collected from all five MMIC receivers when available, and on other occasions from MMIC receivers S1, S3, and S5 only.

### **3.3.3 Second stage down conversion**

Connected directly to the IF output of the MMIC receivers are double-balanced frequency mixers (Mini-Circuits) to down convert the IF to AF. For the purpose of equipment calibration and link budget analysis the conversion loss of the array's second stage mixers was measured. In each case, and for a range of RF signal frequencies, the mean conversion loss was 5.5dB.

### **3.3.4 LO signal generation**

The signal generators providing LO power to the MMIC receivers and second stage mixers are tuneable standard bench equipment. This allows flexibility in the choice of transmitter frequency should a change in carrier frequency be required.

The outputs from the LO signal generators are evenly divided five ways by standard components (MCLI). The connections between the power dividers in the signal conditioning unit and antenna units are 5m lengths of phase matched flexible waveguides (Reynolds industries).

The LO frequencies were chosen to produce an IF to the data acquisition system of 5kHz. The implication of setting the IF frequency to 5kHz is that the data acquisition system samples at or above 10kHz/channel (Nyquist), and therefore a large data storage facility is required. Such a high sampling frequency is excessive, as the typical frequency of scintillation is generally sub-hertz. The reason for choosing such a high IF is to avoid the contribution of flicker noise ( $1/f$ ) and burst noise ( $1/f^2$ ) to the received signal and to preserve the signal-to-noise ratio. The approach taken to achieve the required sampling rate of 10Hz from the initial sampling rate of 10kHz was to use digital signal processing (DSP). This is described in Section 3.3.6.

### **3.3.5 Filtering and amplification**

The filters and amplifiers of the sensor array were specifically designed for data acquisition systems where accuracy is required at very low input signal levels (micro volts). This requirement ensures the common-mode rejection ratio at typical operating frequencies and gains is greater than 100dB. A diagram of the circuit is shown in Figure 3-6. Descriptions of the functionality of the filter and amplifier are given in the following sections.

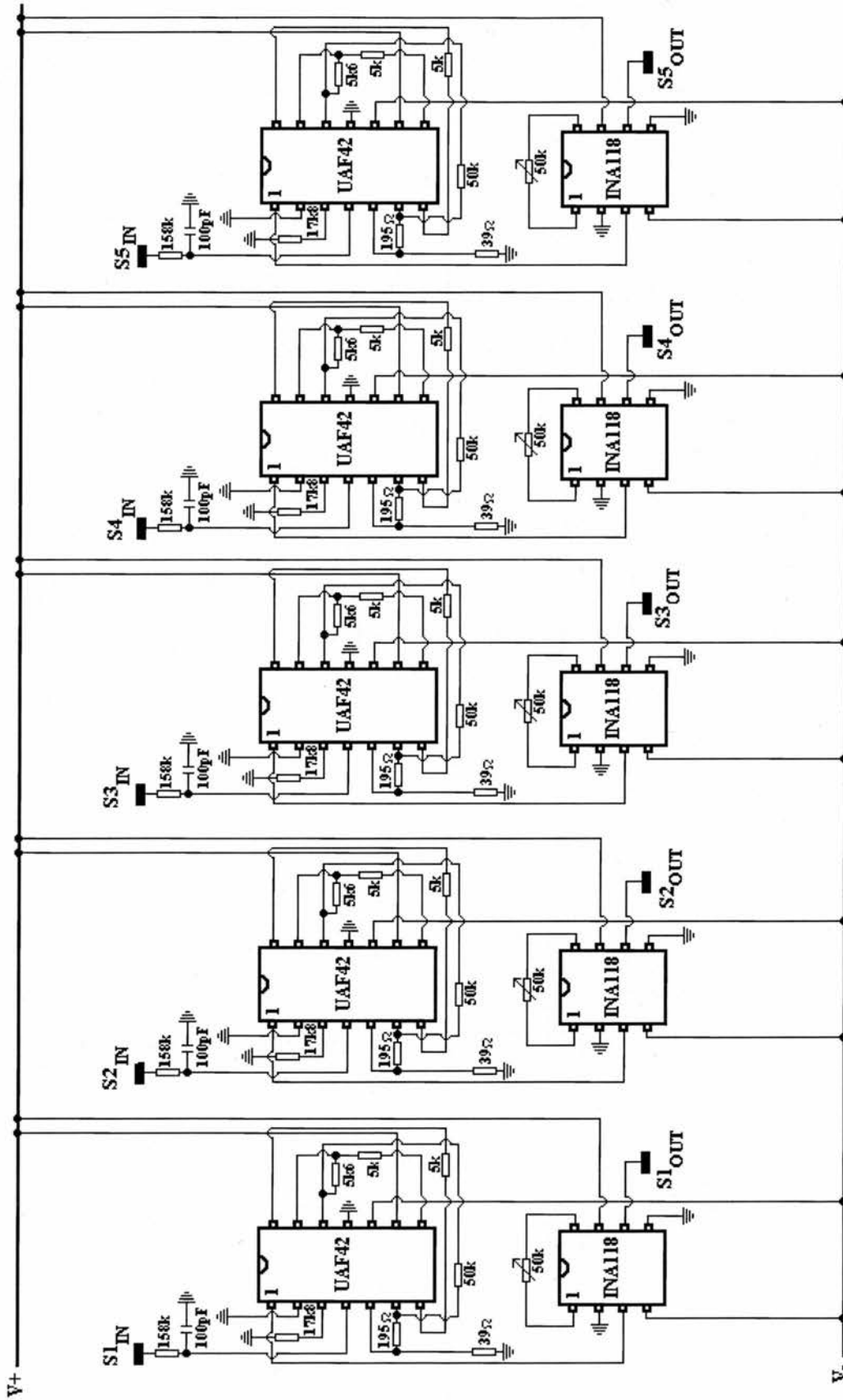


Figure 3-6 The five channel filter (UAF42) / amplifier (INA118) circuit.

### 3.3.5.1 Filter sub-circuit

The filter circuit is required to remove the unwanted spectral components (harmonics) generated from the LO and RF signals during frequency down-conversion. The harmonics to be filtered are the products of the RF and LO producing the IF of 5kHz. As the unwanted spectral components (sum, 2<sup>nd</sup> and 3<sup>rd</sup> order products) are at microwave frequencies a low-order, low pass filter will provide sufficient filtering of these high frequency spectral components. The filter chosen to perform this function is a universal active filter (UAF) 42 (Burr-Brown).

The UAF42 is a second order filter configured as low-pass and implemented as a Butterworth type. The filter IC contains an uncommitted operational amplifier (op-amp) that in this circuit has been used to provide a small amount of gain (pre-amp) and increase the filter's characteristic to third order. The voltage gain ( $G$ ) is given by:

$$G = 20 \log_{10} \left( 1 + \frac{195\Omega}{39\Omega} \right) = 15.6 \text{ dB} \quad (3-1)$$

where the 195 $\Omega$  and 39 $\Omega$  resistors are across pins 5 and 6 of the filter IC. The corner frequency ( $f_c$ ) of the uncommitted op-amp filter is given by:

$$f_c = \frac{1}{2\pi \times (158 \text{ k}\Omega) \times (100\text{pF})} = 10 \text{ kHz} \quad (3-2)$$

where the 158k $\Omega$  resistor and 100pF capacitor are connected to pin 4 of the filter IC.

The 15k $\Omega$  resistors connected between pins 7 and 14 ( $R_{F1}$ ) and pins 8 and 12/13 ( $R_{F2}$ ) of the UAF42 set the second order corner frequency (following the uncommitted op-amp filter). These resistors are related to the corner frequency ( $\omega_n$ ) of the filter by the following expression:

$$\omega_n^2 = \frac{R_2}{R_1 R_{F1} R_{F2} C_1 C_2} \quad (3-3)$$

where  $R_1$  and  $R_2$  are  $50\text{k}\Omega$ , and  $C_1$  and  $C_2$  are  $1000\text{pF}$ . These four components are internal to the filter IC.

The characteristic response of the UAF42s was configured as Butterworth as it offers a flat pass-band response. Its reduced transition band steepness (compared to Chebyshev) is not an issue in this design as the harmonics are at microwave frequencies. The transfer function of a Butterworth filter is given by:

$$\frac{V_{out}}{V_{in}} = \frac{1}{(1 + (f/f_c)^{2n})^{1/2}} \quad (3-4)$$

where  $f$  (Hz) is the frequency and  $n$  is the filter order. Figure 3-7 shows the predicted response given by equation (3-4) compared with the measured filter responses.

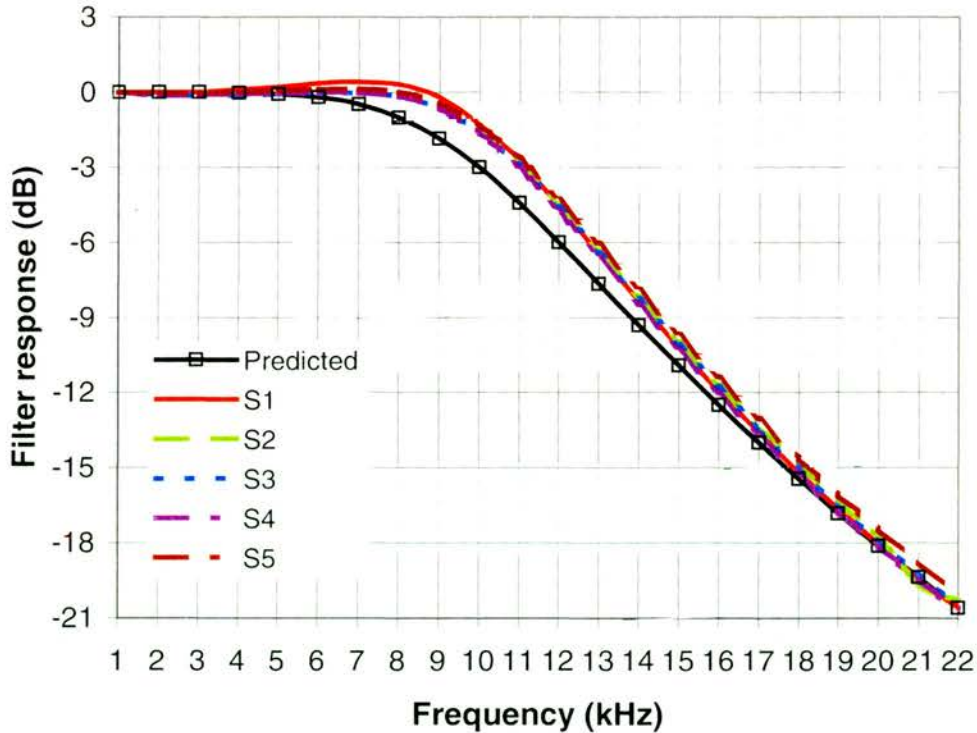


Figure 3-7 Filter response for the five channels of the sensor array compared with the predicted response for a 3<sup>rd</sup> order Butterworth filter. The corner frequency is 10kHz.

The measured filter responses show good agreement with the ideal Butterworth filter. More significantly, the difference between the five filter responses is very small. The average calculated difference (standard deviation) is 0.18dB for the frequency range shown.

### 3.3.5.2 Amplifier sub-circuit

The low power signals following the filter stage are amplified with instrumentation amplifiers (INA118) specifically designed for data acquisition systems (Burr-Brown). The gain of the INA118 amplifier is selected with a single resistor ( $R_G$ ) between pins 1 and 8.  $R_G$  is a 50k $\Omega$  variable resistor that produces a voltage gain factor of between 2 and 10,000 (see equation (3-5)). Practical gains are however limited to  $\leq 100$  ( $R_G = 500\Omega$ ) as the gain can become unstable at lower resistances due to temperature variations in the wiring and sockets. The choice of a variable gain resistor allows amplitude imbalances between the five channels to be removed.

$$G = 1 + \frac{50 \text{ k}\Omega}{R_G} \quad (3-5)$$

Figure 3-8 shows the measured characteristic of each of the five amplifier sub-circuits compared with the ideal predicted response given in equation (3-5). It shows that all five channels are in good agreement with the predicted response except for gains greater 100. For gain settings less than 100 the average calculated voltage gain error (standard deviation) across all five filters is 0.34, where as gains greater than 100 the error is 2.94. This illustrates the gain uncertainty factor above 100 that occurs as a result of wiring resistance and temperature variations.

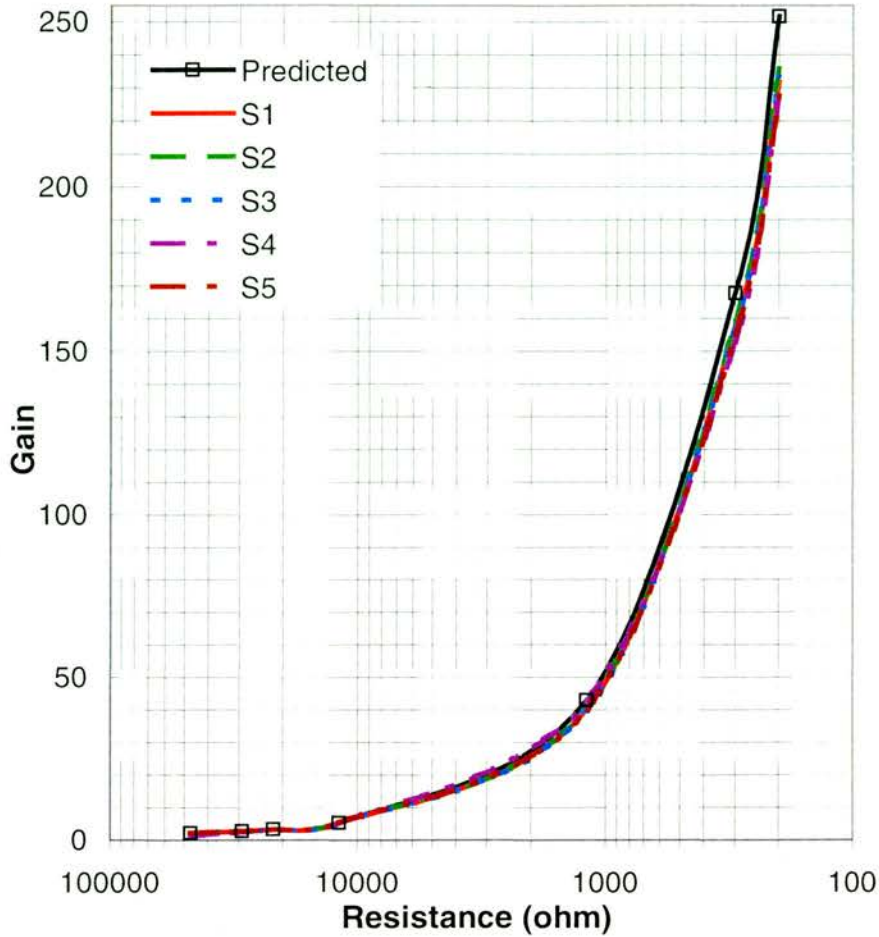


Figure 3-8 Gain response of the INA118 instrumentation amplifier circuits as a function of the gain setting resistor  $R_G$ . All five channels are shown compared with the predicted response of an ideal INA118.

### 3.3.6 Data acquisition

The data acquisition system used is the iDSC 1816 (Microstar Laboratories). It operates by simultaneously sampling up to eight analogue channels at a fixed rate of 9.8304MHz. The sampled data is decimated by a factor of 64 within eight analogue-to-digital converters, then filtered and further decimated by a pair of on board 80MHz digital signal processors. The decimated data is buffered into the host PC where it is stored direct to hard disk. The control of the data acquisition system is by an on-board Intel 486DX4 (96MHz) processor.

The iDSC 1816 was chosen from a variety of data acquisition systems because it offers the ability to define a range of sampling rates, filter configurations with brick wall responses, and bespoke DSP functions that can be written in C++. This ability to extend the functionality was employed to reduce the data storage requirements of the sensor array given the high (5kHz) IF signal frequency (recall Section 3.3.4), i.e. 6Mbytes/minute for 16-bit ADC resolution given Nyquist sampling. Such a data storage requirement would prohibit long-term continuous data collection and make data processing cumbersome and time consuming. The approach taken to reduce data storage was to implement a digital complex filter (Hilbert transform) in the data acquisition system to convert the sampled data to power values and then re-sample at a more appropriate rate, i.e. 100Hz. Post processing further decimated the data down to 10Hz, retaining the 100Hz data as a back up for possible later use. Figure 3-9 illustrates the process of converting a real data stream into a complex data stream using a digital Hilbert transform filter.

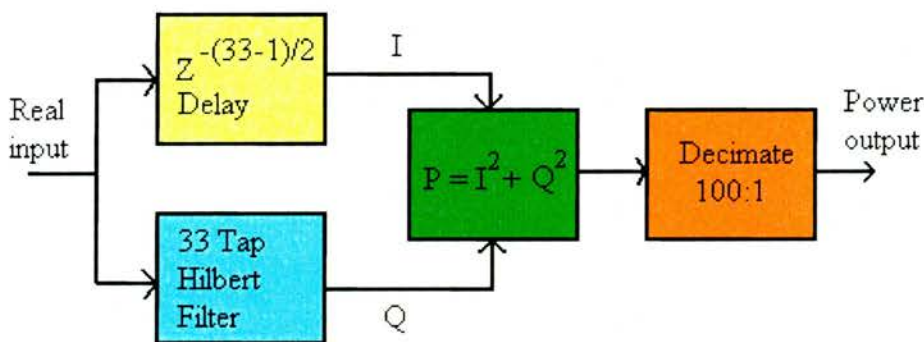


Figure 3-9 A block diagram illustrating the process of a digital Hilbert filter.

Figure 3-9 shows a real (I) to imaginary (Q) complex signal conversion is performed digitally by passing a copy of the real signal through a 33 tap (coefficient) finite impulse response (FIR) filter. The implementation of the FIR filter is shown in Figure 3-10.

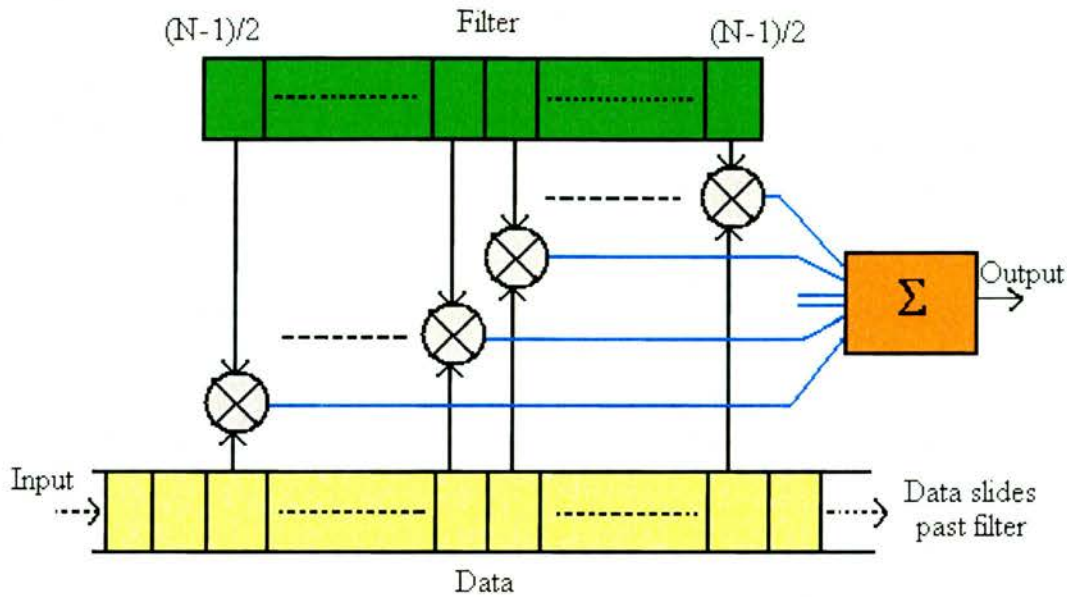


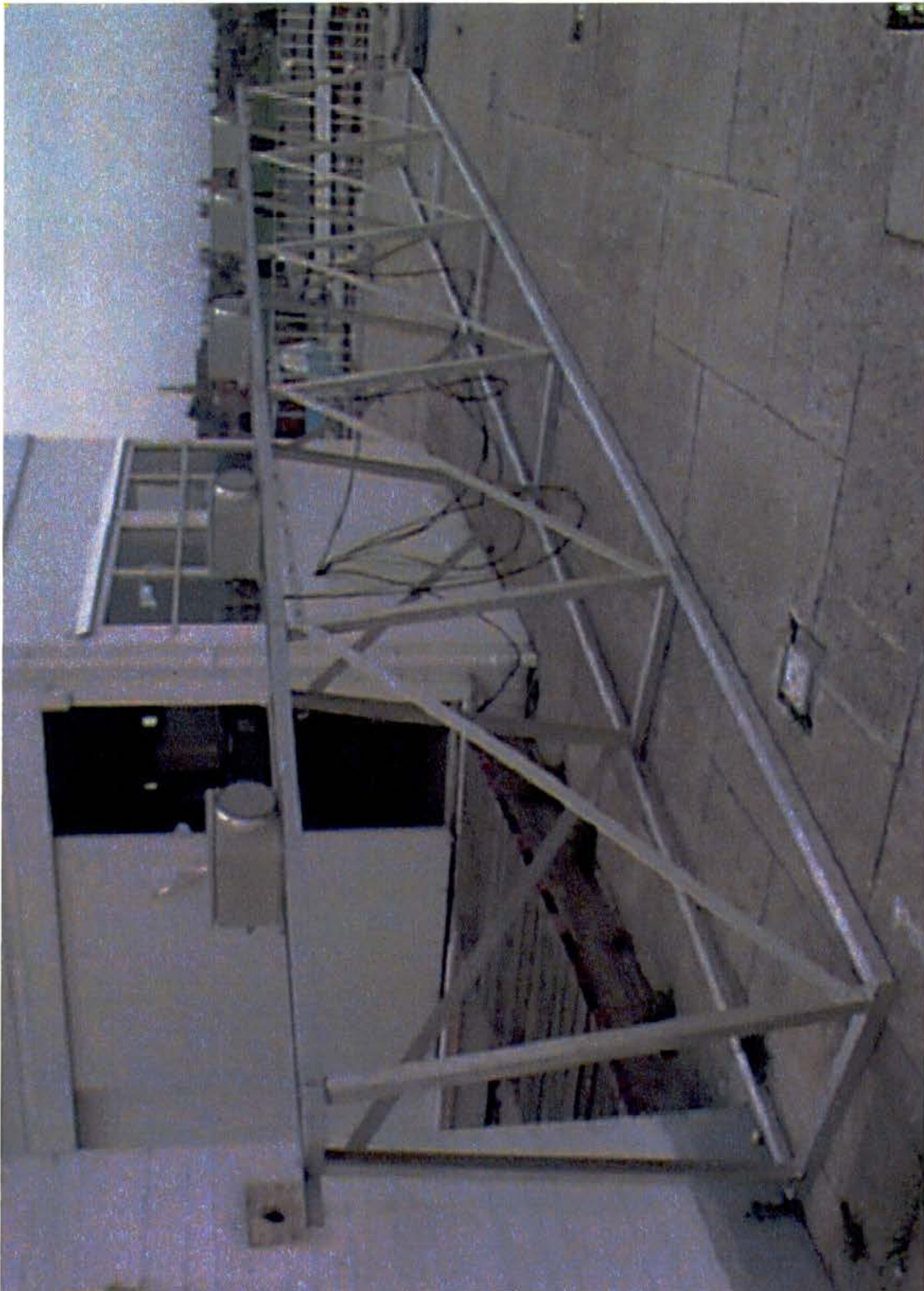
Figure 3-10 The FIR filter is a combination of a shift register and multiplier/summing network that calculates the imaginary signal from a real data stream.

Figure 3-10 shows that an FIR filter is implemented by sliding the data through the filter in one-sample steps, cross multiplying the data with the filter coefficients and summing the result. Because there is a delay through the filter of  $(N-1)/2$  samples, i.e. each output from the filter is a function of past and present values, the real component of the complex signal is delayed ( $Z$ ) by  $(N-1)/2$  samples.

The Hilbert coefficients for the filter implementation used in the sensor array was calculated using the Remez exchange algorithm developed by McClellan and Parks (Embree and Danieli, 1999). It produces approximately unity gain with a  $90^\circ$  phase-shift and a pass band ripple of 0.2dB.

### 3.3.7 Mechanical structure

A rigid framework to minimise the movement of the sensor elements is a design requirement. Variable spacing of the sensor elements is also required to measure scintillation events at a range of spatial separation distances. The frame designed for the sensor array is shown in Figure 3-11.



*Figure 3-11 Photograph of the sensor array (10m long and 1.6m high). The spacing between sensor elements can be varied from 0.5m to 10m. The signal conditioning unit supplying LO power, filtering and amplification is located with the data acquisition system in the building to the rear of the frame.*

Figure 3-11 shows that the mechanical stability requirement was realised with a robust, rigid frame that prevents any significant lifting or twisting in the event of harsh weather conditions. The framework, which is 10m long, provides sensor element fixings at 0.5m intervals all along the frame. The length of the frame allows sufficient spacing for more than five elements to be mounted should further sensor array elements become available at a later time.

### 3.4 Link budget analysis

The link budget for the sensor array experiment, given in terms of the expected received signal power ( $P_R$ ), is expressed mathematically as:

$$P_R = P_T + G_T + G_R - L_s - L_a \quad \text{dB} \quad (3-6)$$

where,  $P_T$  (dB) is the transmitted power.

$G_T$  (dBi) is the transmitter antenna gain.

$G_R$  (dBi) is the receiver antenna gain.

$L_s$  (dB) is free space path loss.

$L_a$  (dB) is the additional atmospheric loss.

Using the parameters below, the predicted received signal level is  $-28.5\text{dB}$  (max).

- i.  $P_T = 20\text{dBm}$ .
- ii.  $G_T = 28\text{dBi}$  (same antenna type as used for the receiver elements).
- iii.  $G_R = \text{antenna gain (28dBi)} + \text{MMIC receiver gain (25dB max)} - \text{mixer conversion loss (5.5dB)} + \text{pre-amp gain (15.6dB)} + \text{instrumentation amplifier gain (40dB max)} = 103.1\text{dB (max)}$ .

iv.  $L_s = 147.9\text{dB}$ . It is calculated from:

$$L_s = 32 + 20 \log(f) + 20 \log(L) \quad \text{dB} \quad (3-7)$$

where  $f$  (MHz) is the frequency and  $L$  (km) is the path length.

v.  $L_a = 1.73\text{dB}$  (gaseous loss calculated by equation (2-1)).

The dynamic range (DR) of the array's sensors depends on the analogue-to-digital converters (ADC) in the iDSC 1816 data acquisition system, which is given by (Young, 1994):

$$DR = 20 \log_{10} \left( \frac{V_{\max}}{V_{\min}} \right) = 20 \log_{10} \left( \frac{V_{FS}}{q} \right) = 20 \log_{10} 2^n \quad \text{dB} \quad (3-8)$$

where  $V_{\max}$  (V) and  $V_{\min}$  (V) are the largest and smallest measurable analogue voltages,  $V_{FS}$  (V) is the ADC full-scale voltage range,  $q$  is the quantisation step size and  $n$  (bits) is the sampling resolution.

The 16-bit sampling of the iDSC 1816 results in a dynamic range of 96.3dB. Given the largest analogue signal ( $V_{\max}$ ) it can sample is +10V (20dB), the effective noise floor ( $N_{\text{eff}}$ ) of the sensor array is -76.3dB. The fade margin ( $M$ ), which is the amount the signal can fade before it is no longer detectable by the sensor array, is given by the following:

$$M = P_r - N_{\text{eff}} = -28.4 - (-76.3) = 47.9 \quad \text{dB} \quad (3-9)$$

From the above calculations the sensor array is capable of measuring power level variations in the range +48.4dB to -47.9dB from a mean received power level of -28.4dB. This measurement range is in excess of that required given reported levels of tropospheric scintillation are no more than  $\pm 6\text{dB}$  (see Section 2.4.1).

### 3.5 System performance

Following laboratory testing of the sensor array (i.e. back-to-back testing) the performance of the array was tested on the experimental link. The performance requirements of the sensor array (given in Section 3.2) are a function of the short-term (minutes, hours) and long-term (days, months) signal variability for a constant input signal, i.e. a benign channel. To illustrate this stability criterion, Figure 3-12 shows a typical time series from a 1-hour segment of data collected by the sensor array (element S3) over the experimental link.

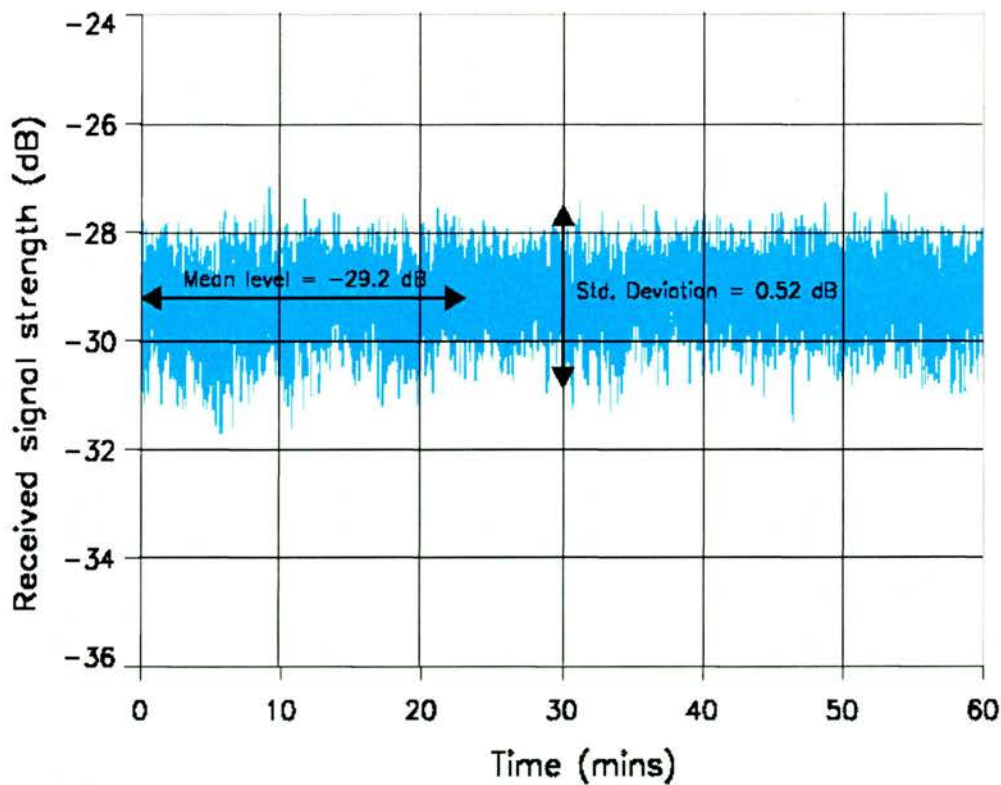


Figure 3-12 A plot of the stability criteria expressed in terms of the mean signal level and fluctuation intensity of the benign channel.

Figure 3-12 shows the mean signal level (-29.2dB) and standard deviation (0.52dB) for a 1-hour period satisfies the requirements given in Section 3.2. The mean signal

level is however slightly lower than the predicted  $-28.4\text{dB}$ , which is attributed to additional losses in connectors that were not taken into account in the link budget.

The intermittent operation of MMIC receivers S2 and S4 discussed in Section 3.3.2 prevented performance comparisons between all five of the sensor elements to be made over continuous periods of days. Comparisons could however be made over periods of several hours (Figure 3-13). In this example the separation distance between sensor elements is:  $S1 \leftrightarrow S2 = 2\text{m}$ ,  $S1 \leftrightarrow S3 = 3\text{m}$ ,  $S1 \leftrightarrow S4 = 6\text{m}$  and  $S1 \leftrightarrow S5 = 8\text{m}$ .

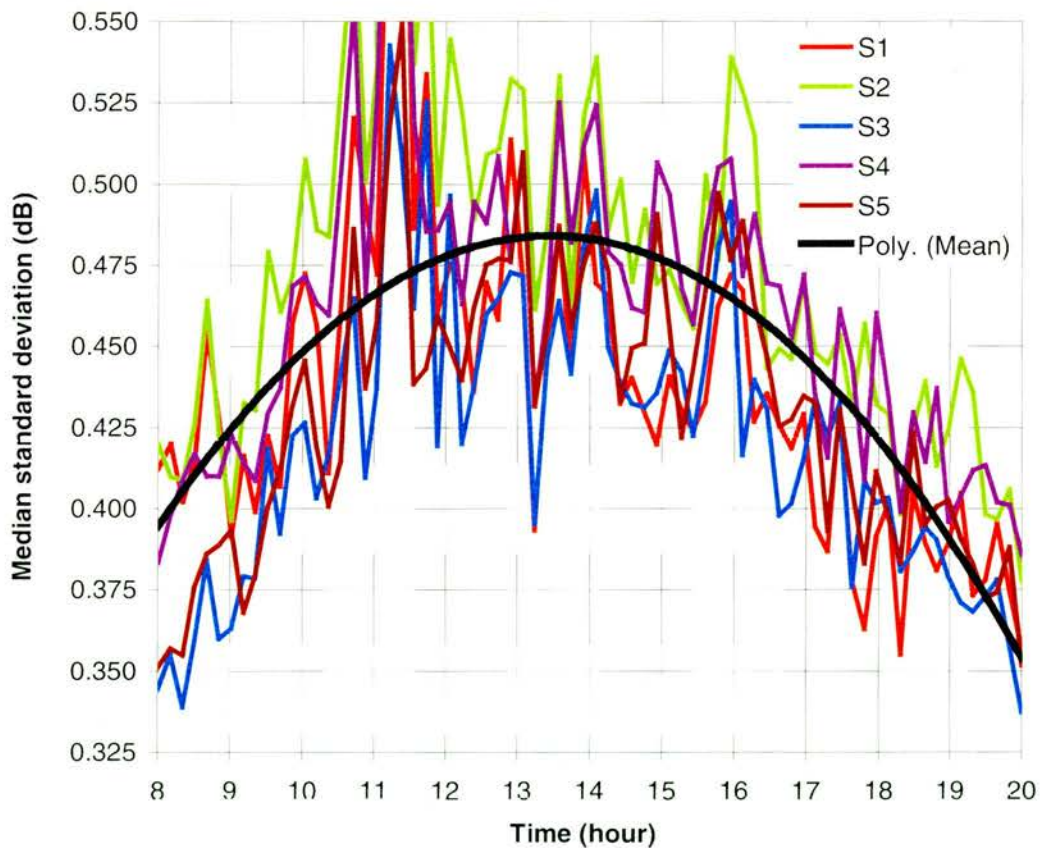


Figure 3-13 10-minute medians of standard deviation calculated at 1 minute intervals over a 12 hour period on the 18/05/00. A polynomial least squares fit calculated from the average of the five sensors illustrates the trend in the data sets.

Figure 3-13 shows good agreement between all five sensors of the array over a period of 12 hours. The trend in the data (polynomial fit) that indicates a predictable cycle of fluctuation intensity will be considered in more detail in Chapters five and six.

The long-term stability (day and month) of sensor array elements S1, S3 and S5 was calculated from the drift in the mean received signal strength and standard deviation of the received signal during periods of benign operation. The mean and standard deviation were calculated from 1-hour segments of data on ten separate occasions over a period of a month. The time of day and measurement interval was varied so that any effects from changes in temperature could be considered. The measured values of mean signal level are shown in Figure 3-14.

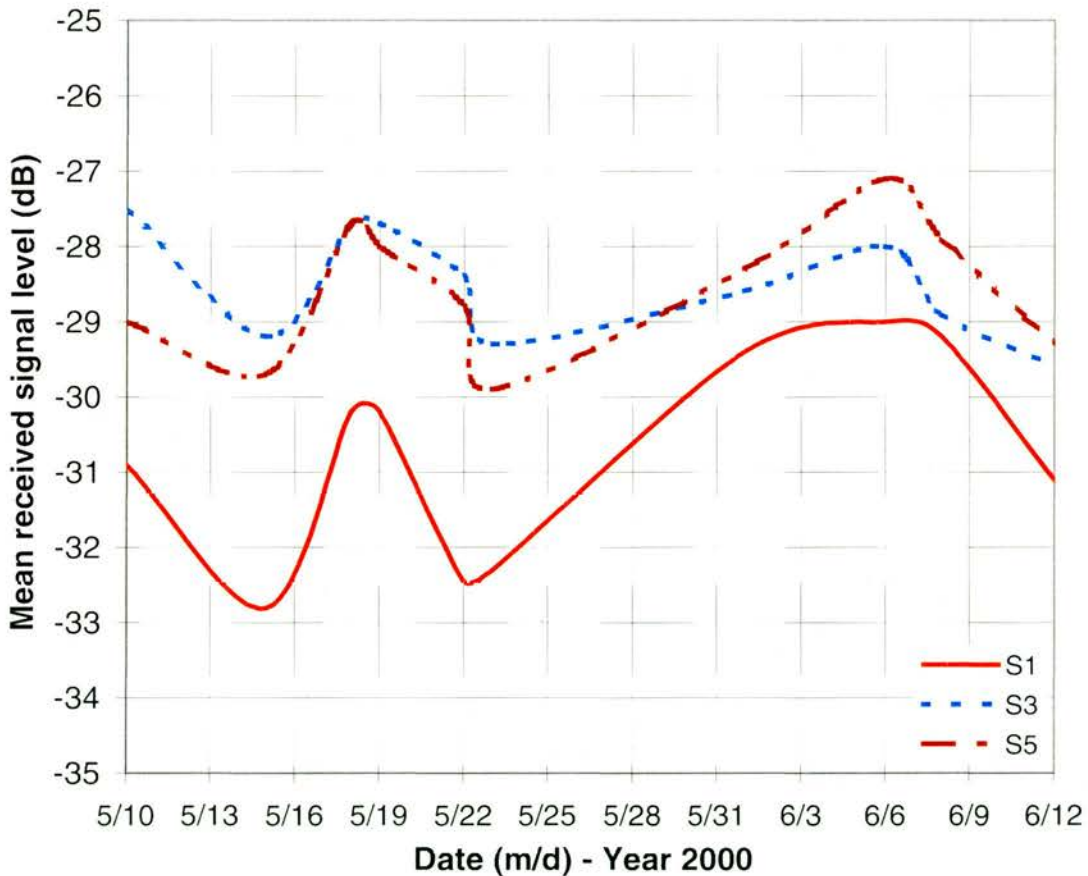


Figure 3-14 Measurement of the mean signal level. The mean level was calculated over a period of 1hr.

Figure 3-14 shows the drift in mean signal level is common to all three sensors, which is assumed to be a result of variations in the atmosphere. This is because instabilities in the sensor array would more probably be differential, and variations in transmitter power were measured at less than 0.5dB.

The mean signal level during the month long measurement period is  $-30.8\text{dB}$  for S1,  $-28.5\text{dB}$  for S3 and  $-28.6\text{dB}$  for S5. These values are close to the predicted level of  $-28.4\text{dB}$ . The  $2\text{dB}$  additional loss in signal level for S1 with respect to S3 and S5 was traced to a faulty potentiometer. A small adjustment of the potentiometer corrected the reduction in gain. The variability in mean signal strength over the month long measurement period is  $\pm 1.9\text{dB}$ ,  $\pm 1.1\text{dB}$  and  $\pm 1.4\text{dB}$  for S1, S3 and S5 respectively.

The standard deviation in received signal strength calculated from 1-hour segments of data on 10 occasions spread over a period of a month is shown in Figure 3-15.

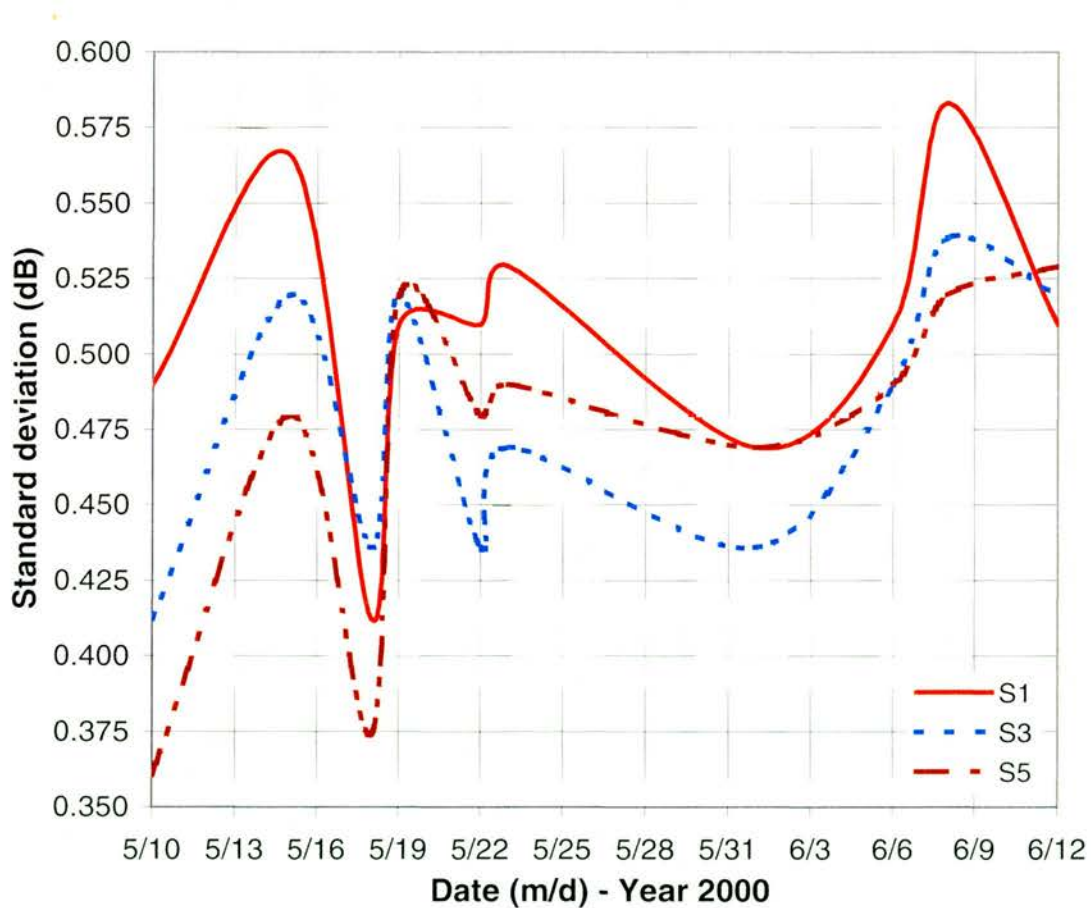


Figure 3-15 Measurement of the standard deviation of signal level. The standard deviation was calculated from 1-hour segments of data on 10 separate occasions over a period of one month.

Figure 3-15 shows that the intensity of fluctuations in signal strength over the month long period is also common to all three sensors. The range in standard deviation is

$\pm 0.09\text{dB}$ ,  $\pm 0.06\text{dB}$  and  $\pm 0.08\text{dB}$  for S1, S3 and S5 respectively. This small difference between sensors further confirms the common mode operation of the sensor array.

The values shown above indicate that the sensor array is performing as a unified system. This ensures that the array will provide a stable and consistent platform for investigating spatial effects such as scintillation.

### **3.6 Summary**

In this chapter an instrument for characterising the temporal and spatial effects of tropospheric scintillation in the surface boundary layer has been presented. The instrument, which has five 36GHz sensors, was designed and constructed specifically for the work carried out in this thesis. It utilises both commercially available components as well as modern MMIC receivers. Disappointingly, two of the MMIC receivers were manufactured incorrectly, resulting in periods of outage. This did not prevent measurements being performed, but in some cases analysis could only be carried out on data from three sensors.

The performance of the array was evaluated at each stage in the instrument from the lens horn antennas to the individual amplifiers and filters. The tests confirmed the operation of the individual sensors and their function as a single instrument. This was corroborated by measurements over the experimental link. Tests showed that the data collected by the five sensors was in good agreement over periods of minutes, hours, days and a month. It is assumed that variations in mean signal level is the result of atmospheric changes and not instrument instability that would most probably have produced uncorrelated variations. It is concluded that the sensor array provides a

stable and consistent platform for investigating the temporal and spatial effects of atmospheric turbulence in the surface boundary layer.

# Chapter Four

## Clear-air Multipath from Tropospheric Layers

### 4.1 Introduction

Before considering the small-scale effects of atmospheric turbulence this chapter first describes an initial analysis of the effect of clear-air refractive layering on millimetre wave propagation. The analysis shown is based on a limited number of events collected from the experimental link using the centre element (S3) of the sensor array. It is suggested that a more detailed measurement campaign be carried out to specifically evaluate the effects of refractive layering that is only briefly considered in this chapter.

### 4.2 Multipath from ground-based layers

Anomalous refractive index layering of the troposphere can lead to multipath fading and enhancement. Figure 4-1 illustrates the clear-air multipath mechanism.

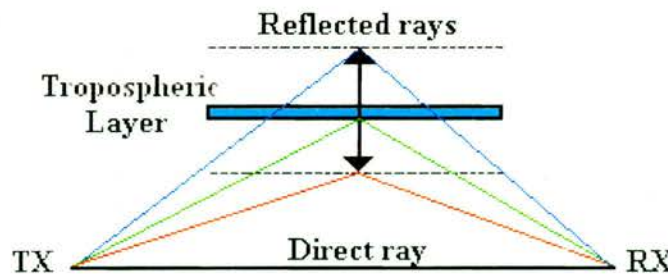


Figure 4-1 The direct ray between the transmitter (TX) and receiver (RX) is combined with a reflected ray from the tropospheric layer.

Multipath signal reception occurs when the direct signal between the transmitter and receiver is combined with the reflected signal from the vertically moving tropospheric

layer, which is considered to be a refractive index discontinuity when (Hall et al, 1996):

$$\Delta h < \frac{14\lambda}{\theta} \quad (4-1)$$

where  $\Delta h$  (m) is the layer thickness,  $\lambda$  (m) is the signal wavelength and  $\theta$  (degs) is the angle of incidence.

Tropospheric layers are formed by evaporation, nocturnal radiation, subsidence inversion and advective meteorological conditions (see Section 2.2.4.3). For over land paths such as the experimental link the mechanism that leads to multipath propagation is nocturnal radiation. This is described next.

#### 4.2.1 Evolution of nocturnal radiative layers

Nocturnal radiation is a mechanism that can lead to ducting and multipath propagation. The evolutionary process of nocturnal radiation, which is often accompanied by nocturnal and morning fogs, is described as follows (Vasseur, 1995):

- a. On clear sunny days the temperature in the lower troposphere decreases approximately linearly at a rate of  $6.5^{\circ}\text{C}/\text{km}$ , resulting in a refractivity gradient of  $-40\text{N}/\text{km}$  (Figure 4-2(A)).
- b. Following sunset, the Earth's surface loses heat through radiation. This results in a layer of cool air close to the ground and a layer of warmer air above (Figure 4-2(B)). This temperature inversion can lead to ducting or multipath reflection depending on signal wavelength and angle of incidence (see equation (4-1)).

- c. During the night the ground radiates more heat, thickening and increasing the height of the layer (Figure 4-2(C)).
- d. At sunrise the sun warms the ground and the air close to it, pushing the ground layer up from the surface (Figure 4-2(D)).
- e. During the morning the ground and air directly above continues to warm, forcing the ground layer higher (Figure 4-2(E)). This can lead to elevated layers that dissolve (break up) around noon.

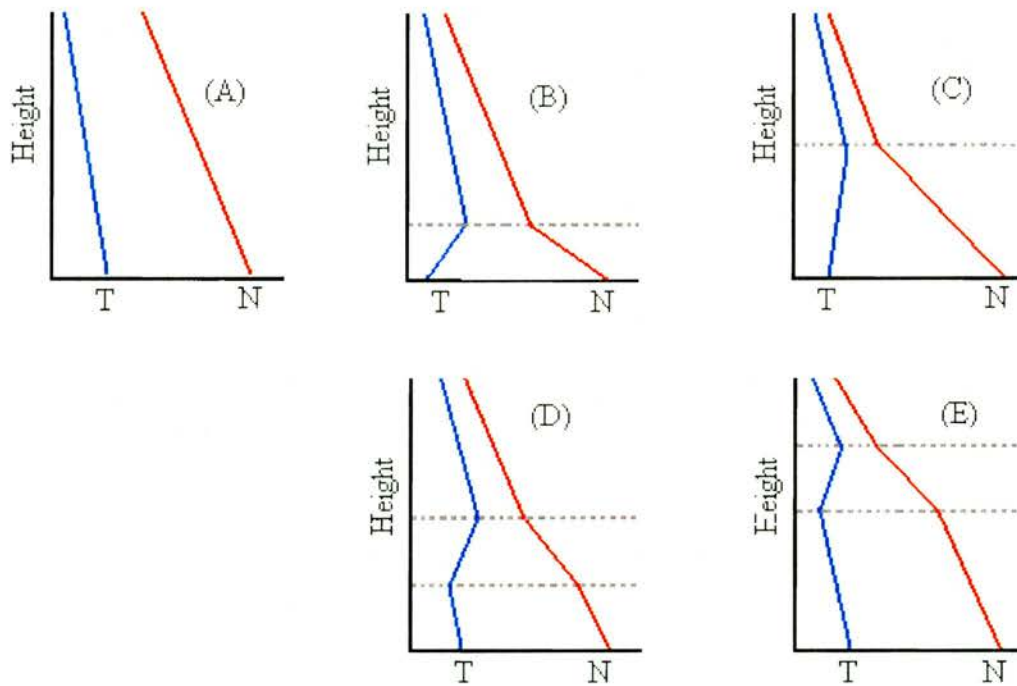


Figure 4-2 The evolution of temperature ( $T$ ) and refractivity ( $N$ ) under nocturnal radiative conditions (Vasseur, 1995).

The meteorological process described above was investigated by Bean and Dutton (1966), and experimentally observed in terms of multipath propagation at microwave frequencies by Craig and Kennedy (1987) and Prasad et al (1992). Webster (1983) also reported that in addition to direct and reflected rays a refracted ray from within the layer might also contribute to received signal strength. The contribution of the

refracted ray to received signal strength is dependent on the thickness of the layer and the elevation angle at which the signal is launched. In most situations where layers are thin and elevation angles high, Webster reported that the refracted ray has a negligible impact in comparison to the direct and reflected rays. Multipath from tropospheric layers can therefore be treated as a simple two-ray model.

To confirm the presence of nocturnal radiative layers during multipath conditions it is advantageous to simultaneously measure the vertical refractive index profile at some point (may be even several points) along the path in a similar way to Cartwright and Tattersall (1977). It may not however be possible to do this and therefore an alternative is required. The alternative method used in this study is to attempt to correlate changes in signal strength to ground based met data. This approach has previously been considered at 15GHz by observing abrupt changes in refractivity during multipath conditions (Touati et al, 1994).

#### **4.2.2 Nocturnal multipath occurrence**

Figure 4-3 shows a multipath event experienced by the experimental link. The series of signal fades occur in the night when the evolutionary period of layer thickening and increasing height illustrated in Figure 4-2(C) occurs. The V-shaped fading indicates signal reflection from changes in the height of the layer that produce differences in time of arrival between the reflected ray and direct ray, resulting in the characteristic two-ray multipath fading.

The ground-based meteorology measured at the receiver and link mid-point was used to calculate the refractivity at the time of the multipath event in Figure 4-3. This is shown in Figure 4-4.

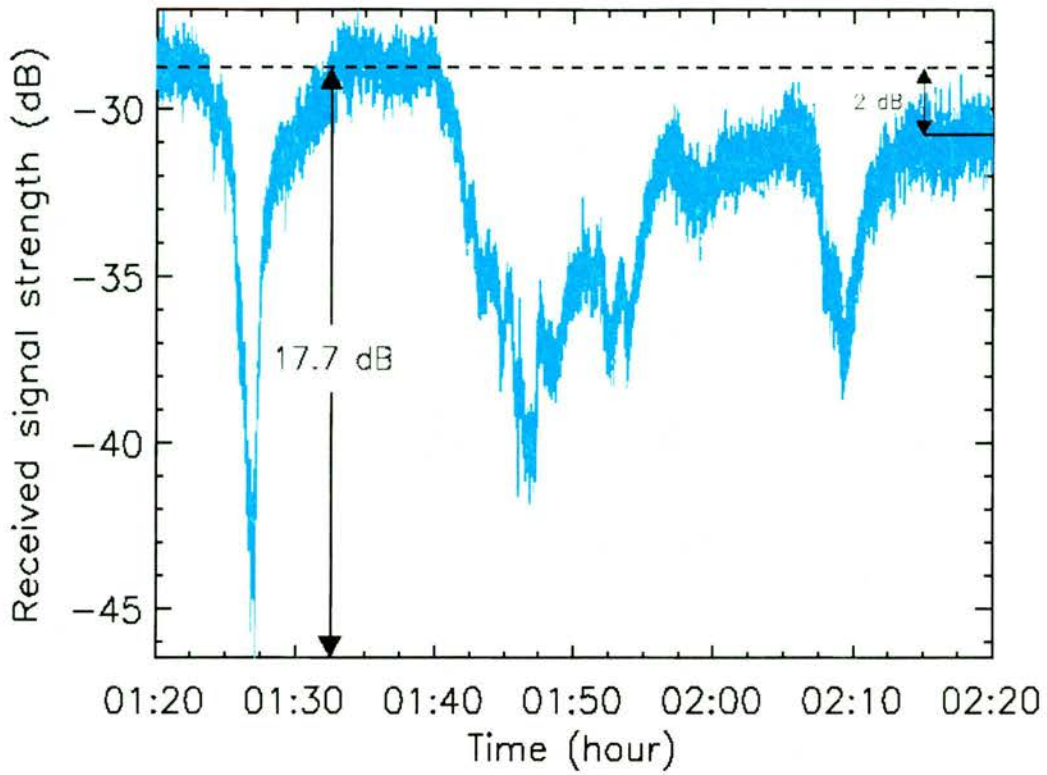


Figure 4-3 Multipath fading on the 4<sup>th</sup> June 2000. The benign condition mean signal level (----) is shown for comparison.

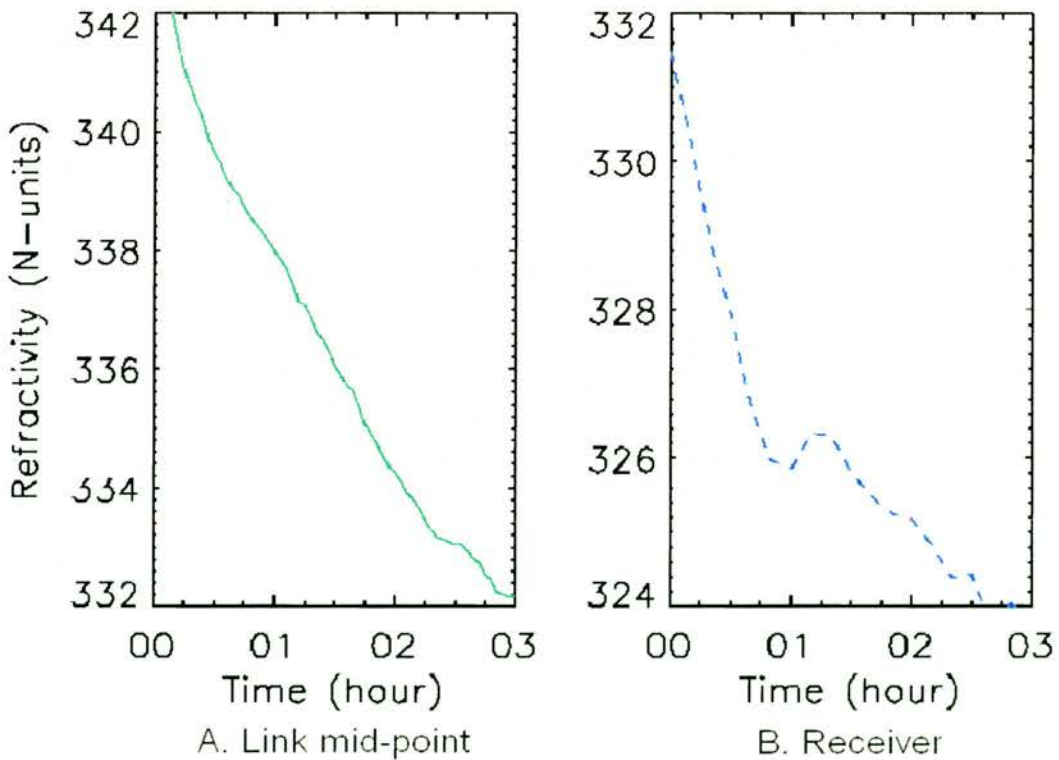


Figure 4-4 The ground refractivity at the link mid-point and receiver during the same period as the multipath time series shown in Figure 4-3.

Figure 4-4 shows the refractivity lapse rate as a function of time for both locations is approximately  $-8$  to  $-10N$ -units in 3 hours. The visible differences between the two refractivity plots is firstly the abrupt change at the receiver at  $\sim 01:00$ , and secondly the increased lapse rate at the receiver between  $00:00$  and  $01:00$  (75% of its 3 hour gradient compared to 40% of its 3 hour gradient at the link mid-point). These differences are explained by Figure 4-5 that shows the temperature and relative humidity measurements used to calculate the refractivity. The figure shows that the air temperature decreases at both locations as would be expected for radiative heat loss (see 4.2.1b). It also shows the temperature is higher at the receiver than the lower altitude link mid-point, indicating a temperature inversion. The refractivity lapse rate difference between  $00:00$  to  $01:00$  is therefore due to the 4.5% decrease in relative humidity at the receiver compared to an almost constant saturated level at the link mid-point. The high level of relative humidity at both met station locations during a period of no rainfall implies a layer of fog, which is associated with the presence of tropospheric layers (Craig and Kennedy, 1987).

The abrupt change in refractivity at the receiver at  $\sim 01:00$  is shown in Figure 4-5 to be due to an increase in relative humidity and a decrease in temperature. This occurs approximately 30 minutes before fading begins. As no change is observed at the link mid-point the change at the receiver possibly indicates the reflection point of the signal is closer to the receiver. The time difference between the change in ground-based meteorology and the start of fading is believed to be the time taken for the layer to move to within the antenna beam.

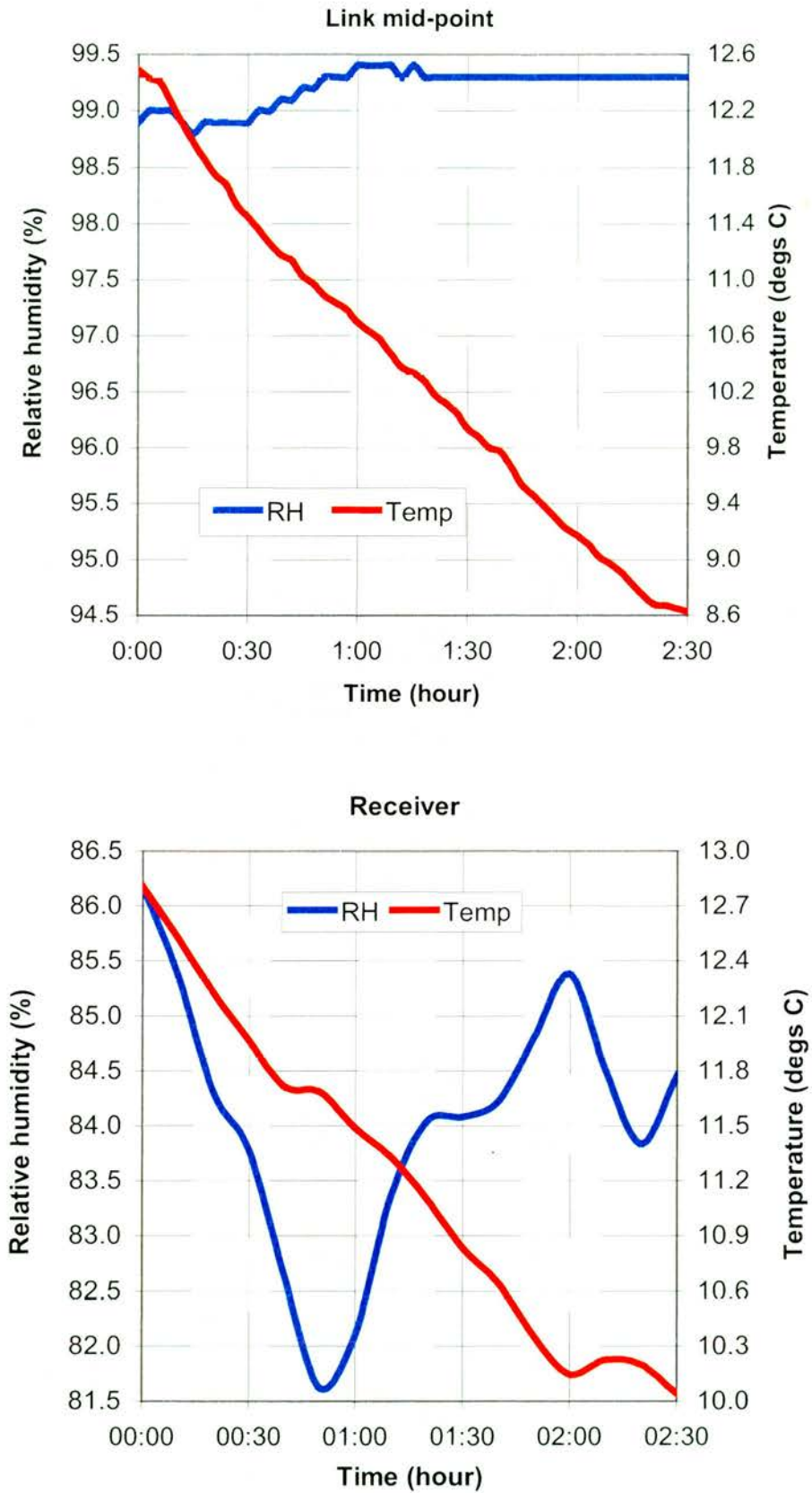


Figure 4-5 Temperature and relative humidity (RH) measured at the link mid point and receiver.

At 02:00, the relative humidity and temperature once again change abruptly and in opposite directions, which coincides with a further V-shaped multipath fade approximately 10 minutes later.

The above indicates a possible connection between multipath fading and ground-based meteorology as observed by Touati et al (1994) at 15GHz. It is evident, however, that for long links such as that considered here (17.3km) ground-based meteorology is not correlated with clear-air multipath fading all along the path, i.e. in this case it is correlated at the receiver but not at the link mid-point. The reason for this is that tropospheric layers do not necessarily extend over the entire link. To further evaluate if a connection exists between multipath fading and ground-based meteorology the next section considers two more examples.

### **4.2.3 Late morning multipath**

The evolutionary process of nocturnal radiation asserts that during the morning the height of the layer increases (Figure 4-2(E)) until around noon when it dissolves. It could therefore be expected that as the height of the layer increases further multipath propagation may occur. This is confirmed with the multipath time series in Figure 4-6. It shows two significant fades separated in time by ~20 minutes. A 3dB enhancement is also observed in this example signifying the height of the layer with respect to the link is such that both the reflected signal and direct signal arrive at the receiver constructively.

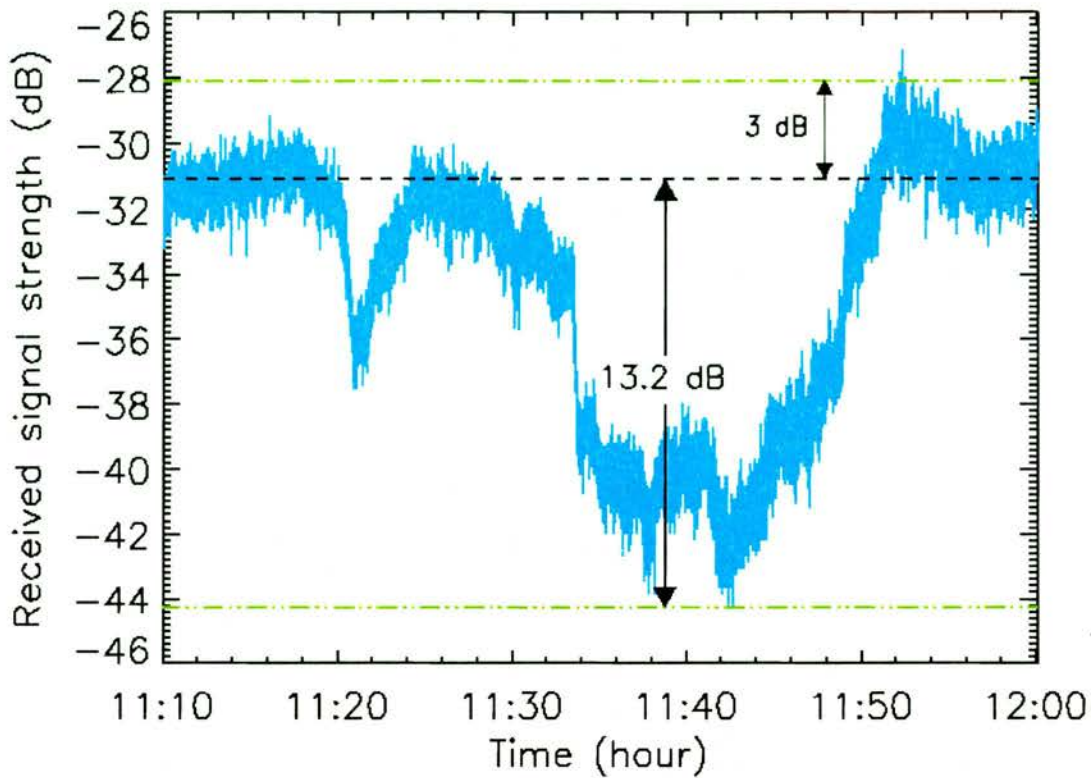


Figure 4-6 Multipath on the 17<sup>th</sup> May 2000. A 3dB enhancement is also observed, further indicating the presence of two dominant rays.

The ground refractivity at the receiver and link mid-point at the time of the above fading is shown in Figure 4-7. They are in general agreement, with the exception of the ~20 minute difference between the occurrence of minimum refractivity. This difference is explained by the temperature and relative humidity measurements used to calculate the refractivity (Figure 4-8). The met data shows that the lag between the occurrence of minimum refractivity at the receiver and link mid-point is due to the ~20 minute lag in the point of maximum temperature. The reason for this is believed to be due to the higher altitude of the receiver met station, and therefore the time lag equates to the time taken for the rising layer to be detected. As in the previous example the temperature at the receiver is higher than the lower altitude link mid-point.

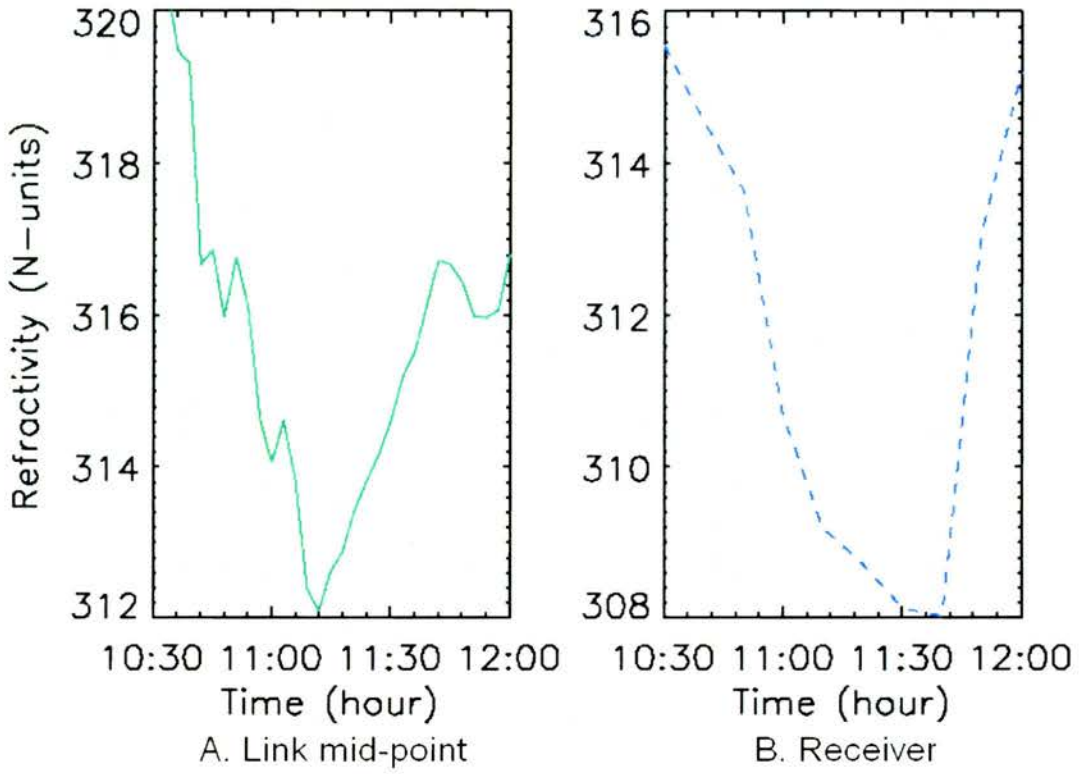
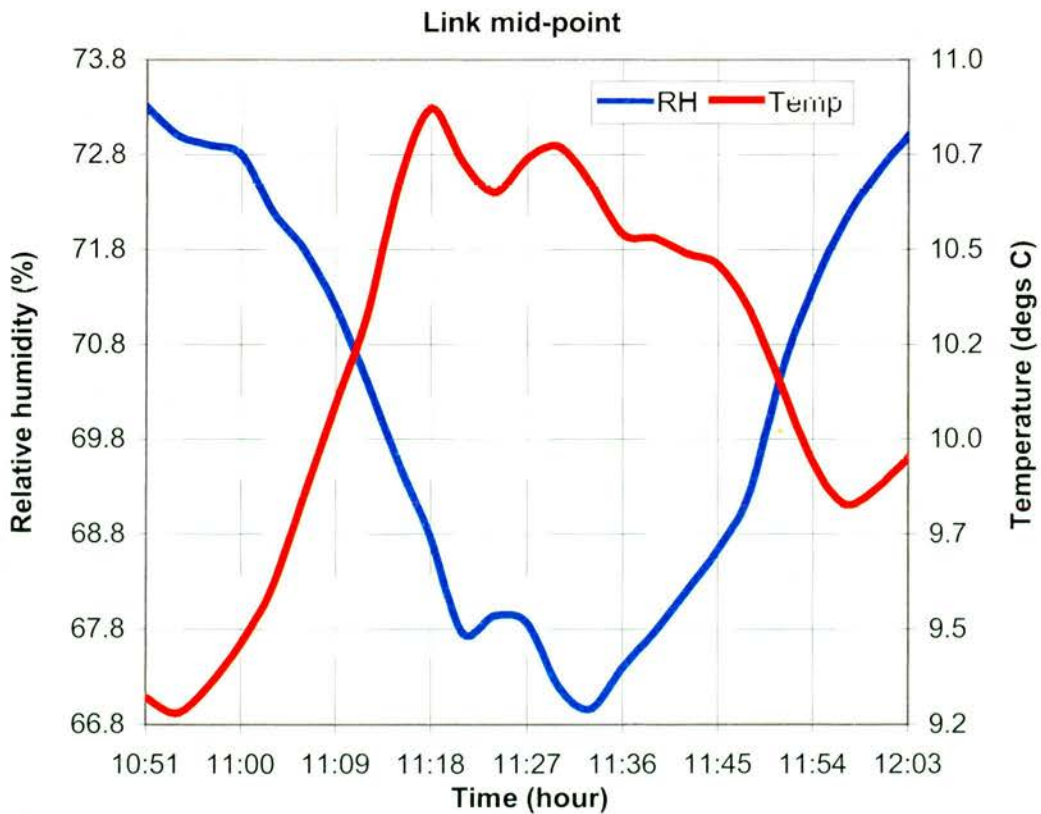


Figure 4-7 The ground refractivity at the link mid-point and receiver during the same period as the multipath time series shown in Figure 4-6.



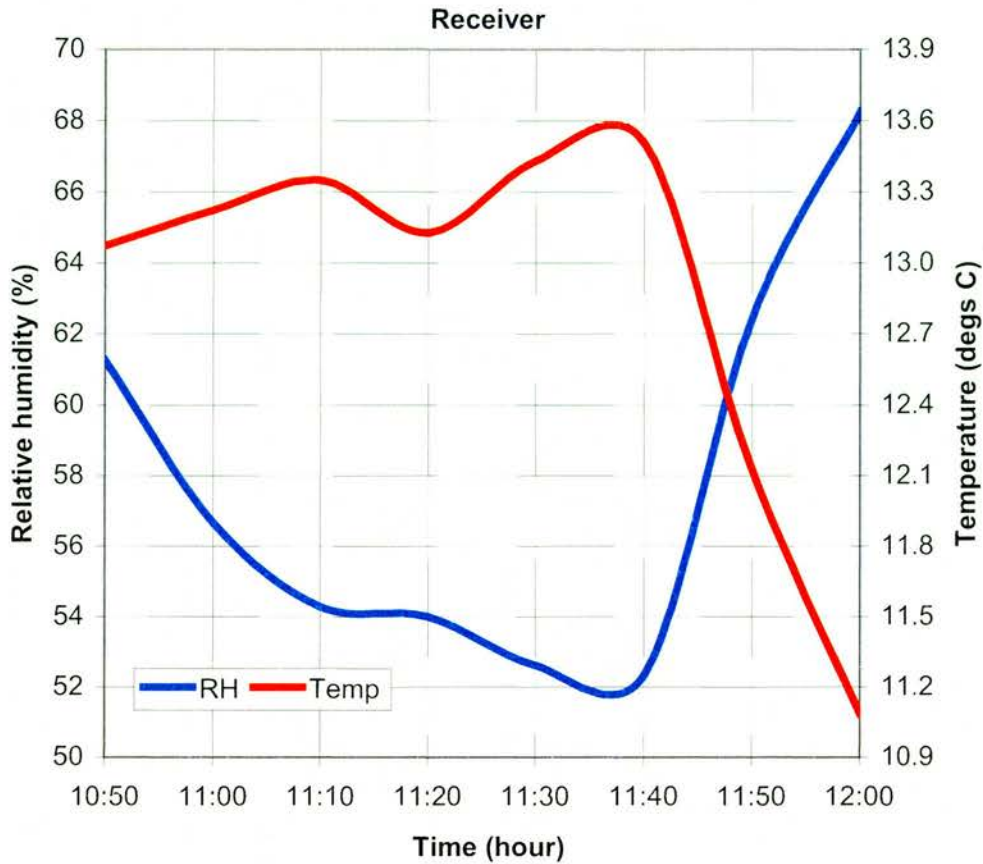


Figure 4-8 Temperature and relative humidity measured at the link mid point and receiver.

The timing of the two fades at 11:20 and 11:40 coincide with opposite and abrupt changes in relative humidity and temperature at both met station locations. These changes occur just before fading begins. This further confirms the correlation between multipath propagation and ground-based meteorology.

The next example of multipath fading to consider is interesting because of its similarity with the events in Figure 4-6. Figure 4-9 shows the same time frame as the events in Figure 4-6 but on the following day. The events occurred during the period of refractivity shown in Figure 4-10, which was calculated from the temperature and relative humidity shown in Figure 4-11.

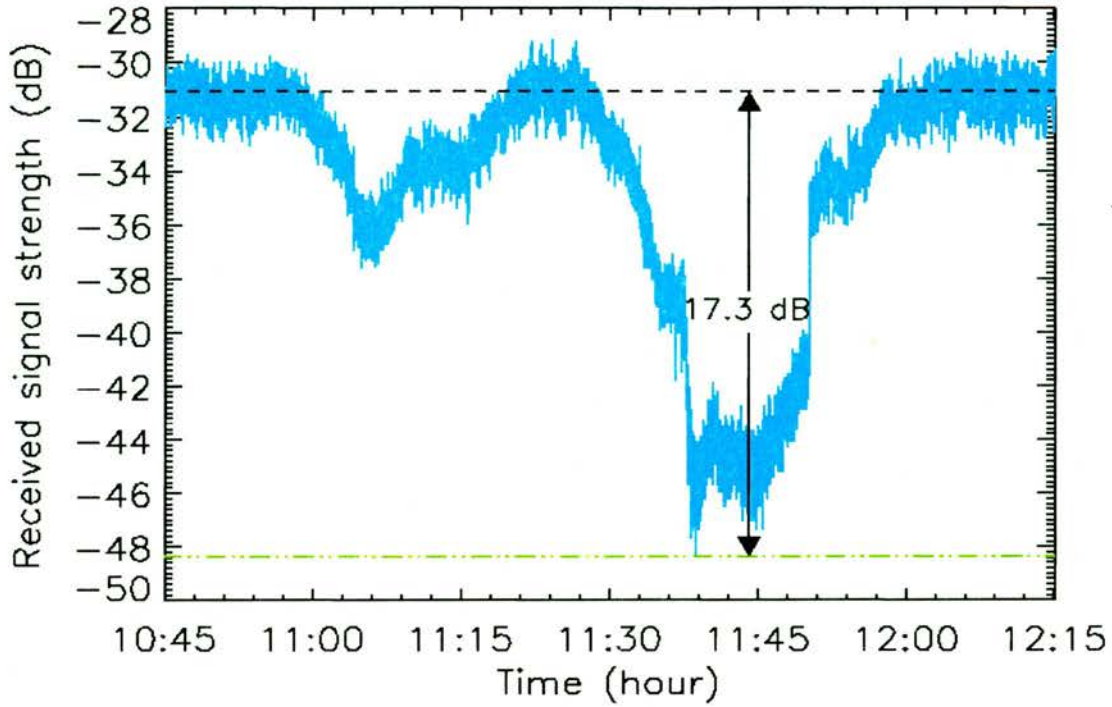


Figure 4-9 Multipath fading on the 18<sup>th</sup> May 2000. The benign condition mean signal level (---) is shown for comparison.

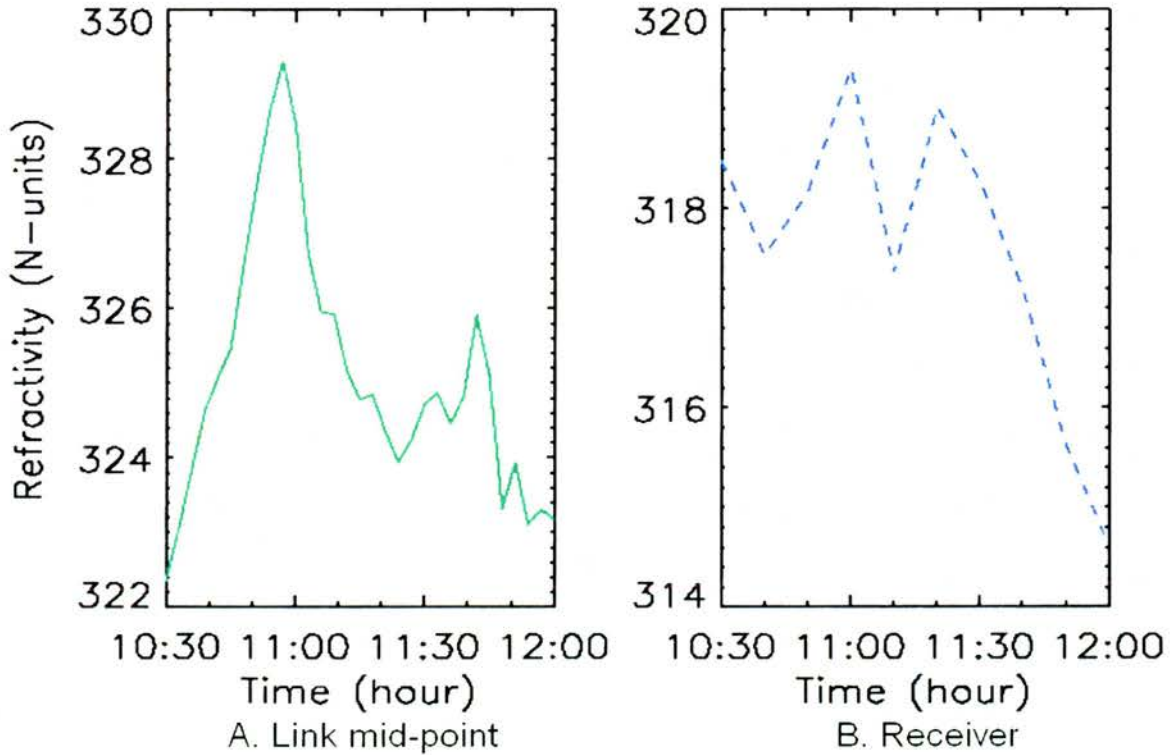


Figure 4-10 The ground refractivity at the link mid-point and receiver during the same period as the multipath time series shown in Figure 4-9.

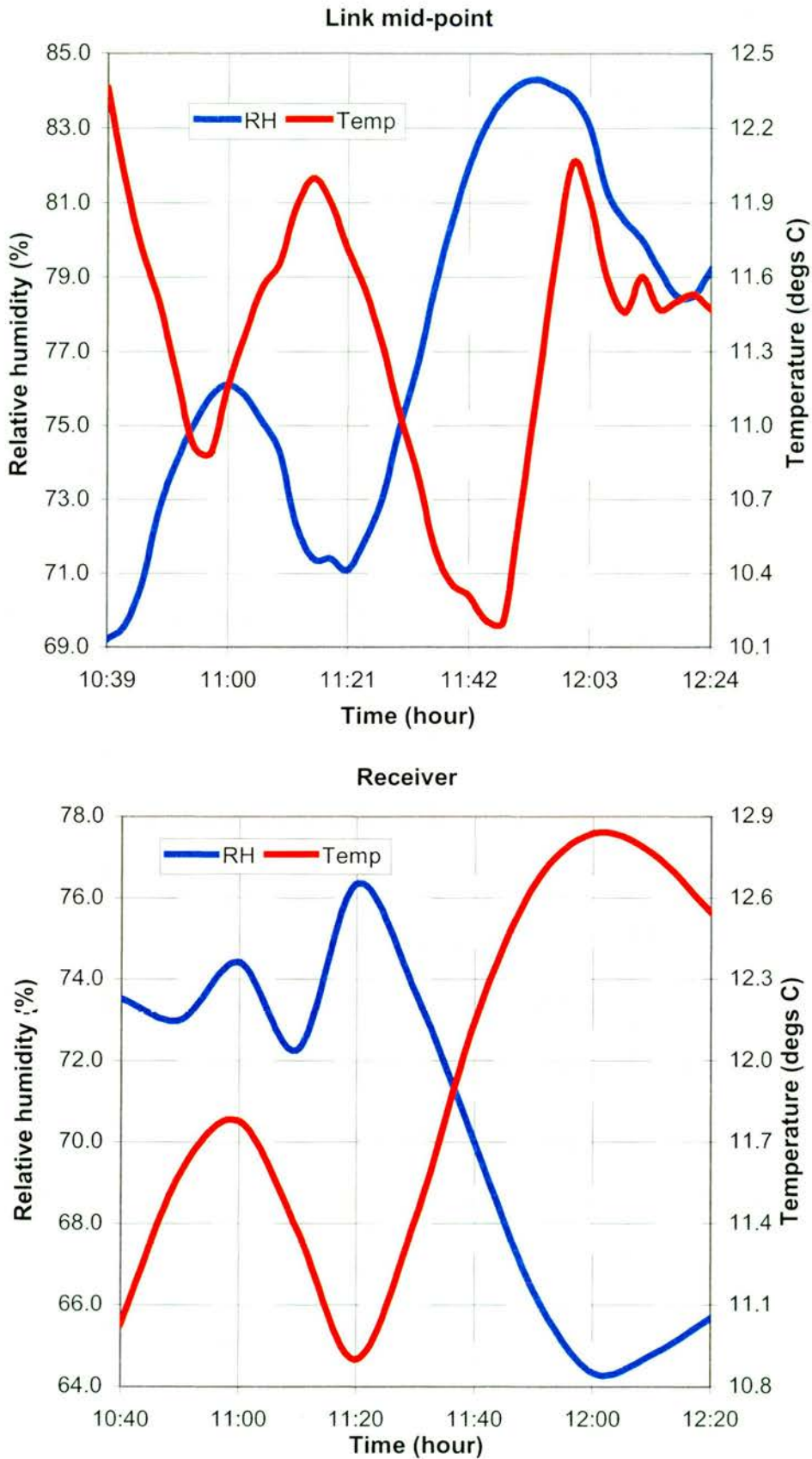


Figure 4-11 Temperature and relative humidity measured at the link mid point and receiver.

Figure 4-11 confirms that the fade at 11:05 occurs just after an abrupt change in relative humidity and temperature. Also, the deep fade at 11:45 occurs just after the second abrupt change in relative humidity and temperature at 11:20.

It appears from the above that multipath propagation is correlated with abrupt changes in air temperature with reciprocal decreases in relative humidity. Other changes, i.e. a change in temperature but not a change in relative humidity, a change in both but in the same direction, or an opposite but slow change in both do not correlate with multipath propagation.

The depth of fading in the multipath examples shown above has been greater than 17dB and lasted for periods of several minutes. The impact of this depth and duration of fading could lead to significant impairment to communications systems. This is described in Section 4.4.

### **4.3 Multipath from oscillating layers**

In the previous clear-air multipath example the classic V-shaped characteristic was observed. A further type of multipath behaviour is associated with vertically oscillating layers. This could be the result of ground-based layers such as that described above, or from elevated layers called gravity waves. As in the case of ground-based layers a reflected signal from an elevated layer combined with a direct signal can result in classical two-ray multipath that varies in relation with the movement of the layer. The mechanism that drives the movement of the gravity layer is the mixing or entraining of the drier air aloft into the moist air below that is convected from the ground (Stull, 1998). In essence, the oscillatory motion of a

gravity layer is due to the buoyancy of the atmosphere. Figure 4-12 illustrates the gravity layer multipath mechanism.

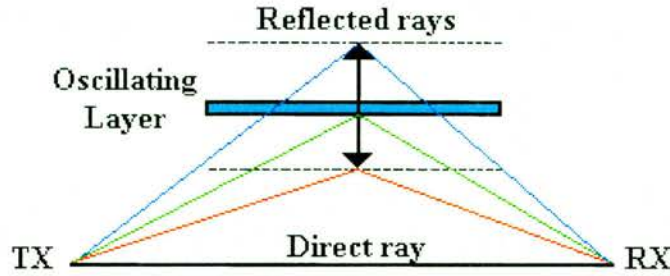


Figure 4-12 A two-ray multipath model. The direct ray between the TX and RX is combined with a reflected ray from an oscillating layer.

Previous experiments have observed gravity waves from sound detection and ranging (SODAR) echoes (Claverie and Klapsz, 1985) and amplitude/angle-of-arrival measurements made at microwave frequencies (Webster and Scott, 1987). The Webster and Scott measurements found that the periodicity of gravity waves was in the order of 1 minute. An example of multipath behaviour believed to be from an oscillating layer (the only significant example recorded) is shown in Figure 4-13. It shows a fading/enhancement cycle indicating the periodic motion of the layer, which results in the addition of a direct signal and reflected signal from the moving layer. This effect is more clearly illustrated with a close-up look at one of the sinusoids (Figure 4-14). This provides a clear indication of a two-ray time-varying multipath mechanism. The frequency of oscillation is 15.5mHz, which equates to approximately 64 seconds. This is in agreement with the measurements reported by Webster and Scott (1987) of gravity wave oscillations. The second oscillation in Figure 4-14 occurred approximately 10 minutes later, on that occasion the cycle was reversed.

The ground-based meteorology at the receiver and link mid-point at the time of the oscillatory multipath is shown in Figure 4-15.

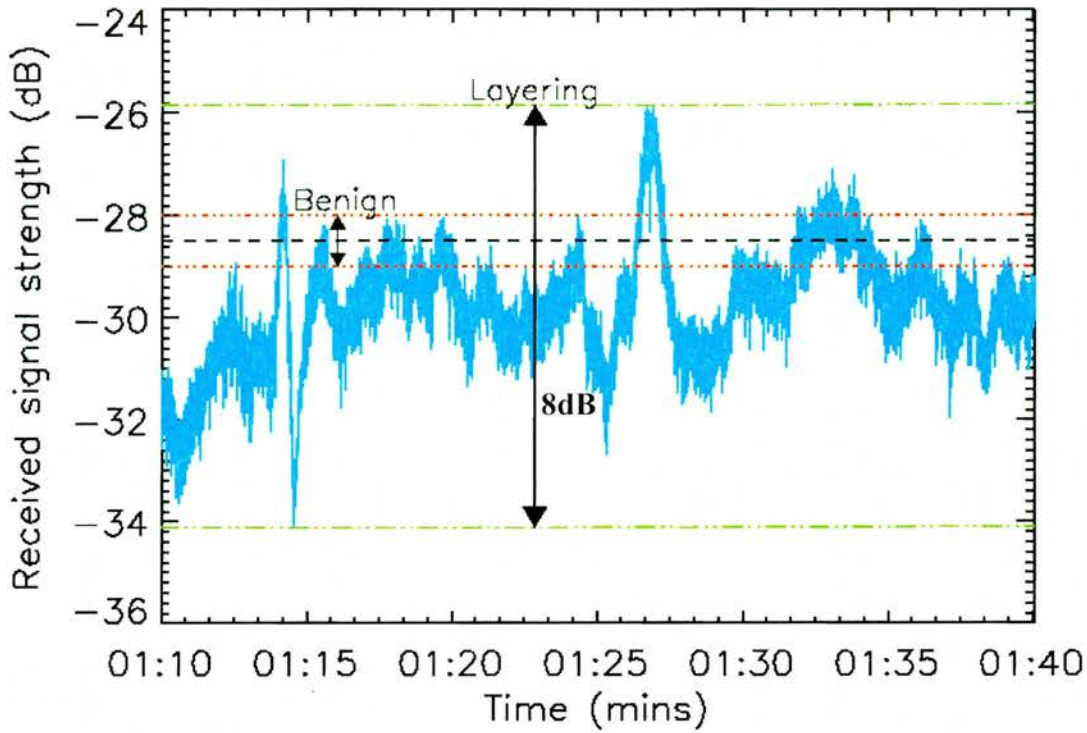


Figure 4-13 Oscillatory signal strength on the 14<sup>th</sup> May 2000. The peak-to-peak variation is 8dB (---). This is compared to the mean signal level (----) and variance (.....) during benign channel conditions.

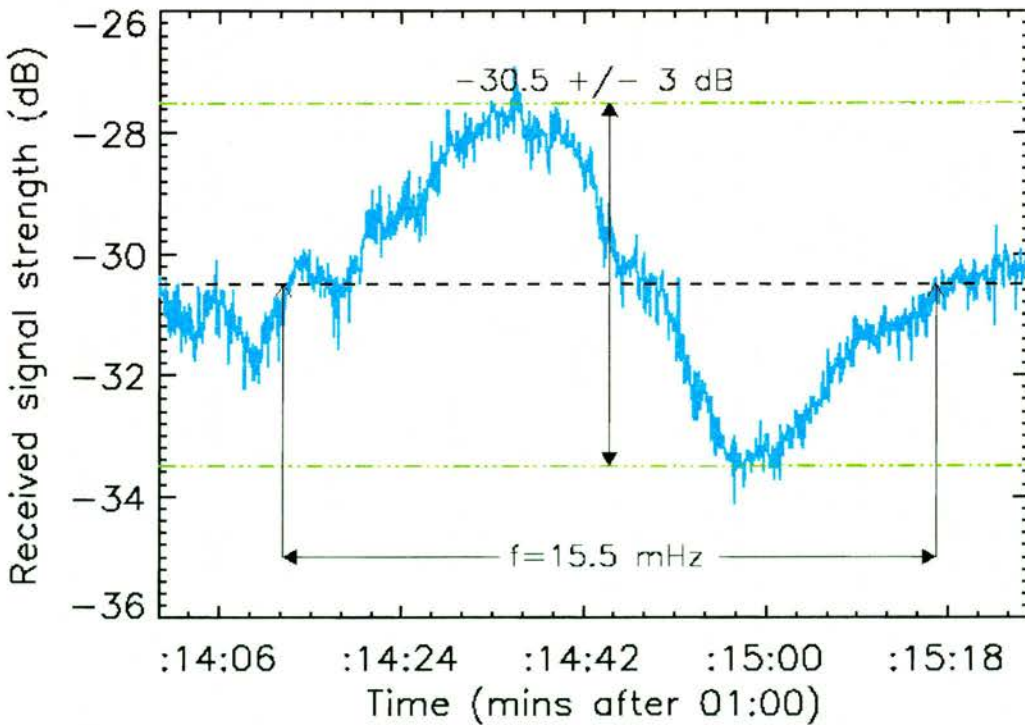


Figure 4-14 The mean signal strength for the period is shown (----) together with the peak-to-peak variation of  $\pm 3$ dB from the mean (---).

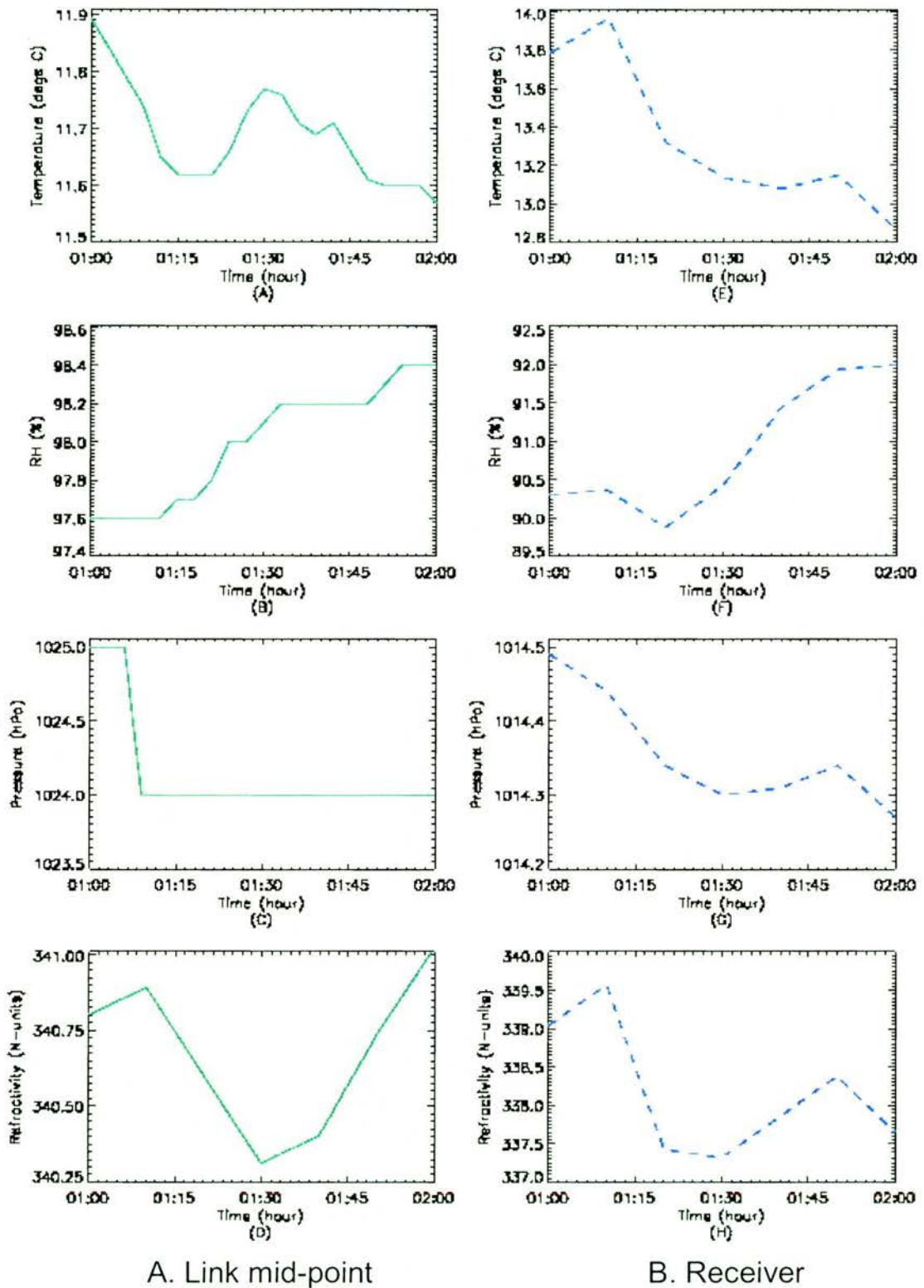


Figure 4-15 Measurements of the temperature, humidity, pressure and the calculated refractivity at the link mid-point (A,B,C,D) and sensor location (E,F,G,H) on the 14<sup>th</sup> May 2000.

Allowing for the difference in sampling rate between the two met stations the graphs of pressure, temperature, relative humidity and refractivity show good agreement. The refractivity shows a cyclic variation over the 1-hour period of data shown. It is however not possible to study the met data variation over the 1 minute period of signal oscillation shown in Figure 4-14 given the 3 and 10 minute sampling intervals of the met data. It can therefore only be hypothesised that the 1-minute multipath cycle relates to small-scale buoyancy variations superimposed on the slower variability observed in the ground-based meteorology.

#### 4.4 Impact of clear-air multipath on system performance

It has been shown in this chapter that clear-air multipath fading can be very significant, in some cases exceeding 17dB. This depth of fading could reduce the performance of communication links resulting in some cases with link outage (depending on the system's fade margin), or a decrease in signal-to-noise ratio leading to a reduction in data throughput.

To highlight the effect of clear-air multipath on millimetre wave communication systems the reduction in channel capacity  $C$  (bps) due to fading is evaluated. This is calculated using the Shannon limit of a noisy channel (Young, 1994):

$$C = B \log_2 \left( 1 + \frac{S}{N} \right) \text{ bps} \quad (4-2)$$

where  $B$  (Hz) is the bandwidth,  $S$  (W) is signal power and  $N$  (W) is noise power.

Using equation (4-2) with example parameters  $B=5\text{MHz}$  and signal-to-noise ratio (SNR)=24dB, the maximum channel capacity during non-fading conditions is

40Mbps. This equates to a bandwidth efficiency of 8bps/Hz given by the expression (Halsall, 1996):

$$\varepsilon = \frac{C}{B} \text{ bps/Hz} \quad (4-3)$$

The 8bps/Hz bandwidth efficiency indicates that a multi-level modulation scheme is required. This is because a simple two level binary scheme could only provide a theoretical maximum of 10Mbps. The number of modulation levels ( $M$ ) needed to satisfy the 8bps/Hz bandwidth efficiency is given by the Nyquist theorem for a noiseless channel (Halsall, 1996):

$$\log_2 M = \frac{C}{2B} \quad (4-4)$$

This results in a 16 level modulation scheme, e.g. 16-QAM.

The above calculations define the performance of a non-fading communication link: 5MHz bandwidth with 16-QAM to satisfy a service requiring a channel capacity of 40Mbps. If a 17dB clear-air multipath fade such as that shown in Figure 4-9 occurred (new SNR=7dB), the channel capacity would be reduced to 12.93Mbps. This is equal to a 68% reduction in channel capacity for the several minutes of the fade.

## 4.5 Summary

This chapter has described an initial investigation into the correlation between clear-air multipath and ground-based meteorology. It was shown using a limited number of clear-air events that abrupt changes in temperature and relative humidity can be correlated with multipath propagation. This result confirmed previous observations at microwave frequencies (Touati et al, 1994).

The effect of the measured multipath fading on millimetre wave communication systems was evaluated in terms of channel capacity. It was shown that for periods of several minutes during multipath fading the channel capacity could be significantly reduced. This shows that clear-air multipath could have a considerable impact on millimetre wave communication systems. It is therefore recommended that a detailed study of tropospheric layering be performed to fully evaluate its impact on millimetre wave terrestrial radio links as well as the benefits from mitigation techniques such as frequency and space diversity. Such a study could also investigate the effect of multipath dispersion (also called delay spread) that causes intersymbol interference. This is especially important for high data communications (one of the main reasons for using millimetre wave frequencies) where bit intervals are very short.

# Chapter Five

## Tropospheric Amplitude Scintillation

### 5.1 Introduction

The temporal characteristics of amplitude scintillation are of interest to both theoreticians and system designers. The theorist's interest is primarily in remote sensing the turbulent atmosphere while the system designer is concerned with the impact on communication and radar system performance. In this chapter, the temporal properties of tropospheric amplitude scintillation measured by the sensor array (element S3) are presented. The first parameter considered is the log-amplitude scintillation.

### 5.2 Log-amplitude scintillation

Log-amplitude scintillation ( $\chi$ ) is the ratio of the instantaneous signal amplitude to the mean signal amplitude calculated with a moving average window. This technique allows scintillation events to be separated from long-term instabilities in the receiver or slowly varying gaseous attenuation. It is expressed mathematically as:

$$\chi = 20 \log_{10} \left( 1 + \frac{E_t}{\left( \sum_{t-m/2}^{t+m/2} E_t \right) / (m+1)} \right) \text{ dB} \quad \text{for } t = \left( 1 + \frac{m}{2} \right) \text{ to } \left( n - \frac{m}{2} \right) \quad (5-1)$$

where  $E_t(V)$  is the instantaneous amplitude,  $m$  is a 1 minute averaging window (Vasseur, 1995) centred on sample point  $t$  and  $n$  is the total number of samples in the

time series. Figure 5-1 shows an example of a scintillation event in log-amplitude form.

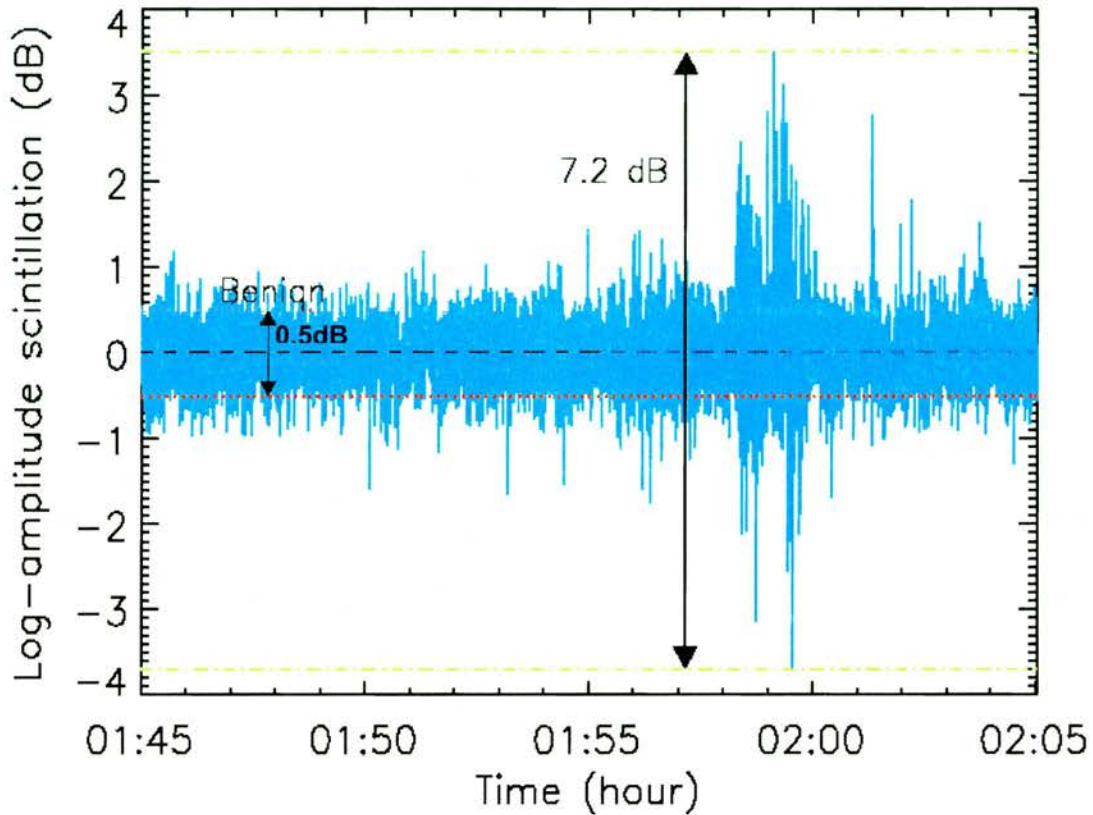


Figure 5-1 A zero-mean scintillation event in the early hours of June 3<sup>rd</sup> 2001. The peak-to-peak amplitude is 7.2dB. The fluctuation level during benign conditions ( $\pm 0.5$ dB) is shown for comparison.

The log-amplitude scintillation event above clearly shows the extent of signal power variation associated with a turbulent structure crossing the propagation path. The peak-to-peak amplitude, which compared to benign channel conditions is more than four times larger, introduces two potential problems to communication systems. The first is fading that could result in link outage for systems with inadequate fade margin. The second, and the reciprocal of fading, is increased power. Though a signal level enhancement is not normally an issue for the intended receiver additional power could be a source of interference to nearby links (although not as significant as ducting).

The event in Figure 5-1 is one example of many during the month long measurement period. Figure 5-2 shows a selection of other events. These events occur at different times of day, last for periods ranging from a few seconds to almost 20 minutes and have peak-to-peak amplitudes ranging from  $\pm 1\text{dB}$  to more than  $\pm 3\text{dB}$ . The most significant events (longest duration and largest amplitude fluctuations) generally occur in the early and mid-morning hours, while the least significant (shortest duration and smallest amplitude fluctuations) generally occur in the afternoon and early evening. This implies that scintillation occurrence follows a diurnal cycle. This will be considered in detail in Section 5.5.

### 5.3 Log-amplitude scintillation variance

Log-amplitude scintillation variance ( $\sigma_\chi^2$ ) is a measure of fluctuation intensity as a function of event duration. It is calculated from log-amplitude scintillation using a moving average window of 1 minute (Vasseur, 1995). This is expressed mathematically as follows:

$$\sigma_\chi^2 = \frac{\sum \left( \chi_t - \left[ \frac{\sum_{t-m/2}^{t+m/2} \chi_t}{m+1} \right] \right)^2}{m-1} \text{ dB}^2 \quad \text{for } t = \left(1 + \frac{m}{2}\right) \text{ to } \left(n - \frac{m}{2}\right) \quad (5-2)$$

An example of the log-amplitude scintillation variance of the event in Figure 5-1 is shown in Figure 5-3. It illustrates the intensity of the scintillation event compared to the benign level. The magnitude of the log-amplitude scintillation variance indicates the extent of turbulent mixing, i.e. an increase in variance indicates an increase in the turbulent mixing that produces refractive index inhomogeneities.

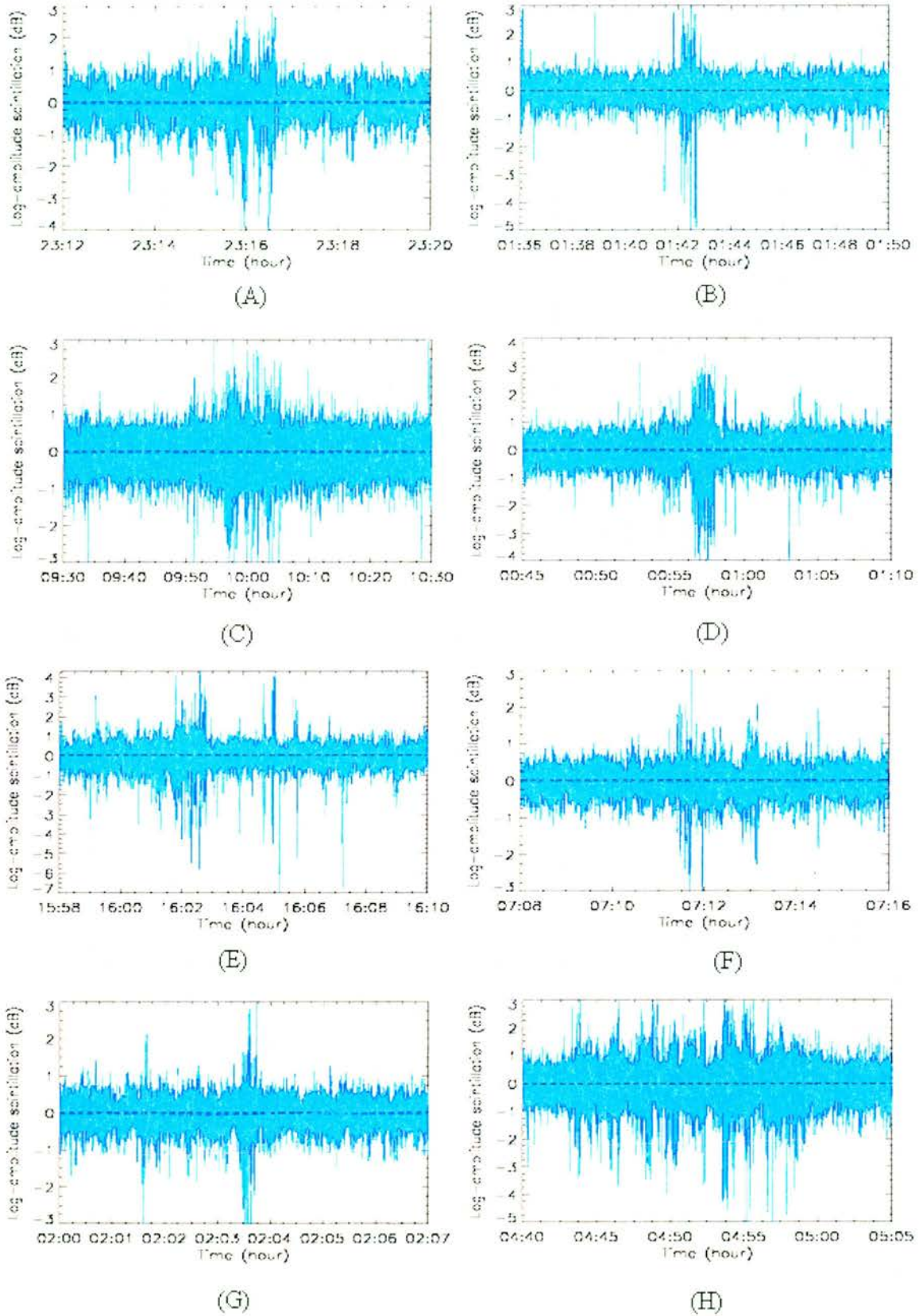


Figure 5-2 Examples of measured scintillation events.

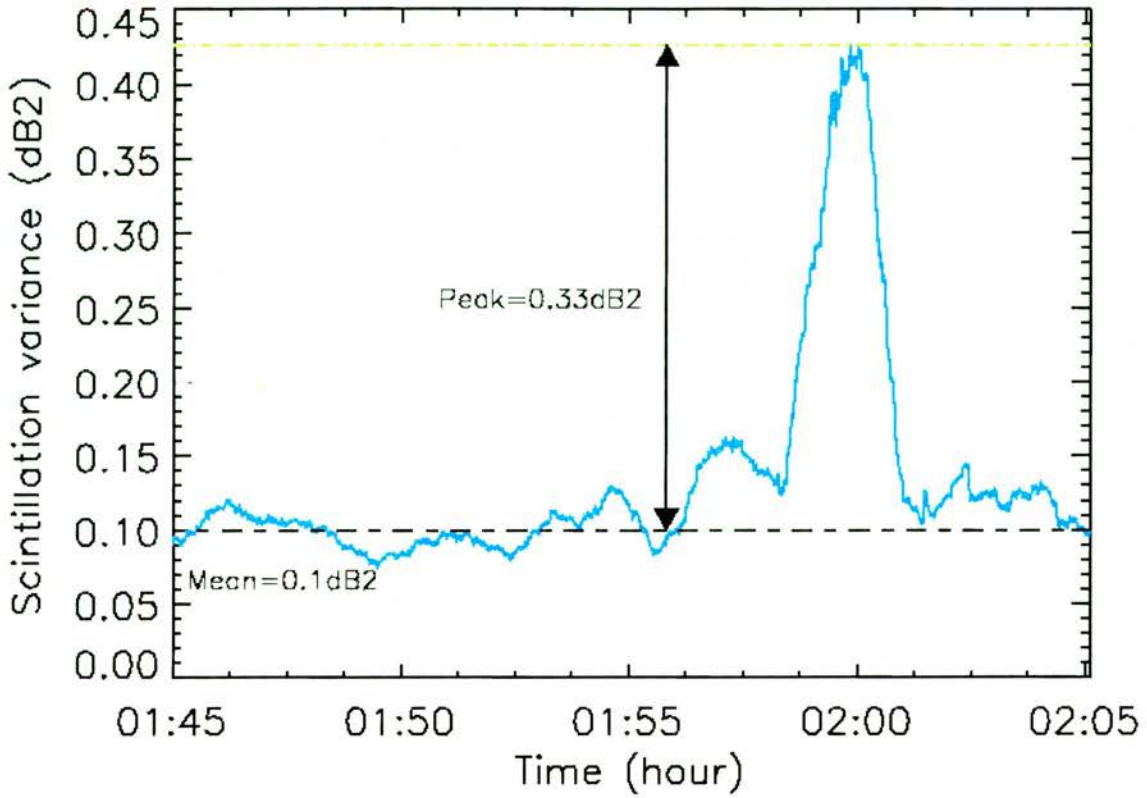


Figure 5-3 The log-amplitude scintillation variance calculated from the event shown in Figure 5-1. The mean value during benign conditions is shown for comparison.

Log-amplitude scintillation variance is a key parameter in the theory of wave propagation in a turbulent medium. It is important because it directly relates to the turbulent activity along the propagation path. Tatarski (1961) showed this relationship using Kolmogorov’s spectrum of turbulence. This is shown in equation (5-3).

$$\sigma_{\chi}^2 = \begin{cases} 185.58 l_0^{-7/3} C_n^2 L^3 & \sqrt{\lambda L} \ll l_0 \\ 23.39 C_n^2 k^{7/6} L^{11/6} & l_0 \ll \sqrt{\lambda L} \ll L_0 \\ 75.44 (\overline{An})^2 k^2 L L_n & L_0 \ll \sqrt{\lambda L} \end{cases} \quad \text{dB}^2 \quad (5-3)$$

where  $L_0$  (m) is the outer scale of turbulence,  $l_0$  (m) is the inner scale of turbulence,  $L$  (m) is the length of the turbulent part of the path,  $L_n$  (m) is the integral scale of

turbulence (same order of magnitude as  $L_0$ ),  $k$  ( $\text{m}^{-1}$ ) is the wavenumber ( $=2\pi/\lambda$ ),  $\lambda$  (m) is the wavelength,  $\overline{(\Delta n)^2}$  is the mean square of the refractive index fluctuations and  $C_n^2$  ( $\text{m}^{-2/3}$ ) is the refractive index structure function parameter.

Tatarski's models are also based on Rytov's (1937) first iteration solution (also called the method of smooth perturbations) for diffraction through a turbulent medium. As Rytov's method is applicable to weak turbulence only this restriction is also placed on Tatarski's models. Rytov's definition of weak turbulence is expressed as follows:

$$\sigma_\chi^2 \ll 1 \quad (5-4)$$

In practice, the value of unity has been reported as too high (Moulsley and Vilar, 1982). A more practical value given by Ishimaru (1978) is:

$$\sigma_\chi^2 < 0.2 - 0.5 \quad (5-5)$$

If  $\sigma_\chi^2$  is greater than  $0.5\text{dB}^2$  the turbulence is considered strong and the above theory is no longer applicable. For microwave and millimetre wave propagation in the surface boundary layer  $\sigma_\chi^2$  is generally less than  $0.5\text{dB}^2$  (Ishimaru, 1978). This is confirmed experimentally in Figure 5-4 by the plots of log-amplitude scintillation variance calculated from the measured events shown in Figure 5-2. This shows the largest value is  $0.45\text{dB}^2$ .

The next characteristic of scintillation to be investigated in this chapter is the probability density function.

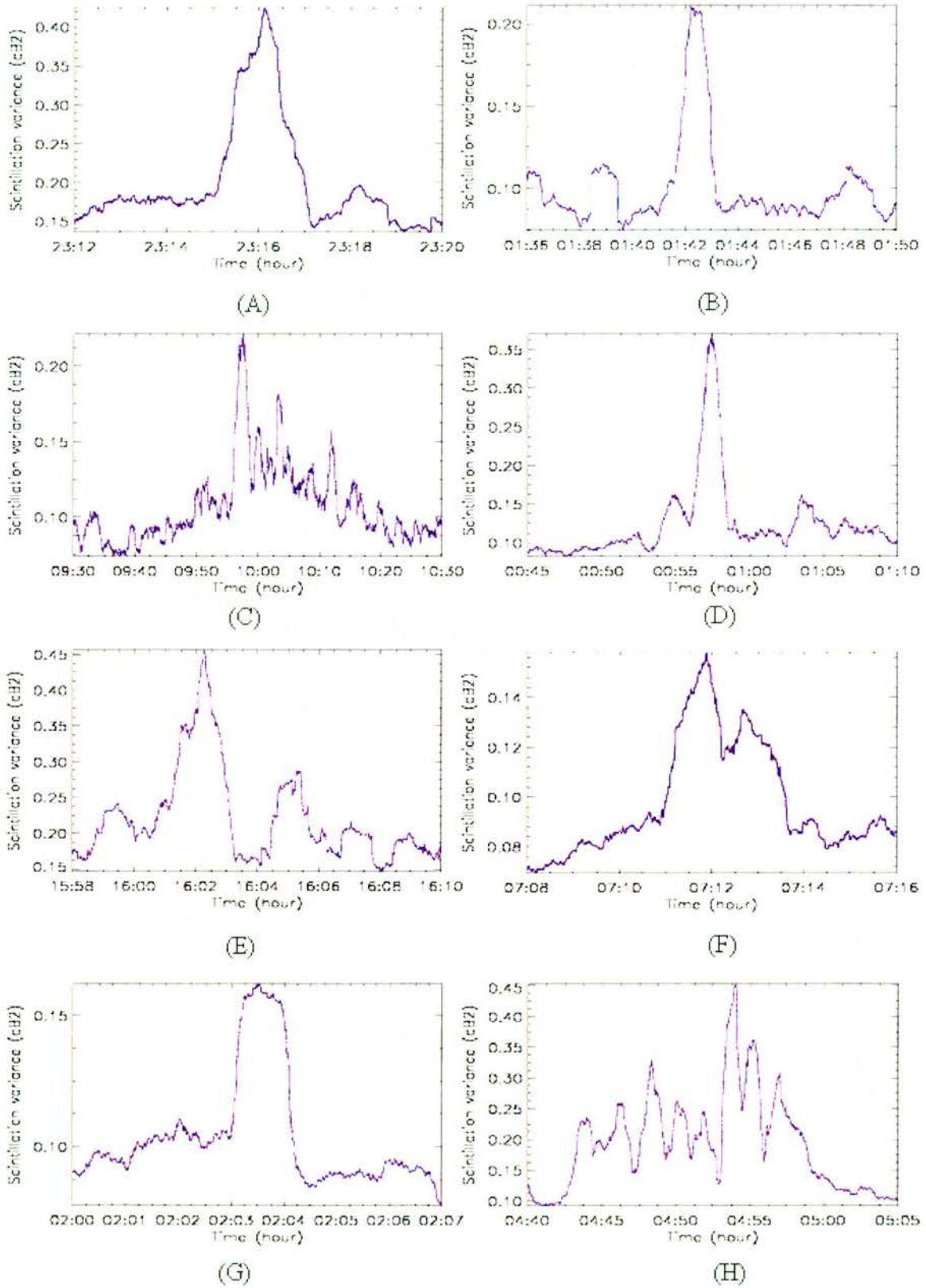


Figure 5-4 Log-amplitude scintillation variance of the events shown in Figure 5-2.

## 5.4 Probability density

Investigations into the statistical distribution of log-amplitude scintillation have been performed by a number of researches on data collected from satellite down links (Ortgies, 1985). The results showed that the short-term (up to 10 minutes) probability density of log-amplitude scintillation is stationary and can be fitted to a Gaussian variable given by:

$$P(\chi, \sigma) = \frac{1}{\sqrt{2\pi\sigma^2}} \exp\left[-\frac{(\chi - \bar{\chi})^2}{2\sigma^2}\right] \quad (5-6)$$

where  $\sigma^2$  is the variance.

To confirm the applicability of equation (5-6) to long terrestrial paths the scintillation event in Figure 5-1 was evaluated. The resulting distribution, shown in Figure 5-5, is compared with a Gaussian variable. The figure shows good agreement between scintillation and a normal distributed variable. The cumulative frequency distribution of the event is also shown.

To validate the normal distribution of tropospheric scintillation in the surface boundary layer the eight events in Figure 5-2 were also examined (Figure 5-6). The calculated distributions all show good agreement to the fitted Gaussian distributions, with standard deviations ranging from 0.35 to 0.45dB. The longer duration events, which in some cases last for up to 20 minutes, also show good agreement with a Gaussian distribution.

The final characteristic of scintillation to be investigated in this chapter is the power spectral density of scintillation.

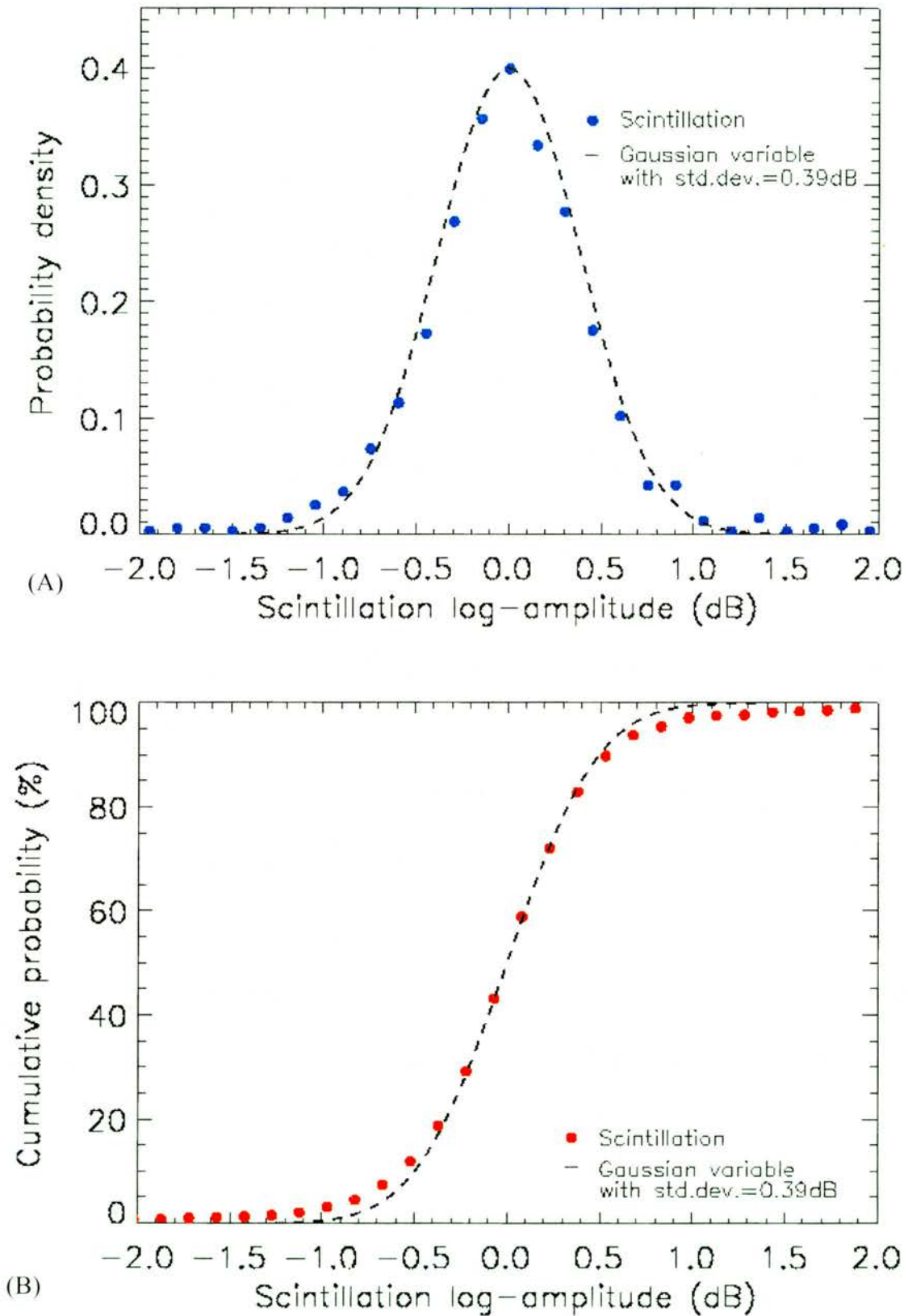
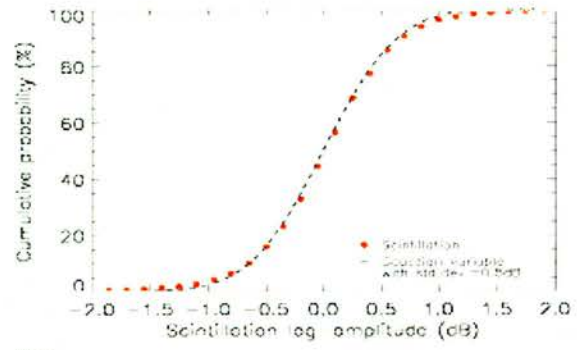
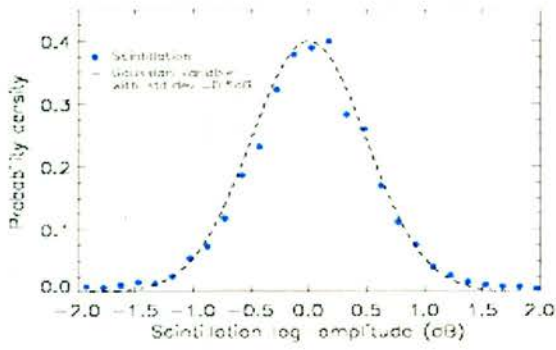
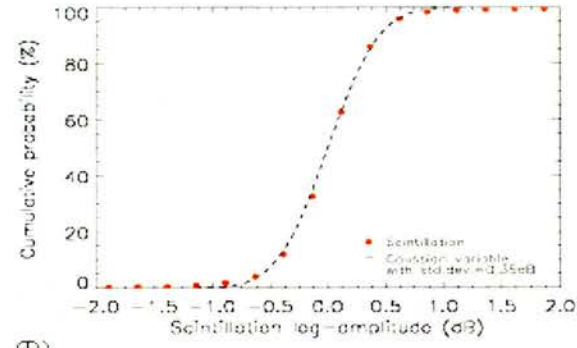
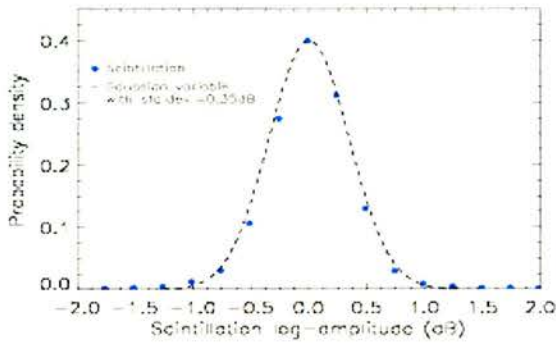


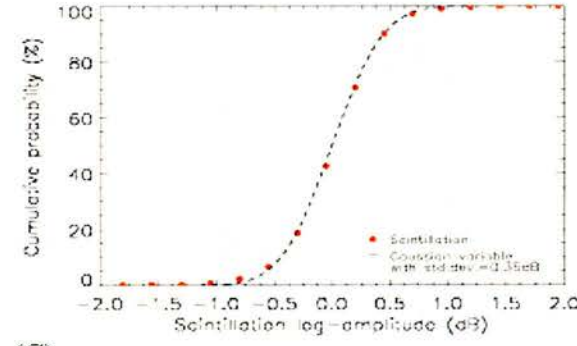
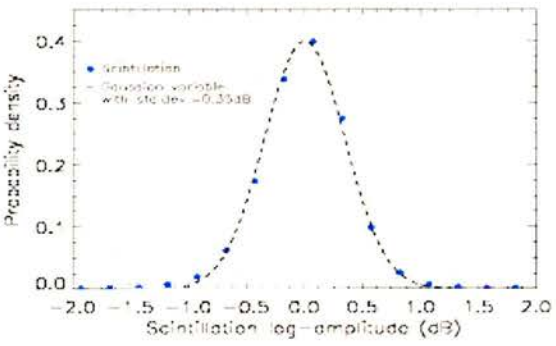
Figure 5-5 (A) A comparison between the distribution of the log-amplitude scintillation event shown in Figure 5-1 and a Gaussian distributed variable. (B) The cumulative probability of scintillation.



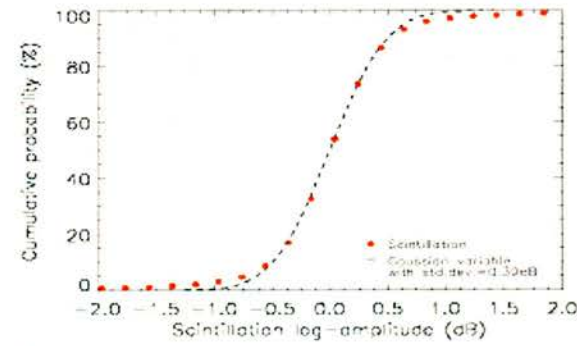
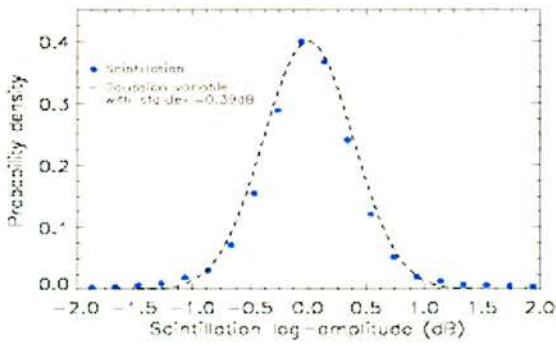
(A)



(B)



(C)



(D)

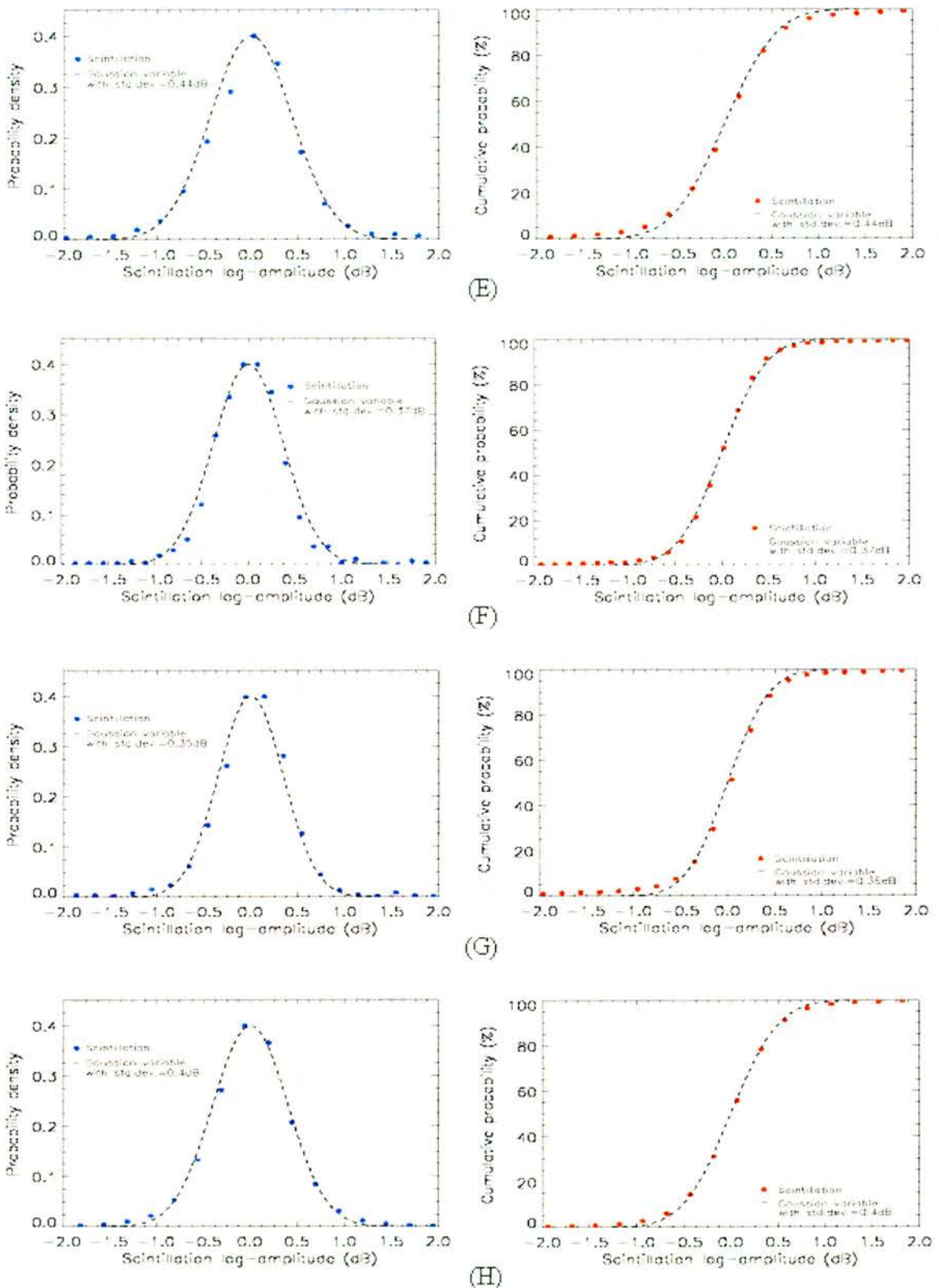


Figure 5-6 Probability density and cumulative probability distribution of the events shown in Figure 5-2.

## 5.5 Power spectral density

The spectral characteristics of tropospheric scintillation provide important information about signal fluctuation bandwidth and the turbulent atmospheric conditions that produce scintillation. This information can be used by communication system designers to specify adaptive power control loops to mitigate scintillation, and by remote sensing scientists to study the transport of atmospheric turbulence.

The spectral density of tropospheric scintillation was derived by Ishimaru (1978) and is based on the work of Taylor (1938), Kolmogorov (Frisch, 2001) and Tatarski (1961). Ishimaru's theory describes the power spectral density (PSD) of signal level fluctuations ( $W_\chi(w)$ ). It is expressed by the following two asymptotes:

$$\begin{aligned} W_\chi^0(w) &\rightarrow 0.85 \frac{C_n^2 k^{-2/3} L^{7/3}}{U_t} & (5-7) \\ &= 2.765 \frac{\sigma_\chi^2}{\omega_t} \text{ rads} & (\text{as } \omega \rightarrow 0) \end{aligned}$$

$$\begin{aligned} W_\chi^\infty(w) &\rightarrow 2.19 \frac{C_n^2 k^{2/3} L^{7/3}}{U_t} \left( \frac{\omega}{\omega_t} \right)^{-8/3} & (5-8) \\ &= 7.13 \frac{\sigma_\chi^2}{\omega_t} \left( \frac{\omega}{\omega_t} \right)^{-8/3} \text{ rads} & (\text{as } \omega \rightarrow \infty) \end{aligned}$$

where  $U_t$  (m/s) is the mean wind speed transverse to the direction of the propagation path of length  $L$  (m),  $k = 2\pi / \lambda$  where  $\lambda$  (m) is the signal wavelength,  $\omega$  (rads) is the fluctuation frequency ( $= 2\pi \times \text{frequency}$ ),  $\sigma_\chi^2$  (dB<sup>2</sup>) is the log-amplitude variance of amplitude fluctuations,  $C_n^2$  (m<sup>-2/3</sup>) is the structure function parameter, and

$$\omega_t = U_t \sqrt{\frac{k}{L}} \quad \text{rads} \quad (5-9)$$

The two asymptotes in equations (5-7) and (5-8) meet at the corner frequency ( $\omega_c$ ) given by:

$$\omega_c = 1.43\omega_t \quad \text{rads} \quad (5-10)$$

From the above, Ishimaru's description of the spectral density of signal fluctuations is visualised as consisting of a flat (substantially constant) spectral region from DC to a corner frequency  $\omega_c$ , and from  $\omega_c$  to  $\infty$  the response decays as  $\omega^{-8/3}$ . This description of the spectrum of scintillation is valid as long as the inertial sub-range of turbulence is applicable ( $l_0 \ll \sqrt{\lambda L} \ll L_0$ ). Departures from an  $\omega^{-8/3}$  slope indicate that either the inertial sub-range is not applicable or the log-amplitude variance is not constant.

### 5.5.1 Analysis method for extracting scintillation spectra

To extract scintillation spectra a similar approach was taken to that of Ho et al (1978), which also evaluated scintillation spectra at 36GHz on a terrestrial path. The method used is as follows:

1. The received signal time series was divided into segments for processing. The segment length ( $t_l$ ) was selected to provide the same spectral resolution ( $f_{res}$ ) as Ho et al, i.e.

$$f_{res} = \frac{1}{2 \times t_c \times t_l} = 0.0195\text{Hz} \quad (5-11)$$

where  $t_c(s) = 1/f_c$  ( $f_c$  is the sampling frequency). For this spectral analysis the 100Hz sampled data required a segment length of 2560 samples.

- ii. Each 2560 sample segment was windowed (Hanning window) to reduce the effects of discontinuities between sequences (spectral leakage).
- iii. After data windowing, each segment was processed by fast Fourier transform (FFT) and the 1-sided PSD ( $P_h(f)$ ) calculated from:

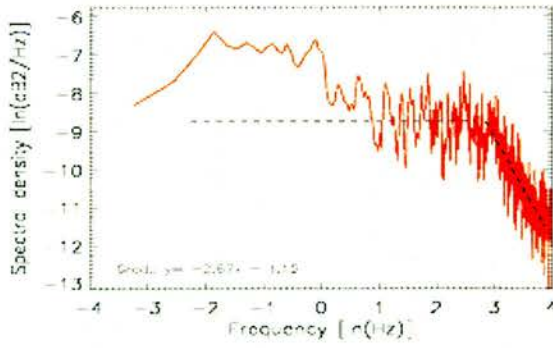
$$P_h(f) = 2|H(f)|^2 \quad (5-12)$$

where  $H(f)$  is the frequency spectrum of the scintillation time series  $h(t)$ .

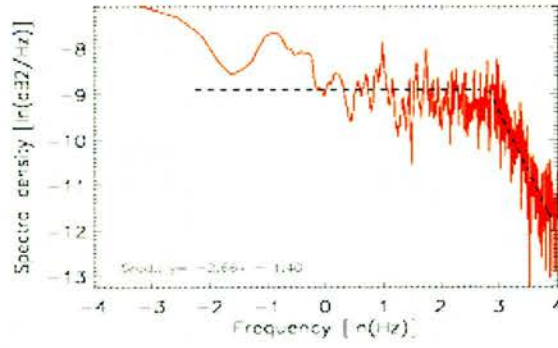
- iv. The resulting spectra were filtered (smoothed) and averaged (over 2 consecutive spectra) to reduce the variance in the spectral estimation. No other filtering was performed.

### 5.5.2 Experimental data

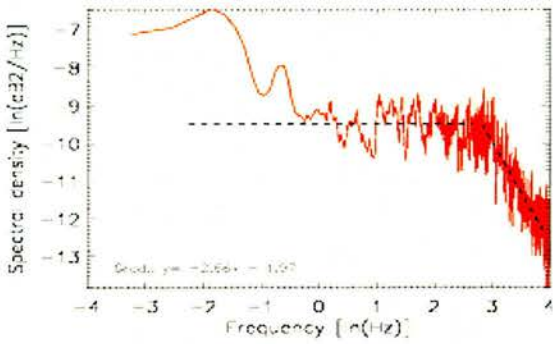
The analysis method described above was applied to the scintillation events shown in Figure 5-2. The resulting spectra, shown in Figure 5-7, are plotted on a Napierian grid for the convenience of fitting Ishimaru's straight-line asymptotes using linear regression.



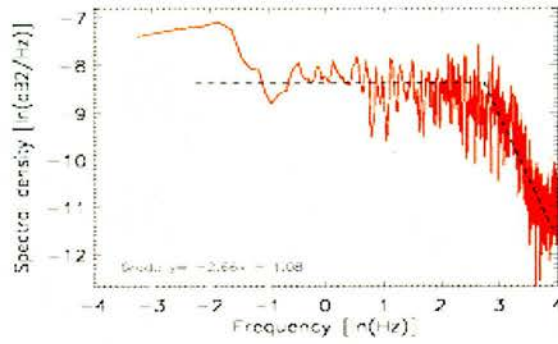
(A)



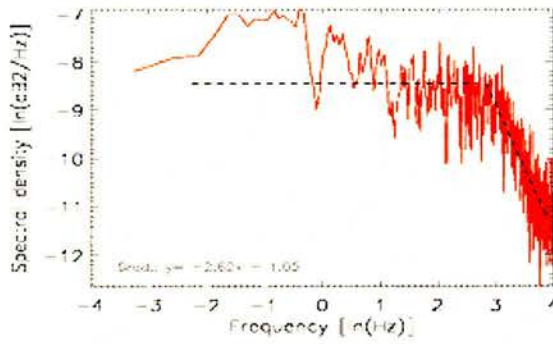
(B)



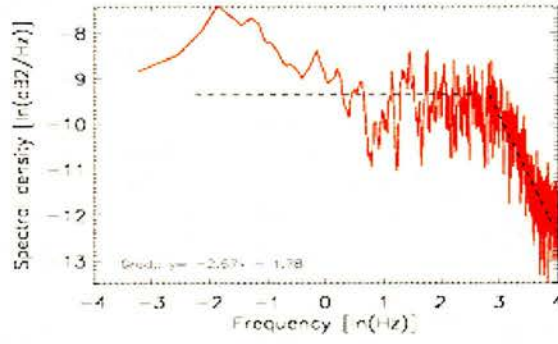
(C)



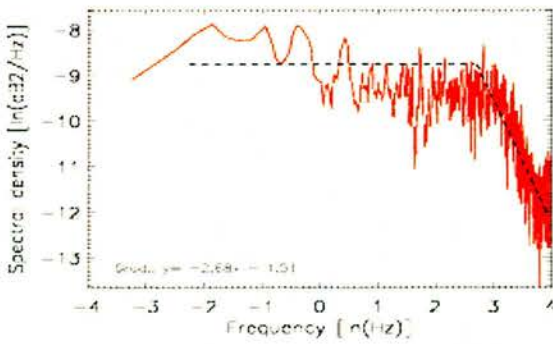
(D)



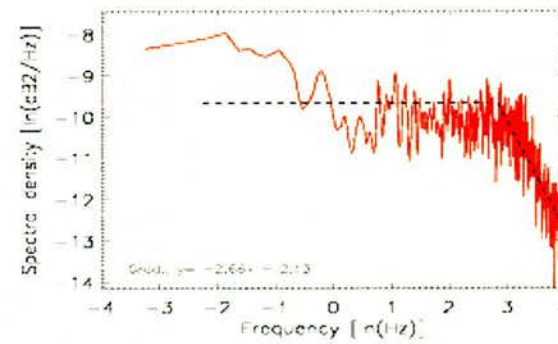
(E)



(F)



(G)



(H)

Figure 5-7 Power spectral density of the events shown in Figure 5-2.

The PSDs in Figure 5-7 show good agreement with the two straight-line asymptotes predicted by Ishimaru. Both a spectral region from DC to a corner frequency  $\omega_c$ , and from  $\omega_c$  to  $\infty$  with a response decaying at  $\sim \omega^{-8/3}$  is observed. This indicates that the turbulence producing the scintillation events is within the inertial sub-range of the spectrum of turbulence, i.e.  $l_0 \ll \sqrt{\lambda L} \ll L_0$ .

The corner frequency was estimated by visual inspection. The average value, from the events above and generally throughout the measurement campaign, is  $\sim 16\text{Hz}$ . This value is higher than would be expected (typical values are in the range of sub-hertz to a few hertz) based on mean wind speed alone, i.e. equation (5-10). The reason for the higher than expected corner frequency could not be determined from the data set analysed in this thesis. It would therefore be necessary to collect further scintillation data and meteorological measurements to identify the mechanism that produced these higher corner frequencies.

## 5.6 Diurnal variation

The characteristics of scintillation described above are concerned with individual events. For longer durations, i.e. hours and days, the statistics of scintillation could be expected to change as the atmosphere changes. Previous satellite path studies have shown that the long-term (>10 minutes) probability density of scintillation is lognormal rather than Gaussian (Moulsley and Vilar, 1982; Ortgies, 1985). This differs from the above examples of terrestrial path scintillation which show that events lasting for up to 20 minutes (the longest measured) remained normally distributed. This indicates that turbulence in the surface boundary layer remains

statistically stationary for longer periods than turbulence generated by cloud layer mixing.

The evolution of turbulence and its effect on satellite paths has also been investigated (Otung et al, 1993). This showed that scintillation intensity has a diurnal cycle that responds to changes in air temperature, with a maximum in the afternoon and minimum at night. Maximum scintillation intensity therefore coincides with the thickening of cloud cover produced by thermal convection. As less evaporation occurs during the night there is less turbulent energy (convection) imparted into the capping inversion layer.

The evolution of turbulence and its effect on terrestrial paths was investigated for comparison to the slant path observations. The approach taken was to divide the measured data into 1-minute segments from which the standard deviation (fluctuation intensity) was calculated and then expressed as a 10-minute median. This process filters anomalous samples such as data dropouts so that the gross trend in the data set could be observed. The result of this signal processing for a 1-day data set is shown in Figure 5-8.

Figure 5-8 shows the variation of fluctuation intensity as a function of time. It is clear from the fitted polynomial trend line that the fluctuation intensity follows a definite diurnal cycle. The maximum fluctuation intensity ( $\sim 0.5\text{dB}$ ) occurs during the afternoon and the minimum ( $\sim 0.3\text{dB}$ ) during the night. This cycle agrees with the slant path measurements at 20GHz by Otung et al (1993).

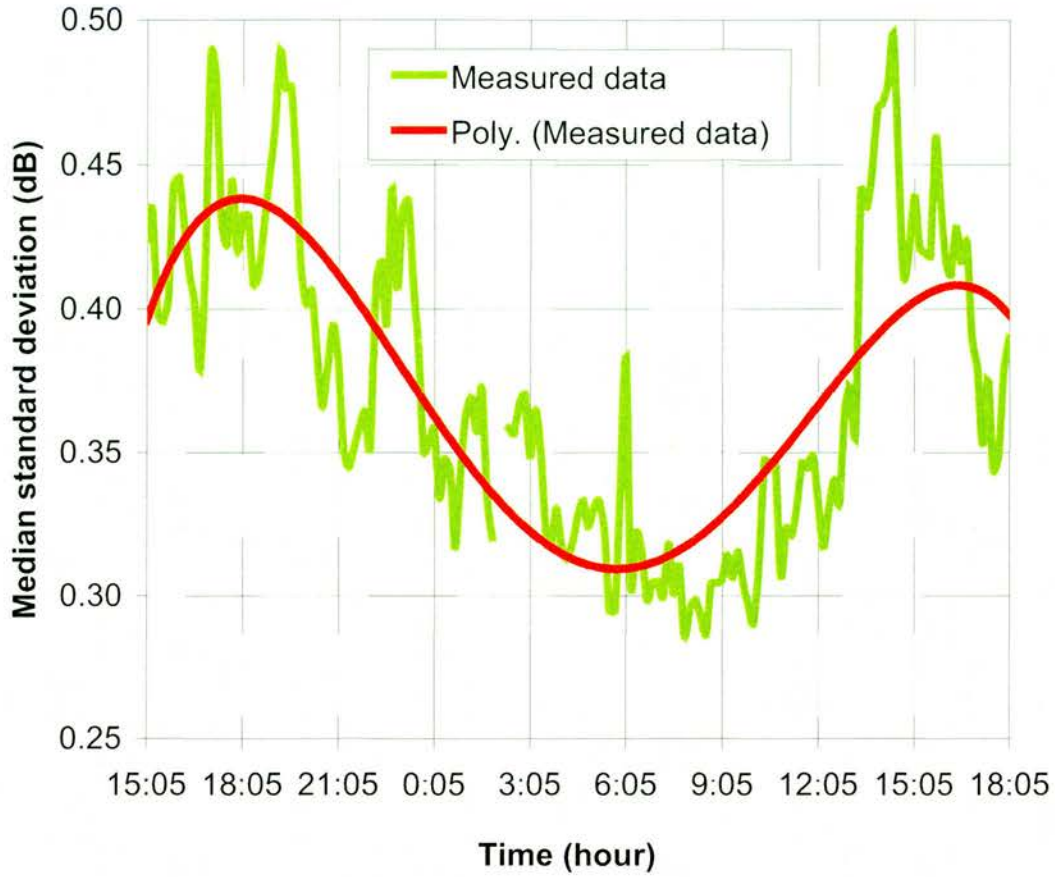


Figure 5-8 Measured 10-minute medians of fluctuation intensity (standard deviations) calculated at 1 minute intervals over a 24 hour period during the 1<sup>st</sup> and 2<sup>nd</sup> June 2000. A polynomial least squares fit illustrates the diurnal trend of scintillation intensity.

The air temperature and relative humidity measured at the same time as the fluctuation data in Figure 5-8 is shown in Figure 5-9. It shows the expected inverse relationship between air temperature and relative humidity, and the evident connection between signal fluctuation intensity and air temperature. In addition to the gross similarity there are also observable similarities over relatively short periods. For example, just after 21:00 there is an irregular increase in temperature (with opposing decrease in relative humidity), which corresponds to an increase in fluctuation intensity.

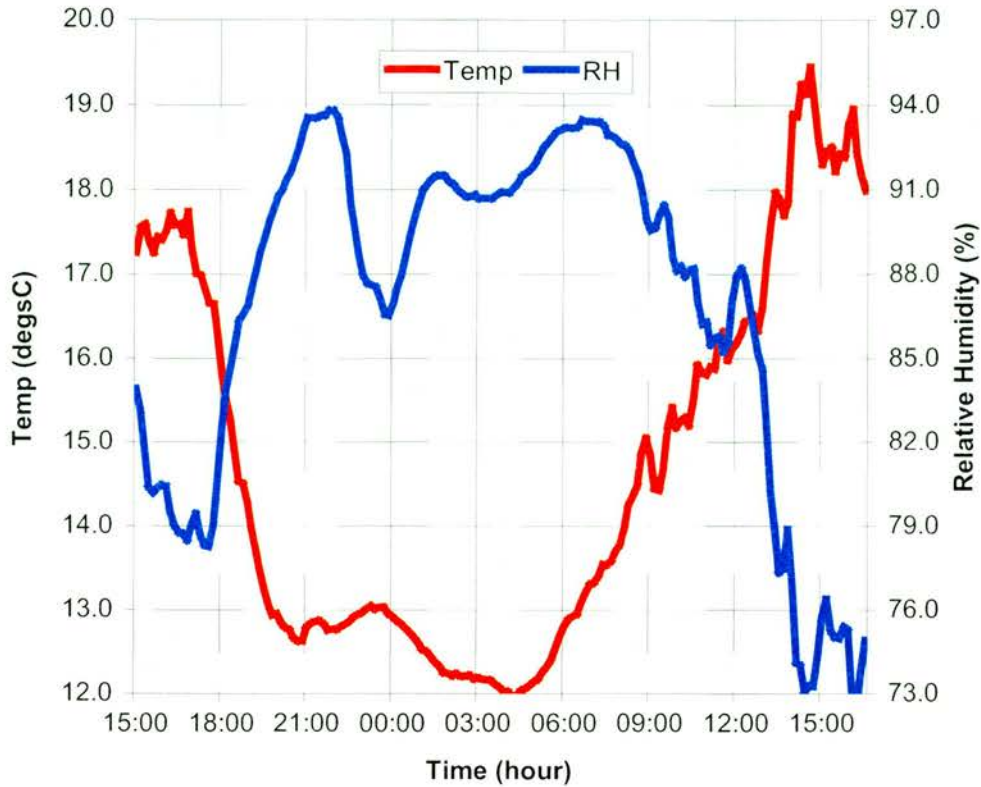
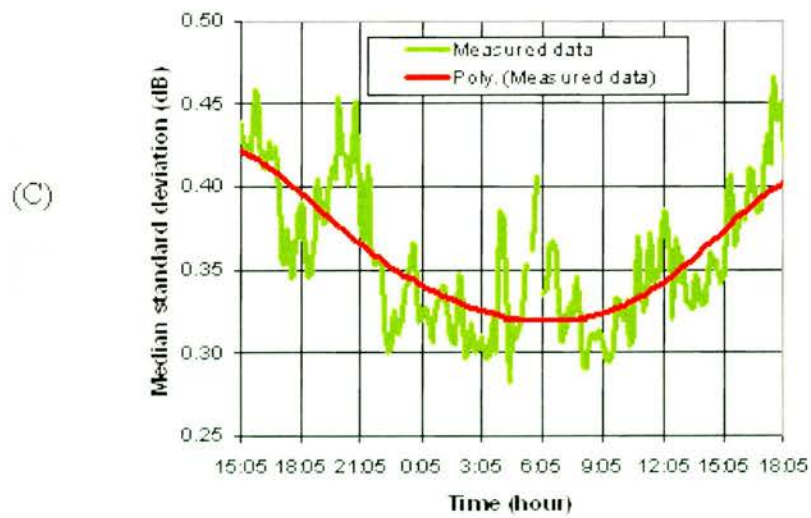
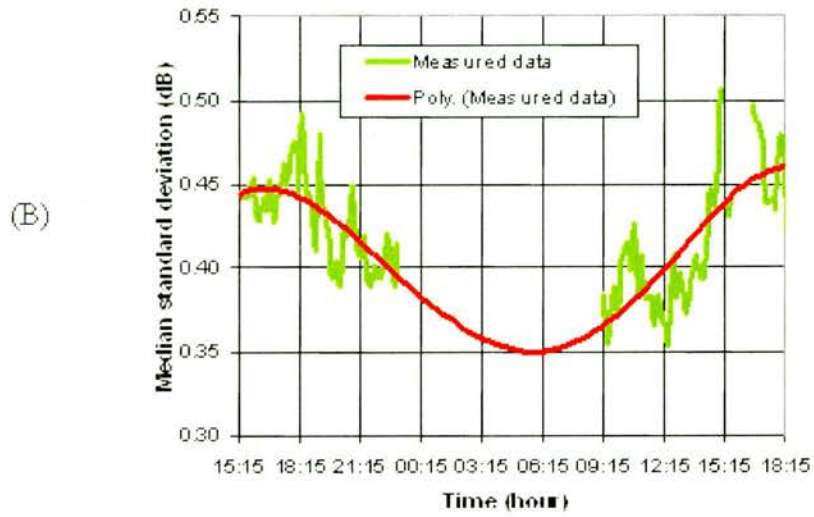
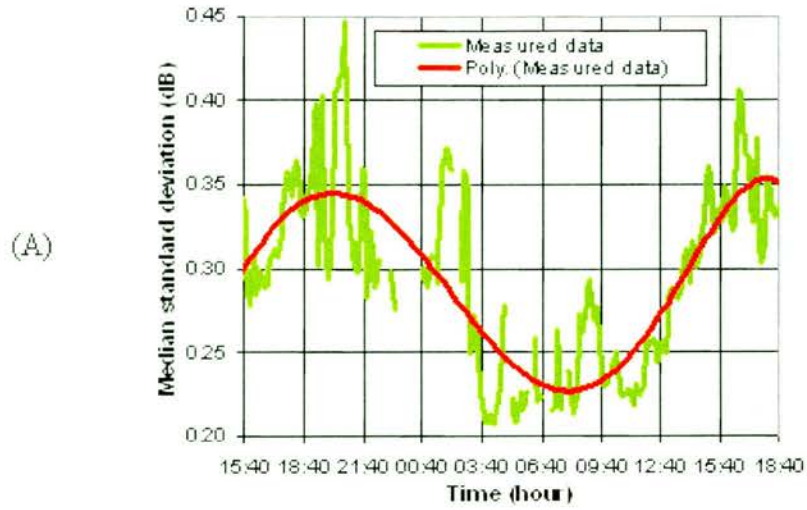


Figure 5-9 Temperature and humidity measurements corresponding to the fluctuation intensity data in Figure 5-8.

The diurnal (temperature) dependent variation of scintillation intensity was investigated throughout the month long measurement campaign. The cycle of scintillation intensity remained approximately the same with only small differences observed between days. This is illustrated in Figure 5-10 with six further examples of the diurnal variation of scintillation intensity.

Figure 5-10 shows the daily variation of scintillation ranges from 0.2dB at night to 0.55dB during the afternoon. It is assumed that as the measurements were made during the early summer months (late May to early June) the annual peak fluctuation intensity would occur during July and August (British summer time) and be slightly larger than 0.55dB.



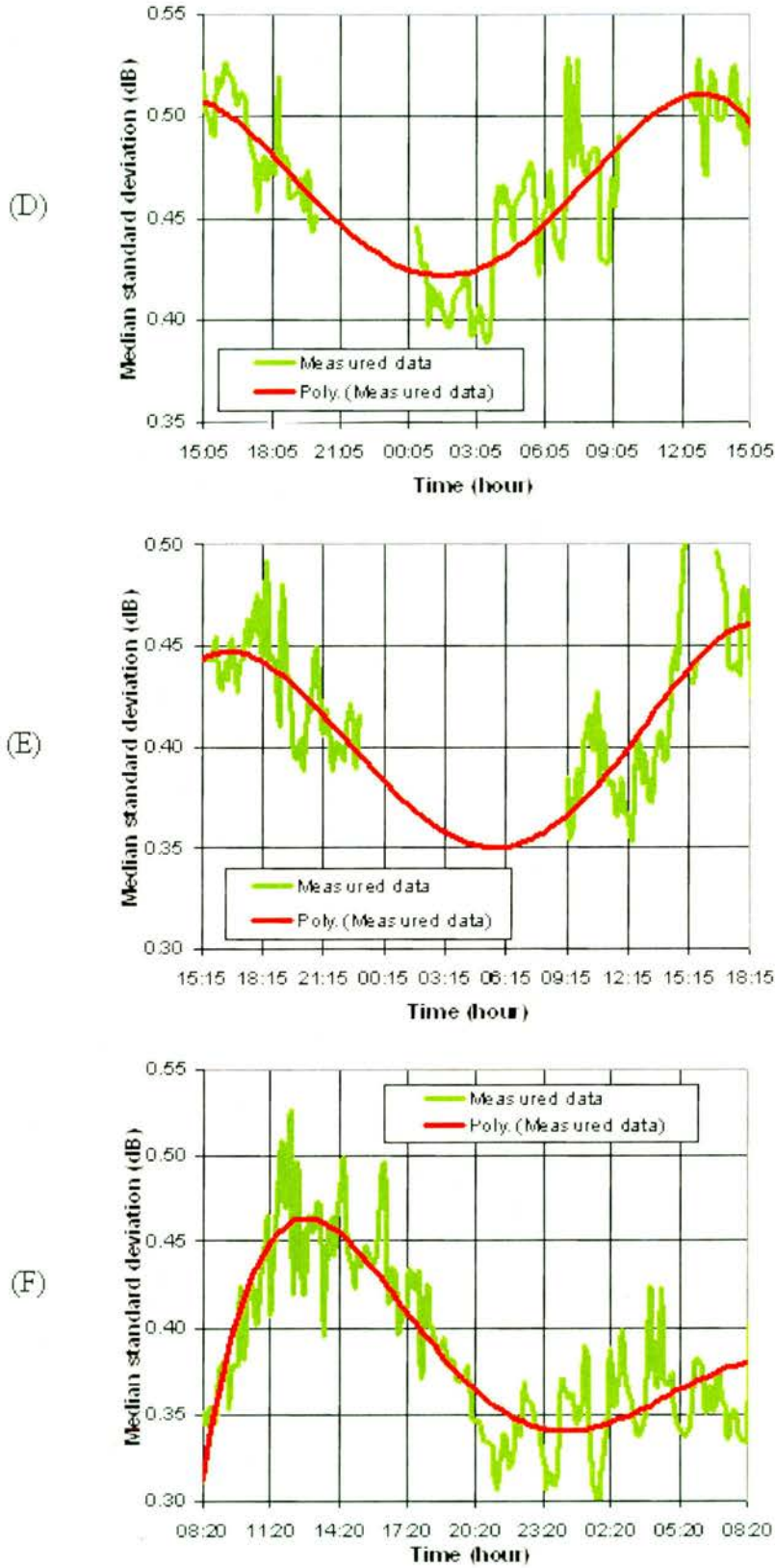
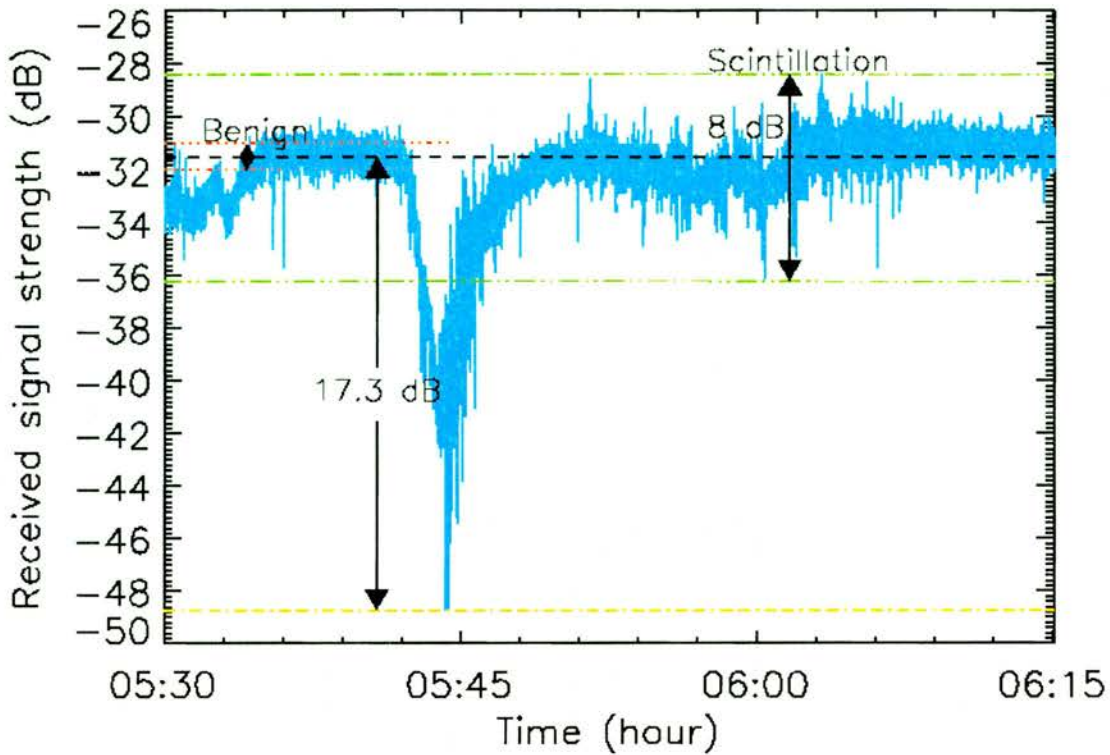


Figure 5-10 Six examples (A-F) of the diurnal cycle of fluctuation (scintillation) intensity. Missing data periods are due to rain events / data dropouts.

The occurrence of significant scintillation events ( $>\pm 1$  dB above benign conditions) during the diurnal cycle of scintillation intensity was also considered. It showed that the most significant events occurred during the night and early morning (refer to the examples in Figure 5-3). The reason for the inverse relationship between diurnal scintillation intensity and the most significant scintillation events is the variability of relative humidity. Relative humidity peaks during nocturnal hours and dips during daylight hours due to the heating (drying) effect of the sun. However, the peak in relative humidity occurs when the generation of turbulence is at a minimum. This is because thermal convection (the kinetic energy input mechanism to turbulence in the surface boundary layer) is a minimum. Therefore although the atmosphere contains more moisture during nocturnal hours than daylight hours there is less opportunity for the mixing of air masses that leads to refractive index anomalies. The strong scintillation events observed during nocturnal hours are therefore due to sporadic turbulence during periods of high relative humidity.

## **5.7 Simultaneous scintillation and clear-air multipath**

In the previous chapter clear-air multipath was shown to have a significant effect on millimetre wave propagation. The nocturnal radiation mechanism that produces refractive index layering may also provide the kinetic energy input mechanism to drive turbulence that produces scintillation. The result is that clear-air multipath and scintillation may occur at the same time. Figure 5-11 illustrates this with an example.



*Figure 5-11 An example of a clear-air multipath signal fade (17.3 dB) and scintillation event of 8dB peak-to-peak.*

Figure 5-11 shows a measured time series of a characteristic V-shaped multipath fade followed by a scintillation event. The time series was measured in the early hours of the morning and is indicative of multipath fading from atmospheric layering. The scintillation event that follows the multipath fade has an 8dB peak-to-peak variation and lasts for approximately 18 minutes. It is also apparent from visual inspection of the multipath fade that fast signal fluctuations are superimposed on the fade slope. This is more clearly illustrated by expressing the time series in log-amplitude form. This is shown in Figure 5-12.

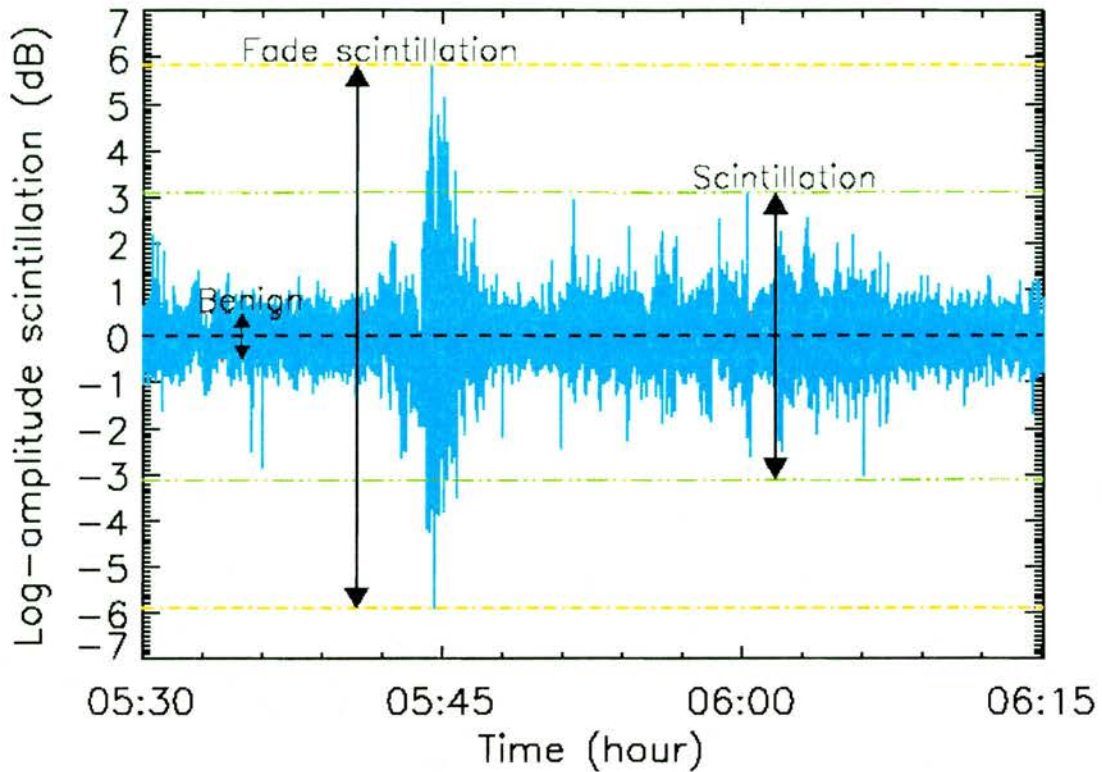


Figure 5-12 The log-amplitude variation of the received signal shown in Figure 5-11. The rapid variation in signal strength on the fade slope is clearly indicated.

Figure 5-12 shows the log-amplitude signal processing has filtered the relatively slow fading due to clear-air multipath leaving only the fast fluctuations from turbulence. It shows there is considerable signal power fluctuations superimposed on the slow variation of the multipath fade. The scintillation event that follows the multipath fade appears to be a continuation of the signal fluctuation overlaying the deep fade.

## 5.8 Summary

This chapter has shown that atmospheric turbulence in the surface boundary layer can have a significant effect on millimetre wave propagation. Amplitude scintillations with peak-to-peak variations of 10dB above mean benign channel conditions were shown, with event durations ranging from 1 to 20 minutes.

The log-amplitude variance and probability density of scintillation was investigated. It was shown that the largest log-amplitude variance was  $0.45\text{dB}^2$ , which is less than the maximum value ( $\sigma_{\chi}^2 < 0.5\text{dB}^2$ ) that can be applied to the models of Tatarski (1961) and Ishimaru (1978). This will be important in Chapter seven when spatial phase differences are evaluated.

The probability density of scintillation was considered. It was shown to be Gaussian distributed, and remained Gaussian for periods up to 20 minutes with no evidence of a change to a lognormal distribution as found on satellite paths.

The PSD of scintillation was also evaluated. It was shown that the two-asymptote spectrum predicted by Ishimaru (1978) was in good agreement with measured data. The estimated corner frequency was however higher than expected.

The strongest scintillation events occurred during the night and early morning. This is contrary to the mean signal fluctuation intensity that was shown to follow a diurnal cycle dependant on air temperature. The strongest events appear to be the result of sporadic turbulence rather than convection. It is therefore concluded that the greatest impact of clear-air effects (layering and turbulence) on terrestrial millimetre wave communication systems is during the night and early morning.

From the analysis in this chapter the impact of amplitude scintillation on millimetre wave communication systems is twofold. Firstly, signal fading can cause link outage for systems with inadequate fade margin. Secondly, signal strength enhancements can be a source of interference to other closely sited systems. To mitigate these effects a possible technique could be fast response adaptive power control loops. Such a technique would need to adapt to the slow variation of multipath signal fading from

tropospheric layers, fast fluctuations from turbulence, and the simultaneous occurrence of both impairments as was shown above.

In addition to the temporal properties of scintillation the spatial characteristics were evaluated. This is considered in the next chapter.

# Chapter Six

## Spatial Characteristics of Amplitude Scintillation

### 6.1 Introduction

The size of eddies that lead to amplitude scintillation define two important spatial characteristics. Firstly, it specifies the spatial diversity required to mitigate tropospheric scintillation. Secondly, it determines the distance over which a wavefront can be coherently combined and therefore the maximum gain of an antenna array. Both of these characteristics are defined by the small-scale spatial decorrelation of scintillation. This chapter describes measurements of the spatial decorrelation of amplitude scintillation using the five-element sensor array described in Chapter three.

### 6.2 Theory

The method used to examine the spatial effects of atmospheric turbulence is the cross-correlation function shown in equation (6-1).

$$P_{xy} = \frac{\sum_{k=0}^{N-1} (x_k - \bar{x})(y_k - \bar{y})}{\sqrt{\left[ \sum_{k=0}^{N-1} (x_k - \bar{x})^2 \right] \left[ \sum_{k=0}^{N-1} (y_k - \bar{y})^2 \right]}} \quad (6-1)$$

where  $N$  is the number of samples in the data set,  $k$  is an index to the elements in the data set and  $P_{xy}$  is the correlation coefficient.

Equation (6-1) is interpreted as follows. If parameters  $x$  and  $y$  change equally the value of  $P_{xy}$  tends to +1. If  $x$  and  $y$  change randomly  $P_{xy}$  tends to 0. If  $x$  and  $y$  have proportional but opposite changes then  $P_{xy}$  tends to -1. Therefore applying the cross-correlation function to the spatially separated receivers of the antenna array produces a correlation coefficient as a function of antenna separation (called decorrelation scale lengths). Using this technique it could be expected that as the separation distance between antennas increase the correlation between received signals decrease. When the correlation between received signals is zero the signal paths from the transmitter to the spatially separated receivers are independent.

Spatial decorrelation of atmospheric turbulence was originally modelled for optical propagation (Tatarski, 1961), but is also considered to be applicable to millimetre wave frequencies. However, there has to date been only one experiment in the surface boundary layer that has compared spatial correlation measurements to Tatarski's model (Lee and Waterman, 1968). The measured decorrelation showed good agreement with Tatarski's model using a limited data set and non-contiguous spatial measurements. The results presented in this chapter are therefore the first spatial measurements of scintillation at millimetre wave frequencies to be carried out simultaneously.

### 6.2.1 Tatarski's correlation function

Tatarski's models for fluctuation spectral density and spatial decorrelation were first introduced in Chapter two. It was shown that the spatial decorrelation distance depends on the size and position of eddies in relation to the first Fresnel zone ( $f_1$ ) given by:

$$f_l = \sqrt{\lambda L} \quad \text{m} \quad (6-2)$$

where  $L$  (m) is the turbulent path length and  $\lambda$  (m) is the signal wavelength.

If  $f_l$  is smaller than the inner scale of turbulence the decorrelation distance is  $l_o$ . If  $f_l$  is greater than the outer scale of turbulence the decorrelation distance depends on the turbulence generation mechanism. If  $f_l$  is between the inner and outer scale of turbulence the decorrelation distance is proportional to  $\sqrt{\lambda L}$ . This condition was shown to be the most significant as eddies the size of  $f_l$  cause the largest signal fluctuations. Based on this condition, Tatarski derived the spatial correlation function:

$$b_x(r) = \begin{cases} 1 - 2.80 \left( \frac{kr^{2.4}}{L} \right)^{5/6} l_o^{-1/3} & (r < l_o) \\ 1 - 2.36 \left( \frac{kr^2}{L} \right)^{5/6} + 1.71 \left( \frac{kr^2}{L} \right) - 0.024 \left( \frac{kr^2}{L} \right)^2 & (l_o < r < \sqrt{\lambda L}) \\ - \left( \frac{kr^2}{L} \right)^{-7/6} & (r > \sqrt{\lambda L}) \end{cases} \quad (6-3)$$

where  $r$  (m) is the sensor separation distance and  $k=2\pi/\lambda$ .

Equation (6-3) shows that the correlation between signals measured by spaced receivers depends on the factor  $kr^2/L$ . With the exception of a small difference in the range exponent for the condition ( $r < l_o$ ), the value of the correlation coefficient is directly proportional to:

$$\frac{kr^2}{L} = 2\pi \left( \frac{r^2}{\lambda L} \right) \quad (6-4)$$

This indicates that when the separation distance between receivers is small the correlation coefficient is approximately 1, and when  $r$  equals  $\sqrt{\lambda L}$  the correlation coefficient is a minimum, i.e.  $-0.12$ . Figure 6-1 illustrates  $b_z(r)$  graphically.

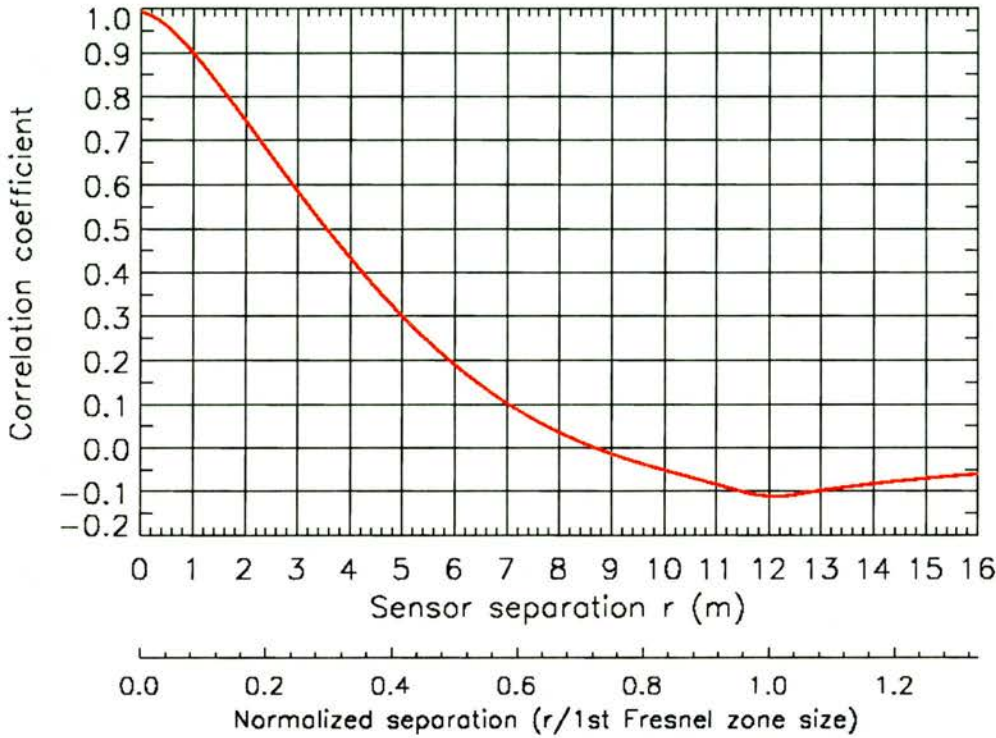


Figure 6-1 Tatarski's correlation function when  $\sqrt{\lambda L} = 12$ , i.e.  $L = 17,300m$  and  $\lambda = 8.33mm$ .

Figure 6-1 shows the correlation function for the experimental path used to collect data presented in this chapter. This function will be compared with the decorrelation scale lengths calculated in the next section.

## 6.3 Experiment results

### 6.3.1 Sensor array configuration

The five-element array was configured so that spatial correlation could be evaluated at sensor separation distances from 1 to 8m. This range of scale lengths provides 1m spatial measurement intervals using five sensors. According to Tatarski's correlation

function, a scale-length of 8m should result in approximately zero correlation for the experimental path length of 17.3km and signal wavelength of 8.33mm (see Figure 6-1). The configuration of the array and associated decorrelation scale lengths is shown in Figure 6-2.

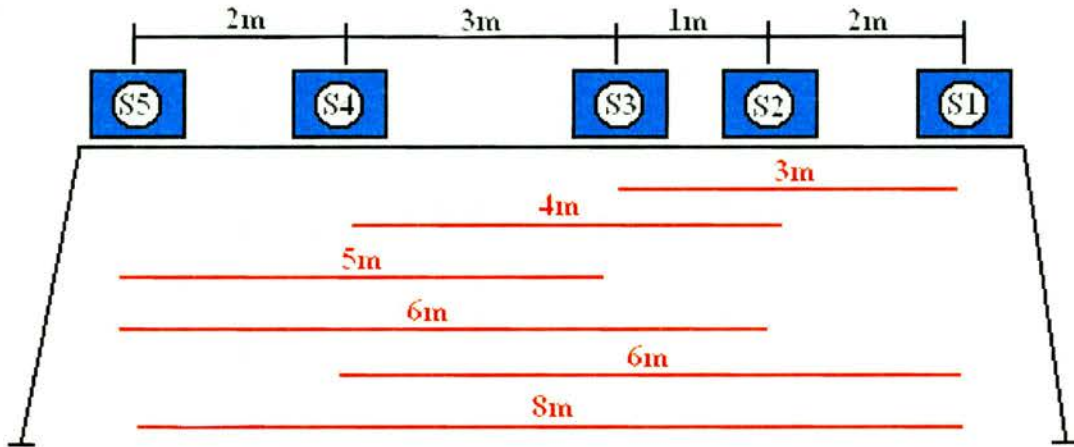


Figure 6-2 Spacing of sensors and associated correlation distances using the five element array.

Figure 6-2 illustrates that with five antennas scale lengths of 1, 2, 3, 4, 5, 6 and 8m can be measured simultaneously (where the same scale-length is measured twice the average is taken). However, as described in Chapter three, sensors S2 and S4 functioned intermittently. For this reason more measurements were made of 3, 5 and 8m scale lengths.

### 6.3.2 Results

The received signal strength from the five sensors of the array was evaluated by calculating the standard deviation of fluctuations and the cross-correlation coefficient. An example of a 12-hour period of received signal strength from the five sensors expressed as 10-minute medians of the standard deviation of fluctuations calculated every minute is shown in Figure 6-3.

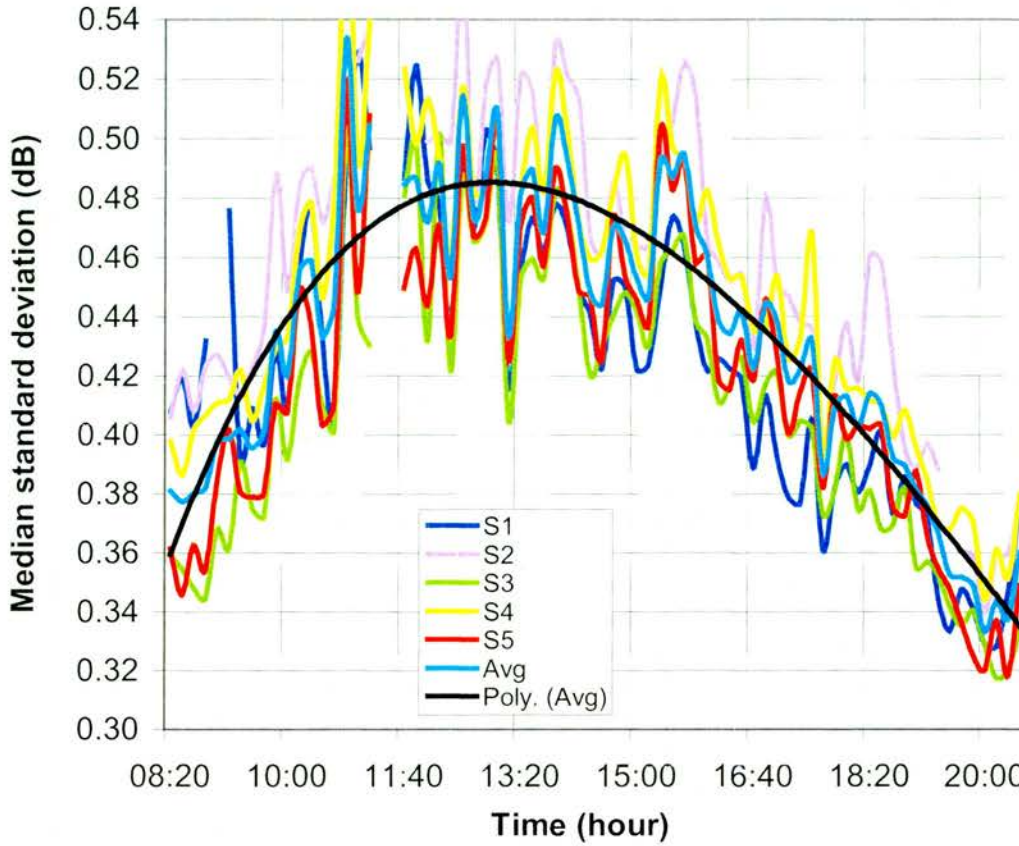
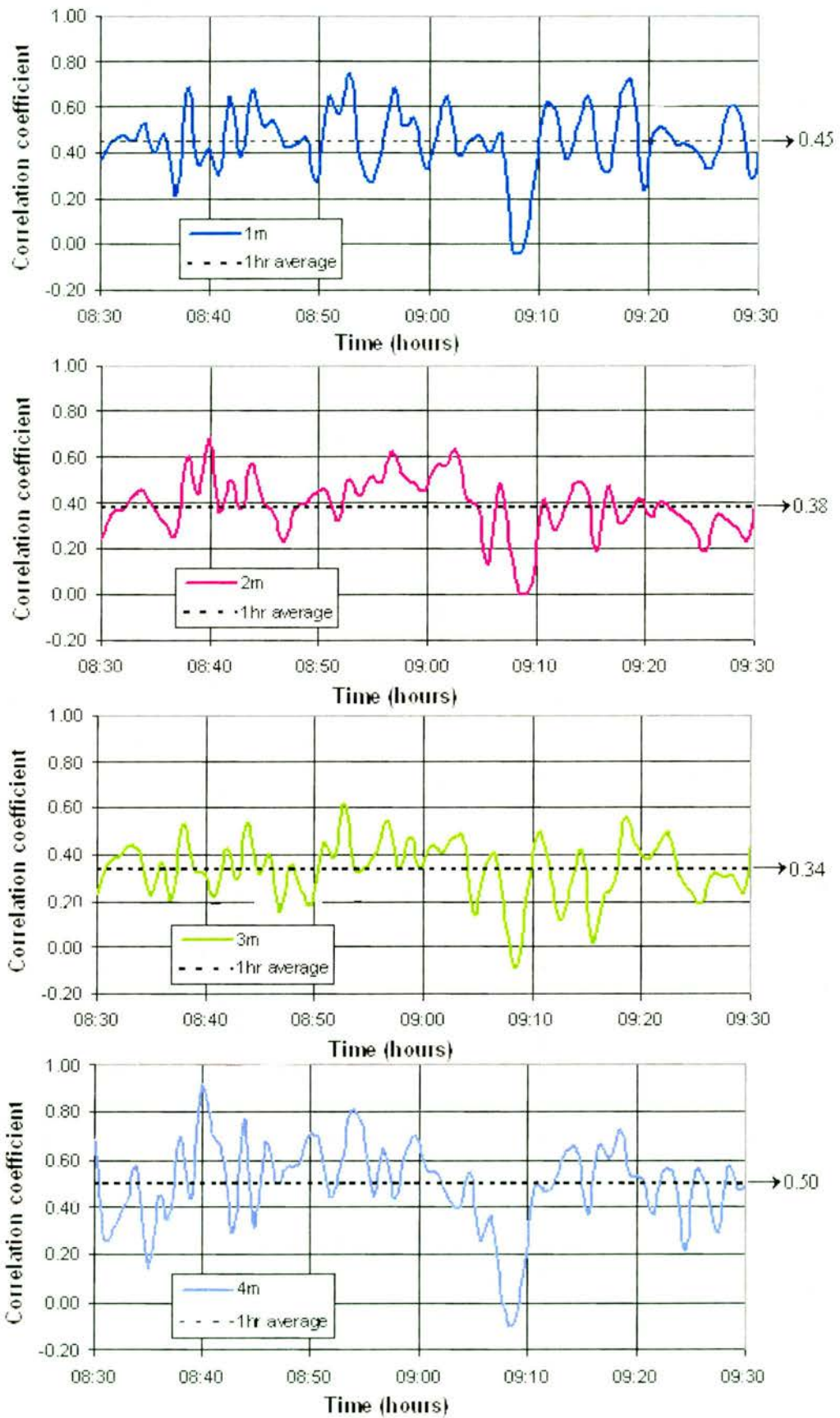


Figure 6-3 12-hour period of signal strength fluctuations. Data is expressed as 10 minute medians of standard deviations calculated every 1 minute.

Figure 6-3 shows 12 hours of data expressed as signal strength fluctuation intensity. As with the single sensor examples shown in Chapter five, all five sensors show that signal fluctuation intensity peaks during the afternoon.

The spatial correlation of signal strength fluctuations was evaluated for each scale-length during the period of data shown in Figure 6-3. Figure 6-4 shows the correlation coefficient calculated at 1-minute intervals between 08:30 and 09:30, and Figure 6-5 shows the cross correlation coefficient calculated at 1-minute intervals between 13:30 and 14:30. The plots show the correlation at each scale-length varies over a range of values during the 1-hour period considered. The average correlation coefficient for each scale-length is also shown, which in Figure 6-6 are illustrated as morning and afternoon decorrelation functions.



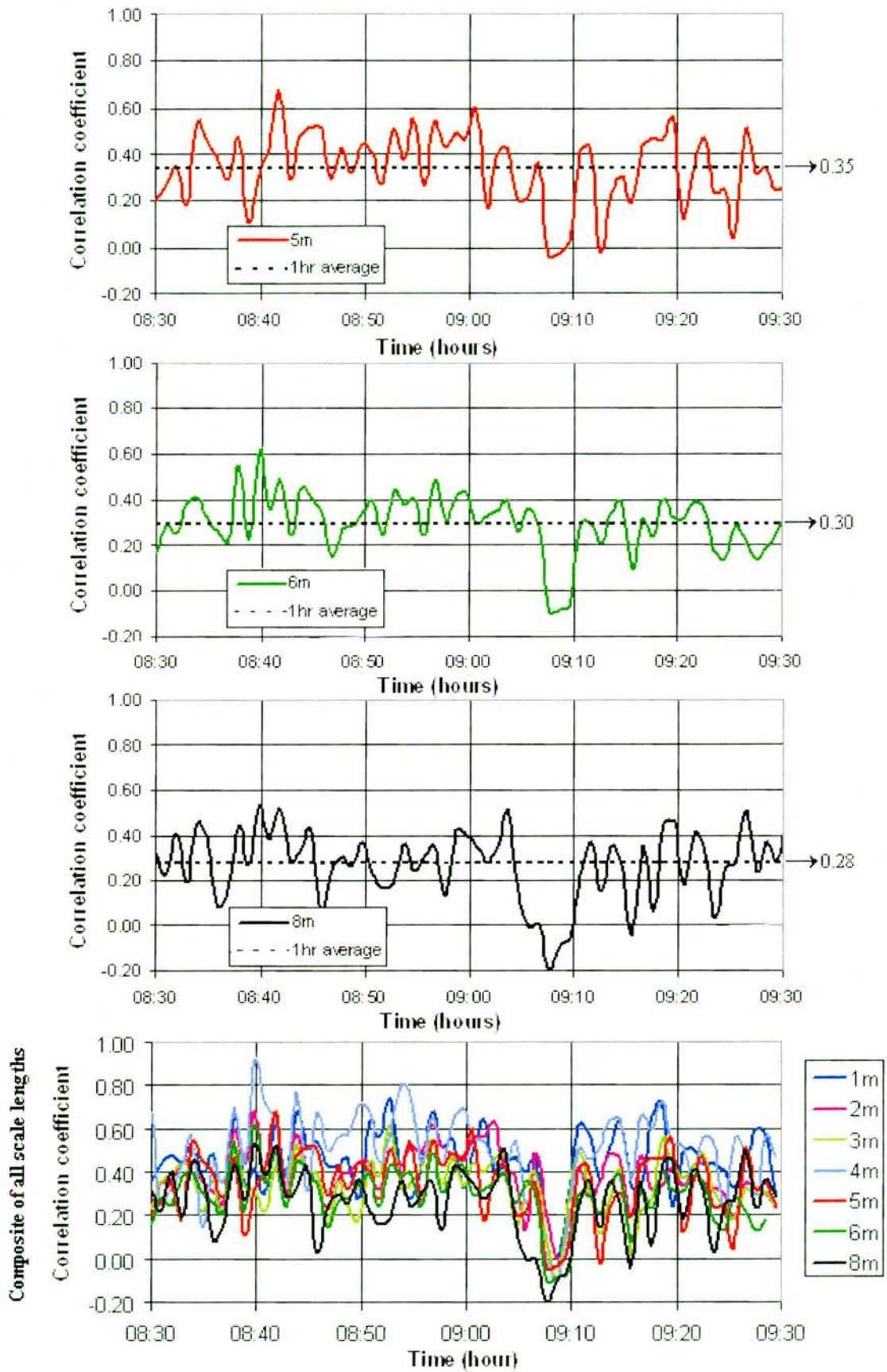
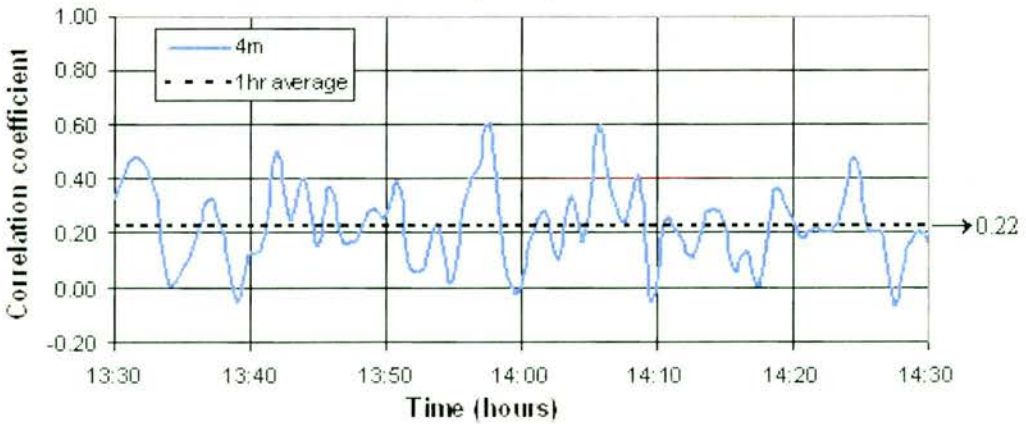
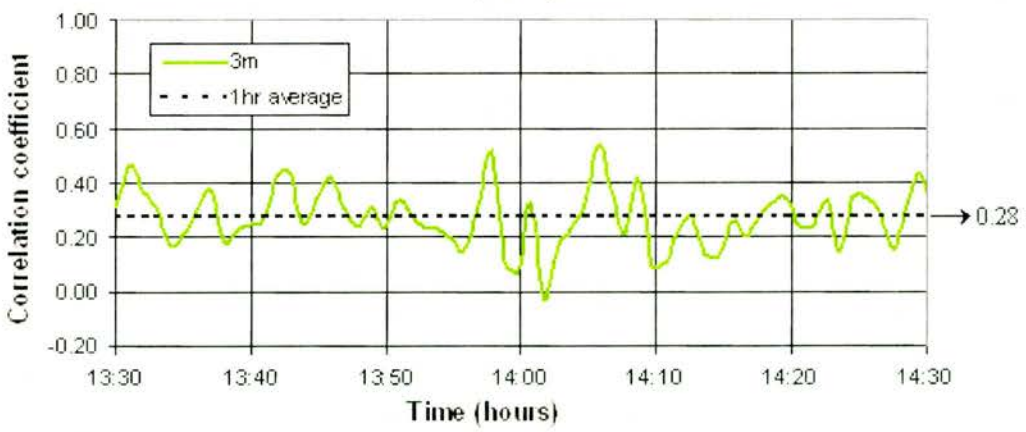
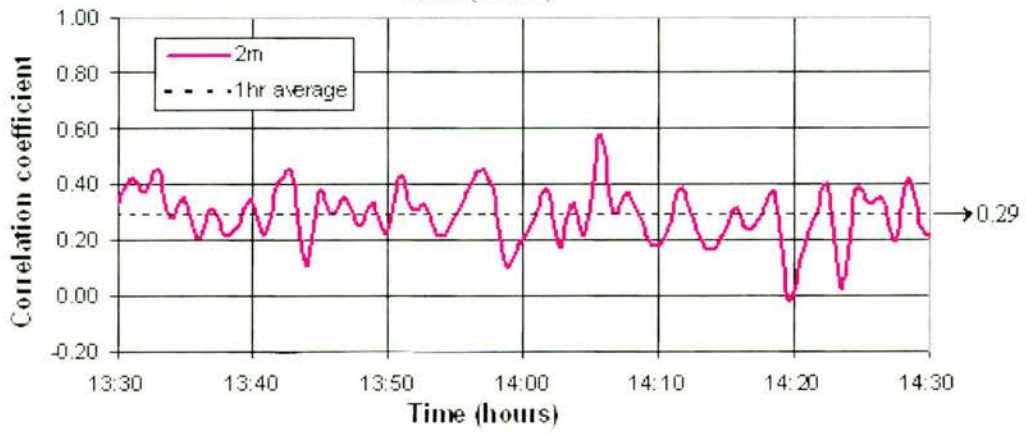
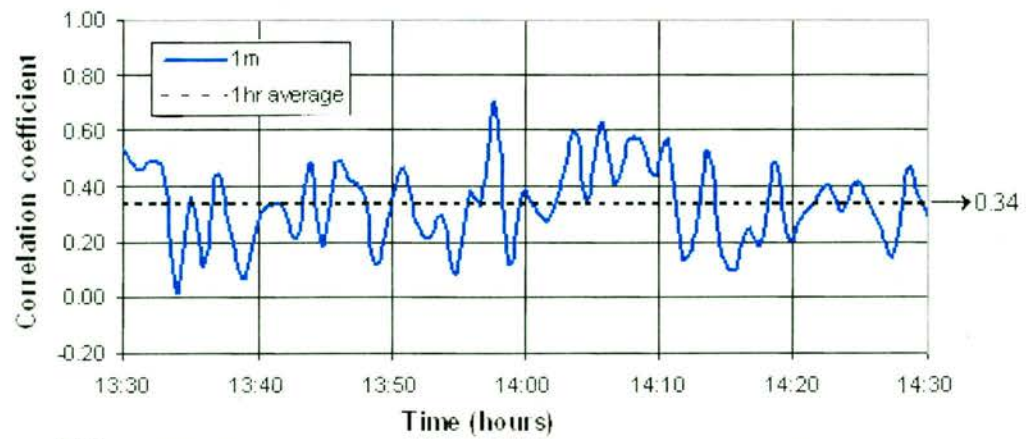


Figure 6-4 Spatial correlation of received signal strength fluctuations for each scale-length for the period 08:30 to 09:30 shown in Figure 6-3.



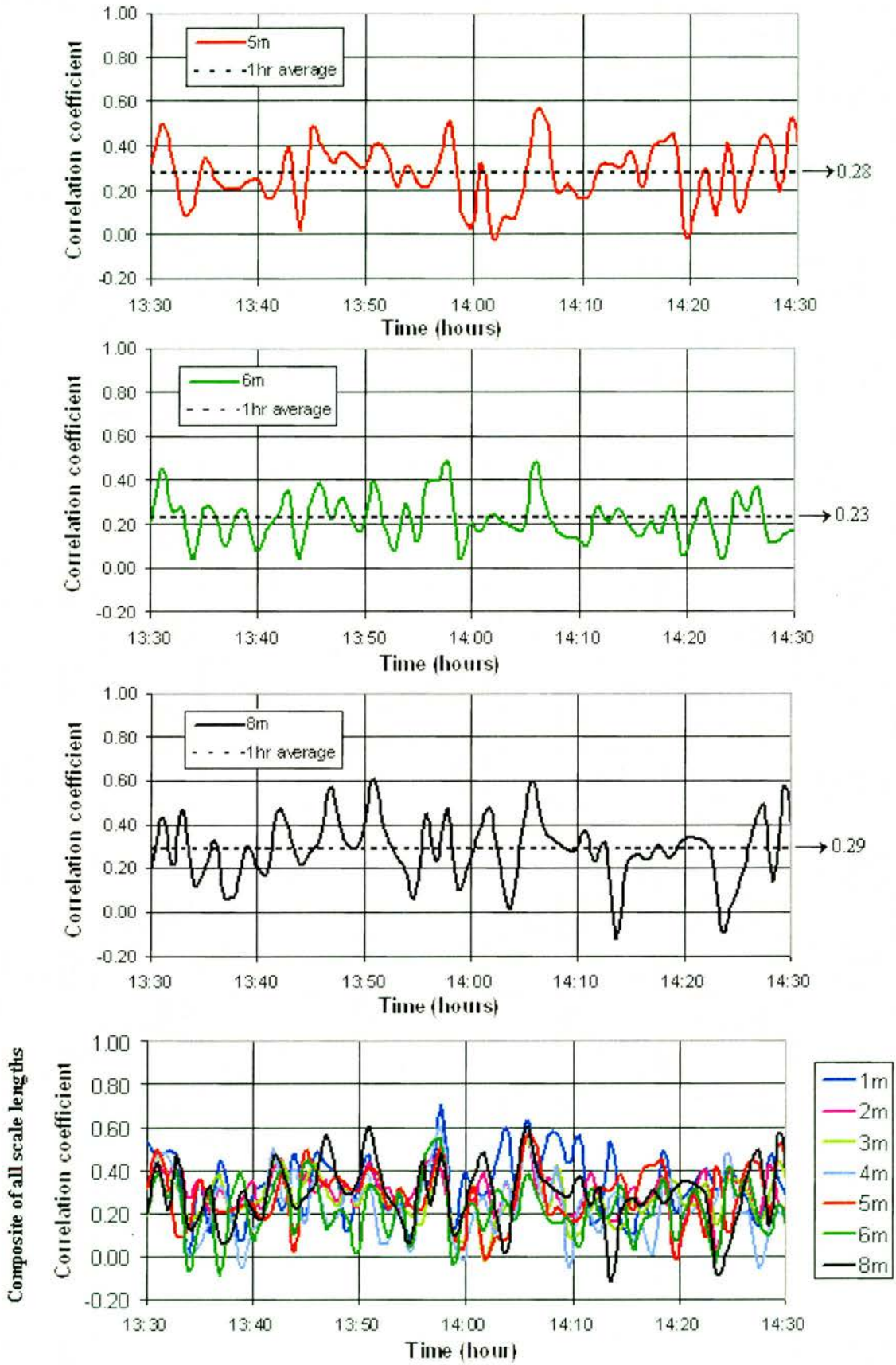


Figure 6-5 Spatial correlation of received signal strength fluctuations for each scale-length for the period 13:30 to 14:30 shown in Figure 6-3.

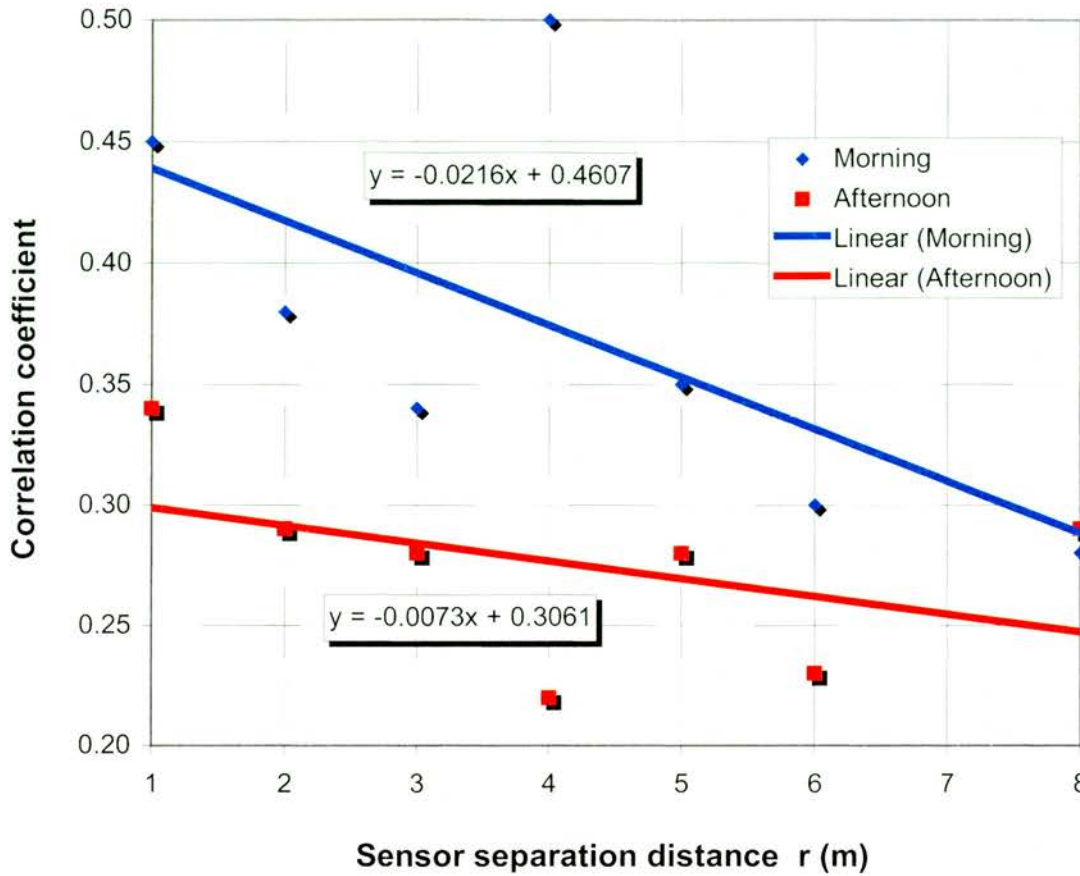


Figure 6-6 Spatial decorrelation of signal power fluctuations using the 1-hour average values in Figure 6-4 (morning) and Figure 6-5 (afternoon).

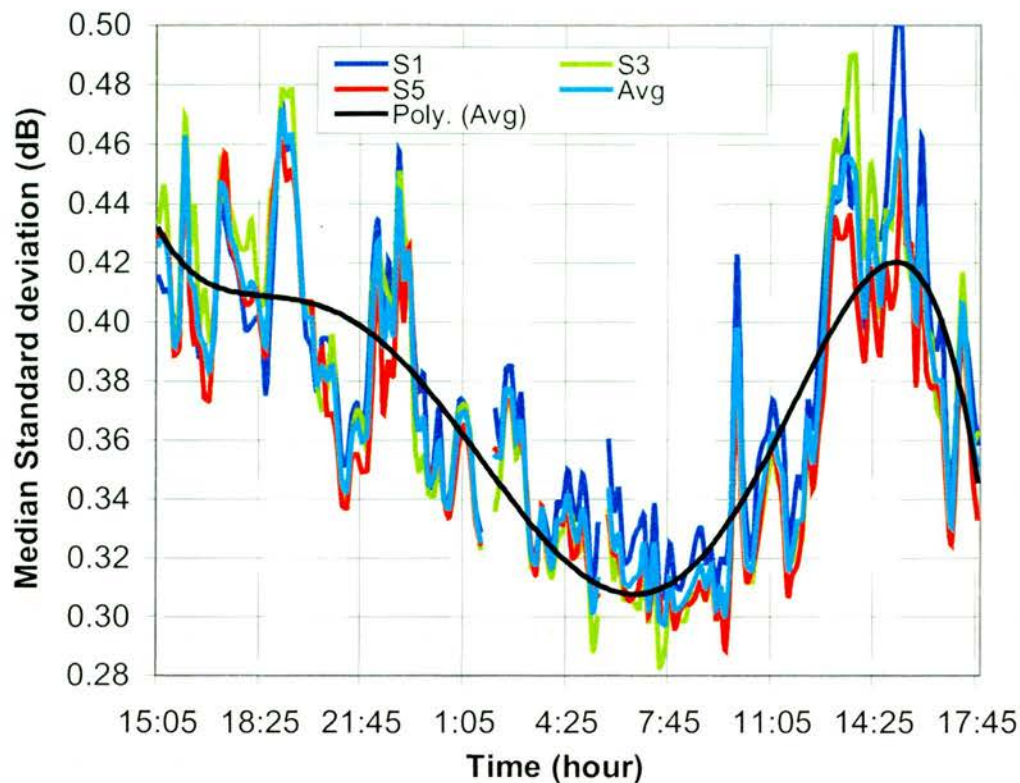
Figure 6-6 indicates the decorrelation of signal power fluctuations is different in the morning than in the afternoon. The two differences are:

- i. The gradient of spatial decorrelation is greater for the morning data than for the afternoon data. This indicates that larger eddies have a greater effect than smaller eddies in the morning than in the afternoon.
- ii. The average correlation coefficient at each scale-length is higher for the morning data than the afternoon data. This indicates that turbulent activity is more significant during the afternoon than during the morning, which corroborates the diurnal variability of signal fluctuation intensity described in Chapter five.

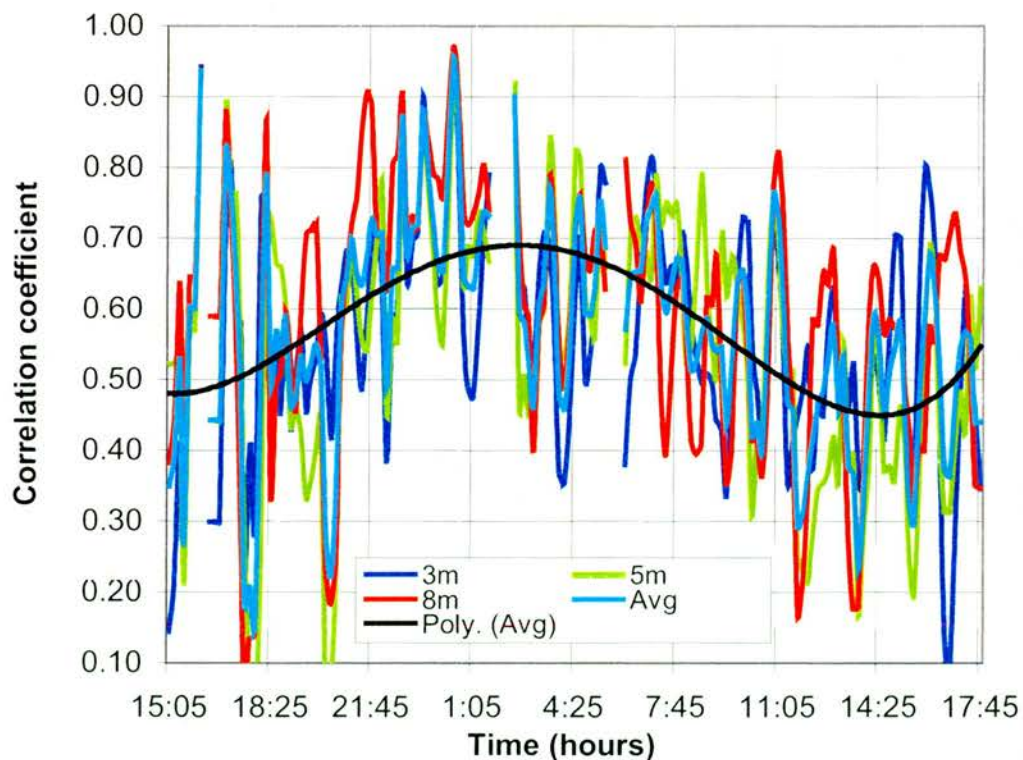
The correlation calculations shown above suggest that the spatial decorrelation of scintillation is a function of time of day. This would not seem unreasonable given turbulence intensity was shown in Chapter five to follow a diurnal cycle. To test this hypothesis the variability of spatial correlation was calculated and compared to the diurnal variation of signal power intensity. Figures 6-7, 6-8 and 6-9 show three examples where this comparison was performed. They confirm that spatial correlation follows a diurnal cycle that peaks during nocturnal hours, i.e. the inverse cycle of signal power fluctuation intensity. Hence, spatial correlation is at its lowest during the most turbulent part of the day and at its highest during the least turbulent part of the day.

The amplitude scintillation events in Chapter five showed that event durations are typically a few minutes. To capture the spatial correlation of individual events it is necessary to calculate the correlation coefficient over shorter periods than the 10 minutes used in the diurnal variation analysis. The method used by Lee and Waterman (1968) for this purpose was to calculate the cross-correlation of received signal strength (mean removed) every 3 minutes. The same processing method will be used in the following analysis.

Figure 6-10 shows the cross-correlation coefficient calculated every 3 minutes for the same data as shown in Figure 6-3. It shows that a linear regression trend line fitted to the median correlation coefficient decreases with increasing spatial separation. The gradient of spatial decorrelation is approximately  $-1/24\text{m}^{-1}$ .

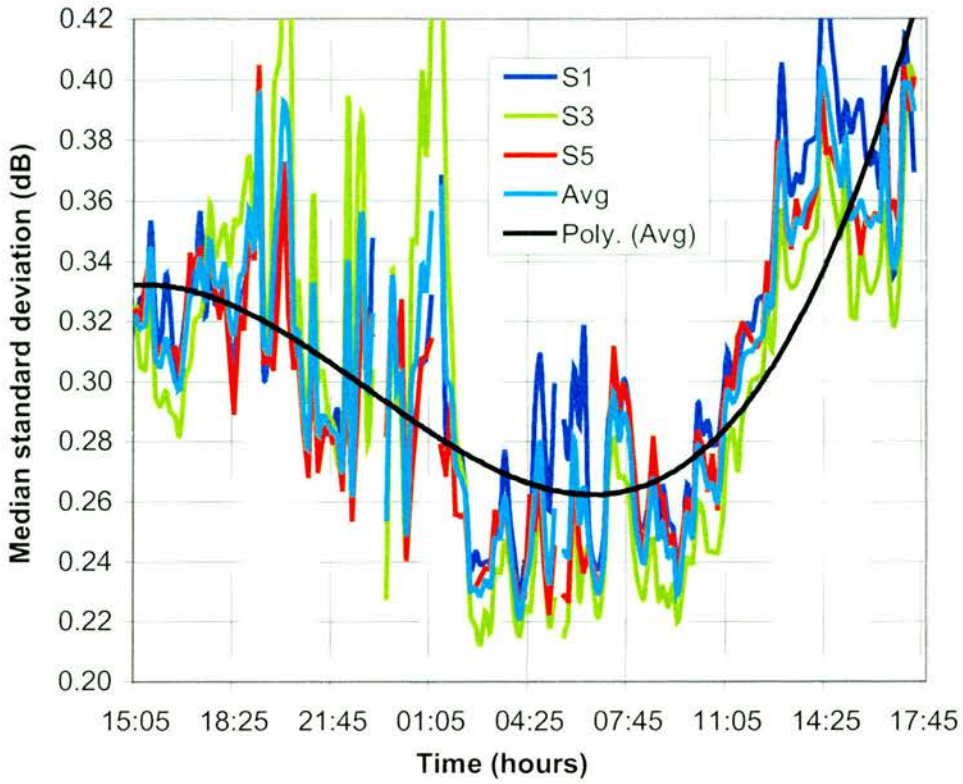


(A)

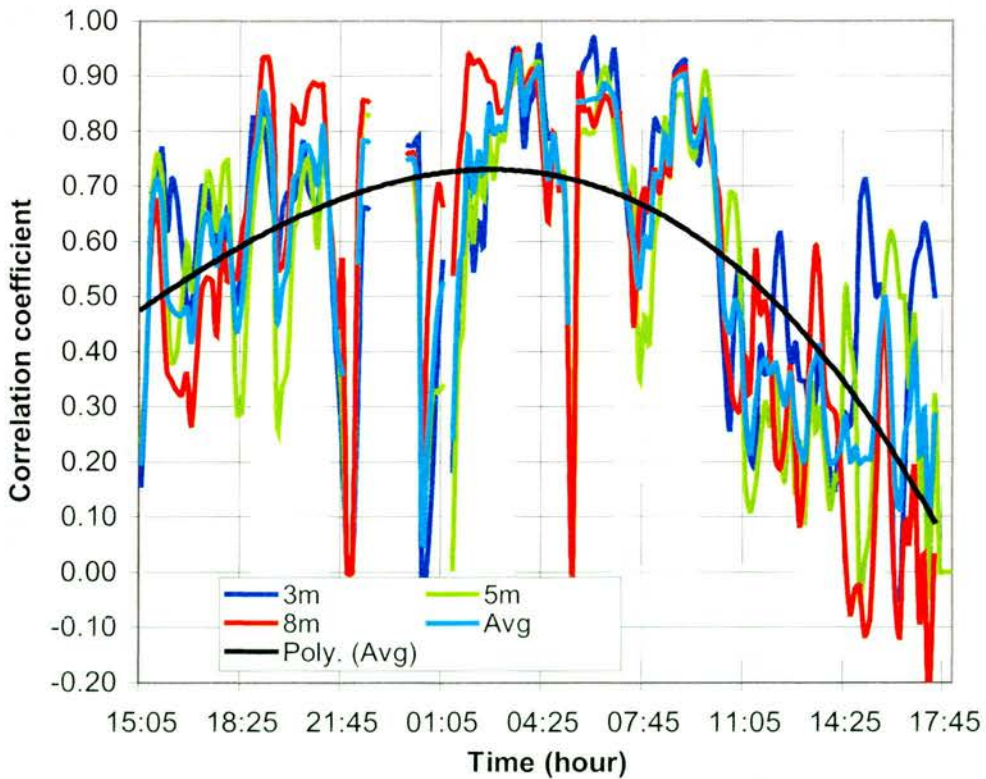


(B)

Figure 6-7 Example 1 - Diurnal variation of received signal strength fluctuations for spaced sensors S1, S3 and S5. (A) 10 minute median of standard deviations calculated every 1 minute. (B) Correlation coefficient calculated from 10 minute periods of 1 minute standard deviations for sensor separations of 3, 5 and 8m.

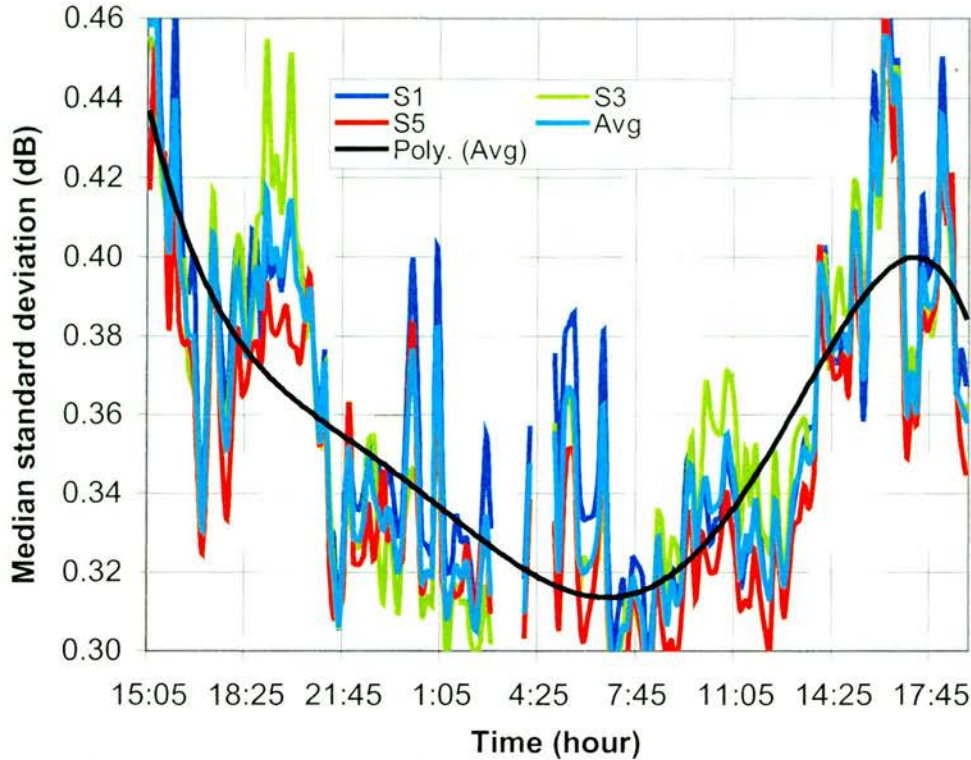


(A)

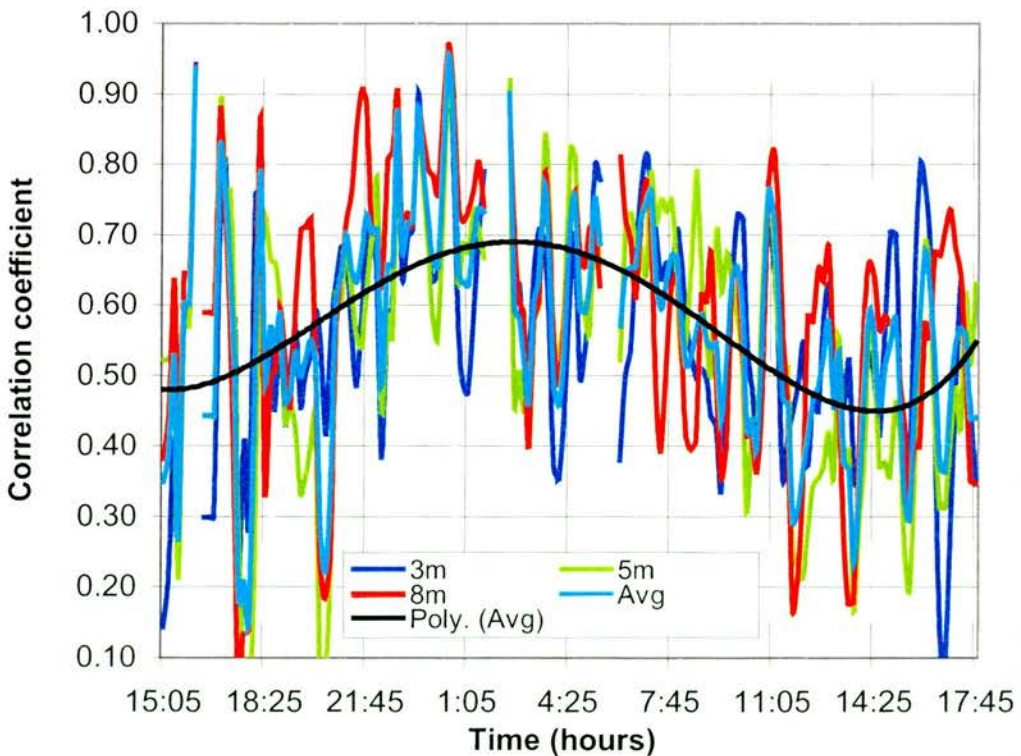


(B)

Figure 6-8 Example 2 - Diurnal variation of received signal strength fluctuations for spaced sensors S1, S3 and S5. (A) 10 minute median of standard deviations calculated every 1 minute. (B) Correlation coefficient calculated from 10 minute periods of 1 minute standard deviations for sensor separations of 3, 5 and 8m.



(A)



(B)

Figure 6-9 Example 3 - Diurnal variation of received signal strength fluctuations for spaced sensors S1, S3 and S5. (A) 10 minute median of standard deviations calculated every 1 minute. (B) Correlation coefficient calculated from 10 minute periods of 1 minute standard deviations for sensor separations of 3, 5 and 8m.

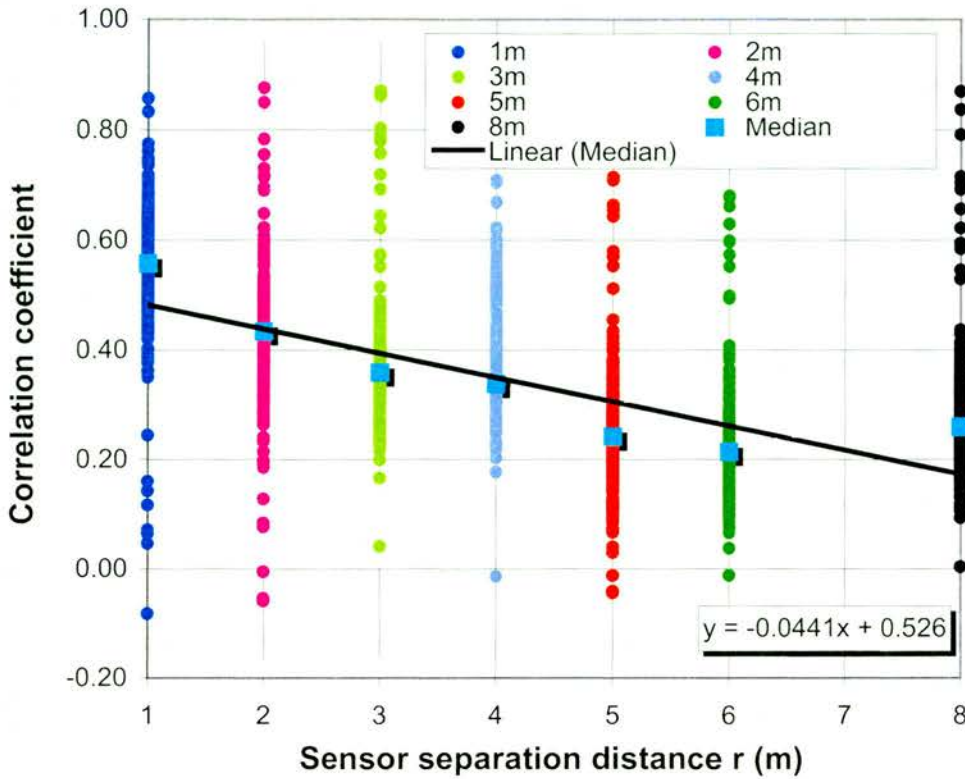
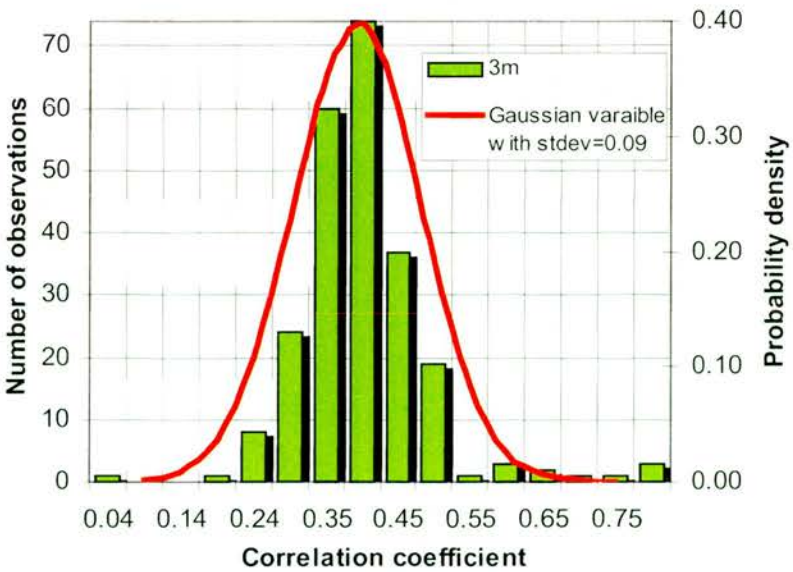
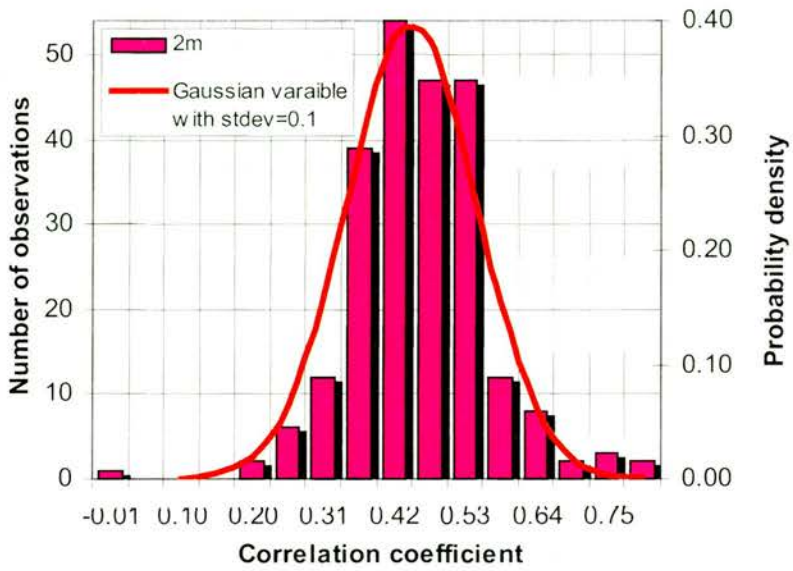
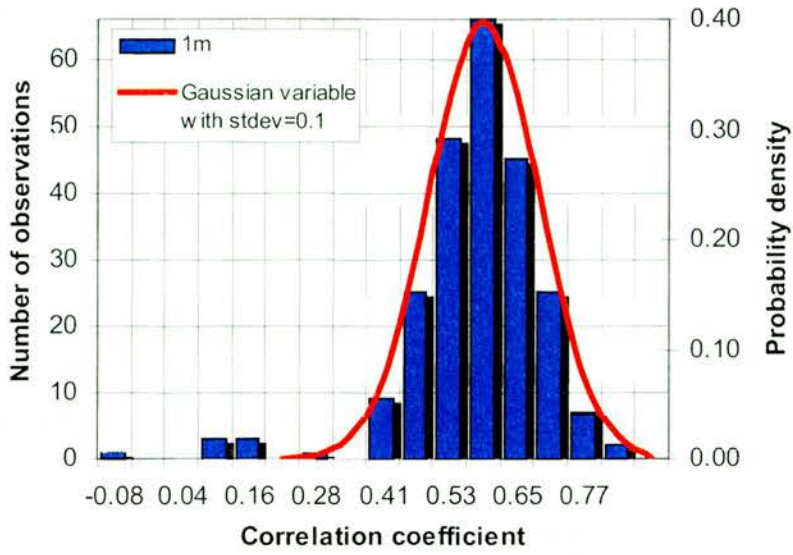
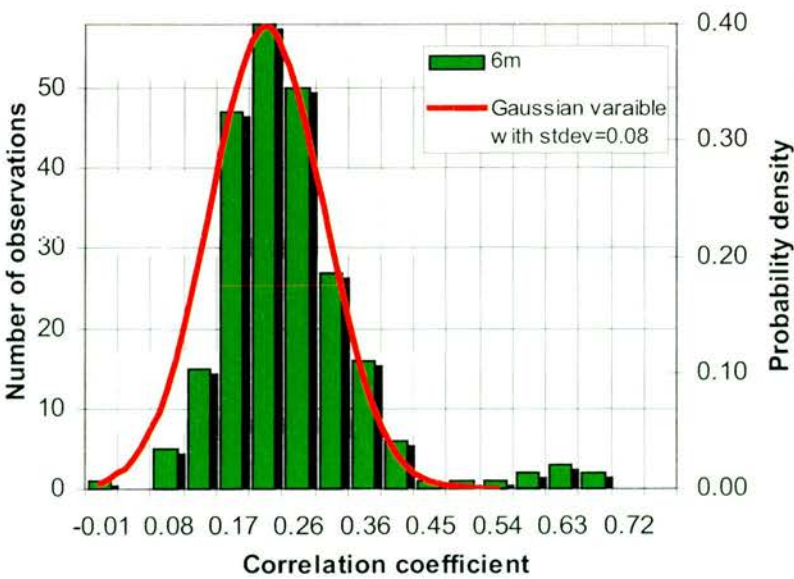
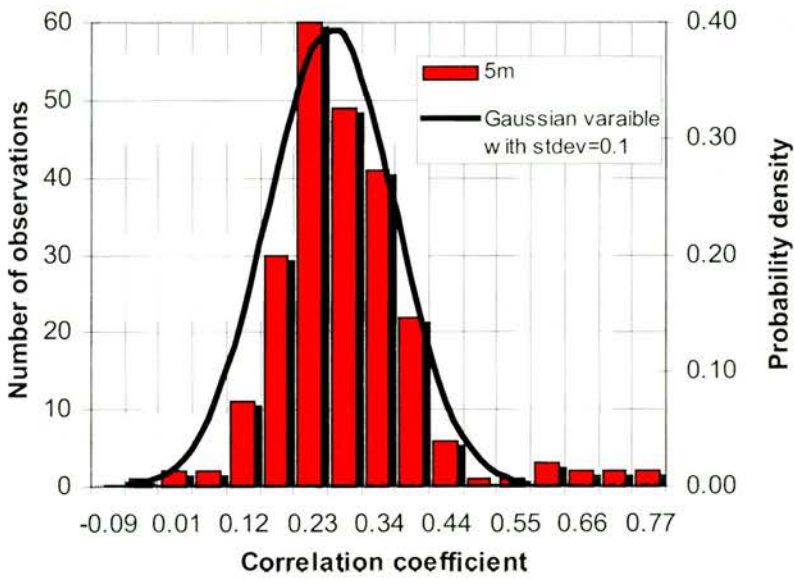
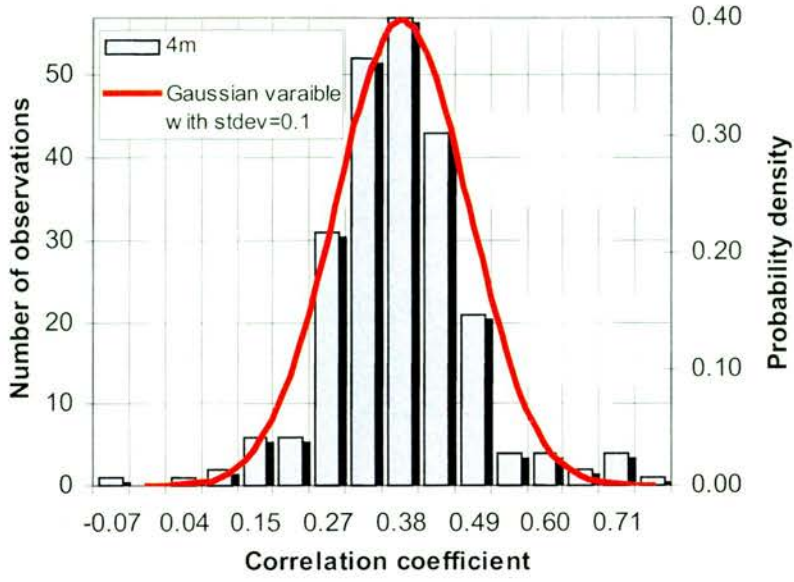


Figure 6-10 Spatial cross-correlation coefficient calculated every 3 minutes for the 12 hour period of data shown in Figure 6-3.

The dispersion of correlation coefficients at each of the scale lengths in Figure 6-10 was also evaluated. Figure 6-11 illustrates the dispersion of coefficients as a histogram for each scale-length. Three note worthy features of the histograms are:

- i. The histograms clearly show decreasing mean correlation as a function of increasing scale-length.
- ii. The dispersions are all in good agreement with a Gaussian distribution. This indicates that spatial correlation of atmospheric turbulence-induced fluctuations result in a random correlation scale-length with a central mean.
- iii. The dispersion of correlation coefficients at each scale-length is approximately the same, with a standard deviation of 0.1.





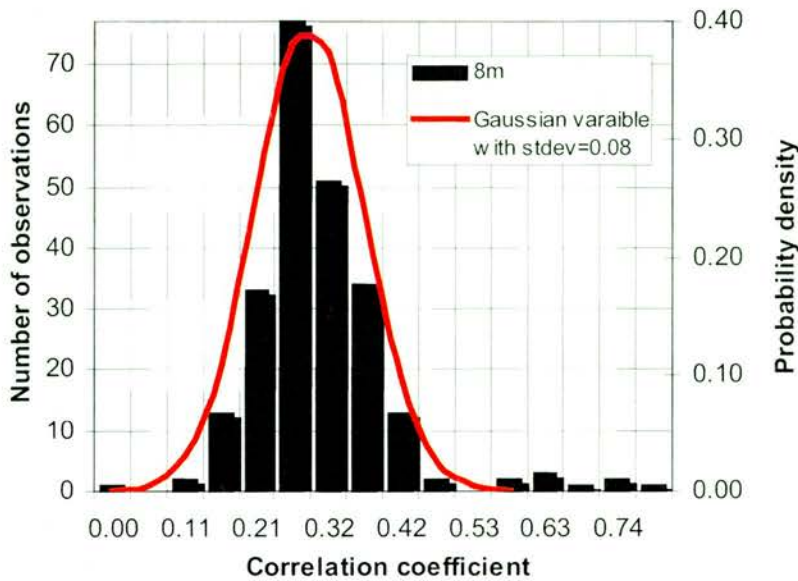


Figure 6-11 Correlation coefficient dispersions at each scale-length for the data shown in Figure 6-10.

The decorrelation of scintillation shown in Figure 6-10 was calculated from data collected over a 12-hour period. It shows that while the instantaneous correlation coefficient at each scale-length varies with time the process is stationary with a relatively small dispersion of observations. The mean value of correlation is therefore a reasonable estimate of the spatial decorrelation of tropospheric scintillation.

It is also of interest to consider changes in spatial correlation over periods of several days. Figure 6-12 shows such an analysis for 18 days of data, which is expressed as daily medians of 3 minutely calculated values of cross-correlation coefficients. The graph shows that a linear regression trend line fitted to the median correlation coefficient decreases with increasing spatial separation in a manner similar to that shown in Figure 6-10. The gradient of the trend line is also in good agreement, i.e. approximately  $-1/27 \text{ m}^{-1}$ .

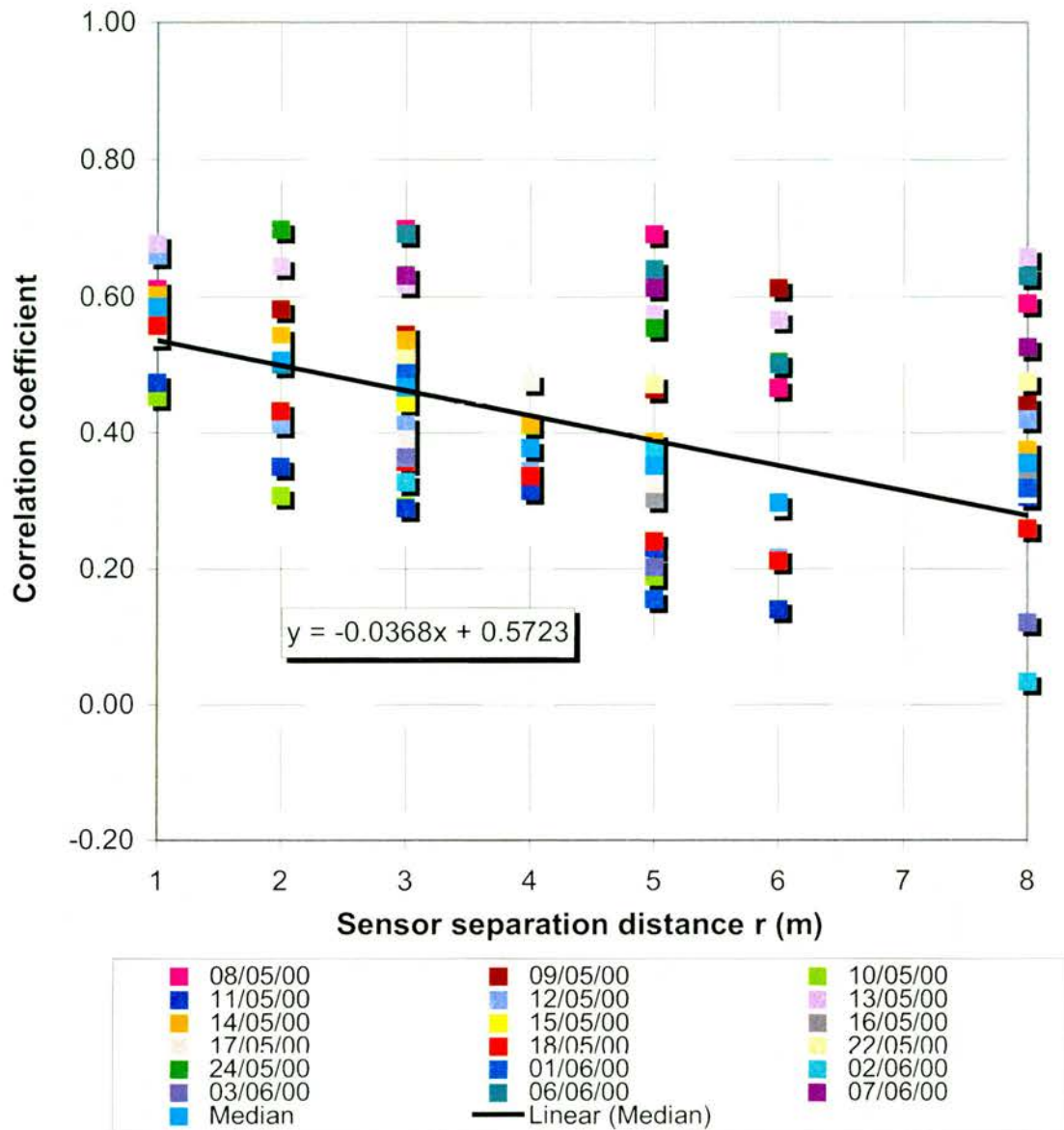


Figure 6-12 Daily median of 3 minutely calculated values of spatial cross-correlation coefficient for 18 days of data.

The linear trend line calculated from measured data shown in Figure 6-12 is compared to Tatarski's theoretical correlation function in Figure 6-13. It shows that the measured decorrelation gradient is less than that predicted by Tatarski by a factor of four. This may signify that for the data collected in this study eddies could be on average larger than the size of the first Fresnel ( $\sqrt{\lambda L}$ ). It could also indicate that instead of an eddy being advected past the sensor array a number of eddies are

simultaneously being convected past the sensor elements. Hence scintillation occurs at each element in the array but not necessarily from the same eddy.

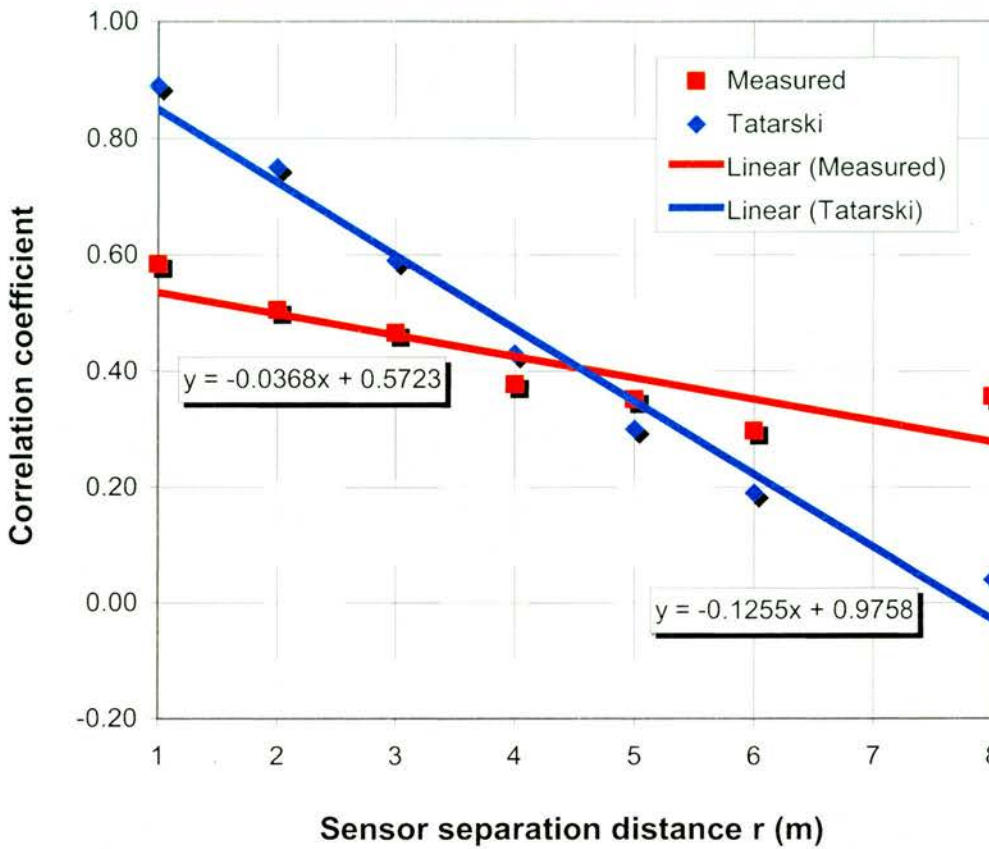


Figure 6-13 Comparison between measured correlation function and Tatarski's (1961) predicted correlation function.

#### 6.4 Implication of measured decorrelation scale-length

The decorrelation scale-length of scintillation has two important implications for communication / sensing systems. The first is that it defines the spatial diversity required to mitigate scintillation fading, and the second is that it defines the maximum size (gain) that an antenna array can be to coherently combine signals. Both of these parameters are characterised by the spatial separation distance at which the correlation coefficient equals zero. This is illustrated in Figure 6-14.

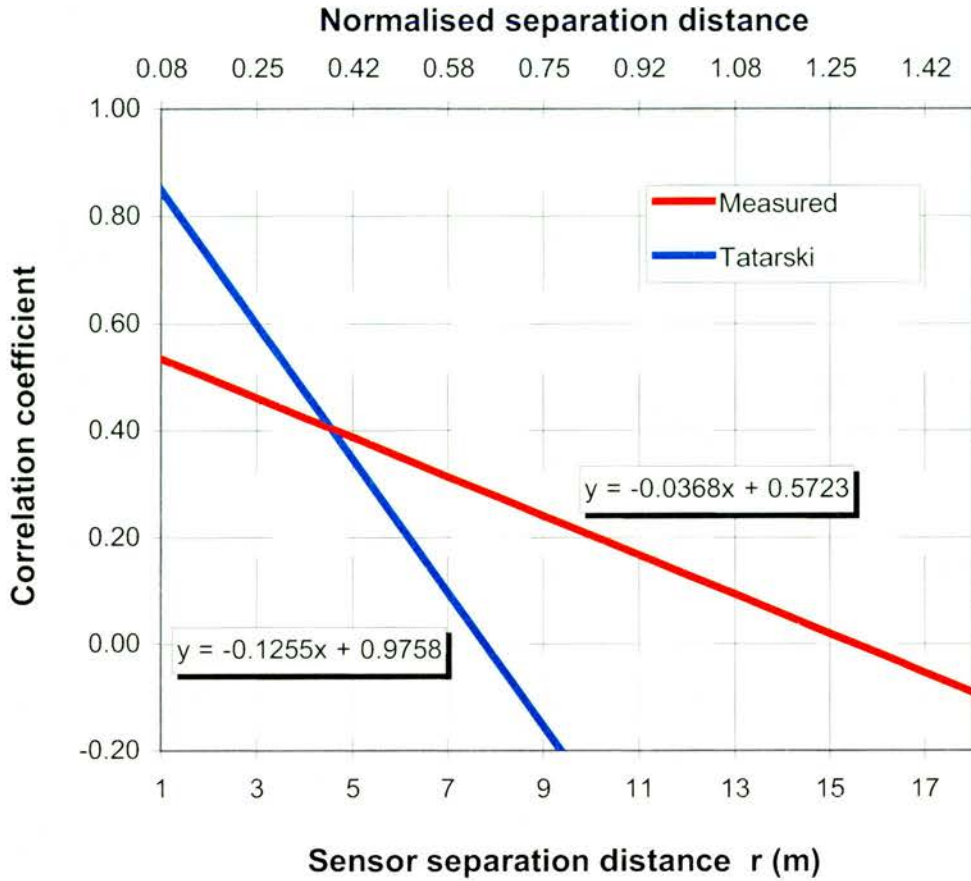


Figure 6-14 Forward projection of cross-correlation coefficients using the linear equation calculated from measured data and Tatarski's model. Normalised separation distance is given by  $r / \sqrt{\lambda L}$ .

Figure 6-14 shows the zero crossing point given by Tatarski's theory occurs at  $\sim 7.8\text{m}$  or 0.65 normalised units, where as the measured crossing point occurs at  $\sim 15.5\text{m}$  or 1.3 normalised units. Hence based on measured data, the antenna separation distance ( $r_d$ ) required to mitigate tropospheric scintillation by spatial diversity is:

$$r_d = 1.3\sqrt{\lambda L} \quad (6-5)$$

The decorrelation distance given in equation (6-5) is also used to calculate the maximum gain ( $G_{max}$ ) of a coherent millimetre wave antenna array. It defines the maximum number of antenna elements ( $E_{max}$ ), which is given by:

$$E_{\max} = \left( \frac{1.3\sqrt{\lambda L}}{A_e} \right)^2 \quad (6-6)$$

where  $A_e$  ( $\text{m}^2$ ) is the effective area of each antenna element in a square array.

The gain of a single antenna element ( $G_E$ ) in the array is given by (Colin, 1985):

$$G_E = 10 \log_{10} \left( \frac{4\pi A_e}{\lambda^2} \right) \quad \text{dB} \quad (6-7)$$

The gain of an array of antenna elements is therefore given by combining equations (6-6) and (6-7):

$$\begin{aligned} G_{\max} &= 10 \log_{10} \left( \frac{4\pi A_e E_{\max}}{\lambda^2} \right) \quad \text{dB} \quad (6-8) \\ &= 10 \log_{10} \left( \frac{6.76\pi L}{A_e \lambda} \right) \quad \text{dB} \end{aligned}$$

Equation (6-8) shows the maximum gain of a millimetre wave coherent antenna array is a function of signal wavelength, turbulent path length and antenna size. For example, with a turbulent path length of 17.3km, wavelength of 8.33mm (36GHz) and antenna element area of  $0.1\text{m}^2$ , the maximum gain is 86.5dB.

The above calculations have important implications for the design of single antenna links that are required to mitigate scintillation by spatial diversity, and future array based applications that assume coherent wavefronts to beam form. This subject is considered further in the next chapter.

## 6.5 Summary

This chapter has described an analysis of the spatial characteristics of tropospheric scintillation based on measured data from a five-element array. It was shown that the spatial correlation of atmospheric turbulence follows a diurnal cycle that is inversely related to air temperature. The cross-correlation coefficient variability with time was evaluated and found to be in good agreement with a Gaussian distribution of standard deviation 0.1, which is centred on a mean correlation value that depends on antenna separation distance.

The correlation between spaced receivers was considered for 18 days of data. The median cross-correlation coefficient at seven points in the range 1-8m showed correlation decreased for increasing antenna separation at a rate of  $\sim -1/27\text{m}^{-1}$ . This is a slower decrease than proposed by Tatarski's correlation function, which suggests the decorrelation of scintillation in the horizontal direction is approximately 2 times larger than predicted, i.e.  $2\sqrt{\lambda L}$ . A possible reason for this could be that eddies producing scintillation in the data analysed are on average larger than  $\sqrt{\lambda L}$ . Alternatively, it could mean that instead of an eddy being advected past the sensor array a number of eddies are simultaneously being convected past the sensor elements. Hence scintillation occurs at each element in the array but not necessarily as a result of the same eddy. To confirm this hypothesis requires a vertical array of elements. Such an array has been designed and built for a future measurement campaign (see Chapter eight).

The measured scintillation decorrelation distance described in this chapter specified the horizontal separation distance required between antennas to mitigate scintillation

in a spatial diversity system. It also defined the maximum gain of a coherent millimetre wave antenna array, which was shown to be a function of signal wavelength and turbulent path length in addition to the physical size of the array.

In addition to the spatial variation of amplitude fluctuations that result from atmospheric turbulence there is also phase variability. This is considered in the next chapter.

# Chapter Seven

## Wavefront Distortion

### 7.1 Introduction

Wavefront distortion is a turbulence-induced impairment to antenna array systems that conventionally rely on planar wavefronts for angle-of-arrival estimation and coherent beam forming. In this chapter, the effect of atmospheric turbulence-induced wavefront distortion is evaluated in terms of phase errors, angle-of-arrival variations and tracking errors for mobile platforms. The approach taken is to use temporal amplitude scintillation data from the sensor array to evaluate spatial phase differences through the use of structure functions.

### 7.2 Structure functions

In Chapter two a brief description of the Kolmogorov spectrum of turbulence was presented. In developing the model for well-developed turbulence Kolmogorov used structure functions for analysing velocity fluctuations. Such functions are used in situations where average quantities are neither stationary nor homogeneous. Structure functions are applied extensively in meteorology (Stull, 1998) for studying the variability of wind, temperature, pressure etc. They describe inhomogeneous functions  $f(r)$  in terms of positional differences ( $r$ ):

$$f(r) = |f(r_0) - f(r_1)| \quad (7-1)$$

where  $f(r_0)$  and  $f(r_1)$  are spatial functions separated by a distance  $r$ .

For positional differences limited by appropriate boundary conditions slow changes in spatial functions do not affect the value of the difference (they are correlated). So although temporal functions are non-stationary, the spatial difference is considered loosely stationary. Using this hypothesis, Kolmogorov defined the structure function of velocity ( $v$ ) fluctuations:

$$D_v(r) = \overline{[v(r_0) - v(r_1)]^2} \quad \text{m}^2/\text{s}^2 \quad (7-2)$$

The structure function of velocity fluctuations is considered locally homogeneous and isotropic. This is illustrated in Figure 7-1. It shows that in a medium that satisfies Kolmogorov's spectrum, fluctuations in any direction are equal (isotropic) and at any point are equal (homogeneous).

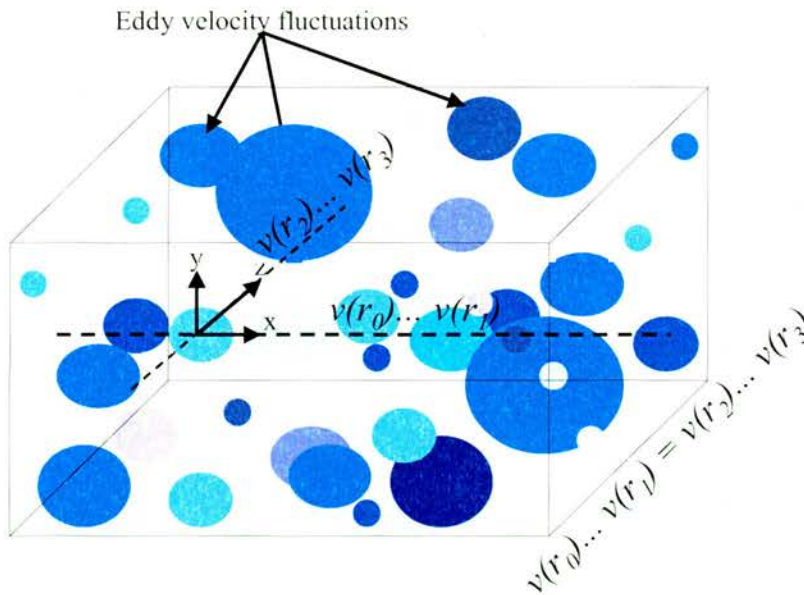


Figure 7-1 A 3D volume illustrating a medium that is isotropic (direction independent) and homogeneous (location independent).

From structure function analysis Kolmogorov developed the two-thirds law. This law approximates the intensity of turbulent fluctuations as a function of positional difference, with boundary conditions specified in terms of the inner and outer scales of turbulence  $l_0$  and  $L_0$  respectively:

$$D_v(r) \propto \begin{cases} r^{2/3} & \text{for } l_0 \ll r \ll L_0 \\ r^2 & \text{for } r \ll l_0 \end{cases} \quad (7-3)$$

The two-thirds law has far reaching implications for studying wave propagation in a turbulent medium. This is because velocity fluctuations are directly related to refractive index fluctuations. The structure function of refractive index ( $n$ ) variations is given by:

$$D_n(r) = \langle |n(r_1 + r) - n(r_1)|^2 \rangle \quad (7-4)$$

Tatarski (1961) employed the two-thirds law to formulate the structure function of refractive index fluctuations:

$$D_n(r) = \begin{cases} C_n^2 r^{2/3} & \text{for } l_0 \ll r \ll L_0 \\ C_n^2 l_0^{2/3} \left(\frac{r}{l_0}\right)^2 & \text{for } r \ll l_0 \end{cases} \quad (7-5)$$

where  $C_n^2$  is the structure function parameter of refractive index fluctuations given by:

$$C_n^2 = 1.91 \overline{(\Delta n)^2} L_0^{-2/3} \quad \text{m}^{-2/3} \quad (7-6)$$

where  $\overline{(\Delta n)^2}$  is the mean square of refractive index fluctuations which is of the order of  $10^{-12}$ . If the turbulent path is inhomogeneous, the value of  $C_n^2$  is obtained by integrating along the path.

From the structure function of refractive index fluctuations Tatarski derived a model for phase fluctuations. In a similar way to the velocity structure function the phase structure function is a measure of spatial phase differences, which may be used to investigate wavefront distortion. The phase structure function is given by:

$$D_{\phi}(r) = \begin{cases} 1.72 C_n^2 l_0^{-1/3} k^2 L r^2 & \text{for } r \ll l_0 \\ 1.46 C_n^2 k^2 L r^{5/3} & \text{for } l_0 \ll r \ll \sqrt{\lambda L} \\ 2.91 C_n^2 k^2 L r^{5/3} & \text{for } r \gg \sqrt{\lambda L} \end{cases} \quad \text{rad}^2 \quad (7-7)$$

where  $L$  is the turbulent path length and  $k = 2\pi / \lambda$ .

It is evident from the phase structure function in equation (7-7) that if  $C_n^2$  is known and the correct boundary conditions are applied the phase difference across a wavefront can be predicted. Methods to obtain  $C_n^2$  are presented in the next section.

### 7.2.1 The refractive index structure function parameter

There are two types of refractive index structure function parameter. The first is the optical form that is used by astronomers (Tyson, 1991) and has been widely investigated and modelled (Hufnagel, 1974). The second is the radio form that has mostly been studied at microwave frequencies for applications in radar (Brown, 1977). It is measured by one of three ways:

- i. The first method uses refractometer measurements and fast response meteorological instruments (to measure  $L_0$ ) to implement the model given in equation (7-6).
- ii. The second approach uses sensitive radars to relate backscatter (which is defined as the radar backscattering cross section per unit volume) from eddies to  $C_n^2$  by the following equation (Brown, 1977):

$$C_n^2 = 2.65 \eta \lambda^{1/3} \quad \text{for } l_0 \ll 0.5\lambda \ll L_0 \quad \text{cm}^{-2/3} \quad (7-8)$$

where  $\eta$  ( $\text{m}^2/\text{m}^3$ ) is radar reflectivity.

iii. The third method uses radio links to measure signal variance, which is related to  $C_n^2$  by Tatarski's log-amplitude function ( $\sigma_\chi^2$ ). This function was introduced in Chapter five, and for convenience is repeated below:

$$\sigma_\chi^2 = \begin{cases} 185.58 l_0^{-7/3} C_n^2 L^3 & \sqrt{\lambda L} \ll l_0 \\ 23.39 C_n^2 k^{7/6} L^{11/6} & l_0 \ll \sqrt{\lambda L} \ll L_0 \\ 75.44 (\overline{\Delta n})^2 k^2 L L_n & L_0 \ll \sqrt{\lambda L} \end{cases} \quad \text{dB}^2 \quad (7-9)$$

where,  $L_n$  (m) is the integral scale of turbulence which is the same order of magnitude as  $L_0$ .

Measurements of  $C_n^2$  using refractometers found values range from  $10^{-13}$ - $10^{-17} \text{m}^{-2/3}$  for altitudes up to of 29,000ft (Thompson et al, 1980). The larger values relate almost exclusively to altitudes below 10,000ft (the most turbulent part of the atmosphere).

Measurements of  $C_n^2$  at millimetre wave frequencies using log-amplitude variance data and refractometers have been performed at frequencies ranging from 35 to 220GHz. The most notable experiment (Ho et al, 1978) compared values obtained by a refractometer to log-amplitude variance data collected from a 4.1km, 50m-high link operating at 36GHz. The study found very good agreement between both methods of measurement, with typical refractometer values of  $0.32 \times 10^{-14} \text{m}^{-2/3}$  and log-amplitude scintillation variance values of  $0.25 \times 10^{-14} \text{m}^{-2/3}$ .

The frequency and path length dependency of  $C_n^2$  has also been investigated using log-amplitude variance data (Cole et al, 1978). Measurements at 36GHz and 110GHz on the 4.1km path described above confirmed a  $k^n$  dependency, where  $n$  is 7/6 or 2 depending on the size of  $L_0$  (see equation (7-9)). This relationship was further confirmed at frequencies ranging from 35 to 220GHz using path lengths of 152m and 610m (4m in height) (McMillan and Bohlander, 1987). The same measurement campaign also confirmed the length dependency  $L^{11/6}$  of log-amplitude variance.

The results from the above experiments confirm the validity of equation (7-9) for calculating  $C_n^2$  from log-amplitude variance measurements at millimetre wave frequencies. The same approach will be applied to the log-amplitude variance measurements presented in Chapter five so that  $C_n^2$  can be calculated for the experimental link. This will enable spatial phase differences to be predicted from temporal amplitude measurements.

### 7.3 Calculation of $C_n^2$ from measured values of $\sigma_\chi^2$

Equation (7-9) shows the value of  $C_n^2$  depends on three boundary conditions. The first condition,  $\sqrt{\lambda L} \ll l_0$ , is not normally applicable to millimetre wave propagation as path lengths are typically too long, i.e. upwards of several hundred metres. It is therefore considered that the inner scale of turbulence has a negligible impact on millimetre wave propagation (Strohbehn, 1968).

The second condition,  $L_0 \ll \sqrt{\lambda L}$ , is applicable to millimetre wave propagation. To establish the size of  $L_0$  so that the applicability of this boundary condition can be

determined requires fast response temperature or humidity spectra from the radio link location (Cole et al, 1978; Gjessing et al 1963). The alternative is to use the empirical method proposed by Fante (1980) that approximates the size of  $L_0$  as a function of the height ( $h$ ) of the radio link above the ground:

$$L_0 \approx \frac{h}{3} \quad (7-10)$$

This approximation method suggests that the size of  $L_0$  for the experimental link is ~30m. This is based on the ~90m height at the centre of the link. This suggests the boundary condition  $L_0 \ll \sqrt{\lambda L}$  is not applicable in this case given  $\sqrt{\lambda L} = 12\text{m}$ . Also, given the eddy size that resulted in a zero correlation coefficient in the spatial analysis in the previous chapter was  $1.3\sqrt{\lambda L} = 16\text{m}$ , it seems reasonable to assume that the  $L_0 \ll \sqrt{\lambda L}$  condition is not applicable to the measured data.

Based on the above, the third condition  $l_0 \ll \sqrt{\lambda L} \ll L_0$ , is considered to be applicable to the measured data. The value of  $C_n^2$  is therefore obtained from log-amplitude variance measurements by re-arranging equation (7-9) as follows:

$$C_n^2 = \frac{\sigma_\chi^2}{23.39 k^{7/6} L^{11/6}} \quad \text{for } l_0 \ll \sqrt{\lambda L} \ll L_0 \quad \text{m}^{-2/3} \quad (7-11)$$

Using equation (7-11) the value of  $C_n^2$  was calculated from the log-amplitude scintillation variance data presented in Chapter five. The results are shown in Figure 7-2.

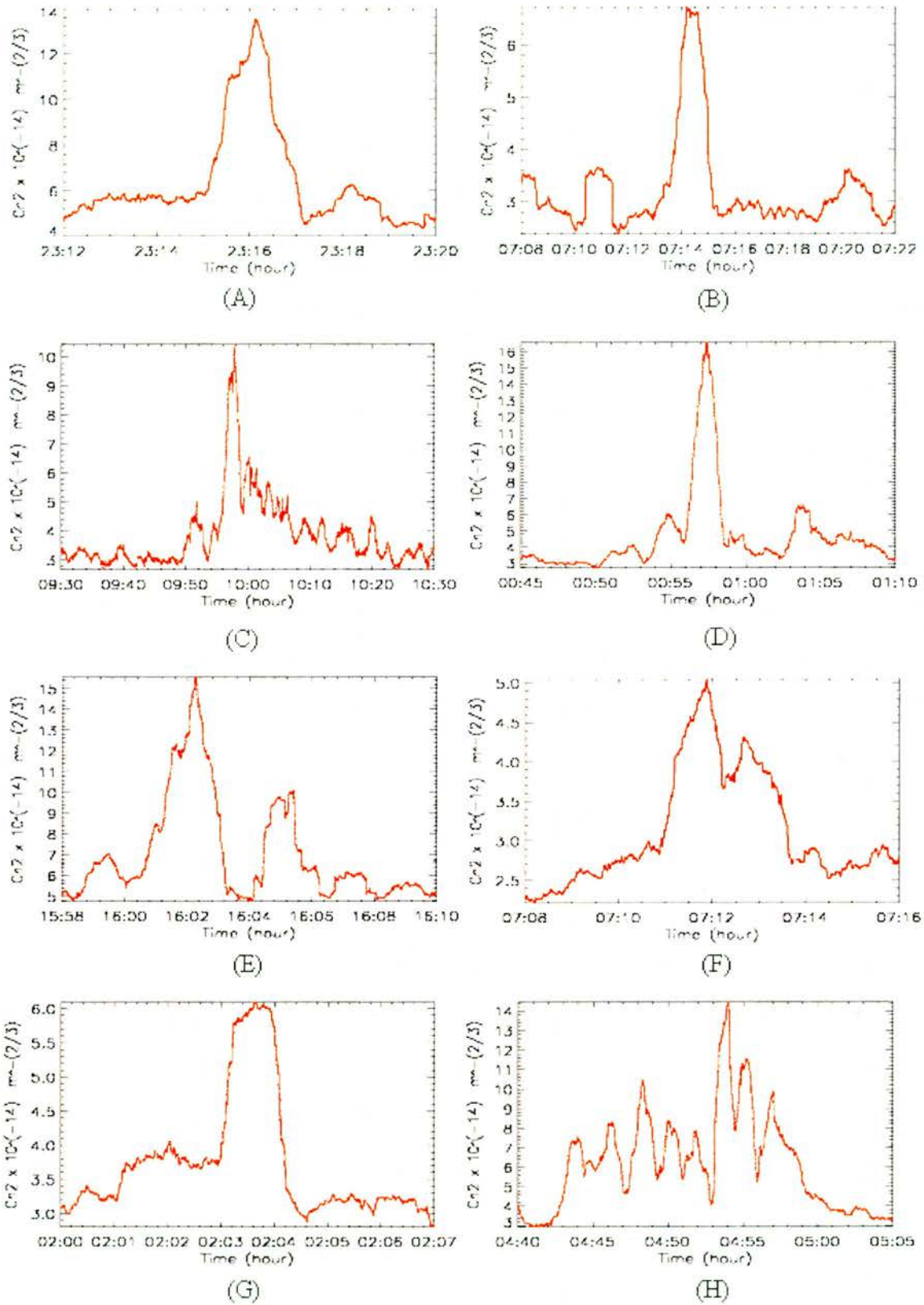


Figure 7-2 Calculated values of  $C_n^2$  from log-amplitude scintillation ( $\sigma_\chi^2$ ) measured data.

The calculated values of  $C_n^2$  in Figure 7-2 range between 3 and  $16.5 \times 10^{-14} \text{m}^{-2/3}$ . These are large compared to previously reported values (Ho et al) due to the much longer propagation path, e.g. 17.3km compared to 4.1km. The next section evaluates these higher values of  $C_n^2$  using equation (7-11).

### 7.3.1 Evaluation of $C_n^2$ calculated values

Equation (7-11) shows that the value of  $C_n^2$  is dependent on path length by the scaling factor  $L^{11/6}$ . It is therefore possible to scale values of  $C_n^2$  according to different path lengths. This enables measurements from previous experiments to be scaled and compared to the calculated values shown above.

The previous measurement data that will be used to evaluate the calculated  $C_n^2$  values above is from the Ho et al (1978) experiment. The experiment used a 4.1km link at a height of 50m and a beacon frequency of 36GHz. It confirmed the validity of calculating  $C_n^2$  from log-amplitude data using simultaneous refractometer measurements. It showed that the mean value of  $C_n^2$  obtained from log-amplitude scintillation variance data was  $0.25 \times 10^{-14} \text{m}^{-2/3}$ . This value will therefore be used as the basis for comparison with data from the 17.3km experimental link.

The mean value of  $C_n^2$  for the experimental link is shown in Figure 7-3. The mean value of  $3.2 \times 10^{-14} \text{m}^{-2/3}$  is typical of the daily mean value of  $C_n^2$  for the 17.3km path, which is evident from Figure 7-2 that shows values of  $\sim 3 \times 10^{-14} \text{m}^{-2/3}$  at times outside of the strong scintillation events.

The scaled value of the Ho et al data to a 17.3km path is shown in equation (7-12). It shows the predicted value of  $3.5 \times 10^{-14} \text{m}^{-2/3}$  is in good agreement with the measured mean of  $3.2 \times 10^{-14} \text{m}^{-2/3}$  from the experimental link.

$$C_n^2 = (0.25 \times 10^{-14}) \times \left( \frac{17.3}{4.1} \right)^{11/6} \quad (7-12)$$

$$= 3.5 \times 10^{-14} \text{ m}^{-2/3}$$

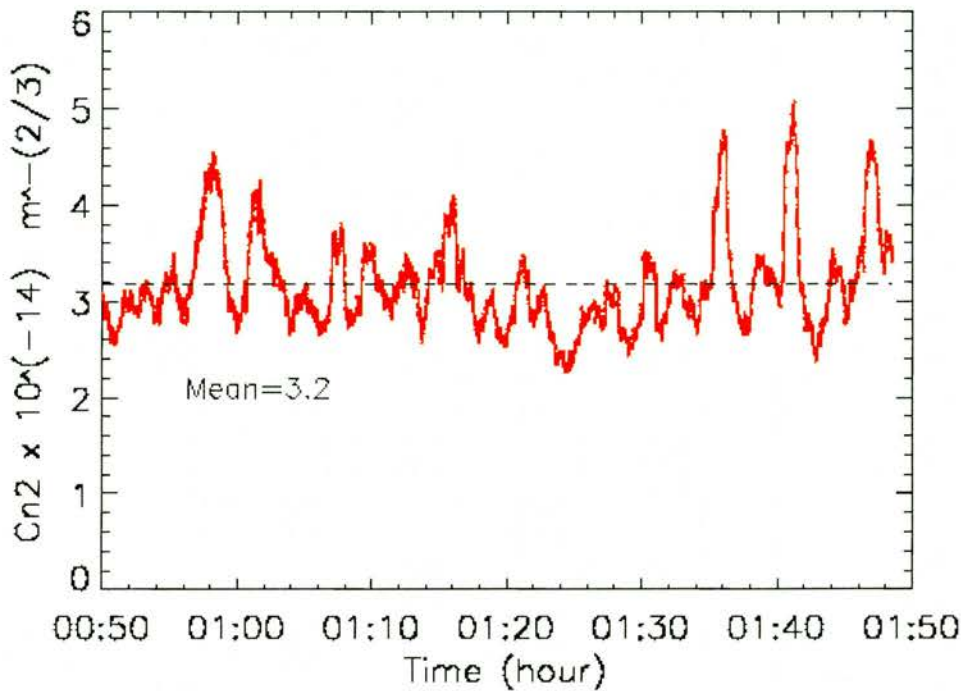


Figure 7-3 A typical 1-hour time series of  $C_n^2$  calculated from measured data. The mean value is  $3.2 \times 10^{-14} \text{m}^{-2/3}$ .

The scaling of the 4.1km Ho et al data to 17.3km lends plausibility to the measured data, and also corroborates the path dependency factor in Tatarski's model for millimetre wave frequencies. It is believed this dependency has in the past only been confirmed for relatively short path length differences, i.e. the McMillan and Bohlander (1987) experiment that compared data from path lengths of 152m and 610m.

The values of  $C_n^2$  shown in Figure 7-2 ( $3-17 \times 10^{-14} \text{m}^{-2/3}$ ) are in the following sections used to predict spatial fluctuations in refractive index, phase and angle-of-arrival.

### 7.4 Refractive index fluctuations

Figure 7-4 shows the predicted spatial fluctuations in refractive index using the structure function given in equation (7-5). It is expressed as refractivity  $((n-1) \times 10^6)$  for convenience, using  $C_n^2$  values in the range 3 to  $17 \times 10^{-14} \text{m}^{-2/3}$ .

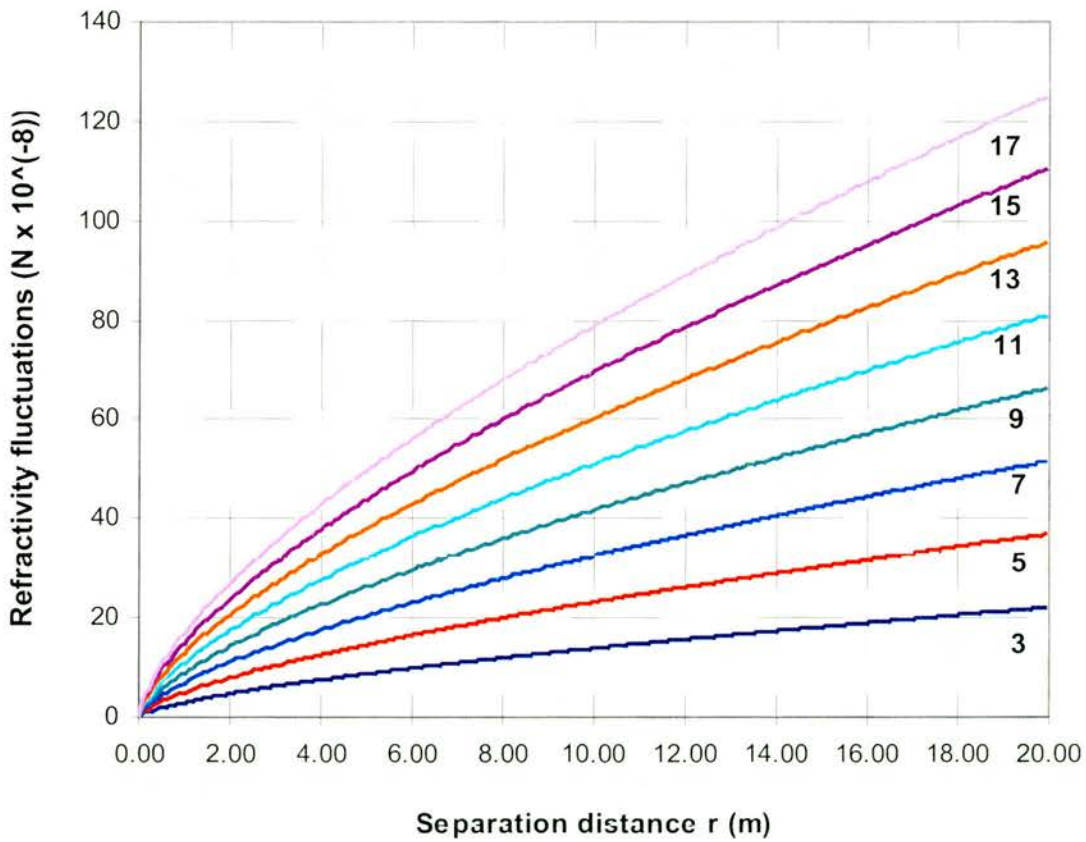


Figure 7-4 Predicted fluctuations in refractivity using Tatarski's refractive index structure function.  $C_n^2$  values in the range 3 to  $17 \times 10^{-14} \text{m}^{-2/3}$  are taken from measured scintillation data.

Figure 7-4 shows the predicted fluctuations in refractivity are small ( $<10^{-6}$ ) when compared to the thousands of N-unit gradients that occur during ducting conditions.

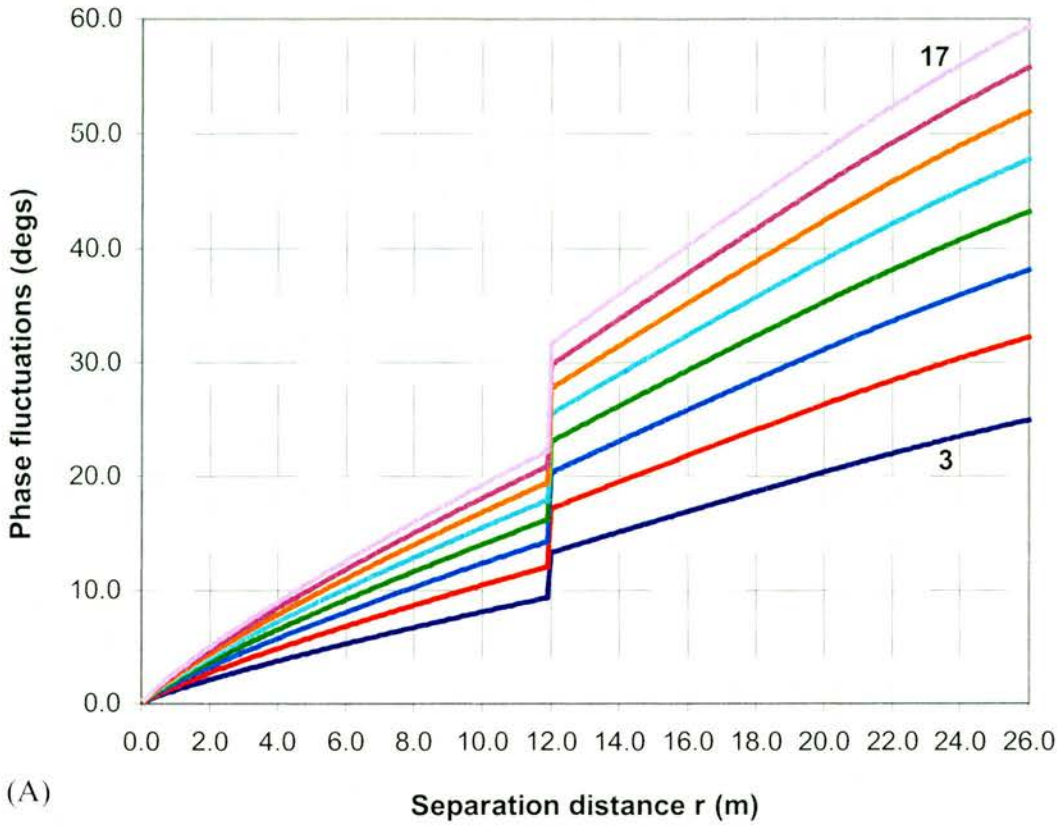
The values indicate the small differences in refractive index that define eddies, which in previous chapters were shown to result in many decibels of signal power fluctuation. Their effect on phase is considered in the next section.

## 7.5 Phase fluctuations

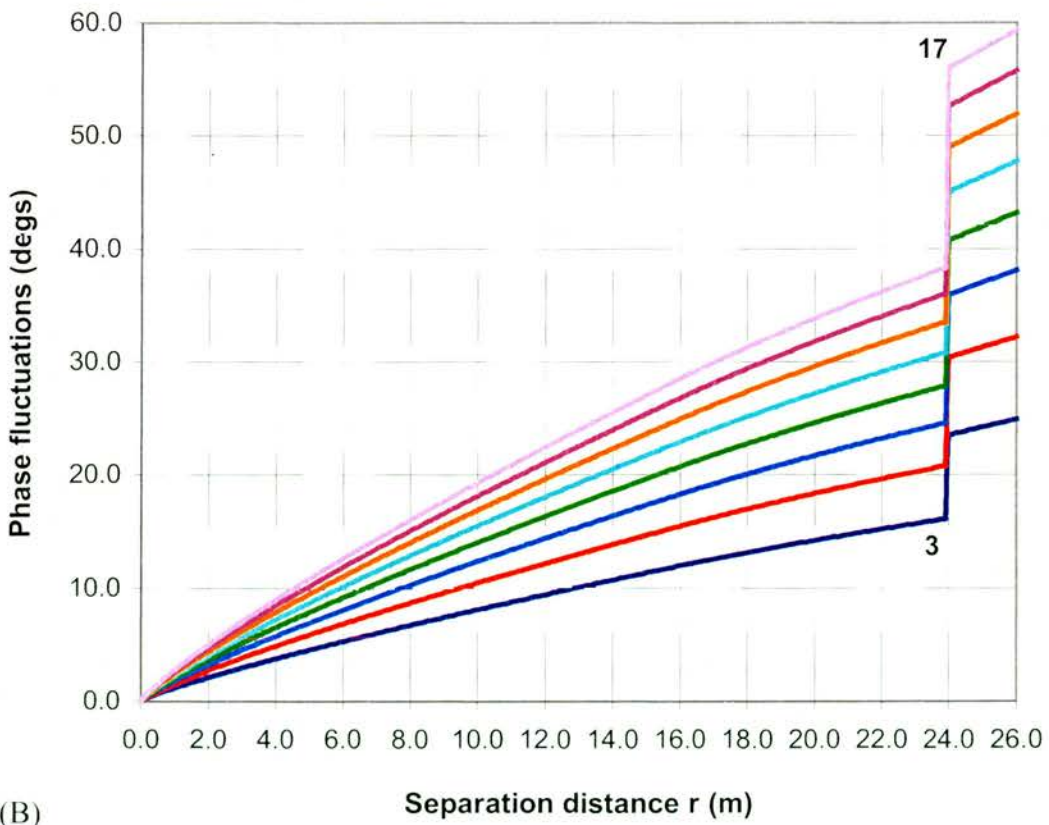
Wavefront distortion was shown in equation (7-7) to be a function of path length, wavenumber, sensor separation distance and  $C_n^2$ . The boundary conditions state that the difference in phase fluctuations is a factor of two times larger when the separation distance ( $r$ ) between sensors is greater than the size of the first Fresnel zone ( $\sqrt{\lambda L}$ ). However, in the previous chapter the measured scintillation decorrelation distance (the point at which the correlation coefficient is zero) was  $1.3\sqrt{\lambda L}$  compared to Tatarski's predicted  $0.65\sqrt{\lambda L}$ . This implies that the boundary condition in equation (7-7) could be  $2\sqrt{\lambda L}$ .

The difference in the boundary condition from  $\sqrt{\lambda L}$  to  $2\sqrt{\lambda L}$  increases the size that an antenna array could be with up to half the predicted intensity of phase fluctuations, i.e. the longer decorrelation scale-length acts to reduce the amount of wavefront distortion. This difference is reflected in Figure 7-5.

Figure 7-5 illustrates the predicted difference in phase fluctuations for boundary conditions  $\sqrt{\lambda L}$  and  $2\sqrt{\lambda L}$ . The doubling in decorrelation scale-length for the  $2\sqrt{\lambda L}$  case results in a predicted reduction in phase fluctuations of up to 12° for a  $C_n^2$  value of  $17 \times 10^{-14} \text{ m}^{-2/3}$  and antenna separation distance of 16m.



(A)



(B)

Figure 7-5 Phase fluctuations calculated from measured scintillation data. Step at 12m (A) and 24m (B) indicates boundary conditions  $\sqrt{\lambda L}$  and  $2\sqrt{\lambda L}$  respectively.

The predicted wavefront distortion illustrated by Figure 7-5 could significantly impair the ability of large (>10m) antenna arrays. An application that would be particularly impaired by such wavefront distortion is radar imaging. Such systems are dependent on planar wavefronts to resolve fine detail, which at millimetre wave frequencies is ultimately limited by the turbulent atmosphere. This has been shown to be the case for synthetic aperture radar at microwave frequencies (Porcello, 1970), but to date has not been reported in the open literature for millimetre wave frequencies. For communication systems the predicted phase fluctuations will limit the discrimination required for higher order digital modulation schemes, e.g. 64-QAM. The limitation will become more significant as the spatial separation distance increases and / or the modulation order (number of levels) increase. Phase fluctuations will also impact the ability of antenna arrays to accurately track mobile sources (Godara, 1997). For long-range millimetre wave applications where beam widths are typically 2-4°, fluctuations in angle-of-arrival may lead to periods of communication outage and lost target acquisition because the receiving antenna is unable to track the transmitter. The effect of angle-of-arrival fluctuations is considered in the following section.

## 7.6 Angle-of-arrival fluctuations

The angle-of-arrival of a wavefront impinging upon spatially separated antennas may be calculated from spatial phase fluctuation data. The method employed is illustrated in Figure 7-6. It shows a wavefront at oblique angle of incidence to receiving antennas RX1 and RX2. The path length difference ( $\Delta r$ ) between the signals arriving at RX1 and RX2 is equal to  $r \sin(\theta_{AOA})$ , and the time difference between the arrival of the signals is given by equation (7-13).

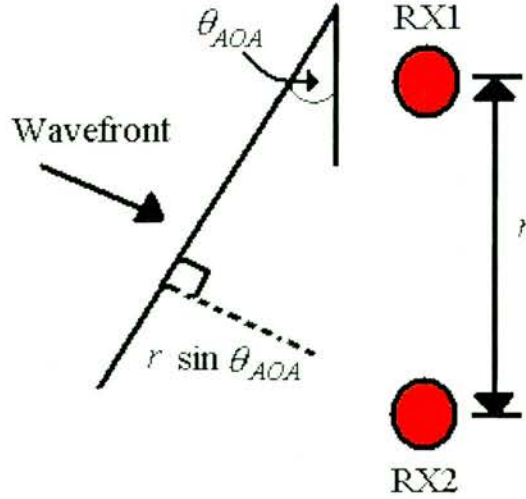


Figure 7-6 Geometry of angle-of-arrival ( $\theta_{AOA}$ ) calculation using phase fluctuation data.

$$\Delta t = \frac{\Delta r}{\lambda f} \quad (7-13)$$

where  $f$  (Hz) is the signal frequency. The phase difference ( $\Delta\phi$ ) corresponding to the time delay  $\Delta t$  is given by:

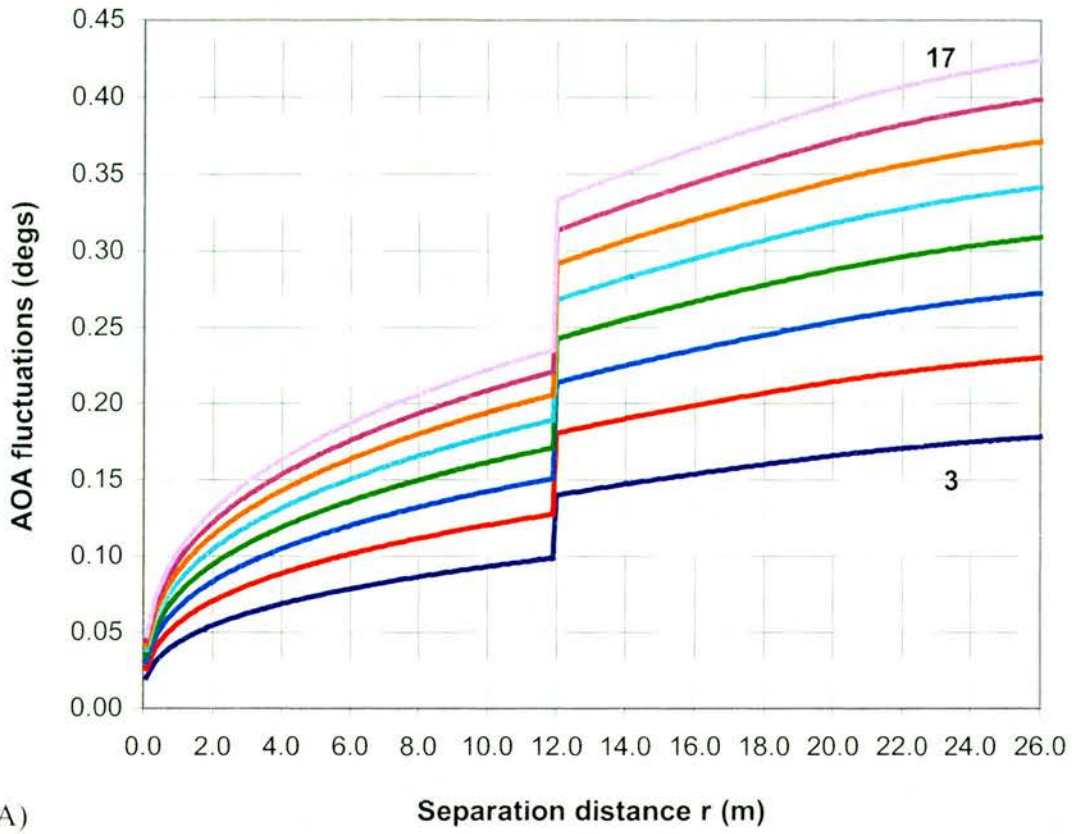
$$\Delta\phi = \Delta t \times 2\pi \times f \quad (7-14)$$

$$\begin{aligned} \therefore \Delta\phi &= \frac{2\pi}{\lambda} r(\sin \theta_{AOA}) \\ &= k r(\sin \theta_{AOA}) \end{aligned}$$

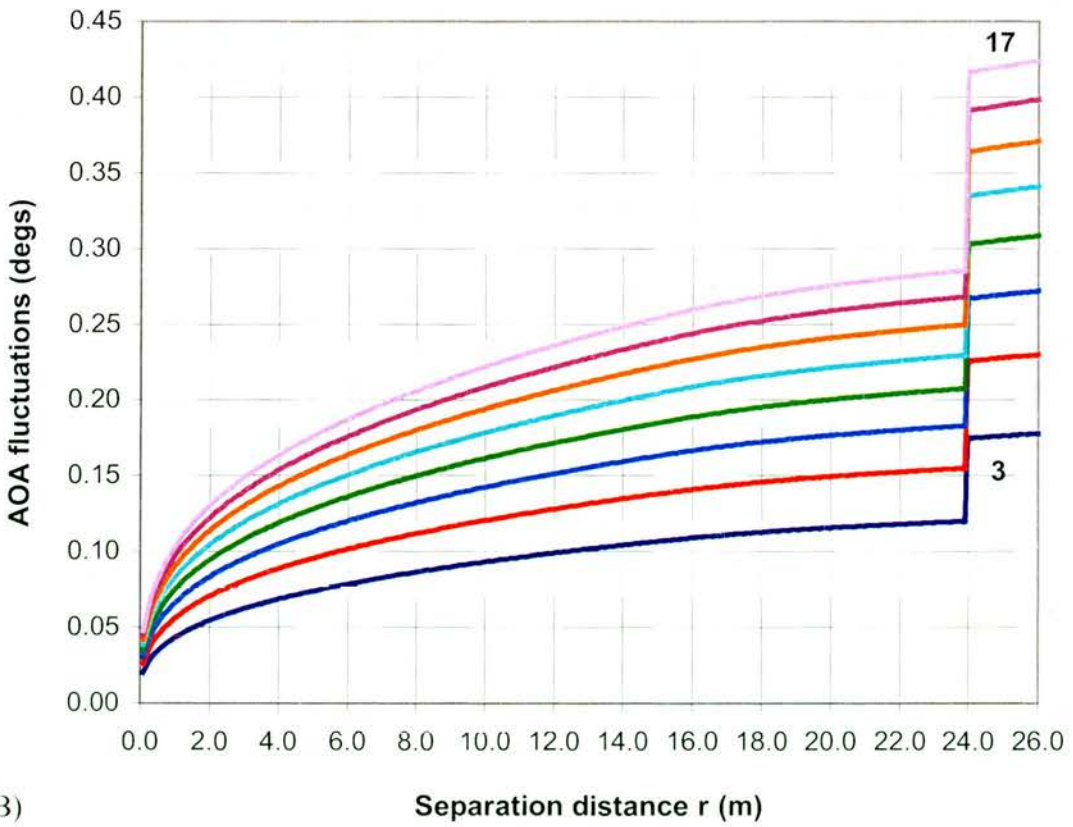
By rearranging equation (7-14) the angle-of-arrival for phase difference  $\Delta\phi$  is given by:

$$\theta_{AOA} = \sin^{-1}\left(\frac{\Delta\phi}{kr}\right) \quad (7-15)$$

Using equation (7-15) with  $\Delta\phi$  given by the predicted phase fluctuation data shown in Figure 7-5, the predicted angle-of-arrival fluctuations for boundary conditions set by  $\sqrt{\lambda L}$  and  $2\sqrt{\lambda L}$  are shown in Figure 7-7.



(A)



(B)

Figure 7-7 Angle-of-arrival fluctuations calculated from the phase fluctuations shown in Figure 7-5.

Figure 7-7 shows the predicted difference in angle-of-arrival for boundary conditions  $\sqrt{\lambda L}$  and  $2\sqrt{\lambda L}$ . It illustrates a significant decrease in angle-of-arrival going from the  $2\sqrt{\lambda L}$  to  $\sqrt{\lambda L}$  boundary conditions, e.g.  $\sim 0.12^\circ$  for antenna separation distances of 16m.

Angle-of-arrival fluctuations can result in significant tracking errors where long propagation paths are concerned. For example, Figure 7-8 shows that the predicted tracking errors given by equation (7-16) could extend up to 200m for a path length of 50km, antenna separation distances of 10m and angle-of-arrival fluctuations given in Figure 7-7.

$$T_{error} = L \sin(\theta_{AOA}) \quad (7-16)$$

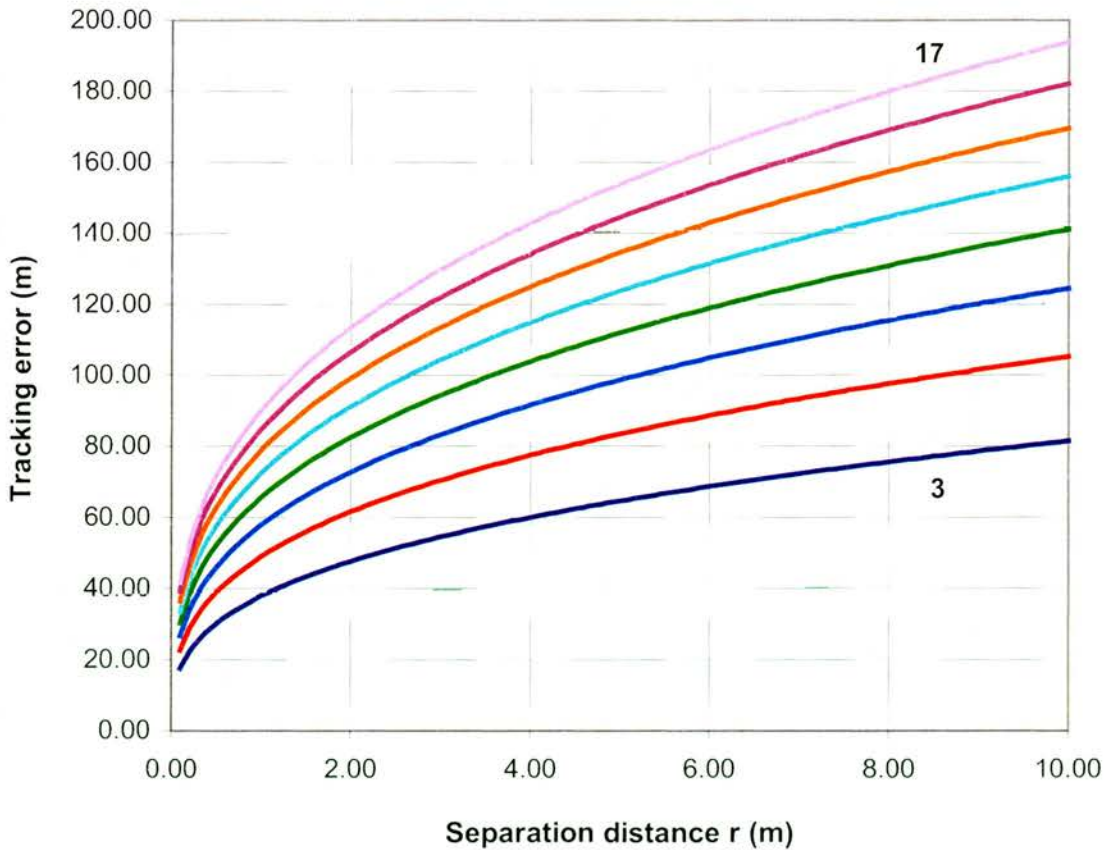


Figure 7-8 Tracking errors calculated from angle-of-arrival predictions.

## 7.7 Summary

This chapter has considered wavefront distortion using temporal measurements of power fluctuations. Tatarski's structure function models were used with values of  $C_n^2$  derived from measured scintillation events. The mean value of  $C_n^2$  was shown to be in good agreement with previous studies and lend support to the applicability of Tatarski's path length scaling law for long-link millimetre wave propagation.

It was shown that calculated values of  $C_n^2$  ranged from  $3 \times 10^{-14} \text{m}^{-2/3}$  during benign channel conditions to  $17 \times 10^{-14} \text{m}^{-2/3}$  during periods of scintillation. This almost factor of five increase was reflected in the predicted refractive index fluctuations of  $10^{-6}$  N-units and  $20^\circ$  phase fluctuations for antenna separation distances (array sizes) of 10m. It was shown that the increase in decorrelation scale-length measured in the previous chapter ( $2\sqrt{\lambda L}$ ) would reduce the intensity of predicted phase fluctuations due to the change in applicability of the phase structure function boundary conditions.

The addition of phase incoherent signals from spatially separated receivers will limit the phase discrimination required for higher order multi-level digital modulation schemes, e.g. 64-QAM. It will also limit the achievable resolution of imaging systems and the tracking accuracy of mobile platforms, especially radar systems where millimetre wave frequencies are employed specifically to track small objects. For example, predicted angle-of-arrival fluctuations of  $0.23^\circ$  for antenna separation distances of 10m would result in tracking errors of up to 200m for path lengths of 50km. In practice, tracking errors could be much larger for airborne radar applications where path lengths may extend beyond 100km.

# Chapter Eight

## Conclusions

### 8.1 Purpose of research

The purpose of the research presented in this thesis was to investigate the effects of atmospheric turbulence on millimetre wave propagation in the surface boundary layer. A specially designed millimetre wave array consisting of five sensors (antennas) was designed for this purpose. It enabled both temporal and small-scale spatial properties of tropospheric amplitude scintillation to be studied.

The sensor array was used for a month long measurement campaign. Data was collected at 36GHz using a 17.3km link traversing open countryside. Meteorological stations sited close to the link mid-point and sensor array location provided environmental information to correlate with propagation data. The following summarises the results from this experiment.

### 8.2 Summary of results

The first stage of the research consisted of designing and testing the sensor array. Tests of the full system and individual components confirmed the array was operating within design tolerances over short (minutes) and long (hours, days) measurement periods. Data from all five sensors was collected, with some downtime experienced from two of the sensors due to faulty MMIC receivers.

An initial study of refractive layering effects using a limited number of multipath events showed that nocturnal radiation could lead to significant signal fading, i.e. >17dB. The occurrence of fading was correlated with abrupt changes in ground-based meteorology, which confirmed previous observations at microwave frequencies (Touati et al, 1994; Craig and Kennedy, 1987).

The effect of multipath fading on millimetre wave communication systems was evaluated in terms of channel capacity. It was shown that for periods of several minutes during multipath fading the channel capacity could be reduced to a level that could appreciably impair the quality of service offered by commercial link operators.

A study of the temporal characteristics of tropospheric amplitude scintillation showed measured events with peak-to-peak variations of 10dB and durations of up to 20 minutes. In all cases the probability density of scintillation followed a Gaussian distribution with the strongest events having log-amplitude variances of  $0.45\text{dB}^2$ .

The strongest scintillation events occurred during the night and early morning. This is contrary to the mean signal fluctuation intensity that was shown to follow a diurnal cycle aligned with air temperature. Scintillation was also found superimposed on clear-air multipath events. It is therefore concluded that the most significant impact of clear-air effects (layering and turbulence) on terrestrial millimetre wave systems is during the night and early morning.

The spectral characteristics of tropospheric amplitude scintillation were also analysed. It was shown that the two-asymptote spectrum predicted by Ishimaru (1978) was in good agreement with measured data. The estimated corner frequency was however higher than expected. The reason for the higher than expected corner frequency could

not be determined from the data set analysed in this thesis. It would therefore be necessary to collect further scintillation data and meteorological measurements to identify the mechanism that produced these higher corner frequencies.

It was shown that the spatial correlation of atmospheric turbulence follows a diurnal cycle that is inversely related to air temperature. The spatial correlation variability with time was evaluated and found to be in good agreement with a Gaussian distribution with a standard deviation of 0.1dB centred on a mean correlation value that depends on antenna separation distance.

The median correlation between spaced receivers was evaluated for 18 days of data at seven points in the range 1-8m. It showed that correlation decreased for increasing antenna separation at a rate of  $\sim 1/27\text{m}^{-1}$ . This is a slower decrease than proposed by Tatarski's correlation function, which suggests the decorrelation scale-length of scintillation is approximately 2 times larger than predicted. This result indicates the separation distance required between antennas to mitigate scintillation in a spatial diversity system is larger than predicted. Using the same result the maximum gain of a coherent millimetre wave antenna array was shown to be a function of signal wavelength and turbulent path length in addition to the physical size of the array.

In addition to the spatial variation of amplitude fluctuations the phase variability (wavefront distortion) due to atmospheric turbulence was also considered. The analysis was based on Tatarski's structure function models and values of  $C_n^2$  derived from measured scintillation events. It was shown that calculated values of  $C_n^2$  validated using previous measurements ranged from  $3 \times 10^{-14} \text{m}^{-2/3}$  during benign channel conditions to  $17 \times 10^{-14} \text{m}^{-2/3}$  during periods of scintillation. This almost factor

of five increase was reflected in the predicted refractive index fluctuations of  $10^{-6}$  N-units and  $20^\circ$  phase fluctuations for antenna separation distances (array sizes) of 10m. It was shown that the measured increase in decorrelation scale-length reduced the intensity of predicted phase fluctuations due to the change in applicability of the phase structure function boundary conditions.

From the predicted phase fluctuations both angle-of-arrival fluctuations and tracking errors were calculated. It was shown that angle-of-arrival fluctuations of  $0.23^\circ$  with antenna separation distances of 10m would result in tracking errors of up to 200m for path lengths of 50km. In practice, tracking errors could be much larger for airborne radar applications where path lengths may extend beyond 100km.

In conclusion, the research described in this thesis has shown that atmospheric turbulence in the surface boundary layer could significantly impair systems operating at millimetre wave frequencies. Amplitude scintillation could lead to link outages especially for communication systems operating with low fade margins. Phase scintillation from spatially separated receivers will impact the tracking of mobile platforms, especially radar systems where millimetre wave frequencies are employed specifically to track small objects.

### **8.3 Future work**

Two further studies in to the effects of atmospheric turbulence in the surface boundary layer are currently being performed. The first is taking place at the University of St Andrews and the second at the University of Bath.

The study at the University of St Andrews is investigating the possible links between refractive index fluctuations and communication link outages on 38GHz cellular radio back-haul links. The study is using a three-port wideband (25MHz) spatial interferometer (Evans et al, 2001; Evans et al, 2002) to measure amplitude and phase fluctuations across a 28km link.

The study at the University of Bath is using a five-port wideband (80MHz) spatial interferometer (Evans and Smith, 2001) to investigate turbulence in both the vertical and horizontal directions simultaneously, i.e. a cross-shaped array with three elements in the vertical and three in the horizontal. Data from this experiment will be used to develop scintillation prediction models for planning terrestrial communication links.

# References

- AKRAM, A., SHUKLA, A., JONES, S. and HARRISS, A., "*High-Altitude 30-40GHz Radiowave Propagation Experiment (UC)*", DERA report DERA/CIS/CIS1/WP990341, May 1999.
- BARRY, R.G. and CHORLEY, R.J., "*Atmosphere, Weather & Climate*", Routledge, 1998.
- BASILI, P., CIOTTI, P., D'AURIA, G., FERRAZZOLI, P. and SOLIMINI, D., "*Case study of intense scintillation events on the OTS path*", IEEE Transactions on Antennas and Propagation, Vol. 38, No. 1, pp. 107-113, 1990.
- BEAN, B.R. and DUTTON, E.J., "*Radio Meteorology*", National Bureau of Standards Monograph 92, March 1966.
- BLAUNSTEIN, N., "*Radio propagation in cellular networks*", Artech House Publishers, 1999.
- BROWN, W.D., "*A model for the refractive-index structure constant at microwave frequencies*", SAND76-0593, Sandia Laboratories, 1977.
- BRUSSAARD, G., "*A meteorological model for rain-induced cross-polarisation*", AP-24, pp.5-11, 1976.
- BRUSSAARD, G. and WATSON, P.A., "*Atmospheric Modelling and Millimetre Wave Propagation*", Chapman & Hall, 1995.
- CARTWRIGHT, N.E. and TATTERSALL, R.L.O., "*Simultaneous measurements of radio refractivity and multipath fading on 2 July 1975 at 11, 19 and 36 GHz on a 7.5 km path*", Electronics Letters, Vol. 13, No.7, pp.208-210, March 1977.
- CHU, T.S., "*Rain-induced cross polarization at centimetre and millimetre wavelengths*", Bell Sys. Tech. J., Vol. 53, pp.1568-1569, 1974.
- CLAVERIE, J and KLAPSZ, C., "*Meteorological features leading to multipath propagation observed in the PACEM 1 experiment*", Annales des Telecommunications, vol. 40, No. 211-12, pp.660-671, 1985.
- COLE, R.S., HO, K.L. and MAVROKOUKOULAKIS, N.D., "*The effect of the outer scale of turbulence and wavelength on scintillation fading at millimetre wavelengths*", IEEE Trans. on Antennas and Propagation, Vol. AP-26, No. 5, pp.712-715, 1978.
- COLIN, R.E., "*Antennas and radiowave propagation*", McGraw-Hill, 1985.
- COST 235, "*Final report: Radiowave propagation effects on next-generation fixed-services terrestrial telecommunications systems*", European Commission, 1996.

- COX, D.C., ARNOLD, H.W. and HOFFMAN, H.H., "*Observation of cloud produced amplitude scintillation on 19 and 29 GHz earth-space paths*", Radio Science, Vol. 16, pp885-907, 1981.
- CRAIG, K.H., "*Propagation planning procedures for LMDS*", ACTS Project 215, AC215/RAL/RCRU/DR/P/D3P1B/b1, 1999.
- CRAIG, K.H. and KENNEDY, G.R., "*Studies of multipath propagation on a microwave line-of-sight link*", Proc. 17<sup>th</sup> European Microwave conference, pp. 523-528, Italy, 1987.
- DETTMER, R., "*Broadband@home.com*", IEE Review, pp.13-17, January 2000.
- EMBREE, P.M. and DANIELI, D. "*C++ algorithms for digital signal processing*", Prentice Hall, 1999.
- EVANS, M., "*Millimetre wave propagation: Atmospheric turbulence and coherency*", MSc thesis, University of Wales, Swansea, 1999.
- EVANS, M., PRYDE, D.P. and LESURF, J.C.G., "*Development of a 3-port spatial interferometer for studying tropospheric refractive-index fluctuations at millimetre wave frequencies*", CLIMPARA, 2001.
- EVANS, M., SHUKLA, A., LESURF, J.C.G. and EDEN, D., "*Preliminary phase and amplitude fluctuation measurements at 38GHz using spatial interferometry*", URSI GA, 2002.
- EVANS, M. and SMITH, A., "*A 2D array for investigating atmospheric turbulence at Ka band frequencies*", UK-Ireland URSI meeting, pp.25, 2001.
- FANTE, R.L., "*Electromagnetic beam propagation in turbulent media*", Proceedings of the IEEE, Vol. 68, No. 11, 1980.
- FOWLER, T., "*Mesh networks for broadband access*", IEE Review, pp.17-22, January 2001.
- FRISCH, U., "*Turbulence: The legacy of A.N. Kolmogorov*", Cambridge University Press, 2001.
- GJESSING, D.T., KJELAAS, A.G. and GOLTON, E., "*Small-scale atmospheric structure deduced from measurements of temperature, humidity and refractive index*", Boundary-Layer Meteorology 4, pp. 475-492, 1973.
- GODARA, L.C., "*Application of antenna arrays to mobile communications, Part II: Beam-forming and direction-of-arrival considerations*", Proc. Of the IEEE, Vol. 85, No. 8, pp. 1195-1245, 1997.
- GUNN, K.L.S. and EAST, T.W.R., "*The microwave properties of precipitation particles*", Q.J.R. Meteorology, Society of London, Vol. 80, pp. 522-545, 1954.

- HADDON, J. and VILAR, E., "Scattering induced microwave scintillation from clear-air and rain on earth space paths and the influence of antenna aperture", IEEE Trans. AP-34, pp.646-657, 1986.
- Haidara, F. et al, "Measurements of cross-correlation between spaced receivers from the Virginia Tech Olympus experiment", Proc. of the 18<sup>th</sup> OPEX meeting, pp.740-743, 1992.
- HALL, M.P.M, "Effects of the troposphere on radio communication", IEE, 1979.
- HALL, M.P.M. et al, "Propagation of radiowaves", IEE, 1996.
- HALSAL, F., "Data communications, computer networks and open systems", Addison Wesley, 1996.
- HO, K.L., MAVROKOUKOUKAKIS, N.D. and COLE, R.S., "Determination of the atmospheric refractive index structure parameter from refractivity measurements and amplitude scintillation measurements at 36 GHz", Journal of Atmospheric and Terrestrial Physics, Vol. 40, pp.745-747, 1978.
- HUFNAGEL, R., "Variations of atmospheric turbulence", Proc. of the Topical meeting on Optical Propagation through Turbulence, pp. WA1-1 – WA1-4, 1974.
- ISHIMARU, A., "Wave propagation and scattering in random media", Vol. 2, Academic Press, 1978.
- ITU-R P.676, "Attenuation by Atmospheric Gases", 1999.
- ITU-R P.838, "Specific attenuation model for rain for use in prediction methods", 1999.
- ITU-R P.837, "Characteristics of precipitation for propagation modelling", 2001.
- ITU-R P.530, "Propagation data and prediction methods required for the design of terrestrial line-of-sight systems", 1999.
- ITU-R P.618, "Propagation data and prediction methods required for the design of Earth-space telecommunications systems", 2001.
- ITU-R P.840, "Attenuation due to clouds and fog", 1999.
- ITU-R P.836, "Water vapour: surface density and total columnar content", 2001.
- ITU-R P.453, "The radio refractive index: Its formula and refractivity data", 1999.
- ITU-R P.834, "Effects of tropospheric refraction on radiowave propagation", 1999.
- KARASAWA, Y., YAMADA, M., and ALLNUTT, J.E., "A new prediction method for tropospheric scintillation on Earth-space paths", IEEE Transactions on Antennas and Propagation, Vol. 36, No.11, pp.1608-1614, 1988.

- LEE R.W. and WATERMAN A.T., "*Space correlations of 35-GHz transmissions over a 28-km path*", Radio Science, Vol. 3, No. 2, 1968.
- LLORET, V., GIMONET, E. and CASTANET, L., "*Spectral characteristics of propagation impairments on experimental earth-space links at Ka and V bands*", 11<sup>th</sup> International Conference on Antennas and Propagation, Vol. 2, pp.546-550, April 2001.
- LUMLEY, J.L. and PANOFSKY H.A., "*The structure of atmospheric turbulence*", John Wiley & Sons, 1964.
- MARZANO, F.S. and D'AURIA, G., "*Model-based prediction of amplitude scintillation variance due to clear-air tropospheric turbulence on Earth-satellite microwave links*", IEEE transactions on Antennas and Propagation, Vol. 46, No.10, pp.1506-1518, 1998.
- MATRICCIANI, E., MAURI, M and RIVA, C., "*Scintillation and simultaneous rain attenuation at 49.5GHz*", ICAP 95, No. 407, pp.165-168, 1995.
- MCMILLAN, R.W. and BOHLANDER, R.A., "*An investigation of millimetre wave propagation in the atmosphere: measurement program*", Report ADA184837, Georgia Institute of Technology, 1987.
- MEDEIROS FILHO, F.C., JAYASURITYA, D.A.R., COLE, R.S. and HELMIS, C.G., "*Spectral density of millimetre wave amplitude scintillations in an absorption region*", IEEE Transactions on Antennas and Propagation, Vol. AP-31, No. 4, pp. 672-676, 1983.
- MOULSLEY, T.J. and VILAR, E., "*Experimental and theoretical statistics of microwave amplitude scintillations on satellite down-links*", IEEE Trans., AP-30, pp.1099-1106, 1982.
- NORTON, K.A. et al, "*An experimental study of phase variations in line-of-sight microwave transmissions*", National Bureau of Standards, Monograph 33, 1961.
- OGUCHI, T. and HOSOYA, Y., "*Scattering properties of oblate raindrops and cross polarization of radio waves due to rain, (Part II) Calculations at microwave and millimetre wave regions*", J. Radio. Res. Labs. Japan, Vol. 21, pp.191-259, 1974.
- ORTGIES, G., "*Probability density functions of amplitude scintillations*", Electronics Letters, Vol. 21, no. 4, February 1985.
- ORTGIES, G., "*Prediction of slant-path amplitude scintillation from meteorological parameters*", Proc. Int. Symposium on Radio Propagation, pp.218-221, 1993.
- OTT, R.H. and THOMPSON, M.C., "*Atmospheric amplitude spectra in an absorption region*", IEEE Transactions on Antennas and Propagation, Vol. AP-26, No. 2, pp. 329-332, 1978.

- OTUNG, I.E., “*Prediction of tropospheric amplitude scintillation on a satellite link*”, *IEEE Transactions on Antennas and Propagation*, Vol. 44, No.12, pp.1600-1608, 1996.
- OTUNG, I.E., AHMED, B. and EVANS, B.G., “*Diurnal variation of 20GHz amplitude scintillation intensity*”, *Satellite Communications – ECSC-3*, pp.414-418, 1993.
- OTUNG, I.E., AL-NUAIMI, O. and EVANS, B.G., “*Extracting scintillations from satellite beacon propagation data*”, *IEEE Trans. on Antennas and Propagation*, Vol. 46, No 10, pp.1580-1581, 1998.
- PEETERS, G., MARZANO, F.S., D’AURIA, G., RIVA, C: and VANHOENACKER, D., “*Evaluation of statistical models for clear-air scintillation using Olympus satellite measurements*”, *International Journal of Satellite Communications*, Vol. 15, pp.73-88, 1997.
- PORCELLO, L.J., “*Turbulence-induced phase errors in synthetic-aperture radars*”, *IEEE Trans. on Aero. and Elect. Systems*, pp.636-644, Vol. AES-6, No. 5, 1970.
- PRASAD, M.V.S.N., SARKAR, S.K., DUTTA, H.N. and REDDY, B.M., “*Multipath fading characteristics of a digital microwave link in western India*”, *Annales des Telecommunications*, vol. 47, No.1-2, pp.49-55, 1992.
- PRUPACHER, H.R. and PITTER, R.L., “*A semi-empirical determination of the shape of cloud and rain drops*”, Vol. 28, pp.86-94, 1971.
- RIVA, C. and MARZANO, F.S., “*Scintillation modelling: a review*”, COST 280 report PM4002, Prague, 2002.
- RYDE, J.W., “*Attenuation and radar echoes produced at centimetre wavelengths*”, *Meteorological factors in radio-wave propagation*, Phys. Soc., London, 1946.
- RYTOV, S.M, “*Diffraction of light by ultrasonic waves*”, *Izv. Akad. Nauk SSSR, Ser. Fiz.*, no 2, p.223,1937.
- SARMA, A.D. and HERBEN, M.H.A.J., “*Variable cut-off frequency filter for wide scintillation bandwidth measurements*”, *Arch. Elektronik Ubertrag.*, Vol. 43, No. 6, pp. 378-381, 1989.
- SAUNDERS, M.J., “*Cross-polarisation at 18 and 30 GHz due to rain*”, *IEEE Transactions*, AP-19, pp. 273-277, 1971.
- SAVVARIS, A., KASSIANIDES, C.N. and OTUNG, I.E., “*Observed effects of wind on the intensity and spectrum of scintillation*”, 11<sup>th</sup> International Conference on Antennas and Propagation, Vol. 2, pp.546-550, April 2001.
- SHUKLA, A. K. and HARROD, R., “*High temporal-resolution channel characteristics at 40 GHz from a 30 km slant path radiowave propagation experiments*”, *IEE 11<sup>th</sup> International Conference on Antennas and Propagation*, Conference Publication 480, Vol.2, pp.839-843, April 2001.

- STROHBEHN, J.W., "*Line-of-sight wave propagation through the turbulent atmosphere*", Proc. of IEEE, Vol. 56, no8, August 1968.
- STULL, R.B., "*An introduction to boundary layer meteorology*", Kluwer Academic Press, 1988.
- TATARSKI, V.I., "*Wave propagation in a turbulent medium*", McGraw-Hill, 1961.
- TATARSKI, V.I., "*The effects of the turbulent atmosphere on wave propagation*", Israel Program for Scientific Translations, 1971.
- TAYLOR, G.I., "*The spectrum of turbulence*", Proc. Royal Society, A164, pp.476, 1938.
- TENNEKES, H. and LUMLEY, J.L., "*A first course in turbulence*", MIT Press, 1972.
- THOMPSON, M.C. et al, "*Phase and amplitude scintillations in the 10 to 40 GHz band*", IEEE Trans. on Antennas and Propagation, Vol. AP-23, No. 6, pp.792-797, 1975.
- THOMPSON, M.C. and JANES, H.B., "*Measurements of phase-front distortion on an elevated line-of-sight path*", IEEE Trans. on Aero. and Elect. Systems, Vol. AES-6, No.5, pp.645-656, 1970.
- THOMPSON, M.C., MARLER, F.E. and ALLEN, K.C., "*Measurement of the microwave structure constant profile*", IEEE Trans. on Antennas and Propagation, Vol. AP-28, No. 2, pp.278-280, 1980.
- TOUATI, M., EL ZEIN, G., and CITERNE, J., "*Line-of-sight multipath propagation measurements at 15 GHz over 500 MHz bandwidth*", AGARD CP-543, pp.24-1 - 24-10, July 1994.
- TYSON, R.K., "*Principles of adaptive optics*", Academic Press, 1991.
- VAN DE KAMP, M.M.J.L., TERVONEN, J.K., SALONEN, E.T. and POIARES BAPTISTA, J.P.V., "*Improved models for long-term prediction of tropospheric scintillation on slant paths*", IEEE Transactions on Antennas and Propagation, Vol. 47, No.2, pp.249-260, 1999.
- VASSEUR, H., "*Bandwidth limitations on millimetre-wave communications due to tropospheric clear-air phenomena*", PhD thesis, Universite Catholique de Louvain, 1995.
- VASSEUR, H., RAVARD, O. and VANHOENACKER-JANVIER, D., "*Prediction of slant-path scintillation from radiosonde measurements*", CLIMPARA, pp.12-13, 1996.
- VASSEUR, H. and VANHOENACKER-JANVIER, D., "*Characterisation of tropospheric turbulent layers from the radiosonde data*", Electronic Letters, Vol. 34, No.4, pp.318-319, 1998.

- WARNOCK, J.M., VANZANDT, T.E. and GREEN, J.L., "*A statistical model to estimate mean values of parameters of turbulence in the free atmosphere*", 7<sup>th</sup> Symposium on Turbulence and Diffusion, pp.156-159, 1985.
- WEBSTER, A.R., "*Angles-of-arrival and delay times on terrestrial line-of-sight microwave links*", IEEE Transactions on Antennas and propagation, Vol. AP-31, No1, pp.12-17, January 1983.
- WEBSTER, A.R. and SCOTT, A.M., "*Angles-of-arrival and tropospheric multipath microwave propagation*", IEEE Transactions on Antennas and Propagation, Vol. AP-35, No.1, pp.94-99, 1987.
- WILLIS, G.E. and DEARDORFF, J.W., "*On the use of Taylor's translation hypothesis for diffusion in the mixed layer*", Quarterly Journal of the Royal Meteor. Society, 102, pp.817-822, 1976.
- YOUNG, P.H., "*Electronic communication techniques*", Merrill, 1994.

**Data sheet References**

Burr-Brown, INA118 precision instrumentation amplifier, data sheet PDS-1199A.

Burr-Brown, UAF42 filter, data sheet PDS-1070H.

Flann Microwave, lens horn antenna 2282QUCF, Flann Microwave catalogue.

Microstar Laboratories, IDSC1816 data acquisition system.

MCLI, power divider data sheet for PS5-5 and PS5-9, MCLI catalogue.

Mini-Circuits, mixer data sheet for model ZFM-4212, Mini-Circuits catalogue.

QinetiQ Electronics sector, MMIC receiver model 35GHz\_RX.

Reynolds industries, flexible waveguide (Stormflex II), Reynolds industries catalogue.